

Theoretical and Experimental Investigation of Phonon Boundary Scattering in Thin Silicon Membranes

Thesis by
Navaneetha Krishnan Ravichandran

In Partial Fulfillment of the Requirements for the
degree of
Doctor of Philosophy

The logo for the California Institute of Technology (Caltech), featuring the word "Caltech" in a bold, orange, sans-serif font.

CALIFORNIA INSTITUTE OF TECHNOLOGY
Pasadena, California

2017
(Defended August 15, 2016)

© 2017

Navaneetha Krishnan Ravichandran
All rights reserved

ACKNOWLEDGEMENTS

This dissertation would not have been possible without the guidance of my advisor Prof. Austin Minnich. His passion and enthusiasm towards science and research are qualities that I hope to emulate in my professional career. His knowledge and understanding of our research field, and his creative and critical thinking have helped improve the work presented in this dissertation tremendously. I am grateful to Prof. Minnich for providing a research atmosphere that encouraged debates on various research topics, and for giving me the freedom to pursue my research ideas. I sincerely thank him for giving me several opportunities to meet and discuss research with the speakers of the MRL and the MCE seminar series, and for being understanding of my situation when I was going through a major family health crisis during my third year as a graduate student.

I would like to sincerely thank my doctoral committee members: Prof. Melany Hunt, Prof. Guillaume Blanquart and Prof. Andrei Faraon for meeting with me several times and giving me valuable inputs that have improved the quality of this thesis. I am grateful to the Light-Material Interactions Energy Frontier Research Center for funding the first part of my doctoral work, and the Resnick Sustainability Institute and the Dow Chemical Company for funding my fourth and fifth year at Caltech through the Dow-Resnick graduate fellowship. I would also like to thank Dr. Neil Fromer for giving me suggestions to improve my fellowship application, and taking the time to meet with me on several occasions over the past few months to discuss my research. I am grateful to the Kavli Nanoscience Institute for letting me use their facilities, and I am thankful to its staff, particularly, Matt Sullivan, Carol Garland and Melissa Melendes for training me on several sample fabrication and characterization equipments. I would like to thank Prof. Keith Nelson's group at MIT, in particular, Dr. Alex Maznev and Dr. Jeremy Johnson, for giving me valuable suggestions and quick-fixes while setting up the transient grating experiment.

I have been extremely fortunate to work with smart and considerate lab mates over the past few years. I am extremely grateful to Hang Zhang and Xiangwen Chen for patiently answering my questions about optics and sample fabrication, while I was learning to set up my experiment. I would also like to acknowledge Chengyun Hua, Andrew Robbins, Nick Dou, Nate Thomas, Nina Shulumba and the entire Minnich

group for discussions over various research topics, and constructive comments to improve my conference talks during practice sessions.

I would like to thank all my friends at Caltech, in particular, Srivatsan Hulikal, Thevamaran Ramathasan and Mythili Thevamaran for making my stay here a pleasant and memorable one. We have had several unforgettable dinner debates, board game weekends and camping trips, which I thoroughly enjoyed every single time. Finally I would like to thank my family for their love and support. In particular, I would like to thank my mom, my dad and my wife Swetha Veeraraghavan for helping me cope with the ups and downs of graduate study and for being a constant source of encouragement.

ABSTRACT

The thermal transport properties of thin semiconductor membranes play an important role in the performance of many technologies like micro-electronics and solid-state energy conversion. The dominant resistance to heat flow in thin membranes is offered by the scattering of thermal phonons at the membrane boundaries. In this dissertation, we examine the nature of microscopic phonon boundary scattering processes and their effect on the thermal conductivity of the thin membranes using a pump-probe experimental technique and computationally efficient solutions of the phonon Boltzmann transport equation (BTE).

First, we investigate the boundary scattering-limited thermal transport in nanostructures using an efficient variance-reduced Monte Carlo (MC) solution of the BTE to elucidate the impact of specular and diffuse phonon boundary scattering events on the thermal conductivity of the nanostructures. To directly measure the relative frequency of these two boundary scattering events, called the phonon specularly parameter, we design, implement and characterize a non-contact laser-based pump-probe experiment called the transient grating (TG) to perform phonon mode-dependent measurements of the specularly parameter in suspended free-standing thin silicon membranes. We describe the phenomenon of quasiballistic heat conduction, which enables the phonon mode-dependent measurements of the specularly parameter, and derive a transfer function based on the BTE with ab-initio phonon properties as inputs, to connect the specularly parameter with the experimentally measured thermal conductivity of the thin membranes.

Finally, we present the methodology adopted to invert the BTE transfer function to extract the phonon specularly parameter from the thermal conductivity measurements in the TG experiment, while rigorously accounting for the experimental uncertainties. We find that the observed magnitudes and trends of the thermal conductivity of the thin membranes cannot be explained by the 50-year old Ziman's model for the phonon specularly parameter and the Fuchs-Sondheimer theory of phonon boundary scattering. We also find that the partially specular boundary scattering picture of phonon boundary interactions works well for one of the membranes, enabling a direct measurement of the mode-dependent phonon specularly parameter for the first time in an experiment. We discuss the possibility of phonon

mode conversion at the boundaries of a few membranes for which the partially specular phonon boundary scattering picture fails to explain the observed thermal conductivity trends. Considering the importance of understanding phonon boundary scattering to engineer and improve nanoscale device performance, we expect that the new experimental and computational tools developed in this work will advance a variety of nanoscale energy applications and further our understanding of nanoscale heat transport.

PUBLISHED CONTENT AND CONTRIBUTIONS

1. Navaneetha K. Ravichandran and Austin J. Minnich. “Coherent and incoherent thermal transport in nanomeshes”. In: *Physical Review B* 89.20 (May 2014), p. 205432, DOI: 10.1103/PhysRevB.89.205432.

URL: <http://link.aps.org/doi/10.1103/PhysRevB.89.205432>

Contributions: Navaneetha K. Ravichandran participated in the conception of the idea for the project, solved the problem, analyzed the results and participated in writing the manuscript.

2. Navaneetha K. Ravichandran and Austin J. Minnich. “Role of thermalizing and nonthermalizing walls in phonon heat conduction along thin films”. In: *Physical Review B* 93.3 (Jan. 2016), p. 035314, DOI: 10.1103/PhysRevB.93.035314.

URL: <http://link.aps.org/doi/10.1103/PhysRevB.93.035314>

Contributions: Navaneetha K. Ravichandran participated in the conception of the idea for the project, solved the problem, analyzed the results and participated in writing the manuscript.

TABLE OF CONTENTS

Acknowledgements	iii
Abstract	v
Published Content and Contributions	vii
Table of Contents	viii
List of Illustrations	x
Chapter I: Introduction	1
Chapter II: Phonon Boundary Scattering in Nanostructures	8
2.1 Background	8
2.2 Modeling	10
2.3 Results	11
2.4 Conclusion	18
Chapter III: Quasiballistic Heat Transfer	19
3.1 Breakdown of Fourier’s Law of Heat Diffusion	19
3.2 Time-domain Thermoreflectance to Probe Quasiballistic Heat Con- duction	21
Chapter IV: The Thermal Transient Grating Experiment	29
4.1 Recipe to Measure Phonon Specularity Parameter	29
4.2 Working Principle	30
4.3 Lens Arrangement for Laser Alignment	34
4.4 Experiments in Water	35
4.5 Experiments in Gallium Arsenide	38
4.6 Fabrication of Suspended Thin membranes	40
4.7 Experiments on Free-standing Silicon Membranes	43
Chapter V: Model For Transient Grating from the Boltzmann Transport Equa- tion	48
5.1 Introduction	48
5.2 Modeling	50
5.3 Results & Discussion	81
5.4 Extension to Finite Pump-Probe Penetration Depth	88
5.5 Conclusion	89
Chapter VI: Phonon Specularity Parameter Measurement	93
6.1 Ab-initio Bulk Phonon Properties for Silicon	93
6.2 Impurity Scattering Rate in Thin Membranes	94
6.3 Failure of Ziman’s Specularity Model	97
6.4 Bayesian Inference to Extract Specularity Parameter	98
6.5 Optimal Profile for the Specularity Parameter	101
6.6 Possibility of Phonon Mode Conversion at the Membrane Boundaries	102
Chapter VII: Summary and Outlook	111
7.1 Outlook	113

Bibliography	115
Appendix A: The Effect of Finite Laser Penetration Depth on the Thermal Transport through Thin Films	
A.1 Numerical Discretization of the Boundary Conditions	129
A.2 Formulation of the Integral Equation for $\Delta\bar{T}$	136
A.3 The Method of Degenerate Kernels	142
Appendix B: The Effect of Phonon Mode Conversion at Boundaries on the Thermal Transport through Thin Films	
B.1 Numerical Discretization of the Boundary Conditions	150
B.2 Formulation of the Integral Equation for $\Delta\bar{T}$	158
B.3 The Method of Degenerate Kernels	163

LIST OF ILLUSTRATIONS

<i>Number</i>	<i>Page</i>
2.1 The geometry of a single periodic unit cell of the NM with either square and circular pore geometries, on which the Monte Carlo simulations have been performed. Walls (1) and (2) are modeled with periodic heat flux boundary conditions described in [70]. Walls (3) and (4) are modeled as specularly reflecting mirrors. The NM is three dimensional with the third dimension perpendicular to the plane of the paper with a finite non-zero thickness. The top and bottom boundaries in the out-of-plane direction and the walls of the NM pores are modeled as diffusely reflecting mirrors (or for a few simulations that are described in the main text, as partially specularly reflecting boundaries). Both square and circular pore geometries are considered in our simulations as the sample in Yu et al's experiments [29] is likely to have a shape somewhere in between the two extremes.	12
2.2 Thermal conductivity of the NM as a function of temperature. The thermal conductivity of the NM reported by Yu et al. [29] (black diamonds) is significantly lower than our simulation result with square and circular pore geometries.	13
2.3 Thermal conductivity accumulation versus phonon frequency for a NM that reflects phonons with frequency less than 2 THz specularly and the rest diffusely. Even under these conservative assumptions, the reported measurements cannot be explained even by completely neglecting the contribution of these low frequency phonons that could undergo coherent interference.	13

2.4	Thermal conductivity as a function of temperature for different nanostructures in the experiments of Yu et al. [29] and our simulations for (a) 2 nm disordered layer thickness and (b) 3.5 nm disordered layer thickness. The disordered layer is added to both the nanowire-array (NWA) and the NM in our simulations. In these two figures, the red dashed line, pink circles, and pink squares are the MC solutions for the NWA, NM with circular holes, and NM with square holes, respectively. The black diamonds, green triangles, and blue inverted triangles represent the reported thermal conductivity for the NM, the recalculated thermal conductivity for the NM, and the recalculated thermal conductivity for the NWA, respectively, from Yu et al.'s experiments [29].	15
2.5	Fraction of backscattered phonons for the NWA and the NM with circular and square holes for different disordered layer thicknesses.	17
3.1	(a) Schematic illustrating diffusive and quasiballistic heat transfer in the substrate. When the temperature profile decays faster in the substrate, the length scales corresponding to the dominant thermal spatial frequencies are shorter than phonon MFP, resulting in the breakdown of the Fourier's diffusion law, and quasiballistic thermal transport is observed in the substrate. (b) Comparison of impulse response obtained from full BTE simulation and finite-difference solution of the heat equation for a one-dimensional two-layer heat transfer geometry in a TDTR set up. Very good agreement is obtained between the BTE solution and the solution of the heat equation in the diffusive heat transfer regime in the substrate. In the quasiballistic regime, the BTE solution predicts a slower thermal decay, indicating quasiballistic suppression of substrate thermal conductivity. (c) Effective thermal conductivity of the substrate as a function of the modulation frequency of the input heat flux for the two-layer geometry shown in figure(a)	22
3.2	(a) Schematic of the periodic metal line array on single crystal wafer investigated in this work. (b) Impulse response for a line array simulation with 50% duty cycle and 100 nm line width for a long simulation time of $13\mu s$. Surface temperature is sampled once every 65 ps in the simulation, thereby providing sufficient resolution to capture thermal transport features at high frequencies.	23

3.3	TDTR signal obtained from MC simulations and the corresponding fit to a Fourier diffusion model with a single (k, G) pair for both low and high frequency components of the signal for line arrays with 80% duty cycle and $5 \mu\text{m}$ line width at room temperature and 1 MHz modulation frequency	25
3.4	TDTR signal obtained from MC simulations and the corresponding fit to Fourier model with different (k, G) pairs for low and high frequency components of the signal for line arrays with 80% duty cycle and $5 \mu\text{m}$ line width at room temperature and 1 MHz modulation frequency	26
3.5	Thermal conductivities (a) k_0 at 1 MHz modulation frequency, (b) k_0 at 15 MHz modulation frequency, and (c) k_1 , as a function of line width (w) for different line array duty cycles ($DC = w/p$) at 300 K . Thermal conductivities at both low and high modulation frequencies reach a minimum value as line width is decreased. The anomalous increase in thermal conductivity at short line widths at a fixed duty cycle has been attributed to the phenomenon of collective diffusion in literature [84].	27
3.6	Comparison of thermal conductivities k_0 at (a) 1 MHz modulation frequency (b) 7 MHz modulation frequency and (c) 15 MHz modulation frequency as a function of line width between different duty cycles ($DC = w/p$) and an isolated single line at 300 K . The thermal conductivity for isolated lines does not increase with decreasing line widths even for very short line widths at all modulation frequencies, which adds more evidence to the collective diffusion regime hypothesized in ref. [84]	28
4.1	Picture and schematic of the TG experiment. A diffractive optic (binary phase mask) splits pump and probe into ± 1 diffraction orders. Pump beams are focused on the sample by a pair of lenses to generate a thermal transient grating pattern. Probe beam diffracted from the thermal grating on the sample is combined with an attenuated reference beam (from the neutral density (ND) filter) and directed to a fast detector. The relative phase between the probe and reference beams is controlled by adjusting the angle of a glass slide (phase adjust) in the probe beam path.	31

4.2	Focal length of different lens and their locations to shape the pump beam for a target spot size of $440\ \mu\text{m}$ on the sample	34
4.3	Focal length of different lens and their locations to shape the probe beam for a target spot size of $420\ \mu\text{m}$ on the sample	35
4.4	Measured diameter of the probe beam using a beam profiler at the sample location and the corresponding Gaussian fit. The $1/e^2$ diameter of the fit is $420\ \mu\text{m}$	36
4.5	Grating pattern formed at the sample location captured using a Thorlabs scanning slit optical beam profiler for a grating period of $30\ \mu\text{m}$. The interference pattern produced is a convolution of the sinusoidal grating pattern with the Gaussian spot shape of the probe laser beam.	36
4.6	Conservative transient temperature rise on the first $1\ \text{nm}$ of the sample due to pulsed pump heating	37
4.7	Conservative steady temperature rise on the first $1\ \text{nm}$ of the sample due to continuous-wave probe heating	37
4.8	Acoustic waves in water observed in the TG experiment at different grating periods. The oscillations become faster as the grating period is reduced since the waves have to travel shorter distances to interfere with each other	38
4.9	Comparison of the acoustic wave frequency obtained from the TG experiment (Fourier transform of the signal) and calculated from the measurements of sound velocity in water in ref. [86]	38
4.10	TG signals from GaAs wafer at different grating periods, which represent a measure of the heating length scale. The decay rates of the TG signals increase with decreasing grating period, since, in general, heat conduction occurs in shorter times across a shorter separation between hot and cold regions of the thermal grating. The ripples in the signal are due to the surface acoustic waves (SAW) set up due to pump grating excitation on the sample surface.	39

- 4.11 Thermal conductivity of bulk GaAs measured as a function of grating period using the TG experiment at 294 K. Since the grating periods are comparable to phonon MFPs in GaAs at 294 K, long MFP phonons travel ballistically across the thermal grating and contribute to lower heat conduction compared to the prediction by Fourier's diffusion law. This quasiballistic heat conduction phenomenon is observed in the experiment as a decreasing thermal conductivity with decreasing grating period. 39
- 4.12 Schematic of the fabrication procedure for free-standing suspended silicon membranes. We start by spin-coating the SOI chip with a commercial protective layer (ProTEK B3 from Brewer Science Inc.) and open a window on the bottom handle layer by just mechanically scratching off some of the protective material. Next, we dip the SOI chip in KOH hot bath (50% concentration by weight at 70° C) until the etch window has reached the BOX layer. Finally, we remove the protective ProTEK B3 layer using a commercial remover provided by Brewer Science Inc., use wet HF etch to remove the BOX layer and release the remaining silicon device layer into a suspended free-standing single crystal silicon membrane. 41
- 4.13 Reflectometry measurement and fit for an SOI chip with a reported nominal silicon device layer thickness of 1200 ± 100 nm. The fit produced a device layer thickness of 1153 nm, in good agreement with the reported value. 42
- 4.14 SEM cross section image of a free-standing membrane with a device layer thickness of 653 ± 20 nm. The cross-section was created using a focussed ion beam (FIB). A small amount of gallium was deposited to provide contrast and protect the top interface (silicon-gallium interface) from damage due to FIB. 42

- 4.15 Overview of the TEM sample (left) and a high magnification image (right) of the silicon surface on the device layer. The high magnification image shows very good atomic resolution with clear atomic planes in some regions of the image, indicating good electron beam focus in those regions. While preparing this sample, the SOI chip was bonded to a silicon wafer (with a clean, native oxide-free surface) coated with nanocrystalline aluminum. We compared the images of the bond-silicon interface (shown in the right side figure) with the images of nanocrystalline Al-clean silicon interface and determined that the native oxide on the silicon surface of the SOI was less than 1.5 nm thick. 43
- 4.16 Least squares residual function for fitting a biexponential function ($\exp(-\lambda_1 t) - \exp(-\lambda_2 t)$) with decay rates λ_1 and λ_2 . The input profile to be fit with the biexponential function was generated with decay rates $\lambda_1 = 1000$ and $\lambda_2 = 10$ to simulate a larger difference in time scales between electronic and thermal decay in the TG experiment at short grating periods. A sharp minimum is found in the residual at $\lambda_1 = 1000$ and $\lambda_2 = 10$. However, the biexponential fit is, in general, a non-convex fit, with saddle points at large λ_1 along $\lambda_2 = 10$ in this case. 45
- 4.17 Least squares residual function for fitting a biexponential function ($\exp(-\lambda_1 t) - \exp(-\lambda_2 t)$) with decay rates λ_1 and λ_2 . The input profile to be fit with the biexponential function was generated with decay rates $\lambda_1 = 100$ and $\lambda_2 = 10$ to simulate a smaller difference in time scales between electronic and thermal decay in the TG experiment at long grating periods. A shallow minimum is found in the residual at $\lambda_1 = 1000$ and $\lambda_2 = 10$. However, the biexponential fit is, in general, a non-convex fit, with saddle points at large λ_1 with almost no change along λ_2 . Therefore, derivative based fitting methods alone cannot be used to fit the biexponential TG signals when a good initial guess for the decay rates is not available, especially for long grating periods. 45

- 4.18 TG signals and the corresponding biexponential fits (black dashed lines) from a 610 nm thick free-standing silicon membrane at different grating periods at 300 K. The decay rates of the TG signals increase with decreasing grating period, since, in general, heat conduction occurs in shorter times across a shorter separation between hot and cold regions of the thermal grating. Excellent signal to noise ratio is obtained in all of our measurements. The fitting was performed using a stochastic particle swarm algorithm to locate the global minimum well followed by a non-linear least squares method to converge at the global minimum point. 47
- 4.19 Thermal conductivity of a 610 nm thick free-standing silicon membrane measured as a function of grating period using the TG experiment at 300 K and 125 K. At 300 K, phonon MFP in bulk silicon is less than 10 μm , so we do not see any grating period dependence of thermal conductivity at long grating periods. However, for grating periods shorter than 10 μm , we see a weak grating period dependence of the measured thermal conductivity. At 125 K, phonon MFP in bulk silicon is significantly larger than 10 μm . So we observe strong grating period dependence of thermal conductivity even at long grating periods of 30 μm 47

- 5.1 Spatial distribution of the temperature profile and pictorial representation of the boundary conditions (equation 5.2) used in this work. The thin film is assumed to be infinite in extent along the in-plane (x) direction and has a finite thickness (d) in the cross-plane (z) direction. For steady state transport calculations, the temperature gradient exists only in the in-plane (x) direction. For transient transport, the initial temperature distribution is an in-plane sinusoidal distribution with a period λ , but can develop a cross-plane temperature gradient at later times. In the case of non-thermalizing wall, the diffusely reflected component g^{diff} of the distribution function is isotropic but away from local thermal equilibrium at the boundary while for the thermalizing wall, g^{diff} is equal to the local equilibrium distribution function g_0 . For both thermalizing and non-thermalizing boundary conditions, the specular reflection component (g^{spec}) has its direction reversed compared to the incoming distribution g^{in} and is also away from the local thermal equilibrium. In our work, we consider either thermalizing or non-thermalizing boundary conditions for both walls of the thin films at a time. 51

- 5.2 (a) Comparison of the cross-plane distribution of the in-plane steady state heat flux between analytical and Monte Carlo solutions of the BTE at 300 K and film thickness of 100 nm for different boundary conditions. The geometry of the thin film and the coordinate axes used in this work are the same as shown in figure 5.1. (b) Comparison of the steady state thermal conductivity between analytical and Monte Carlo solutions of the BTE at different temperatures and thin film thicknesses. For both (a) and (b), the Monte Carlo solutions are identical for thermalizing and non-thermalizing boundary scattering and agree well with the analytical solution derived in this work for both fully diffuse and partially specular boundary conditions (RMS 0.1 nm). For the partially specular boundary condition, the specularity parameter (p_ω) is calculated from Ziman’s specularity model [6] for a surface RMS roughness of 0.1 nm. (c) Effective MFPs of phonons computed using the Matthiessen’s rule (MR) and the Fuchs-Sondheimer (FS) theory for different film thicknesses and fully diffuse boundary scattering. Matthiessen’s rule underpredicts the effective phonon MFPs in thin films compared to the Fuchs-Sondheimer theory, which is a rigorous BTE solution. 82
- 5.3 (a) Comparison between time traces from the Monte Carlo (colored noisy lines) and the degenerate kernels solutions (black lines) of the BTE for a grating period of 20 μm at 500 K. (b) Comparison of the thermal conductivity predictions from the Monte Carlo (symbols) and the degenerate kernels solutions (black lines) of the BTE for different temperatures and grating periods. For both (a) and (b), the Monte Carlo solutions and the BTE solutions from this work are in very good agreement. (c) Plot showing the difference between the incoming and outgoing heat flux normalized by the incoming heat flux at the thin film boundaries as a function of the temporal frequency normalized by the maximum temporal frequency at which the simulations were performed (η_{max}). Specular and non-thermalizing diffuse boundary conditions conserve heat flux to numerical precision while thermalizing diffuse boundary condition violates heat flux conservation at the film wall under quasiballistic ($T = 100$ K, grating period = 1 μm) and diffusive ($T = 500$ K, grating period = 1000 μm) transport regimes. 85

- 5.4 Comparison of the thermal conductivity (a) and the suppression functions ((b) and (c)) calculated from the models FS I, FS II and by solving the BTE for non-thermalizing diffuse boundary conditions at different temperatures, grating periods (λ) and film thicknesses. In figures (b) and (c), the symbols correspond to the degenerate kernel solution, the solid lines correspond to FS I model and the dashed solid lines correspond to FS II model. For very thin films and long grating periods, the models FS I and FS II are in good agreement with the BTE predictions. For thicker films and shorter grating periods, FS I underpredicts and FS II overpredicts the thermal conductivity at short grating periods (a) and the contribution of phonons with long MFP ((b) and (c)) compared to the complete BTE solution. 88
- 5.5 (a) The sample heating geometry with finite laser penetration depth considered in this chapter. Along with a sinusoidal in-plane (x) distribution, an exponentially decaying initial temperature profile in the cross-plane (z) direction due to the finite penetration depth of the pump laser is also considered. Moreover, the finite penetration depth of the probe laser is also considered while solving the BTE for the experimentally measured signal. (b) Optical penetration depth of silicon from 80 K to 500 K for pump laser with a wavelength of 532 nm. The penetration depth of silicon for 532 nm light is $\sim 1 \mu\text{m}$, which is comparable to the membrane thicknesses in our experiments. (c) Validation of the BTE solution with simulations using the MC technique described in chapter 2 for fully specular boundary scattering in a suspended membrane of 1518 nm thickness at room temperature and a grating period of $11.5 \mu\text{m}$, considering finite penetration depth of light from figure (b). The semi-analytical BTE solution agrees well with the MC solution. Also shown for comparison is the semi-analytical solution for the same parameters, but with uniform cross-plane temperature distribution. The BTE solutions are very different initially for the uniform and exponentially decaying initial cross-plane temperature distributions, when cross-plane conduction is important. At later times, where only in-plane conduction occurs, the two solutions overlap. 90

5.6	Comparison of the temperature decay profiles between the BTE solutions considering finite penetration depth and uniform initial cross-plane temperature excitations for a 600 nm suspended membrane, a grating period of 2 μm and a mean temperature of 400 K while considering (a) fully specular boundary scattering (b) fully diffuse boundary scattering. In both cases, similar difference is observed between the BTE solutions considering finite penetration depth and uniform initial cross-plane temperature excitations.	91
5.7	Comparison of the temperature decay profiles between the BTE solutions considering finite penetration depth and uniform initial cross-plane temperature distributions for (a) a 600 nm suspended membrane, a grating period of 2 μm and a mean temperature of 400 K (b) a 1150 nm suspended membrane, a grating period of 2 μm and a mean temperature of 400 K (c) a 1150 nm suspended membrane, a grating period of 60 μm and a mean temperature of 80 K. In all three figures, specular boundary scattering is considered. In the case of the 600 nm membrane, there is very little difference in the time decay between the two cases even at a high temperature (short penetration depth, see figure 5.5 (b)) and a short grating period. For the 1150 nm membrane, the difference between the BTE solutions with finite penetration depth and uniform temperature distribution is larger than the 600 nm case, but the difference vanishes at lower temperatures and longer grating periods.	92
6.1	Comparison between spectral phonon specific heat accumulation computed using the <i>ab-initio</i> and equivalent isotropic phonon properties at 80 K	95
6.2	Comparison between spectral phonon thermal conductivity accumulation computed using the <i>ab-initio</i> and equivalent isotropic phonon properties at 80 K	95
6.3	Comparison between spectral phonon specific heat accumulation computed using the <i>ab-initio</i> and equivalent isotropic phonon properties at 400 K	95
6.4	Comparison between spectral phonon thermal conductivity accumulation computed using the <i>ab-initio</i> and equivalent isotropic phonon properties at 400 K	95

- 6.5 (a) Difference in the membrane thermal conductivity predicted by the BTE between fully specular and fully diffuse boundary scattering limits. At low temperatures of 100 K, the difference between the specular and diffuse limits is $\geq 60\%$, while at high temperatures of 400 K and short grating periods, the difference between the specular and diffuse limits is less than 10%. (b) Comparison between the experiments and the BTE solution that produced the best fit with the experiments. The impurity scattering rate coefficient A in Tamura's formula (equation 6.2) was extracted from this fit. 97
- 6.6 Measured thermal conductivity of a 525 nm thick membrane as a function of grating period at different temperatures. Also shown are the BTE predictions for fully specular, fully diffuse, and partially specular boundary scattering based on Ziman's specular model (equation 1.1). Ziman's specular model is unable to explain the experimental measurements over a range of temperatures and grating periods. 105
- 6.7 Measured thermal conductivity of a 610 nm thick membrane as a function of grating period at different temperatures. Also shown are the BTE predictions for fully specular, fully diffuse, and partially specular boundary scattering based on Ziman's specular model (equation 1.1). Ziman's specular model is unable to explain the experimental measurements over a range of temperatures and grating periods. 106
- 6.8 Measured thermal conductivity of a 1150 nm thick membrane as a function of grating period at different temperatures. Also shown are the BTE predictions for fully specular, fully diffuse, and partially specular boundary scattering based on Ziman's specular model (equation 1.1). Ziman's specular model is unable to explain the experimental measurements over a range of temperatures and grating periods. 107

- 6.9 (a) Atomic force microscope (AFM) image of the surface roughness profile for one of our membranes. The measured surface RMS roughness varied between $\sim 0.3 - 0.4$ nm. All of our membranes had RMS surface roughness amplitude in this range. (b) Phonon specularly parameter obtained using the Bayesian inference procedure that best fits with the thermal conductivity measurements on a 525 nm thick membrane. The black symbols represent the mean of all the specularly profiles sampled in the Bayesian procedure and the red region has an intensity proportional to the posterior probability density of the specularly profile obtained from Bayes' theorem (equation 6.3). Phonons are more specularly scattered compared to Ziman's predictions (equation 1.1) for the smallest RMS roughness (~ 0.3 nm) measured on the membrane surface. 108
- 6.10 Comparison of thermal conductivity obtained from the TG experiments with the BTE fits obtained using the Bayesian inference approach. Similar to figure 6.9, the black symbols represent the mean of all the specularly profiles sampled in the Bayesian procedure and the red region has an intensity proportional to the posterior probability density of the specularly profile obtained from Bayes' theorem (equation 6.3). The measured thermal conductivity values lie between the fully specular and fully diffuse boundary scattering limits obtained from the BTE at all temperatures and grating periods, indicating partial specular scattering of phonons. 109
- 6.11 Comparison of thermal conductivity measured in experiments with the thermal conductivity from the BTE simulations using random mode conversion parameters $\alpha_{\omega, s' s}^{\text{spec/diff}}$ for the 1150 nm thick membrane studied in this work at (a) 400 K and (b) 125 K. The mode conversion parameters ($\alpha_{\omega, s' s}^{\text{spec/diff}}$) are drawn from a uniform distribution and the thin film thermal conductivity is calculated by solving the BTE using every one of these random mode conversion parameters. The density of points is a measure of the number of mode conversion parameters resulting in the same thermal conductivity. The triangular symbols are the BTE calculations for the case of no mode conversion. 110

Chapter 1

INTRODUCTION

Semiconductor nanowires and thin membranes are ubiquitous in advanced technological devices. For example, the active region in a quantum cascade laser [1, 2] or a light emitting diode (LED) [3] contains semiconductor membranes such as GaAs, AlGaAs, and GaN with thicknesses of 1-10 nm, and nanowires are finding new applications in thermoelectrics [4] and in new generation transistors with better electrostatic gate control [5]. In some of these devices, like the LEDs and quantum cascade lasers, electron transport results in carrier thermalization, which could result in significant overheating and device degradation. Therefore, increasing the thermal conductivity of these devices and their substrates is of utmost importance to remove the excess generated heat, thereby improving their lifetimes. On the other hand, the performance of devices like thermoelectrics can be significantly enhanced by reducing their thermal conductivity [4]. Therefore, controlling the thermal conductivity of nanoscale device systems has been an important topic of research over the past four decades.

In these semiconductor devices, heat is primarily carried by phonons, which are quanta of collective lattice excitations. Phonons in semiconductors are characterized by their mean free path (MFP), which is different for different phonon modes. In nanoscale systems like thin membranes and nanowires, phonon MFP can be significantly affected by scattering at the device boundaries. Since electron MFP is significantly shorter than phonon MFP in most semiconductor materials, phonon boundary scattering provides an elegant way to predominantly affect only phonons without significantly modifying the electronic properties of the nanoscale devices.

To engineer thermal boundary resistance in nanoscale systems, it is important to understand the underlying phonon scattering mechanisms and how they are affected by the irregularities on device boundaries. Conventionally, phonon scattering at a free material surface has been classified into two different types of processes: specular, mirror-like reflection or diffuse scattering, where the direction of phonon propagation gets randomized after interaction with the surface. Fully specular scat-

tering at a material boundary does not resist the flow of heat since there is no loss in phonon momentum in the transport direction, while fully diffuse scattering results in maximum boundary resistance to heat flow. Phonon surface scattering is usually quantified by the phonon specularity parameter, which is the probability of specular scattering of every individual phonon mode. The specularity parameter, which is a function of phonon wavelength and RMS surface roughness amplitude, ranges between 0 (for fully diffuse scattering of phonons off very rough surfaces relative to phonon wavelength) and 1 (for fully specular mirror-like reflection of phonons off very smooth surfaces relative to phonon wavelength). Ziman [6] derived an expression for the specularity parameter $p(\lambda)$ for a random rough surface with an infinite correlation length as,

$$p(\lambda) = \exp(-16\pi^2\eta^2/\lambda^2) \quad (1.1)$$

where η is the RMS roughness amplitude of the surface and λ is the wavelength of the interacting phonon. Ziman's model (equation 1.1), which gives a microscopic theoretical description of the specularity of a phonon based on its wavelength, is about 50 years old and has never been experimentally validated.

However, several research groups in the past have investigated how surface imperfections and roughness affect the phonon-averaged macroscopic thermal conductivity of semiconductors. For example, Pohl and co-workers performed a series of experiments on single crystal wafers with artificially created surface imperfections to measure the extent of diffuse phonon boundary scattering at the surface of their samples [7–11]. They used steady state thermal conductivity measurements over a temperature range of a few millikelvin to room temperature and observed qualitative evidence for partially specular scattering of phonons, especially at low temperatures.

With the recent advances in the nanoscale fabrication techniques [12–14], it is now possible to fabricate nanoscale thin membranes and nanowire devices with atomic precision. Therefore, over the past few years, experimental measurements of thermal conductivity directly in the nanoscale devices themselves have provided us with new insights into phonon scattering within and at the surfaces of these devices. For example, Goodson and co-workers have extensively studied the in-plane thermal conductivity of supported and suspended semiconductor thin membranes

with thicknesses on the order of 100's of nanometers [15–19]. With the help of boundary scattering-limited thermal conductivity measurements in thin membranes of different thicknesses, they provided conclusive evidence that the intrinsic average phonon MFP in silicon at room temperature is about 300 nm, contrary to the earlier accepted value of ~ 43 nm based on estimates neglecting phonon dispersion. Nelson and co-workers have studied thermal transport in suspended thin silicon membranes and, along with Minnich [20], demonstrated the presence of phonons with MFP $\sim 1 \mu\text{m}$ in silicon at room temperature [21]. They also observed predominantly diffuse phonon boundary scattering at room temperature in their membranes [21–23]. Roukes and co-workers developed a method to directly measure thermal conductance of monocrystalline nanostructures [24, 25] and reported partially specular scattering of phonons in their nanostructures at low temperature.

In the case of nanowires, Majumdar and co-workers developed several new techniques to fabricate thin uniform crystalline nanowires with different surface roughness amplitudes and correlation lengths, and studied the effect of these surface imperfections on the thermal conductivity of nanowires [4, 26, 27]. In their experiments, they observed phonon frequency-dependent boundary scattering rates [28] and also measured very low thermal conductivities in their silicon nanowires below the amorphous limit, which led to a thermoelectric figure-of-merit (zT) of 0.6 in their silicon-based thermoelectric device [4]. Heath and co-workers also developed a new technique called Superlattice Nanowire Pattern Transfer (SNAP) to fabricate high quality nanowires [12, 13] and extended the SNAP technique to fabricate two-dimensional devices such as nanomeshes [29]. They observed a significant reduction in the thermal conductivity of their nanowire arrays compared to bulk Si due to enhanced boundary scattering, which resulted in a high thermoelectric figure-of-merit for their devices [30]. In the case of their nanomeshes, they observed an anomalous reduction in thermal conductivity below the diffuse boundary scattering limit (Casimir limit [31]) and tentatively attributed this observation to coherent heat conduction within their nanomeshes [29].

Several theoretical works have tried to explain the boundary scattering-limited thermal conductivity measurements on single crystals at low temperatures in the past. Callaway developed a phenomenological model for the lattice thermal conductivity of bulk single crystals at low temperature (where boundary scattering dominates)

assuming isotropic crystal structure and frequency dependent relaxation times, and neglecting phonon dispersion [32]. Holland studied the thermal conductivity of Si and Ge single crystals down to 1.7 K, explicitly considering conduction by both longitudinal and transverse phonons [33]. Klemens studied the scattering of lattice waves by static point imperfections, dislocations and grain boundaries using second order perturbation theory and discussed the frequency-dependence of the scattering rates due to these imperfections [34].

The thermal conductivity reduction in nanostructures due to boundary scattering of phonons is conventionally treated using the Fuchs-Sondheimer theory, which was first derived for electron boundary scattering independently by Fuchs [35] and Reuter and Sondheimer [36] and was later extended to phonon boundary scattering in several works [23, 37, 38]. In the last decade, with the advent of efficient computational techniques and growing computational power, several semi-analytical and numerical computation works have investigated the effect of phonon boundary scattering directly in the nanostructures. In the case of thin membranes and two-dimensional patterned nanostructures, McGaughey and co-workers studied the effect of partially specular phonon boundary scattering on the overall thermal conductivity of these nanostructures by solving the Boltzmann transport equation (BTE) semi-analytically and numerically in steady state, using a MFP sampling technique [38–41]. They concluded that rigorous phonon frequency-dependent modeling of boundary scattering processes are necessary to accurately predict the thermal conductivity measurements of thin membranes. Hadjiconstantinou and co-workers developed a fast, computationally inexpensive variance-reduced Monte Carlo (MC) technique to simulate thermal transport in complex nanostructures by solving the BTE directly in the three-dimensional nanostructure geometry [42–44]. They used this technique to investigate the effect of phonon boundary scattering on the thermal conductivity of lithographically patterned nanostructures [43] and graphene nanoribbons [44]. Aksamija and Knezevic [45] studied the anisotropy in thermal conductivity of Si nanomembranes with different crystal orientations due to phonon boundary scattering, by solving the BTE in the relaxation time approximation. Neogi et al. [46] used two-laser Raman spectroscopy and molecular dynamics (MD) simulations to study the effect of surface imperfections on the thermal conductivity of ultrathin free-standing silicon membranes.

Similarly, in the case of nanowires, Martin et al. [47] treated surface roughness scattering of phonons within the framework of perturbation theory and derived a quadratic dependence of the thermal conductivity of nanowires on (D/Δ) , where D is the nanowire diameter and Δ is the RMS roughness height. Zou and Balandin [48] studied the effect of phonon confinement and partially specular boundary scattering on the thermal conductivity of nanowires with dimensions comparable to phonon MFP. Sadhu and Sinha [49] modeled correlated multiple scattering effects off rough silicon nanowire surfaces to explain the observation of nanowire thermal conductivities below the Casimir limit.

In all of these experimental and theoretical works with the exception of Nelson and co-workers [21–23], the focus has been primarily on explaining different temperature trends of the phonon-averaged macroscopic thermal conductivity observed in the experiments. Moreover, in some of the experiments reporting partially specular scattering of phonons, specularity of phonons has been assumed to be a constant value, independent of the phonon wavelength, and comparisons with the expected thermal conductivity based on Ziman’s specular model (equation 1.1) have not been performed. Though some of the computational techniques (for eg., the MC technique [42]) have direct access to the microscopic scattering processes of phonons with nanostructure boundaries, there are no direct experimental measurements of these microscopic processes to compare with. Even in the works of Nelson and co-workers [21–23], the thermal conductivity measurements are limited to room temperature, where only high frequency phonons carry significant amounts of heat, thereby limiting their resolution to only a part of the phonon spectrum. Recently, several theoretical and experimental works have found that Ziman’s specular model cannot adequately explain the specularity of phonons at an arbitrarily random rough surface [50, 51], possibly due to the violation of several assumptions in the initial derivation of equation 1.1. Although these past works have given us tremendous insights into the effect of phonon boundary scattering on the measured nanostructure thermal conductivity, it would be even more informative and beneficial for engineering phonon thermal boundary resistance in nanoscale devices, if we can directly measure and analyze the interactions of phonons with atomistic surface features at the material boundaries, and characterize these interactions in terms of the extent of surface irregularities.

In this thesis, we primarily focus on directly measuring and analyzing microscopic phonon scattering mechanisms at semiconductor boundaries. We conduct phonon mode-dependent thermal transport experiments on suspended thin membranes with well-characterized surface features and use rigorous modeling of the BTE with *ab-initio* phonon inputs to interpret our experimental observations in terms of phonon wavelength-dependent specular and diffuse boundary scattering mechanisms. We start our investigation in chapter 2 by first looking at the extent of reduction in thermal conductivity achievable in lithographically patterned semiconductor devices due to various phonon boundary scattering mechanisms, by directly solving the BTE in the nanostructure using the computationally efficient MC technique developed by Hadjiconstantinou and co-workers [42]. Next, in chapter 3, we discuss how Fourier’s law of heat conduction breaks down when the heating length scales become comparable to phonon MFP and enables us to probe different parts of the phonon spectrum instead of a phonon-averaged measurement of thermal conductivity. In chapter 4, we describe the design and implementation of the transient grating (TG) experimental technique that we set up to perform phonon mode-dependent thermal transport measurements on thin suspended silicon membranes by realizing non-Fourier heat conduction (also known as quasiballistic heat conduction) in the thin membranes. We also describe the methodology adopted to fabricate and characterize the thin suspended silicon membranes used in our experiments. In chapter 5, we describe our modeling approach to interpret the experimental measurements of membrane thermal conductivity in terms of the phonon boundary scattering parameters. Our model is based on a semi-analytical solution of the BTE in the TG heating geometry, which directly describes the observed thermal conductivity of the thin membranes in the quasiballistic heat transfer regime, in terms of phonon boundary scattering parameter — the phonon mode-dependent specularity. In chapter 6, we discuss our interpretation of the experimental measurements, important results, limitations, and conclusions about the observed phonon specularity parameter. Finally, we tie the thesis together in chapter 7 and provide an outlook for future development of the TG experiment and *ab-initio* BTE modeling approaches which shaped this thesis. We also take a look into the vacancies in our current understanding and their impact on the thermal transport community, which will help establish future research directions to advance our understanding of phonon boundary interactions.

Due to the complexity of the mathematical equations involved in solving the BTE

in chapter 5, we have included a significant portion of the detailed derivations as appendices. In appendix A, we describe the derivation for steady state thermal transport through thin membranes, and in appendix B we describe the derivation for transient thermal transport in the TG experiment through thin membranes. In appendix C and D we extend our semi-analytical solution of the BTE considering the finite penetration depth of the laser in the TG experiment and phonon mode conversion at the membrane boundaries respectively, which are important to interpret the thermal conductivity measurements on some of the thin membranes that we investigated.

*Chapter 2***PHONON BOUNDARY SCATTERING IN NANOSTRUCTURES**

In this chapter, we investigate the extent to which the thermal conductivity of lithographically patterned nanostructures can be reduced due to various phonon boundary scattering mechanisms, by directly solving the BTE in the nanostructure using the computationally efficient MC technique developed by Hadjiconstantinou and co-workers [42]. This chapter has been adapted from:

1. Navaneetha K. Ravichandran and Austin J. Minnich. “Coherent and incoherent thermal transport in nanomeshes”. In: *Physical Review B* 89.20 (May 2014), p. 205432, DOI: 10.1103/PhysRevB.89.205432.
URL: <http://link.aps.org/doi/10.1103/PhysRevB.89.205432>

2.1 Background

Heat conduction in solids at length scales comparable to phonon mean free paths (MFPs) and wavelengths is a topic of considerable interest [52–54]. Recently, nanostructured materials such as nanowires [4, 30], superlattices [55], nanocomposites [56–58], and all-scale nanostructured materials [59] have demonstrated strongly reduced thermal conductivities compared to their parent bulk materials. Many of these nanostructured semiconductor materials show promise for thermoelectric energy conversion [4, 30, 55–60].

Coherent thermal transport, in which the phonon dispersion is modified by the coherent interference of thermal phonons in an artificial periodic material, is an active area of research [29, 61–65]. Unlike classical boundary scattering, which only decreases the relaxation times of phonons, coherent effects can also alter the group velocity and density of states by zone folding of phonons, which was originally observed at specific frequencies using Raman scattering [66]. A number of recent works have studied coherent transport both theoretically [63, 64, 67, 68] and experimentally. Several recent experiments have reported that coherent effects can affect thermal transport in superlattices and nanomeshes [29, 61, 65]. In particu-

lar, exceptionally low thermal conductivities were reported in silicon nanomeshes (NMs) [29, 69] which consist of periodic pores in a thin membrane. However, attributing these low thermal conductivity measurements unambiguously to coherent effects is difficult because boundary scattering can also reduce the thermal conductivity of the NMs. Therefore, despite these experimental observations, the conditions under which coherent thermal transport can occur remain unclear.

Computational studies have attempted to provide insight into coherent transport in artificial periodic nanostructures. Hao et al. [70] used two dimensional Monte Carlo simulations of phonon transport to predict a reduction in thermal conductivity of porous silicon with aligned pores. Jain et al. [41] used a mean free path sampling algorithm to study phonon transport in NM-like structures with features larger than 100 nm, concluding that coherent effects are unlikely to be the origin of the low thermal conductivity in the structures of Hopkins et al. [69]. He et al. [71] investigated NM-like structures with similar surface area to volume ratio as in Yu et al. [29] but the simulated structures were much smaller than those studied experimentally. Dechaumphai and Chen [72] used a partially coherent model, in which phonons with MFP longer than the NM neck size were assumed to be coherent, to explain the observations of Yu et al. [29] but boundary scattering could not be rigorously treated in their analysis. Thus, due to several simplifications and approximations used in these studies, the questions of which phonons are responsible for heat conduction in complex structures like NMs and under what conditions coherent transport can occur in these structures remain unanswered.

To address this issue, we present the first fully three-dimensional simulations of thermal transport in NMs using efficient numerical solutions of the frequency-dependent Boltzmann transport equation (BTE). Using the spectral information in our simulations, we find that coherent thermal transport is likely to occur at room temperature only in structures with nanometer critical dimensions and atomic level roughness, and that boundary scattering dominates transport in structures that can be created lithographically. Our work provides important insights into the conditions in which coherent thermal transport can occur in artificial structures.

2.2 Modeling

We begin by describing our simulation approach. To gain spectral insights into the heat conduction in nanostructures we must solve the frequency-dependent BTE, given by [73],

$$\frac{\partial e_\omega}{\partial t} + \underline{v} \cdot \nabla_r e_\omega = -\frac{e_\omega - e_\omega^0}{\tau_\omega} \quad (2.1)$$

where e_ω is the desired distribution function, ω is the angular frequency, e_ω^0 is the equilibrium distribution function, \underline{v} is the phonon group velocity, ∇_r is the gradient operator in cartesian coordinates, and τ_ω is the frequency-dependent relaxation time.

The phonon BTE has been solved for simple nanostructure geometries using several techniques such as the discrete ordinate method [68], Monte Carlo simulation method [74], the finite volume method [75] and the coupled ordinates method [76]. However, using these methods to accurately simulate transport in the large 3D geometry of the NM is extremely challenging due to computational requirements or due to the use of simplifying approximations that may not be applicable.

We overcome this challenge by solving the BTE with an efficient variance-reduced Monte Carlo algorithm, achieving orders of magnitude reduction in computational cost compared to other deterministic or stochastic solvers [42, 43]. Briefly, this technique solves the linearized energy-based BTE by stochastically simulating the emission, advection and scattering of phonon bundles, each representing a fixed deviational energy from an equilibrium Bose-Einstein distribution. The variance of the simulation is reduced compared to traditional MC by properly incorporating deterministic information from the known equilibrium distribution in a control variates approach. This algorithm enables the first simulations of thermal transport directly in the complex 3D geometry of the NM.

To implement the algorithm, the phonon dispersion is divided into 1000 frequency bins, and the phonon bundles are emitted into the simulation domain according to the appropriate distribution as described by Peraud and Hadjiconstantinou [42]. Since the scattering operator is linearized in this approach, the phonon bundles are advected and scattered sequentially and completely independently of each other.

To compute the thermal conductivity of the NM, we simulate the steady state thermal transport in a single periodic unit cell of the NM using periodic heat flux boundary conditions [70] as indicated in the figure 2.1 (boundaries 1 and 2). The other two periodic walls of the NM (boundaries 3 and 4) are modeled as specularly reflecting boundaries since the unit cell of the NM is symmetric about its center. The top and bottom boundaries in the out-of-plane direction and the walls of the NM pores are modeled as diffusely reflecting mirrors. The thermal conductivity of the NM is computed by adding up the contribution of the trajectory of each phonon bundle to the overall heat flux. We terminate the propagation of phonons after 10 internal scattering events as the change in thermal conductivity of the NM is less than 0.5% between the tenth and the twentieth internal scattering event.

We use an isotropic Si dispersion along the [100] crystal direction and phonon relaxation times used by Minnich et al. [77]. To validate our simulation, we calculate the thermal conductivity of an unpatterned silicon thin film doped with Boron, since the samples in Yu et al.'s experiments [29] are doped with small quantities of Boron. We find that we can explain the reported measurements on silicon thin films (TF) in Yu et al.'s experiments [29] by assuming that the boundaries scatter phonons diffusely and using the impurity scattering rate of the form $\tau_{\text{imp}}^{-1} = 2 \times 10^{-44} \omega^4 \text{ s}^{-1}$, where ω is the angular frequency of phonons. For eg., we find from our simulations that, at 300 K, the thermal conductivity of the TF is reduced from the bulk undoped value (148 W/m-K) by 84% due to diffuse boundary scattering at the TF walls and an additional 5% due to impurity scattering, which is consistent with the measurements by Yu et al. [29]. Recent experiments have also demonstrated that diffuse boundary scattering of phonons is a reasonable approximation for analyzing thermal transport in thin silicon membranes [22], which further justifies the assumptions in our simulations. For the NM simulations, we consider both circular and square pores as the shape of the NM pore is somewhere in between. Electron-phonon scattering is expected to be negligible at the temperatures considered [17] and is not included.

2.3 Results

We begin our analysis by computing the thermal conductivity of a NM structure. To facilitate comparisons with experiment, we simulate the same structure in the experiments of Yu et al. [29] with a periodicity $w = 34 \text{ nm}$, a pore width or diame-

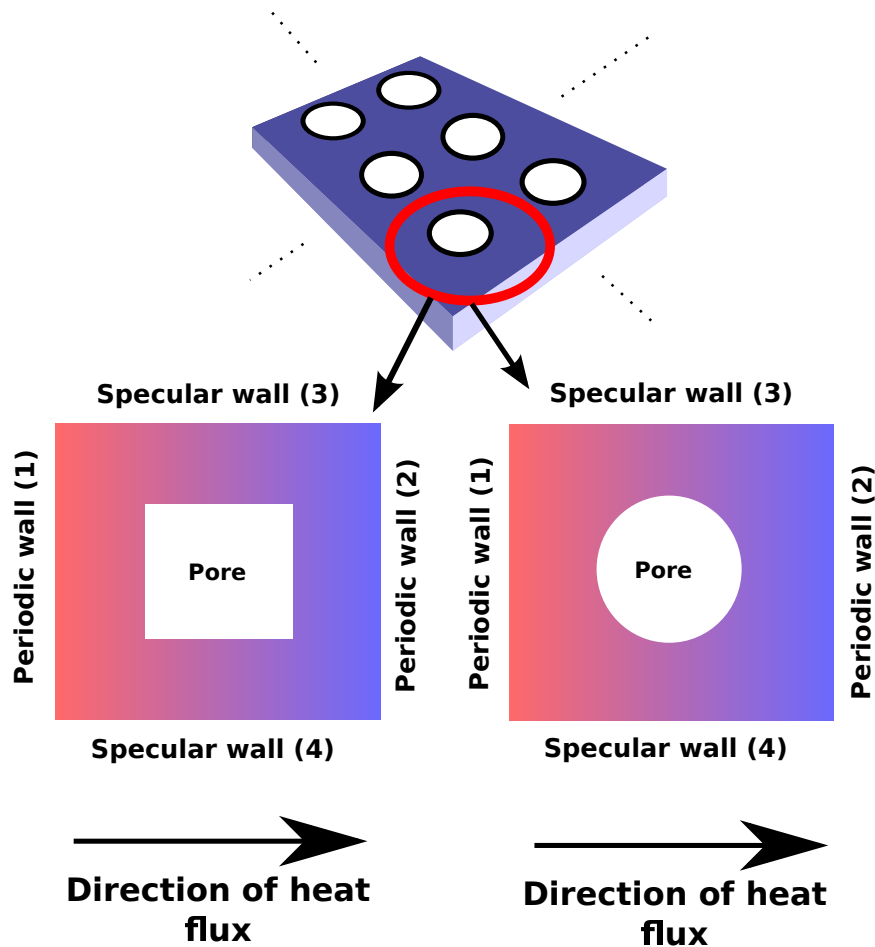


Figure 2.1: The geometry of a single periodic unit cell of the NM with either square and circular pore geometries, on which the Monte Carlo simulations have been performed. Walls (1) and (2) are modeled with periodic heat flux boundary conditions described in [70]. Walls (3) and (4) are modeled as specularly reflecting mirrors. The NM is three dimensional with the third dimension perpendicular to the plane of the paper with a finite non-zero thickness. The top and bottom boundaries in the out-of-plane direction and the walls of the NM pores are modeled as diffusely reflecting mirrors (or for a few simulations that are described in the main text, as partially specularly reflecting boundaries). Both square and circular pore geometries are considered in our simulations as the sample in Yu et al's experiments [29] is likely to have a shape somewhere in between the two extremes.

ter $d = 11$ nm and an out-of-plane thickness $t = 22$ nm. Since all the physical walls of the NM are modeled as diffusely reflecting mirrors, our MC simulations yield the Casimir limit for the thermal conductivity of the NM, which is the theoretical lower limit for the thermal conductivity of the NM with phonons following the unmodified bulk dispersion. It is evident from our simulation results (figure 2.2) that

the experimentally measured thermal conductivity of the NM is considerably lower than the Casimir limit.

We now examine whether coherent transport can explain this exceptionally low thermal conductivity. According to Jain et al. [41], for coherent effects to occur in periodic nanostructures, long wavelength phonons, which are more likely to scatter specularly from a rough boundary and retain their phase, should conduct most of the heat. At present, the phonon frequency corresponding to the minimum phonon wavelength that can scatter specularly from a surface with a given roughness remains unclear, with estimates ranging from 0.64 THz [78] to 2 THz [61], which correspond to phonon wavelengths of about 10 nm and 2 nm respectively. From these experimental observations, we can infer that coherent effects could affect phonons below 2 THz, while the remaining part of the phonon spectrum will still follow the bulk material dispersion and lifetimes.

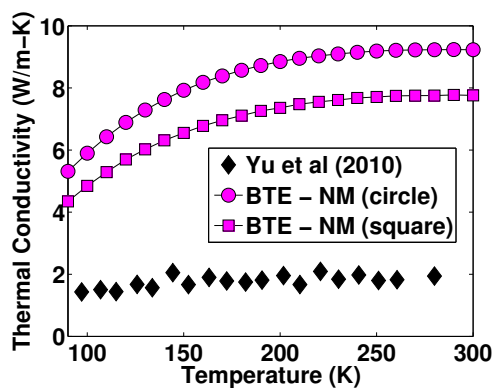


Figure 2.2: Thermal conductivity of the NM as a function of temperature. The thermal conductivity of the NM reported by Yu et al. [29] (black diamonds) is significantly lower than our simulation result with square and circular pore geometries.

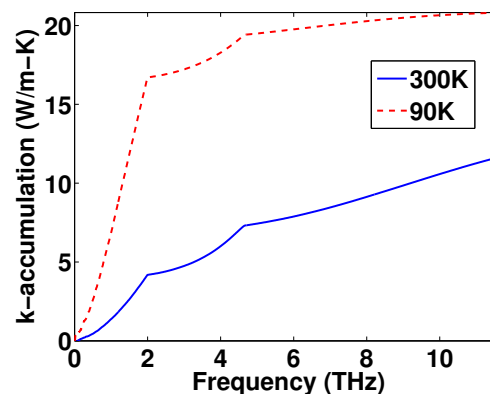


Figure 2.3: Thermal conductivity accumulation versus phonon frequency for a NM that reflects phonons with frequency less than 2 THz specularly and the rest diffusely. Even under these conservative assumptions, the reported measurements cannot be explained even by completely neglecting the contribution of these low frequency phonons that could undergo coherent interference.

Conservatively, let us suppose that phonons with frequency below 2 THz may be

able to follow the new dispersion corresponding to the phononic crystal. When we assume that the boundaries of the NM reflect these low frequency phonons specularly so that their contribution to the relative fraction of heat transport is maximized, we obtain a thermal conductivity of 11.71 W/m-K at 300 K and 20.8 W/m-K at 90 K as shown in figure 2.3. Even if we assume that phonons below 2 THz behave coherently and completely remove their contribution to heat transport, the thermal conductivity of the NM reduces to 7.5 W/m-K at 300 K and 4.12 W/m-K at 90 K, which is still significantly higher than the measured values of 1.95 W/m-K at 300 K and 1.3 W/m-K at 90 K in Yu et al.'s experiments [29]. A similar conclusion is reached if all phonons are scattered diffusely. Therefore, even under the most conservative assumptions, those modes that have the possibility to undergo coherent interference do not carry sufficient heat to explain the measurements.

We now use our simulations to identify the mechanism responsible for the experimentally observed reduction in thermal conductivity. Although Yu et al. [29] assumed that the NM was completely composed of silicon, in other experiments [79] a thin amorphous oxide layer of about 2 – 3 nm thickness is clearly visible using transmission electron microscopy, even though the samples were etched in HF vapor. Other studies have reported that surface damage can result from the reactive ion etching (RIE) process [80] used to create the pores in the NM.

The presence of such a disordered layer substantially affects the phonon transport within the NM. A phonon incident on the disordered layer from silicon has a probability to be backscattered at the interface before reaching the solid-air interface of the NM pores. Even if the phonon penetrates into the disordered layer, it will get scattered nearly immediately due to its short MFP in the disordered layer. Therefore, this disordered layer effectively increases the size of the pore and reduces the cross-sectional area available for heat conduction.

This increased pore size has an important effect on the interpretation of experimental measurements. In the experiments of Yu et al. [29], the thermal conductance of the NM was measured, and the thermal conductivity was calculated by assuming that heat effectively flows through channels between arrays of pores in the NM. If the effective size of the NM pores is larger than assumed, then the width of the heat transport channels is reduced, thereby increasing thermal conductivity for a given

thermal conductance of the NM. Therefore, in order to interpret the experimental measurements of Yu et al. [29] and compare with our simulations, the thermal conductivity of the NM has to be scaled by the ratio of the channel areas without and with the defective layer.

The large pores also lead to additional phonon boundary scattering due to increased surface area of the pores. To account for this effect in our MC simulations, we model the Si-disordered layer interface as a diffusely reflecting mirror. This is a reasonable approximation considering that the microscopic details of phonon scattering at interfaces is poorly understood [81]. The effective pore size is increased by an amount comparable to the thickness of the oxide layer as observed in TEM, which is around 2 – 3 nm [79]. We also include the disordered layer on the top and bottom boundaries of the NM as they were subjected to many of the same etching processes as the pores.

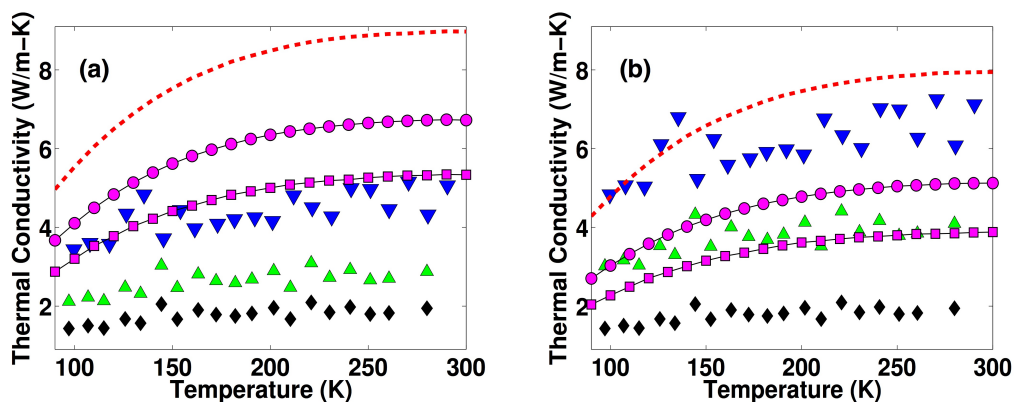


Figure 2.4: Thermal conductivity as a function of temperature for different nanostructures in the experiments of Yu et al. [29] and our simulations for (a) 2 nm disordered layer thickness and (b) 3.5 nm disordered layer thickness. The disordered layer is added to both the nanowire-array (NWA) and the NM in our simulations. In these two figures, the red dashed line, pink circles, and pink squares are the MC solutions for the NWA, NM with circular holes, and NM with square holes, respectively. The black diamonds, green triangles, and blue inverted triangles represent the reported thermal conductivity for the NM, the recalculated thermal conductivity for the NM, and the recalculated thermal conductivity for the NWA, respectively, from Yu et al.’s experiments [29].

We now examine if the increase in the effective pore size can explain the observed

reduction in the thermal conductivity of the NM. Figure 2.4(a) shows that our simulations predict a considerable reduction in thermal conductivity of the NM for a disordered layer thickness of just 2 nm, compared to the case without a disordered layer (figure 2.2). As shown in figure 2.4(b), we are able to explain the experimental observations with a 3.5 nm thick disordered layer. Yu et al. [29] also reported the thermal conductivity for another NM with a larger pore ($d = 16$ nm) at lower temperatures. By following the same simulation procedure, we are able to explain the measurements for this NM using a 2 nm thick disordered layer.

Our simulations can also explain the difference in thermal conductivity between the NM and the nanowire-array (NWA) observed in Yu et al.'s experiments [29]. In their experiments, the reduction in thermal conductivity of the NM was associated with coherent effects primarily because of the lower thermal conductivity of the NM compared to the NWA even though boundary scattering considerations would predict the opposite trend. However, our simulations predict that the thermal conductivity of the NM is consistently lower than that of the NWA without considering any coherent effects.

This difference in thermal conductivity can be explained by backscattering of phonons at the walls of the NM pores [82]. In the NWA, all of the domain walls are aligned parallel to the direction of the thermal gradient and 50% of the incident phonons are backscattered on average. The walls of the NM pores aligned along the temperature gradient also backscatter half of the incident phonons. However, the walls of the NM pores that are not aligned with the temperature gradient backscatter more than half of the incident phonons. Since backscattering reduces the contribution of the phonon to thermal transport, the overall thermal conductivity of the NM is reduced compared to the NWA.

Figure 2.5 shows the fraction of backscattered phonons in the NWA and the NM averaged over all frequencies. We consider a phonon to be backscattered if it returns to the same wall from which it was emitted. For figure 2.5, to isolate the effect of phonon backscattering from the effects of difference in the size of the NWA and the NM, we simulate a NM and NWA with the same effective transport channel area. For the NM, we use a periodicity $w = 34$ nm, pore size $d = 12$ nm and thickness $t = 22$ nm so that it has an effective transport channel area of 22×22 nm². For the NWA, the cross-sectional area is 22×22 nm². To isolate the effect of the

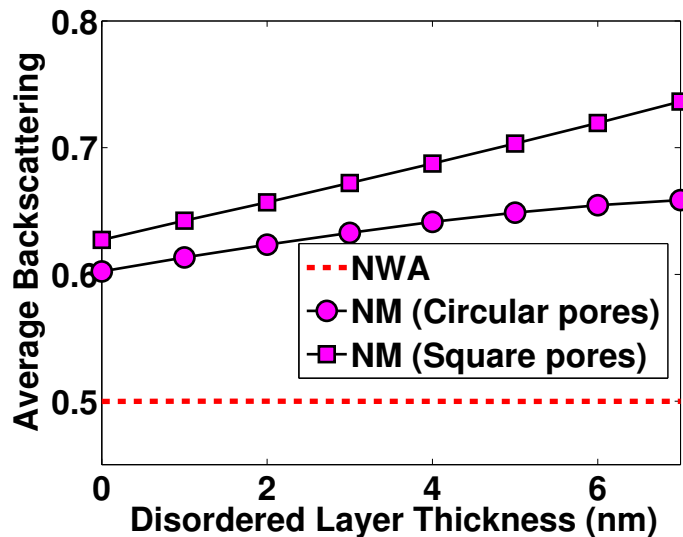


Figure 2.5: Fraction of backscattered phonons for the NWA and the NM with circular and square holes for different disordered layer thicknesses.

geometry, we compute the backscattered fraction from those phonons that do not scatter internally in the domain. As expected for the NWA, 50% of the phonons are backscattered. For the NM with circular and square pores, the fraction of backscattered phonons is 20 – 40% higher than that of the NWA for a range of disordered layer thickness values used in our simulations. Therefore, the difference in thermal conductivity between the NM and NWA can be attributed to the larger fraction of backscattered phonons in the NM along with the smaller transport channel area of the actual NM.

We now examine the conditions under which coherent transport could occur in an artificial structure at room temperature. From the spectral information in our simulations, we find that most of the heat is carried by phonons with frequencies around 5 THz at room temperature, corresponding to a wavelength of about 1 – 2 nm in Si. Therefore, a secondary periodicity on the order of this value is necessary for coherent effects to affect thermal transport in the NM. Further, the surface roughness of an artificial structure must be less than a few Å to preserve the phase of the scattered phonons. Such fine spatial resolution and atomic scale roughness is difficult to obtain using lithographic techniques, but could be met in superlattices with epitaxial interfaces [65]. In lithographically patterned structures, coherent thermal

transport is likely to play a role only at very low temperatures where the dominant thermal wavelength substantially exceeds the surface roughness amplitude.

2.4 Conclusion

In conclusion, we have performed the first fully three-dimensional simulations of thermal transport in nanomeshes using efficient numerical solutions of the frequency dependent BTE. From the spectral information in our simulations, we find that incoherent boundary scattering dominates thermal transport in lithographically patterned structures, and that structures with nanometer critical dimensions and atomic level roughness are required for coherent thermal transport to occur at room temperature. Our results provide important insights into the conditions under which coherent thermal transport can occur in artificial structures.

Chapter 3

QUASIBALLISTIC HEAT TRANSFER

In the previous chapter, we demonstrated the advantage of understanding spectral phonon properties rather than looking at the phonon-averaged thermal properties to accurately estimate the thermal boundary resistance in nanoscale devices. In the case of computer simulations as in the previous chapter, we have access to the trajectories of every individual phonon mode. Therefore, it is possible to probe the change in the heat carrying capacity of each and every phonon due to interactions with the device boundaries. On the other hand, we can only measure averages over an ensemble of phonons in thermal transport experiments. In that case, how can we probe these spectral phonon properties experimentally?

3.1 Breakdown of Fourier's Law of Heat Diffusion

To answer this question, let us take a look at the Fourier's law of heat diffusion (in one dimension, for simplicity) through a sample given by,

$$q = -k \frac{dT}{dx} \quad (3.1)$$

where q is the heat flux along the transport direction x , k is the thermal conductivity along the transport direction, and T is the temperature. In the heat diffusion regime, k is a property of the material. Therefore, for a fixed temperature difference between the hot and the cold side of the sample, the Fourier's heat diffusion equation predicts a diverging heat flux as the hot and cold sides are brought closer to each other.

However, a diverging flux in the case of heat conduction is never observed in reality and this anomalous prediction of diverging heat flux is actually due to the breakdown of the Fourier's law of heat diffusion at small heating length scales. When the separation between the hot and the cold sides of the sample is comparable to the phonon MFP, long MFP phonons traverse the sample from the hot end to the cold end ballistically, without scattering with each other. Due to the lack of internal scattering, the transport is no longer diffusive, and hence the Fourier's law of heat diffusion can no longer be used to describe the heat transfer properties of these long

MFP phonons. In reality, the heat flux carried by these ballistic phonons is lower than the Fourier law prediction.

Phonons in semiconductor materials constitute a wide spectrum with MFP spanning over two orders of magnitude. For example, it is known that, in silicon, phonon MFP ranges from ~ 10 nm to $10 \mu\text{m}$ at room temperature. If the sample under consideration is made of silicon, as the separation between the hot and cold ends are decreased, long MFP phonons transport heat ballistically while short MFP phonons transport heat diffusively across the sample (known as the quasiballistic heat transfer regime). This gradual change in the distribution of phonons carrying heat as the heating length scale is decreased in the quasiballistic regime gives us the necessary resolution to probe different parts of the phonon spectrum individually, instead of probing an average over the entire phonon spectrum in the case of heat diffusion experiments.

This phenomenon of quasiballistic heat conduction is illustrated in figure 3.1 (a). When a metallic transducer layer is heated with a temporally sinusoidal heat flux, an exponentially decaying steady state temperature distribution is set up in the substrate below the transducer. The $1/e$ decay rate of the exponentially decaying temperature distribution (the thermal penetration depth) is shorter for an input heat flux modulated at a higher frequency. Therefore, by increasing the modulation frequency, the dominant spatial frequencies of the substrate temperature profile are increased, thereby enabling a transition from diffusive to quasiballistic heat conduction in the substrate. This regime transition for heat conduction in the substrate modifies the distribution of phonons carrying heat away from the transducer into the substrate, as the modulation frequency of the input heat flux is increased.

The failure of the Fourier's law is also evident from figure 3.1 (b), where we have shown the impulse response of the two-layer Aluminium-Silicon system in figure 3.1 (a) calculated using the MC solution of the BTE described in chapter 2, in comparison with a finite-difference solution of the Fourier heat equation. When the phonon relaxation time in the substrate is truncated to 3 picoseconds, the phonon MFP in the substrate is very short, resulting in predominantly diffusive heat conduction. Therefore, the Fourier solution agrees with the BTE solution in this case. On the other hand, when the phonon MFP is not artificially truncated in the sub-

strate, the thermal transport is in the quasiballistic heat conduction regime, and the BTE solution predicts a slower thermal decay compared to the Fourier model.

3.2 Time-domain Thermorefectance to Probe Quasiballistic Heat Conduction

In a typical laser-based pump-probe experiment on the two-layer geometry (figure 3.1 (a)), thermal response to a single impulsive excitation at the surface is difficult to probe due to limitations in the achievable signal-to-noise ratios. This challenge can be overcome by using a train of modulated pump pulses and using lock-in detection of the probe laser as in the time-domain thermorefectance (TDTR) technique. As a result, a modified form of the impulse response of the system can be measured in the TDTR experiment. The modified form of the impulse response is given by [83],

$$Z(\tau, \omega_0) = \sum_{q=0}^{\infty} h(qT + \tau) e^{-i\omega_0(qT + \tau)} \quad (3.2)$$

In this expression, $h(t)$ is the impulse response from the MC simulation, T is the time between two consecutive pump laser pulses in the TDTR experiment, τ is the delay time between the pump and the probe pulses, and ω_0 is the frequency at which the pump pulses are modulated. By fitting the TDTR signal to a Fourier heat diffusion model, the effective thermal conductivity of the substrate as a function of the modulation frequency (and therefore, as a function of the spatial frequencies in the substrate) can be obtained. Figure 3.1 (c) shows a decreasing trend in the effective thermal conductivity in our simulations with increasing modulation frequency, a signature of quasiballistic thermal transport in the substrate.

Instead of indirectly setting up different thermal spatial frequencies in the substrate by changing the modulation frequency of the input heat flux, we can also directly set up the necessary spatial heating frequencies in the substrate by replacing the uniform transducer layer with a periodic transducer line array as shown in figure 3.2 (a). In this sample geometry, the necessary variation in the spatial frequencies required to observe quasiballistic behavior comes from studying samples with different line width (w) and line array pitch (p). In the rest of this chapter, we take advantage of the predictive power of the MC simulations to simulate the TDTR signal on the line array-substrate geometry at several line width and line array pitch

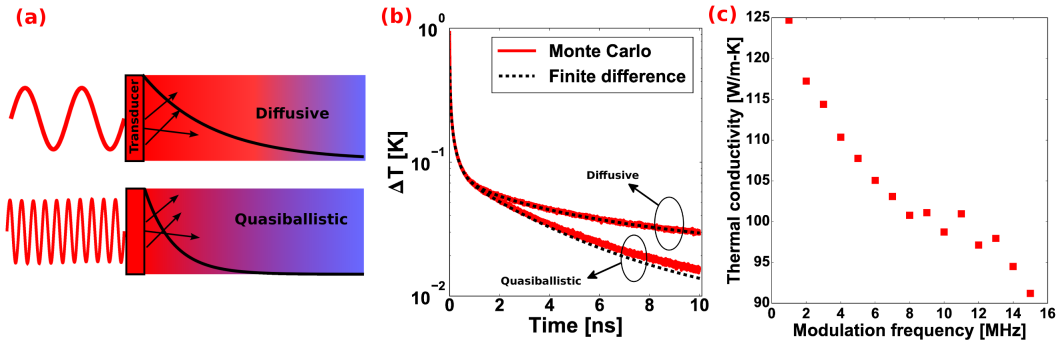


Figure 3.1: (a) Schematic illustrating diffusive and quasiballistic heat transfer in the substrate. When the temperature profile decays faster in the substrate, the length scales corresponding to the dominant thermal spatial frequencies are shorter than phonon MFP, resulting in the break down of the Fourier’s diffusion law, and quasiballistic thermal transport is observed in the substrate. (b) Comparison of impulse response obtained from full BTE simulation and finite-difference solution of the heat equation for a one-dimensional two-layer heat transfer geometry in a TDTR set up. Very good agreement is obtained between the BTE solution and the solution of the heat equation in the diffusive heat transfer regime in the substrate. In the quasiballistic regime, the BTE solution predicts a slower thermal decay, indicating quasiballistic suppression of substrate thermal conductivity. (c) Effective thermal conductivity of the substrate as a function of the modulation frequency of the input heat flux for the two-layer geometry shown in figure(a)

parameters, and investigate the effect of changing the geometrical parameters of the line arrays on the observed effective thermal conductivity of the substrate.

For our simulations, we assume the line array to be made of aluminum and the substrate to be made of silicon, though the choice of transducer and substrate materials will not affect our analysis of transport though this sample geometry. The MC technique provides the temperature response at the line surface to an impulsive heating at time $t = 0$ on the surface. Equation 3.2 contains an infinite sum, which requires 100’s of terms to achieve convergence. Therefore, MC simulations have to be performed for very long run-times to obtain the impulse response at very long times (longest $qT + \tau$ required for convergence of equation 3.2 are on the order of 10’s of μs compared to typical phonon-phonon scattering times on the order of picoseconds to a few nanoseconds). To enable such long simulation times, we massively parallelized our MC code, using 100’s of CPUs simultaneously on the Hooke supercluster to obtain results in realistic time frames. To enable parallelization, we developed a fast thread-safe in-house random number generator routine, which is

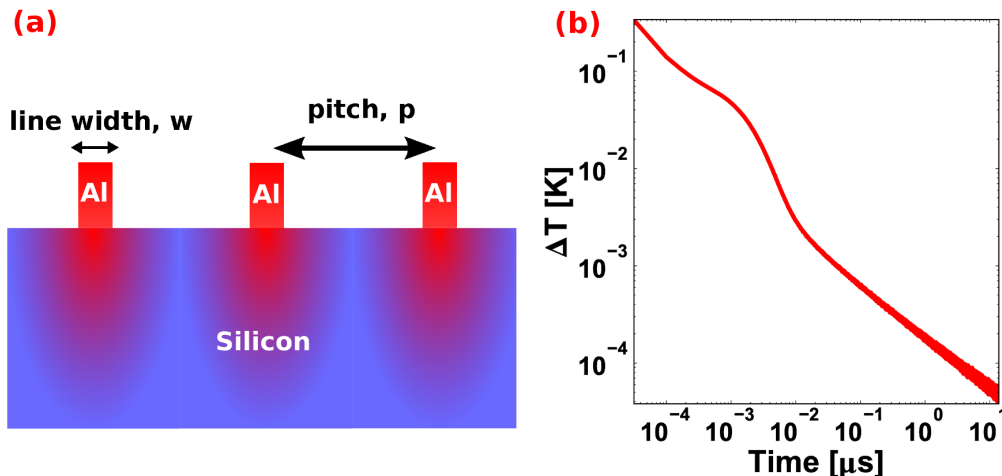


Figure 3.2: (a) Schematic of the periodic metal line array on single crystal wafer investigated in this work. (b) Impulse response for a line array simulation with 50% duty cycle and 100 nm line width for a long simulation time of 13μ s. Surface temperature is sampled once every 65 ps in the simulation, thereby providing sufficient resolution to capture thermal transport features at high frequencies.

the most frequently called function in the MC algorithm. Each one of these simulations typically consume 1200 CPU hours on a processor with 2.67 GHz clock speed.

To obtain the thermal conductivity and interface conductance of the line array-substrate simulation geometry from the BTE impulse response solution, we transform the impulse response to TDTR signal using equation 3.2 and fit it to a Fourier diffusion model [83] with an effective substrate thermal conductivity k (to account for the break down of Fourier's law. Fourier's law assumes that the thermal conductivity is a property of the material and does not depend on experimental conditions. However, at short length and time scales of heat transfer, the thermal conductivity is no longer just a property of the material but becomes an effective fitting parameter in the Fourier's diffusion model dependent on the experimental conditions too.) and the interface conductance G as the fitting parameters. There are two important changes to the Fourier model used in this work compared to [83]. First, we account for the in-plane periodicity of the transducer line-array using a Fourier series expansion of the heating source. Second, we fit low and high frequency components of the TDTR signal (terms with $q = 0$ and $q > 0$ respectively in equation 3.2) with different k and G , since a Fourier model with single k and G cannot capture the fre-

quency dependence of the substrate thermal conductivity due to quasiballistic heat conduction [77]. An example of a failed fitting using a single k and single G for all frequency components of the TDTR signal is shown in figure 3.3 for a simulation geometry with $5 \mu\text{m}$ line width and 80 % duty cycle (defined as the ratio of line width to pitch of the line array). As shown in figure 3.3, very good fit is obtained between the TDTR signal and the Fourier model by using different k 's and G 's for low and high frequency components of the signal. We call the fit variables for low frequency components as (k_0, G_0) and for the high frequency components as (k_1, G_1) .

We simulated the TDTR experiment on line arrays over a range of line widths, duty cycles (w/p), and modulation frequencies. Figure 3.5 shows the thermal conductivities (a) k_0 at 1 MHz modulation frequency, (b) k_0 at 15 MHz modulation frequency, and (c) k_1 , as a function of line width (w) for different line array duty cycles (w/p) obtained by fitting the simulated TDTR signal to the Fourier model at 300 K. Several important observations can be made from figure 3.5:

1. As the modulation frequency increases, the observed thermal conductivity decreases.
2. For every duty cycle, the observed thermal conductivity starts decreasing with decreasing line width, reaches a minimum value and then starts increasing again. This trend in thermal conductivity is observed strongly in the low frequency component k_0 (figure 3.5 (a, b)) compared to the high frequency component k_1 (figure 3.5 (c)).
3. At a fixed modulation frequency, the line width at which the thermal conductivity reaches a minimum increases with increasing duty cycle.
4. For a given duty cycle, the line width at which the thermal conductivity reaches a minimum decreases with increasing modulation frequency.

The effect of modulation frequency on the observed thermal conductivity trends can be qualitatively explained by simply comparing the results with the observed trends in the one-dimensional uniform transducer-substrate geometry described earlier (figure 3.1 (c)). As the modulation frequency increases in the 1D case, the thermal penetration depth within the substrate decreases. When the thermal penetration

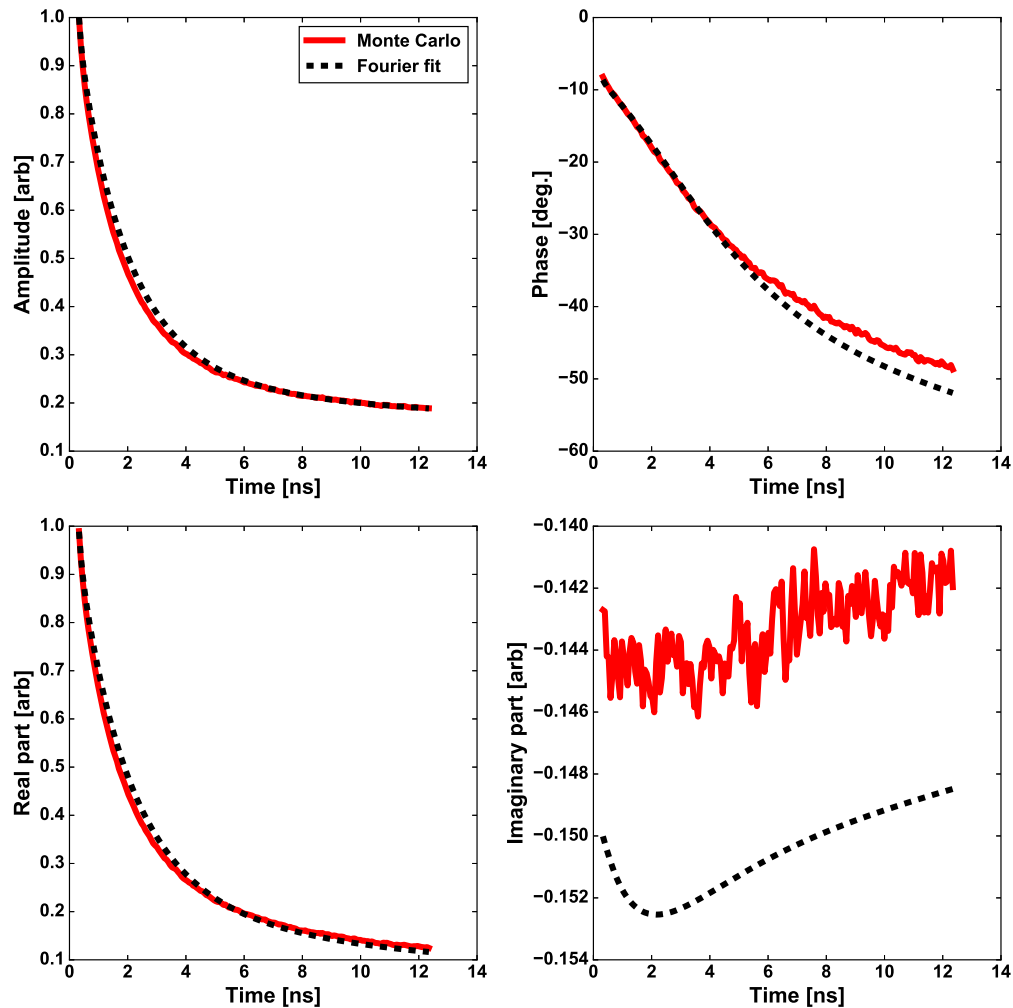


Figure 3.3: TDTR signal obtained from MC simulations and the corresponding fit to a Fourier diffusion model with a single (k, G) pair for both low and high frequency components of the signal for line arrays with 80% duty cycle and $5 \mu\text{m}$ line width at room temperature and 1 MHz modulation frequency

depth becomes comparable to phonon MFP in the substrate, the observed substrate thermal conductivity decreases due to quasiballistic heat conduction. Similarly, the observed trend of decreasing thermal conductivity with decreasing line width at larger line widths ($\gg 1 \mu\text{m}$) can be qualitatively explained by the onset of quasiballistic heat conduction due to decreasing heater size [77]. However, the observation of increasing thermal conductivity with decreasing line width at shorter line widths ($\ll 1 \mu\text{m}$) cannot be explained by quasiballistic effects.

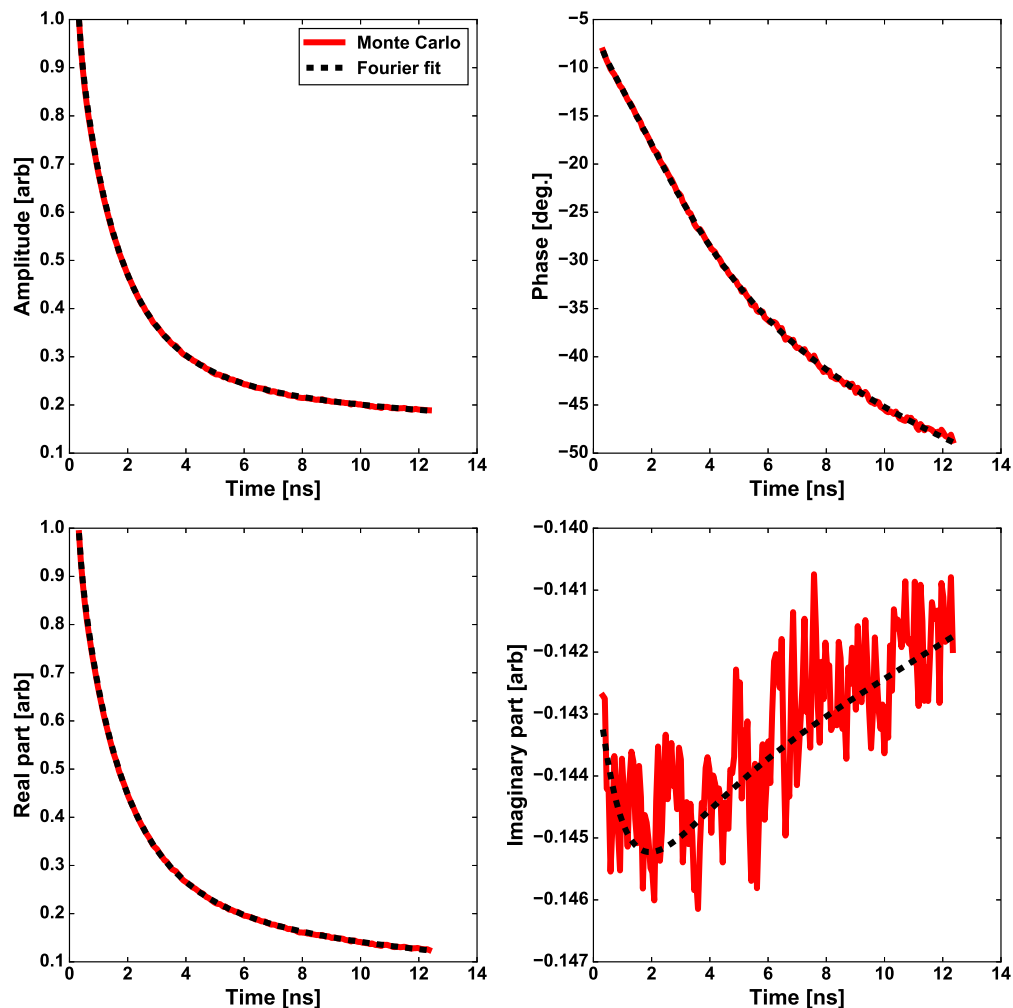


Figure 3.4: TDTR signal obtained from MC simulations and the corresponding fit to Fourier model with different (k, G) pairs for low and high frequency components of the signal for line arrays with 80% duty cycle and $5 \mu\text{m}$ line width at room temperature and 1 MHz modulation frequency

Recently reported experiments on samples with similar geometry have also observed this anomalous minimum in the thermal conductance in their samples [84] as the heater lines are brought closer together within distances comparable to phonon MFP in the substrate. They have attributed this observation to a collectively diffusive thermal transport in the substrate, where the long-MFP phonons originating from neighboring heat sources enable more efficient diffusive-like heat transfer. To investigate if the collectively diffusive transport behavior explain our simulations, we simulated thermal transport through a single isolated line at different line widths.

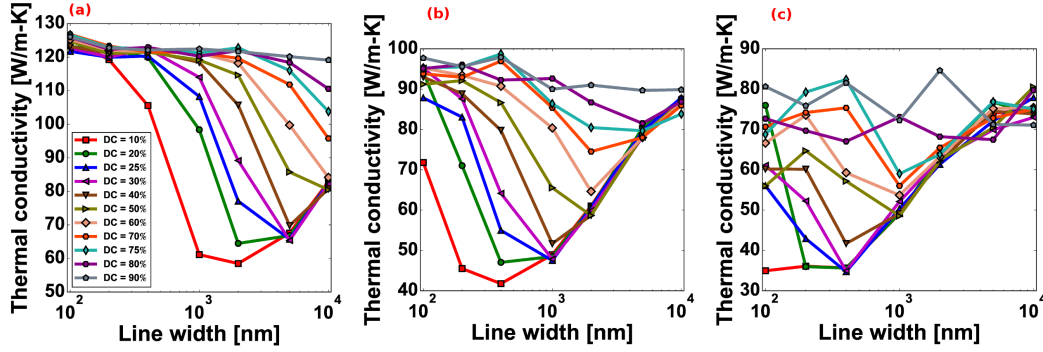


Figure 3.5: Thermal conductivities (a) k_0 at 1 MHz modulation frequency, (b) k_0 at 15 MHz modulation frequency, and (c) k_1 , as a function of line width (w) for different line array duty cycles ($DC = w/p$) at 300 K. Thermal conductivities at both low and high modulation frequencies reach a minimum value as line width is decreased. The anomalous increase in thermal conductivity at short line widths at a fixed duty cycle has been attributed to the phenomenon of collective diffusion in literature [84].

In this case, the MC simulation procedure is mostly identical to the line array, except that there is no in-plane periodicity in the simulation domain and the Fourier model to fit the TDTR signal has to be evaluated at several spatial frequencies. Figure 3.6 shows the thermal conductivity (k_0) of single lines as a function of line width at three different modulation frequencies, compared with the line array values. Unlike the line arrays, the thermal conductivity for isolated lines does not increase with decreasing line widths even for very short line widths at all modulation frequencies, which adds more evidence to the collective diffusion regime hypothesized in ref. [84].

Although the two layer sample geometry is a good test system to demonstrate quasiballistic effects, the presence of an interface complicates the interpretation of the modulation frequency-dependent thermal conductivity directly in terms of the phonon properties in the substrate. Since our goal is to measure the spectral phonon boundary scattering at a free material surface, we choose to set up and use another optical non-contact pump-probe experiment called the transient grating (TG) well suited to perform phonon mode-dependent thermal conductivity measurements on a suspended semiconductor thin membrane geometry. The TG experiment is capable of heating the sample at a single spatial frequency (a sinusoidal excitation)

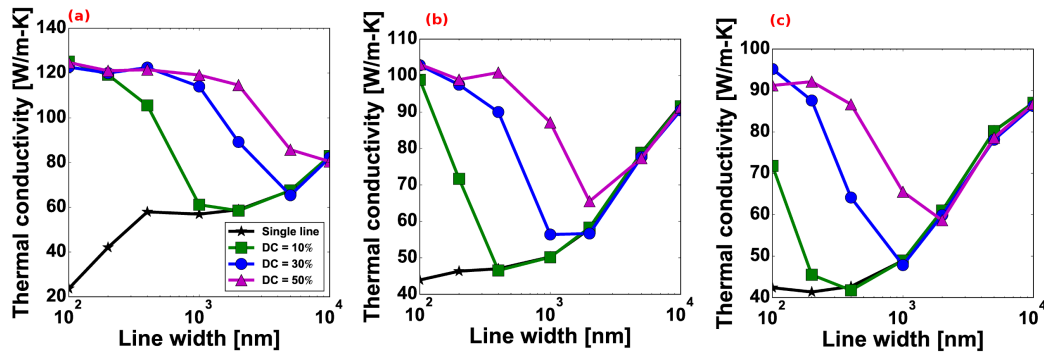


Figure 3.6: Comparison of thermal conductivities k_0 at (a) 1 MHz modulation frequency (b) 7 MHz modulation frequency and (c) 15 MHz modulation frequency as a function of line width between different duty cycles ($DC = w/p$) and an isolated single line at 300 K. The thermal conductivity for isolated lines does not increase with decreasing line widths even for very short line widths at all modulation frequencies, which adds more evidence to the collective diffusion regime hypothesized in ref. [84]

unlike the exponential temperature decay in the TDTR two-layer geometry, and the modeling to connect the measured thermal conductivity with the phonon specularity parameter is simpler, as shown in chapter 5.

Chapter 4

THE THERMAL TRANSIENT GRATING EXPERIMENT

In chapter 2, we demonstrated the extent to which diffuse phonon boundary scattering can reduce the thermal conductivity of nanostructures. Diffuse phonon boundary scattering provides a lower limit for the thermal conductivity in boundary-scattering dominated nanostructures and it is the most likely boundary scattering mechanism for phonons at room temperature in lithographically patterned nanodevices, whose surface roughness amplitude could be a few nanometers. However, with the recent advances in the nanoscale fabrication techniques like molecular beam epitaxy, it is now possible to fabricate nanodevices with atomically flat boundaries. How do phonons scatter with such near-perfect surfaces? In particular, what is the specular parameter for phonons at such near-perfect surfaces?

4.1 Recipe to Measure Phonon Specularity Parameter

In this work, we measure the mode-dependent phonon specularity parameter by measuring the heating length scale-dependent thermal conductivity of thin membranes in the quasiballistic heat transfer regime. Under quasiballistic conditions, the measured thermal conductivity is related to the phonon specularity parameter through a transfer function,

$$k^{\text{Expt}} = H(p_\lambda, \Lambda)$$

where Λ is the heating length scale, p_λ is the specularity parameter for a phonon mode λ and k^{Expt} is the measured thermal conductivity in the experiment. It is this heating length scale-dependent transfer function H in the quasiballistic heat transfer regime, that enables mode-dependent phonon specularity measurements, instead of just a phonon-averaged overall thermal conductivity of the thin membranes. We obtain the transfer function $H(p_\lambda, \Lambda)$ by solving the BTE under the exact experimental conditions of the thermal conductivity measurement, and invert the transfer function H to obtain the specularity parameter p_λ , which will be described in the subsequent chapters. In this chapter, we describe the design and construction of a non-contact pump-probe optical technique called the transient grating (TG) that we set up to perform the first task of measuring the heating length scale-dependent

thermal conductivity in free standing unpatterned silicon membranes with different thickness and roughness properties. In the following sections, we first describe the working principle of the experiment, followed by the details of its construction and characterization using different test samples. Next, we discuss the fabrication and characterization of the samples used in our study. Finally, we present the fitting procedure and data analysis required to obtain the thermal conductivity of the membrane from the measured signal under various experimental conditions.

4.2 Working Principle

Figure 4.1 shows a picture and a schematic of the TG experiment that we set up in the Minnich lab at Caltech. In this technique, a pulsed pump laser beam (wavelength: 532 nm, pulse width: ~ 1 ns, energy per pulse: $5 \mu\text{J}$ (rated at 10 kHz) repetition rate: 1 kHz, manufacturer: Concepts Research Corporation) is first split into several diffraction orders at a diffraction grating (binary phase mask in figure 4.1) and the two first order diffraction beams are focussed onto the sample using a pair of lenses (lens 1 and 2 in figure 4.1). Let the optical fields in the ± 1 order diffracted pump laser beams after imaging through the two lens system be:

$$E_{\pm 1e} = E_{0e} a_e \exp \left[i \left(k_e^2 - q^2/4 \right)^{1/2} z \mp i (q/2) x - i \omega_e t \right]$$

where E_{0e} is the complex amplitude of the pump beam incident on the phase mask, a_e is a measure of the diffraction efficiency of the binary phase mask and includes a phase factor due to the optical path through the imaging lens system, $q = (f_1/f_2) 4\pi/d$ with f_1 and f_2 being the focal length of the lens 1 and 2 and d being the period of the binary phase mask, k_e is the wave vector, and ω_e is the circular frequency of pump electric field ($\omega_e/k_e = c$, the speed of light) and, x and z are the in-plane and cross-plane directions at the sample respectively. The interference of these two first order diffraction beams forms a sinusoidal intensity pattern given by,

$$I_e = |E_{+1e} + E_{-1e}|^2 \propto [1 + \cos(qx)]$$

which is then absorbed by the sample to form a sinusoidal temperature grating pattern with grating period $\Lambda = 2\pi/q = (f_2/f_1) d/2$. This instantaneously set-up sinusoidal heating pattern diffuses through the sample with time.

The temporal evolution of the pump heating pattern on the sample due to heat diffusion is monitored using a continuous wave (CW) probe laser (wavelength: 514

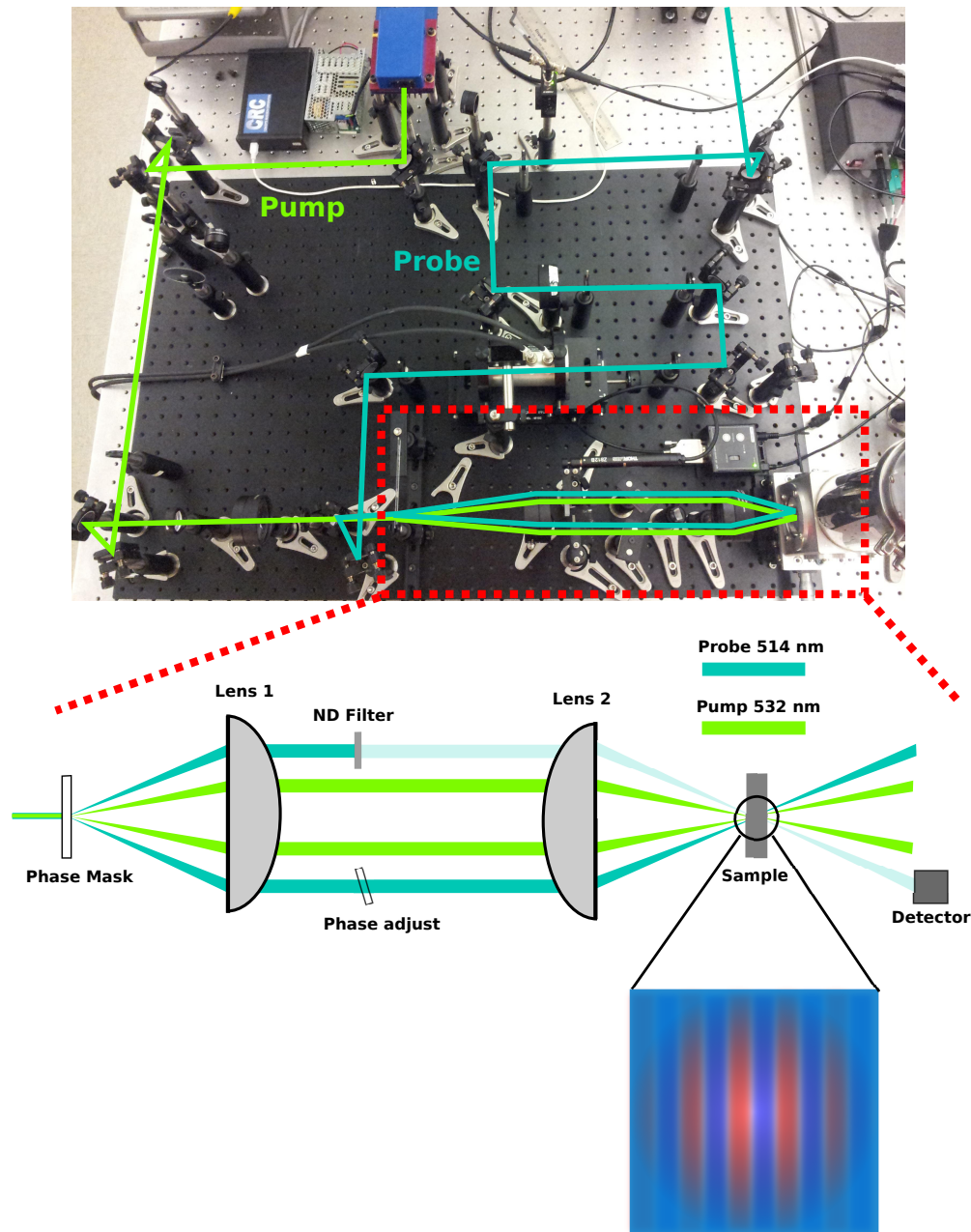


Figure 4.1: Picture and schematic of the TG experiment. A diffractive optic (binary phase mask) splits pump and probe into ± 1 diffraction orders. Pump beams are focused on the sample by a pair of lenses to generate a thermal transient grating pattern. Probe beam diffracted from the thermal grating on the sample is combined with an attenuated reference beam (from the neutral density (ND) filter) and directed to a fast detector. The relative phase between the probe and reference beams is controlled by adjusting the angle of a glass slide (phase adjust) in the probe beam path.

nm, max. power: 500 mW, manufacturer: Coherent Lasers Inc.). In order to avoid overheating of the sample, the CW probe beam is chopped using an electro-optic modulator (EOM) at 20% duty cycle. Next, the chopped probe beam is also split into several diffraction orders at the same phase mask as the pump laser beam and the first order diffraction probe beams are focussed on to the sample at the same spot as the pump beams. The optical fields of the two first order diffraction probe beams are given by,

$$E_{p(\pm 1)} = E_{0p} a_p \exp \left[i \left(k_p^2 - q^2/4 \right)^{1/2} z \mp i (q/2) x - i \omega_p t \right] \quad (4.1)$$

where the symbols represent similar properties as those of the pump beam.

For a thin grating, the effect of the pump excitation of the sample on the probe beam can be expressed as a variation in the complex transfer function relating input and output optical fields as,

$$\tau(x, t) = \tau_0 [1 + (\tau'(t) + i\tau''(t)) \cos(qx)] \quad (4.2)$$

where $|\tau_0|^2$ is the optical transmission of the sample at the probe wavelength in the absence of the pump excitation and $\tau'(t)$ and $\tau''(t)$ are the contributions from the amplitude and phase gratings respectively, which are explained in ref. [85]. Due to the sinusoidal spatial modulation in the optical transmission of the sample (equation 4.2), the first order probe beam, $E_{p(-1)}$, is diffracted at the sample once again, with the new +1 order diffracted optical field (called the signal beam) given by,

$$E_{p,s(+1)} = E_{0p} a_p t_r \tau_0 (\tau'(t) + i\tau''(t)) \exp \left[i \left(k_p^2 - q^2/4 \right)^{1/2} z \pm i (q/2) x - i \omega_e t + i \phi_p \right] \quad (4.3)$$

and the corresponding field intensity is given by,

$$I_s = I_{0p} A_p T_0 (\tau'^2(t) + \tau''^2(t)) \quad (4.4)$$

where $T_0 = |\tau_0|^2$, $A_p = |a_p|^2$, and ϕ_p is the absolute phase of the signal beam after passing through the sample. With time, the instantaneous excitations $\tau'(t)$ and $\tau''(t)$ are washed away due to heat diffusion within the sample and eventually, the diffracted signal I_s vanishes.

For a small temperature rise (~ 10 K) on the sample, I_s is usually very weak. In order to improve the signal-to-noise ratio in our experiment, we realize optical heterodyning in our set up. To optically heterodyne the diffracted signal, we first attenuate one of the probe beams ($E_{p(+1)}$ in equation 4.1, called the reference beam) before reaching the sample using a neutral density (ND) filter and spatially combine the diffracted component of the probe beam at the sample ($E_{p,s(+1)}$), with the transmitted (0^{th} order) component of the reference beam. The 0^{th} order reference beam, after being transmitted through the sample, has an optical field given by,

$$E_R = E_{0p} a_p t_r \tau_0 \exp \left[i \left(k_p^2 - q^2/4 \right)^{1/2} z + i (q/2) x - i \omega_e t + i \phi_R \right] \quad (4.5)$$

where t_r is the attenuation ratio of the neutral density (ND) filter and ϕ_R is the phase picked up by the reference beam after passing through the ND filter and the sample. It is evident from the phase factors in equations 4.3 and 4.5 that the reference and the signal beams are naturally collinear and their interference results in a signal intensity given by,

$$I'_s = I_{0p} A_p T_0 \left[t_r^2 + \left(\tau'^2(t) + \tau''^2(t) \right) + 2t_r \left(\tau'(t) \cos \phi - \tau''(t) \sin \phi \right) \right]$$

where $\phi = \phi_R - \phi_P$ is the total phase difference between the transmitted (0^{th} order) reference beam and the +1 order diffracted signal beam after the sample. The heterodyned part of the signal is given by,

$$I_s^{\text{het}} = I_{0p} A_p T_0 \left[2t_r \left(\tau'(t) \cos \phi - \tau''(t) \sin \phi \right) \right] \quad (4.6)$$

It is evident from equation 4.6 that the heterodyne component of the signal is linearly proportional to $\tau'(t)$ and $\tau''(t)$ unlike the unheterodyned signal intensity given by equation 4.4 (where the signal is proportional to $(\tau'(t))^2$ and $(\tau''(t))^2$). Since $\tau'(t), \tau''(t) \ll 1$, the heterodyned signal (I'_s) has a significantly higher signal-to-noise ratio compared to the unheterodyned signal (I_s). An additional feature of optical heterodyning is that we can select to measure either the amplitude grating (corresponding to $\tau'(t)$) or phase grating (corresponding to $\tau''(t)$) signal by changing the relative phase (ϕ) between the reference and signal beams using a rotating phase adjust glass window. This feature is particularly useful while measuring the thermal conductivity of thin semiconductor membranes, where the phase grating contains contributions from both temperature grating and surface displacement grating produced by thermal expansion, while the amplitude grating contains contributions only from the temperature grating on the sample.

4.3 Lens Arrangement for Laser Alignment

In order to obtain a good signal to noise ratio in the TG experiment, it is important to achieve good pump-probe overlap on the sample. Moreover, to operate in the linear thermal transport regime, the temperature rise has to be limited to $< \approx 10\%$ of the operating temperature by adjusting the pump spot area on the sample. Initially, we found that simple trial and error lens selection and positioning resulted in too weak signals or sample damage due to overheating. To overcome these challenges, we solved the lens maker's equation for Gaussian optics to select the optimal types of lens and lens positions. The final types of lenses and their locations for the pump and probe beams with a spot size ($1/e^2$ diameter) of $440 \mu\text{m}$ and $420 \mu\text{m}$, respectively, are shown in figures 4.2 and 4.3, respectively. Figure 4.4 shows the

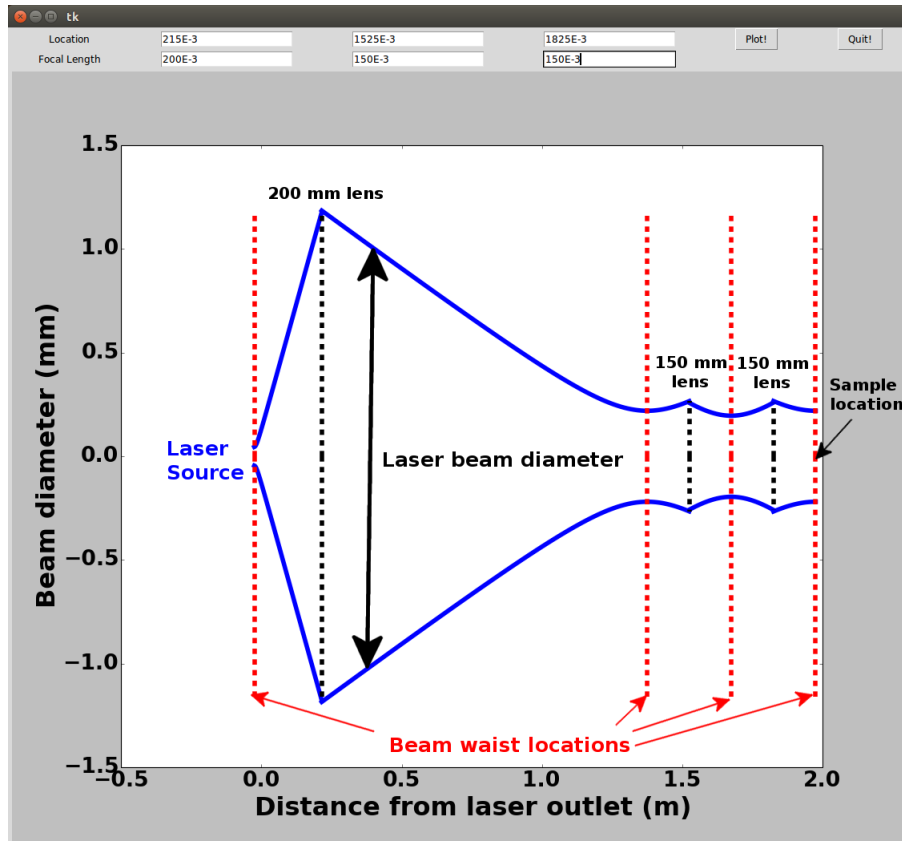


Figure 4.2: Focal length of different lens and their locations to shape the pump beam for a target spot size of $440 \mu\text{m}$ on the sample

measurement of the probe beam profile at the sample location. Good agreement is observed between the design and the measured probe diameter. Figure 4.5 shows a trace of the grating pattern formed at the sample location captured using a beam

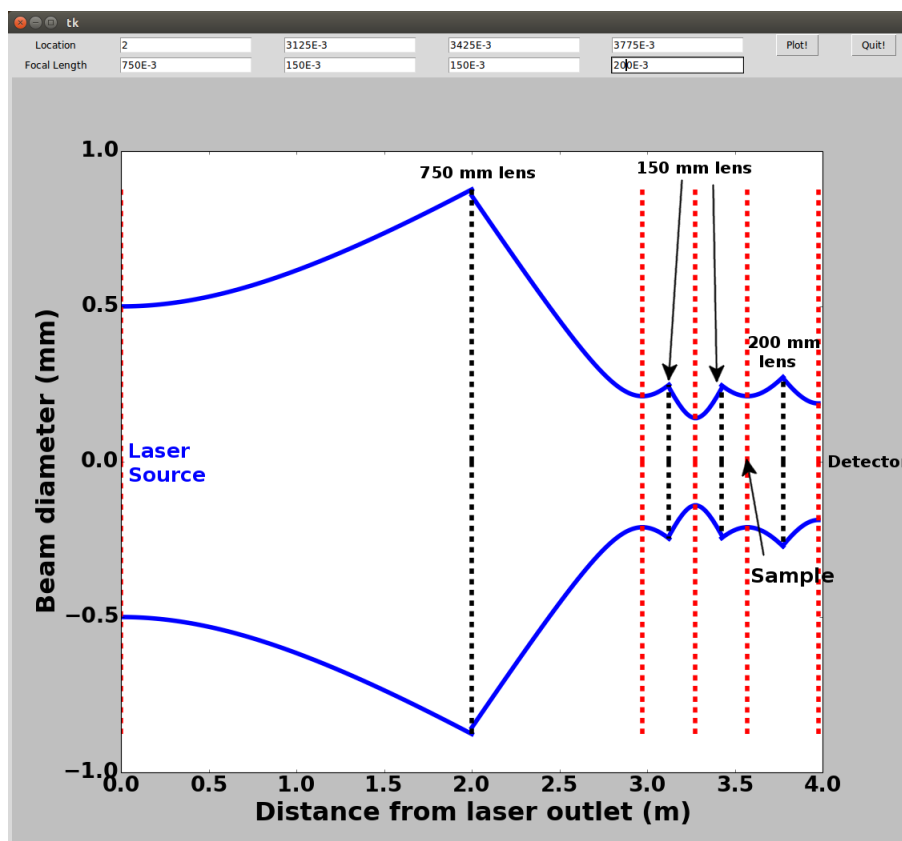


Figure 4.3: Focal length of different lens and their locations to shape the probe beam for a target spot size of $420 \mu\text{m}$ on the sample

profiler. It is evident that uniform grating spacings are obtained throughout the entire laser spot at the sample location.

Figures 4.6 and 4.7 show the conservative estimates for the transient and steady temperature rise due to pulsed pump and CW probe lasers, respectively. The conservative transient temperature rise is under 8 K for all of the mean sample temperatures investigated in this study. For the probe steady heating, the temperature rise is negligible (in mK). The steady temperature rise due to the pump heating is negligible since the repetition rate of pump pulses is very low (1 kHz).

4.4 Experiments in Water

Before using TG to measure thermal transport in thin membranes, we validate our set up by measuring the velocity of sound in water. Since water does not absorb sufficient pump or probe light, we add a small quantity of red food dye (easter egg

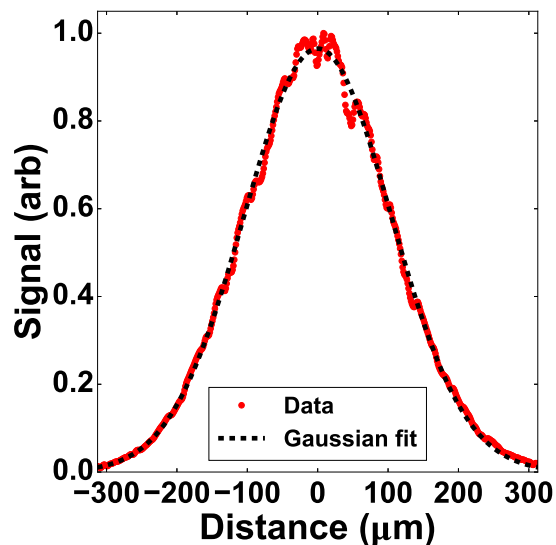


Figure 4.4: Measured diameter of the probe beam using a beam profiler at the sample location and the corresponding Gaussian fit. The $1/e^2$ diameter of the fit is $420 \mu\text{m}$.

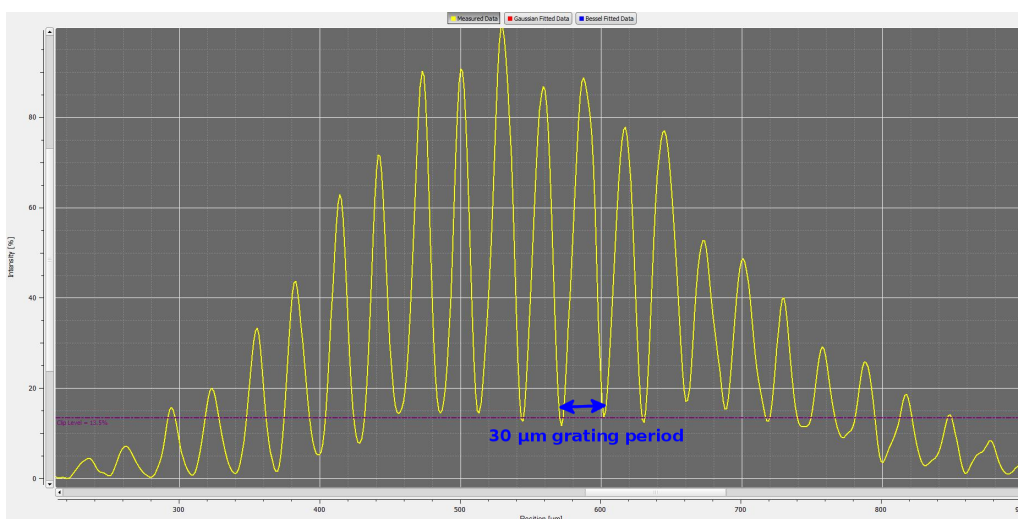


Figure 4.5: Grating pattern formed at the sample location captured using a Thorlabs scanning slit optical beam profiler for a grating period of $30 \mu\text{m}$. The interference pattern produced is a convolution of the sinusoidal grating pattern with the Gaussian spot shape of the probe laser beam.

dye) as an absorbing medium. In the case of water, the two pump beams set up a series of counter-propagating acoustic waves (which travel with the velocity of

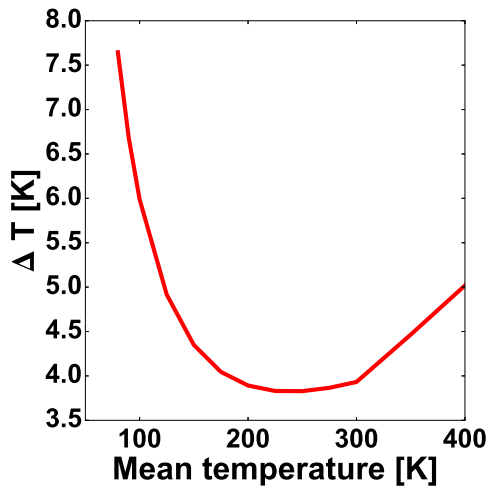


Figure 4.6: Conservative transient temperature rise on the first 1 nm of the sample due to pulsed pump heating

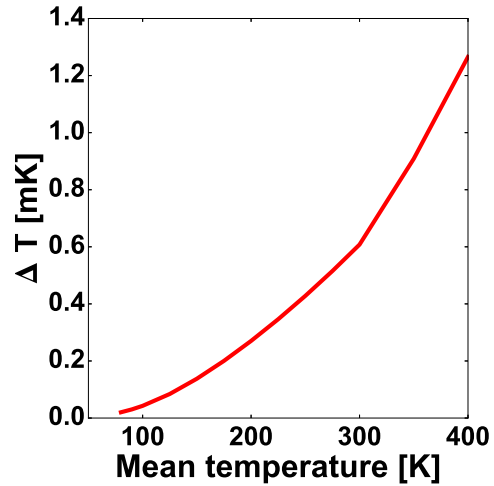


Figure 4.7: Conservative steady temperature rise on the first 1 nm of the sample due to continuous-wave probe heating

sound in water) along with a thermal grating. Since these waves travel in opposite directions within a grating period, the relative velocity between any two approaching waves is twice the sound velocity, resulting in an oscillatory diffraction signal with twice the frequency of the acoustic waves in water superimposed over a slowly decaying thermal decay signal. Figure 4.8 shows the oscillations observed in the signal from water at different grating periods. As the grating period is reduced, the waves interfere with each other more frequently owing to their shorter separation (and constant sound velocity). Therefore, the oscillations in figure 4.8 become faster with decreasing grating periods.

Figure 4.9 shows the frequency of the acoustic waves obtained from the TG experiment compared with the calculated frequencies from the reported sound velocity measurements in water [86]. Very good agreement is obtained between our measurements and calculated acoustic wave frequencies, indicating formation of uniform periodic pump gratings on the sample and good heterodyne overlap of the reference and diffracted signal probe beams.

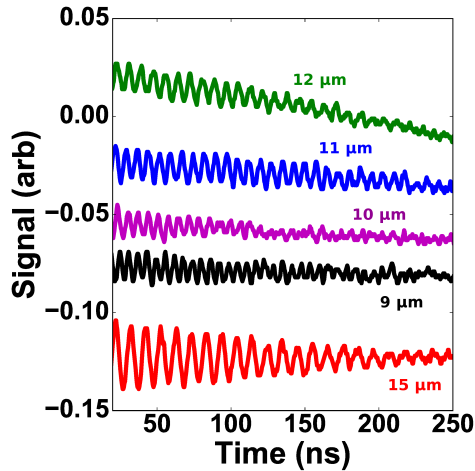


Figure 4.8: Acoustic waves in water observed in the TG experiment at different grating periods. The oscillations become faster as the grating period is reduced since the waves have to travel shorter distances to interfere with each other

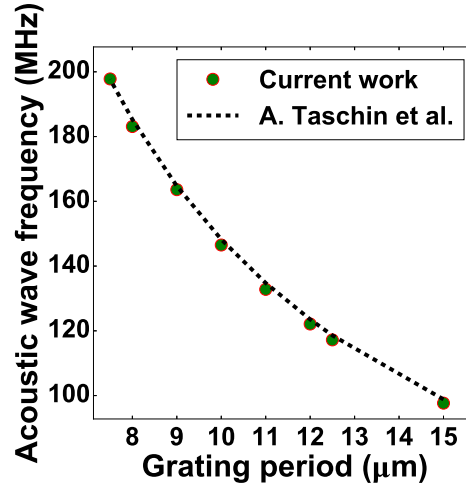


Figure 4.9: Comparison of the acoustic wave frequency obtained from the TG experiment (Fourier transform of the signal) and calculated from the measurements of sound velocity in water in ref. [86]

4.5 Experiments in Gallium Arsenide

In the case of bulk solids like GaAs wafers, the TG has to be modified to measure the heterodyned signal in the reflection geometry, as described in ref. [85]. The working principle and the lens design remain the same. Figure 4.10 shows the signal obtained in the TG experiment at different grating periods for a single crystal GaAs wafer. The period of the transient thermal grating represents the in-plane heating length scale on the GaAs wafer sample. The decay rates of the TG signals increase with decreasing grating period, since, in general, heat conduction occurs in shorter times across a shorter separation between hot and cold regions of the thermal grating. The ripples in the signal are due to the surface acoustic waves (SAW) set up due to pump grating excitation on the sample surface.

We can further fit the temporal decay signal to a thermal model to extract the thermal conductivity of bulk GaAs at different grating periods. The thermal model, which can be derived by solving the Fourier heat diffusion equation in two dimensions (in-plane x and cross-plane z) with an initial condition of periodic surface

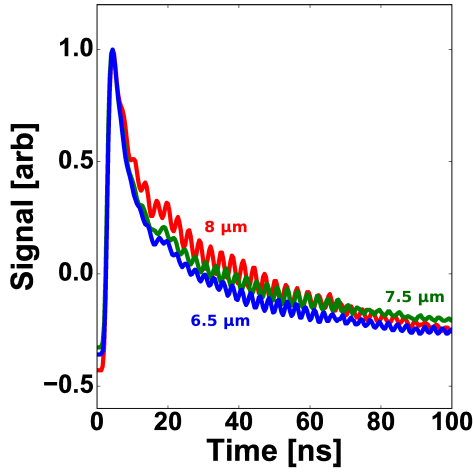


Figure 4.10: TG signals from GaAs wafer at different grating periods, which represent a measure of the heating length scale. The decay rates of the TG signals increase with decreasing grating period, since, in general, heat conduction occurs in shorter times across a shorter separation between hot and cold regions of the thermal grating. The ripples in the signal are due to the surface acoustic waves (SAW) set up due to pump grating excitation on the sample surface.

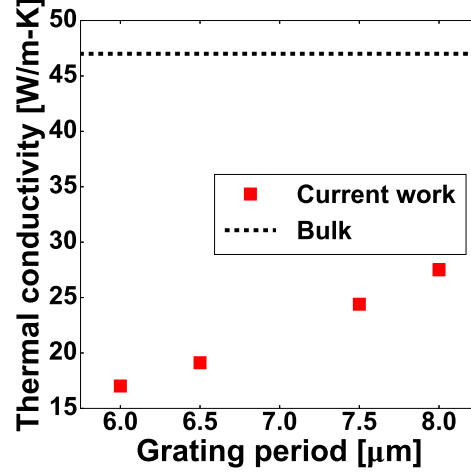


Figure 4.11: Thermal conductivity of bulk GaAs measured as a function of grating period using the TG experiment at 294 K. Since the grating periods are comparable to phonon MFPs in GaAs at 294 K, long MFP phonons travel ballistically across the thermal grating and contribute to lower heat conduction compared to the prediction by Fourier's diffusion law. This quasi-ballistic heat conduction phenomenon is observed in the experiment as a decreasing thermal conductivity with decreasing grating period.

heating, has a surface temperature solution of the form [85]:

$$T(z=0) = \frac{A}{\sqrt{\alpha_z t}} \exp(-\alpha_x q^2 t) \quad (4.7)$$

where α_x and α_z are the in-plane and cross-plane thermal diffusivities of the material and $q = \frac{2\pi}{\Lambda}$ is the in-plane grating wave vector. Since GaAs is a small bandgap semiconductor ($E_g = 1.43$ eV at 294 K), it has a very short penetration depth for both pump and probe light. Therefore, equation 4.7 can be used to fit the TG signals from GaAs. Moreover, since GaAs is a cubic zinc blende crystal, the thermal conductivity tensor is isotropic. Therefore, $\alpha_x = \alpha_z = \alpha$. Figure 4.11 shows the thermal conductivities obtained by fitting the TG signals from GaAs at different grating periods at 294 K. Since the grating periods in this study are comparable to phonon

mean free paths in GaAs at 294 K, long mean free path phonons travel ballistically across the thermal grating and contribute to lower heat conduction compared to the prediction by Fourier's diffusion law [87–90]. As discussed earlier, the breakdown of Fourier's law of heat conduction for grating periods comparable to phonon mean free path allows us to fit the experimental signal to the Fourier model with an effective thermal conductivity (instead of the bulk, grating period-independent thermal conductivity of the material). In particular, this quasiballistic heat conduction phenomenon is observed in the experiment as a decreasing thermal conductivity with decreasing grating period. Note that all of the measured thermal conductivities are below the bulk values reported in literature for GaAs [91].

4.6 Fabrication of Suspended Thin membranes

In the previous sections, we have confirmed that the TG experiment is able to measure acoustic sound velocities in water accurately. We have also shown that the measured thermal conductivity in single crystal GaAs at short grating periods is below the bulk GaAs crystal thermal conductivity reported in literature confirming the capability of the TG experiment to measure quasiballistic heat conduction. Next, we perform thermal transport measurements on free-standing suspended silicon membranes to study phonon scattering at the membrane boundaries. We fabricate these suspended membranes from single crystal silicon-on-insulator (SOI) wafer using wet etch techniques. A schematic of the fabrication procedure is shown in figure 4.12. We start the fabrication process by spin-coating the SOI chip with a commercial protective layer (ProTEK B3 from Brewer Science Inc.) and open a window on the bottom handle silicon layer by just mechanically scratching off some of the protective material. Next, we dip the SOI chip in potassium hydroxide (KOH) hot bath (50% concentration by weight at 70° C) until the etch window has reached the buried oxide (BOX) layer. Finally, we remove the protective ProTEK B3 layer using a commercial remover provided by Brewer Science Inc., use wet HF etch to remove the BOX layer, and release the remaining silicon device layer into a suspended free-standing single crystal silicon membrane.

We open 4 windows on each of the 1 cm × 1 cm SOI chip that we tried. Since the silicon device layer on the SOI is single crystal and a few 100 nm thick, it fractures very easily when released from the BOX layer, possibly due to residual stresses in the structure. The success ratio for fabricating a completely suspended

membrane without fracture varies typically between 15% to 40% depending on the membrane thickness, with the thicker membranes having a higher success ratio. We fabricated membranes with three different nominal thicknesses of ~ 525 nm, ~ 625 nm and ~ 1150 nm from two different SOI manufacturers, MEMS Engineering Inc. and Soitec Inc. for our experiments. We measured the thicknesses of these mem-

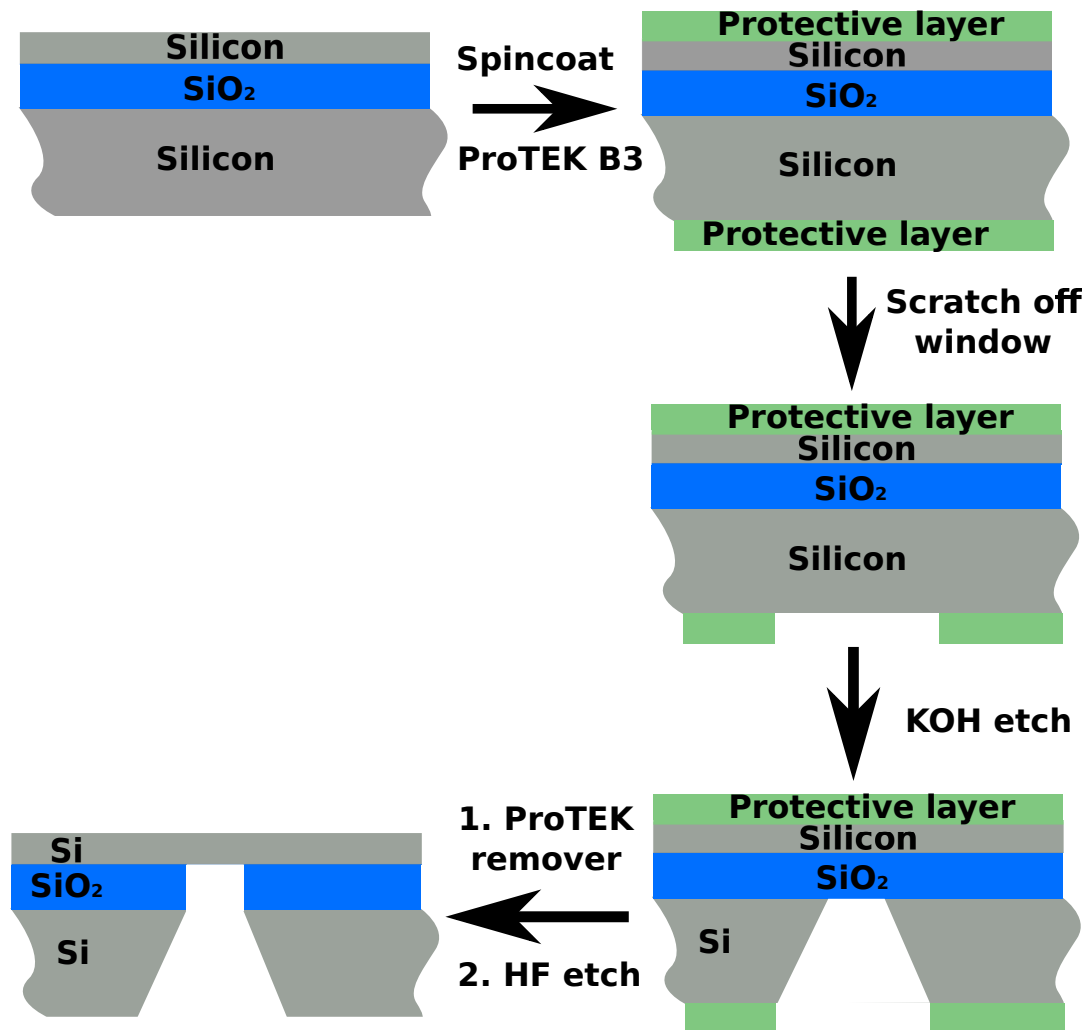


Figure 4.12: Schematic of the fabrication procedure for free-standing suspended silicon membranes. We start by spin-coating the SOI chip with a commercial protective layer (ProTEK B3 from Brewer Science Inc.) and open a window on the bottom handle layer by just mechanically scratching off some of the protective material. Next, we dip the SOI chip in KOH hot bath (50% concentration by weight at 70° C) until the etch window has reached the BOX layer. Finally, we remove the protective ProTEK B3 layer using a commercial remover provided by Brewer Science Inc., use wet HF etch to remove the BOX layer and release the remaining silicon device layer into a suspended free-standing single crystal silicon membrane.

branes using Filmetrics F40 thin-membrane reflectometer (example measurement for a ~ 1150 nm membrane shown in figure 4.13) and scanning electron microscopy (SEM) (example SEM image for a ~ 650 nm membrane shown in figure 4.14). The SEM image shows complete removal of the protective ProTEK B3 layer on top and the BOX layer at the bottom of the suspended membrane.

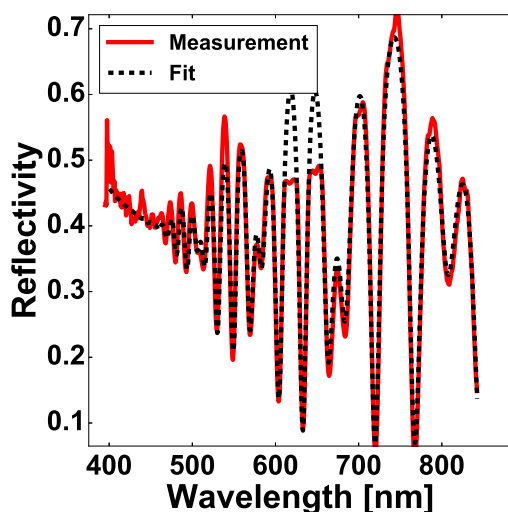


Figure 4.13: Reflectometry measurement and fit for an SOI chip with a reported nominal silicon device layer thickness of 1200 ± 100 nm. The fit produced a device layer thickness of 1153 nm, in good agreement with the reported value.

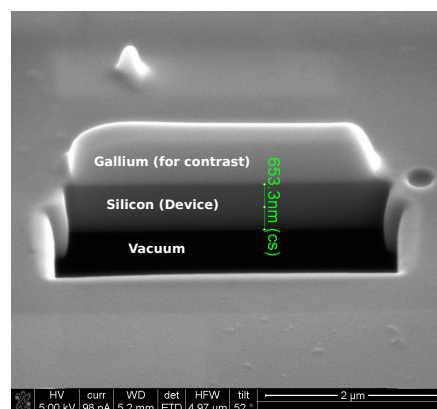


Figure 4.14: SEM cross section image of a free-standing membrane with a device layer thickness of 653 ± 20 nm. The cross-section was created using a focussed ion beam (FIB). A small amount of gallium was deposited to provide contrast and protect the top interface (silicon-gallium interface) from damage due to FIB.

The top surface of the SOI wafer was reported by the manufacturer to be polished and expected to be atomically flat. After fabricating these membranes, the surface quality of the membranes could have changed due to several wet chemical processing steps involved in our fabrication procedure. Therefore, we investigated the surface quality of the membranes using transmission electron microscopy (TEM). Since it is not possible to prepare TEM samples out of suspended membranes, we prepared these samples using the area on the SOI chip adjacent to the suspended membrane region, where the BOX and handle silicon layer were still intact underneath. Figure 4.15 shows one of the images that we obtained using the TF-30 TEM at Caltech. The high magnification image shows very good atomic resolution with

clear atomic planes in some regions of the image, indicating good electron beam focus in those regions. The high magnification image shows 1-2 missing atomic planes at the surface, indicating that the RMS surface roughness is significantly less than a nanometer in this sample. While preparing this sample, the SOI chip was bonded to a silicon wafer (with a clean, native oxide-free surface) coated with nanocrystalline aluminum. We compared the images of the bond-silicon interface (shown in the right-side figure) with the images of nanocrystalline Al-clean silicon interface and determined that the native oxide on the silicon surface of the SOI was less than 1.5 nm thick.

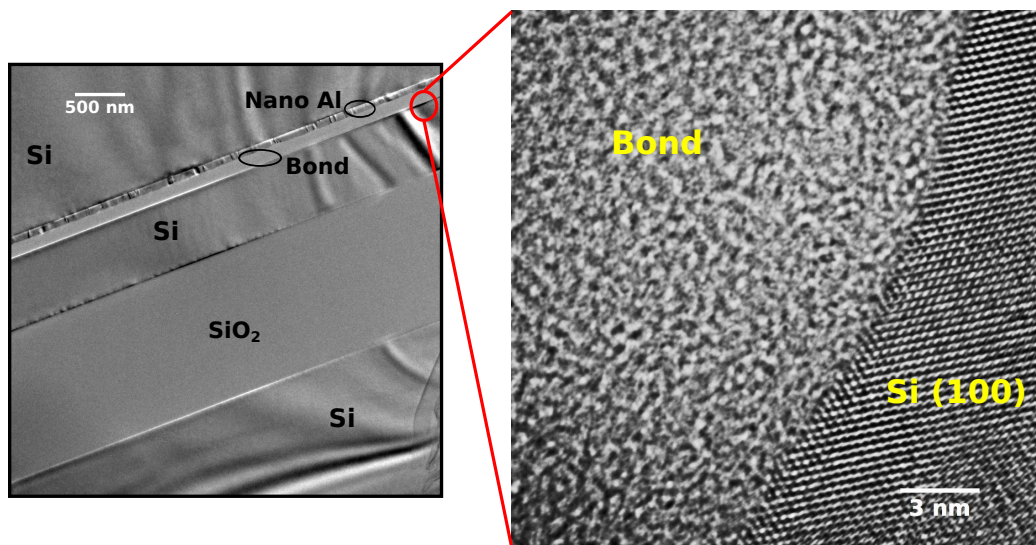


Figure 4.15: Overview of the TEM sample (left) and a high magnification image (right) of the silicon surface on the device layer. The high magnification image shows very good atomic resolution with clear atomic planes in some regions of the image, indicating good electron beam focus in those regions. While preparing this sample, the SOI chip was bonded to a silicon wafer (with a clean, native oxide-free surface) coated with nanocrystalline aluminum. We compared the images of the bond-silicon interface (shown in the right side figure) with the images of nanocrystalline Al-clean silicon interface and determined that the native oxide on the silicon surface of the SOI was less than 1.5 nm thick.

4.7 Experiments on Free-standing Silicon Membranes

We performed TG experiments on 3 different membranes with membrane thicknesses : $d_1 = 525$ nm, $d_2 = 610$ nm and $d_3 = 1150$ nm at ~ 30 grating periods ranging from $3 \mu\text{m}$ to $50 \mu\text{m}$ over a range of mean operating temperatures ranging from 80 K to 450 K. The grating periods on the sample can be simply changed

by changing the binary phase mask shown in figure 4.1. In a semiconductor like Si, absorption of the pump interference pattern results in a carrier population grating, which eventually thermalizes into a temperature grating on the sample. Although the ambipolar carrier diffusion coefficient in Si is about an order of magnitude greater than the thermal diffusivity [92–94], it is important to fit both carrier and phonon diffusion simultaneously in order to accurately determine the thermal diffusivity of the membrane. Both carrier diffusion and heat diffusion in the diffusive and quasiballistic thermal transport regime are simple exponential decays with time. Therefore we fit our signals to a biexponential model (similar to ref. [85]) given by,

$$f_D(t) = A \exp(-\lambda_e t) + B \exp(-\lambda_p t) + C \quad (4.8)$$

where A, B, C, λ_e and λ_p are fitting parameters. Here, λ_e is the decay rate of the electronic component and λ_p is the thermal decay rate. The TG signal given by $f_S(t)$ is fit to the diffusion model $f_D(t)$ by minimizing the least squares residual $\|f_S(t) - f_D(t)\|_2$ and the fitting parameters are determined.

Unlike a single exponential function, a biexponential model such as equation 4.8 could result in a non-convex residual objective function. This becomes especially problematic when the two exponential components are not well separated in time, i.e., have comparable decay rates. Figures 4.16 and 4.17 show a surface plot of the residual $\|f_S(t) - f_D(t)\|_2$ with the simple case of $A = B = 1, C = 0$ plotted against the two fit parameters $\lambda_e = \lambda_1$ and $\lambda_p = \lambda_2$. In figure 4.16, where the optimal fit rates ($\lambda_1 = 1000$ and $\lambda_2 = 10$) result in well separated biexponentials, a simple derivative-based fitting algorithm will predict the slower decay rate (λ_2) accurately. This situation is observed in the TG experiment at short grating periods. However, as evident from figure 4.17, where the optimal fit rates ($\lambda_1 = 1000$ and $\lambda_2 = 100$) result in overlapping exponential components, the residual objective function has saddle points at large λ_1 . This situation is observed in the TG experiment at long grating periods. Therefore, without an initial guess close to the optimal point, derivative-based residual minimization algorithms fail to predict the optimal electronic and thermal decay rates accurately.

To overcome this issue, we use a stochastic global optimization technique called particle swarm optimization to initially locate the optimal well in the parameter

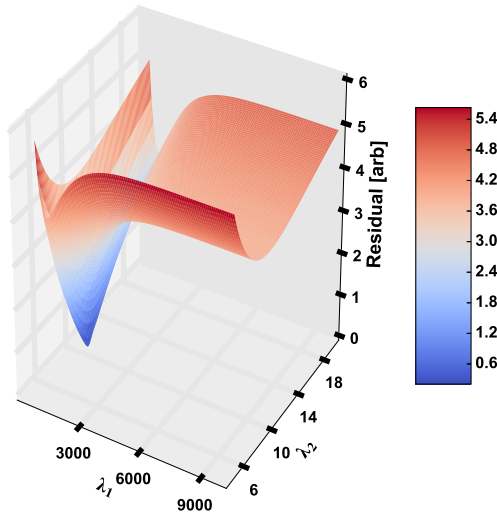


Figure 4.16: Least squares residual function for fitting a biexponential function ($\exp(-\lambda_1 t) - \exp(-\lambda_2 t)$) with decay rates λ_1 and λ_2 . The input profile to be fit with the biexponential function was generated with decay rates $\lambda_1 = 1000$ and $\lambda_2 = 10$ to simulate a larger difference in time scales between electronic and thermal decay in the TG experiment at short grating periods. A sharp minimum is found in the residual at $\lambda_1 = 1000$ and $\lambda_2 = 10$. However, the biexponential fit is, in general, a non-convex fit, with saddle points at large λ_1 along $\lambda_2 = 10$ in this case.

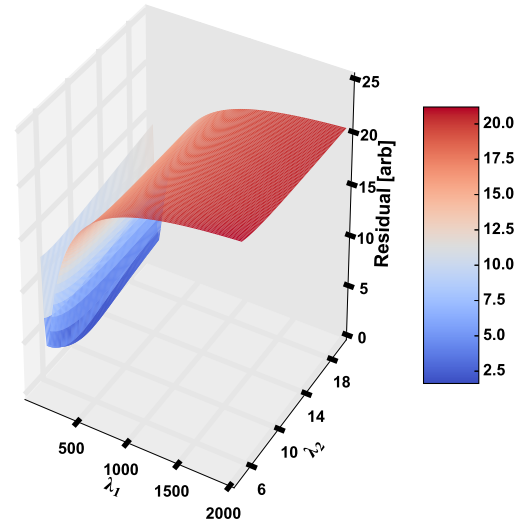


Figure 4.17: Least squares residual function for fitting a biexponential function ($\exp(-\lambda_1 t) - \exp(-\lambda_2 t)$) with decay rates λ_1 and λ_2 . The input profile to be fit with the biexponential function was generated with decay rates $\lambda_1 = 100$ and $\lambda_2 = 10$ to simulate a smaller difference in time scales between electronic and thermal decay in the TG experiment at long grating periods. A shallow minimum is found in the residual at $\lambda_1 = 1000$ and $\lambda_2 = 10$. However, the biexponential fit is, in general, a non-convex fit, with saddle points at large λ_1 with almost no change along λ_2 . Therefore, derivative based fitting methods alone cannot be used to fit the biexponential TG signals when a good initial guess for the decay rates is not available, especially for long grating periods.

space which contains the global minimum, followed by a derivative-based local optimization technique to quickly converge to the optimal solution. Figure 4.18 shows the signals obtained in the TG experiment for a 610 nm thick silicon membrane at

300 K at different grating periods and the corresponding biexponential fits. The initial rising part of the signal is dominated by the electronic component, which is followed by a slowly decaying thermal signal. Very good signal-to-noise ratio is obtained in all of our signals and we also obtain very good fits to the biexponential decay model.

We can obtain the grating period-dependent thermal conductivity (k) of the membrane from the thermal decay rates (γ) as $k = \gamma q^2 c_p$, where $q = 2\pi/\Lambda$ is the grating wave vector and c_p is the volumetric specific heat of silicon, as shown in figure 4.19. At 300 K, phonon MFP in bulk silicon is less than $10 \mu\text{m}$, so we do not see any grating period dependence of thermal conductivity at long grating periods. However, for grating periods shorter than $10 \mu\text{m}$, we see a weak grating period dependence of the measured thermal conductivity. At 125 K, phonon MFP in bulk silicon is significantly longer than $10 \mu\text{m}$. So we observe strong grating period dependence of thermal conductivity even at long grating periods of $30 \mu\text{m}$. In order to interpret these measurements in terms of the phonon specularly parameter at the boundaries of our samples, rigorous BTE solutions with *ab-initio* inputs for phonon properties in the exact same heating and sample geometry are necessary, which is discussed in the following chapter.

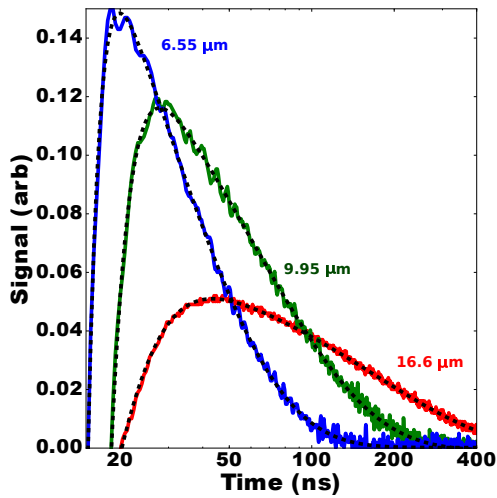


Figure 4.18: TG signals and the corresponding biexponential fits (black dashed lines) from a 610 nm thick free-standing silicon membrane at different grating periods at 300 K. The decay rates of the TG signals increase with decreasing grating period, since, in general, heat conduction occurs in shorter times across a shorter separation between hot and cold regions of the thermal grating. Excellent signal to noise ratio is obtained in all of our measurements. The fitting was performed using a stochastic particle swarm algorithm to locate the global minimum well followed by a non-linear least squares method to converge at the global minimum point.

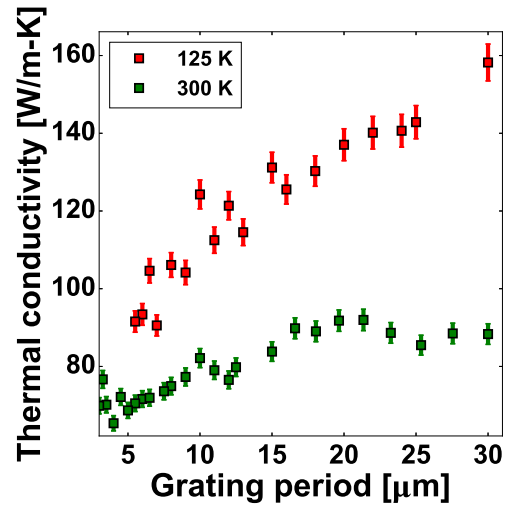


Figure 4.19: Thermal conductivity of a 610 nm thick free-standing silicon membrane measured as a function of grating period using the TG experiment at 300 K and 125 K. At 300 K, phonon MFP in bulk silicon is less than 10 μm, so we do not see any grating period dependence of thermal conductivity at long grating periods. However, for grating periods shorter than 10 μm, we see a weak grating period dependence of the measured thermal conductivity. At 125 K, phonon MFP in bulk silicon is significantly larger than 10 μm. So we observe strong grating period dependence of thermal conductivity even at long grating periods of 30 μm.

*Chapter 5***MODEL FOR TRANSIENT GRATING FROM THE
BOLTZMANN TRANSPORT EQUATION**

As indicated in the previous chapter, here we describe our modeling approach to obtain the transfer function $H(p_\lambda, \Lambda)$ which connects the grating period-dependent membrane thermal conductivity to the phonon mode-dependent specularly parameter. The transfer function H is derived from a semi-analytical solution of the BTE in the TG heating geometry, as described in the following sections. This chapter has been adapted from:

1. Navaneetha K. Ravichandran and Austin J. Minnich. “Role of thermalizing and nonthermalizing walls in phonon heat conduction along thin films”. In: *Physical Review B* 93.3 (Jan. 2016), p. 035314, DOI: 10.1103/PhysRevB.93.035314.
URL: <http://link.aps.org/doi/10.1103/PhysRevB.93.035314>

5.1 Introduction

Engineering the thermal conductivity of nanoscale materials has been a topic of considerable research interest over the past two decades [95]. While applications such as GaN transistors [96, 97] and light emitting diodes (LEDs) [98] require high thermal conductivity substrates to dissipate heat, the performance of thermoelectric and thermal insulation devices can be significantly enhanced by reducing their thermal conductivity [56, 59]. In many of these applications, phonon boundary scattering is the dominant resistance to heat flow, making the detailed understanding of this process essential for advancing applications.

Phonon boundary scattering has been studied extensively both theoretically and experimentally. The thermal conductivity reduction due to boundary scattering of phonons is conventionally treated using the Fuchs-Sondheimer theory, which was first derived for electron boundary scattering independently by Fuchs [35] and Reuter and Sondheimer [36] and was later extended to phonon boundary scattering

in several works [23, 37, 38]. Fuchs-Sondheimer theory is widely used to interpret experiments but makes an important assumption that the diffusely scattered part of the phonon spectrum at a partially specular wall is at a local thermal equilibrium with the wall — the thermalizing boundary condition. The thermalizing boundary condition is also a key assumption in the diffuse boundary scattering limit of Casimir’s theory [31].

Several computational works [38, 45, 70, 99, 100] have studied the reduction in thermal conductivity due to phonon boundary scattering in nanostructures by solving the phonon Boltzmann transport equation (BTE). These works have considered either thermalizing or non-thermalizing boundaries but have never compared the effect of these two different boundary conditions on the thermal conductivity of nanostructures. Several experimental works have also studied the reduction in thermal conductivity of nanomaterials such as nanowires [26, 28, 101], thin films [21–23], and nanopatterned structures [79] due to phonon boundary scattering. These works have used the Fuchs-Sondheimer theory to interpret their measurements. However, it is not clear if the assumptions made in the Fuchs-Sondheimer theory are necessarily applicable for these experiments. In fact, an analysis of the effect of the key assumption made in the Fuchs-Sondheimer theory that the walls are thermalizing has never been investigated due to the challenges involved in solving the BTE for non-thermalizing walls.

Here, we examine the role of thermalizing and non-thermalizing walls in heat conduction along thin films by solving the spectral phonon BTE for a suspended thin film under steady state and transient transport conditions. We find that steady state transport is insensitive to whether phonons are thermalized or not at the boundaries and that Fuchs-Sondheimer theory accurately describes thermal transport along the thin film. In the case of transient transport, we find that the decay rates of the initial temperature distribution (defined by $\gamma = 4\pi^2 k_{\text{eff}} / (C\lambda^2)$, where C is the volumetric specific heat of the material and k_{eff} is the effective thermal conductivity of the thin film at a heating length scale $\lambda/2$) are significantly different for thermalizing and non-thermalizing walls and that Fuchs-Sondheimer theory accurately predicts the thermal conductivity only when the thermal transport is diffusive. Moreover, under transient transport conditions, we find that phonons cannot undergo thermalization at the boundaries in general due to the violation of heat flux conservation. Our re-

sults provide insights into the boundary scattering process of thermal phonons that are useful for interpreting thermal measurements on nanostructures.

5.2 Modeling

Boltzmann Transport Equation

We begin our analysis by considering the two-dimensional spectral transient BTE under the relaxation time approximation for an isotropic crystal, given by,

$$\frac{\partial g_\omega}{\partial t} + \mu v_\omega \frac{\partial g_\omega}{\partial z} + v_\omega \sqrt{1 - \mu^2} \cos \phi \frac{\partial g_\omega}{\partial x} = -\frac{g_\omega - g_o(T)}{\tau_\omega} + \frac{Q_\omega}{4\pi} \quad (5.1)$$

Here, g_ω is the phonon energy distribution function, ω is the phonon frequency, v_ω is the phonon group velocity, τ_ω is the phonon relaxation time, x and z are the spatial coordinates, t is the time variable, $g_o(T)$ is the equilibrium phonon distribution function at a deviational temperature $T = T_0 + \Delta T$ from an equilibrium temperature T_0 , μ is the direction cosine, ϕ is the azimuthal angle, and Q_ω is the rate of volumetric heat generation for each phonon mode. As the in-plane (x) direction is infinite in extent, we require boundary conditions only for the cross-plane (z) direction. In the traditional Fuchs-Sondheimer problem, the boundary conditions enforce that the diffusely scattered phonons are thermalized while also allowing some phonons to be specularly reflected. Here, we generalize these boundary conditions to allow for the possibility of both partial thermalization and partial specularly as:

For $\mu \in (0, 1]$,

$$g_\omega^+(0, \mu, \phi) = p_\omega g_\omega^-(0, -\mu, \phi) + (1 - p_\omega) \left(\sigma_\omega \frac{C_\omega \Delta T(z=0)}{4\pi} - \frac{(1 - \sigma_\omega)}{\pi} \int_0^{2\pi} \int_{-1}^0 g_\omega^-(0, \mu', \phi') \mu' d\mu' d\phi' \right)$$

For $\mu \in [-1, 0)$,

$$g_\omega^-(d, \mu, \phi) = p_\omega g_\omega^+(d, -\mu, \phi) + (1 - p_\omega) \left(\sigma_\omega \frac{C_\omega \Delta T(z=d)}{4\pi} + \frac{(1 - \sigma_\omega)}{\pi} \int_0^{2\pi} \int_0^1 g_\omega^+(d, \mu', \phi') \mu' d\mu' d\phi' \right) \quad (5.2)$$

where d is the thickness in the cross-plane direction, $g_\omega^+(0, \mu, \phi)$ is the phonon distribution leaving the cross-plane wall at $z = 0$, $g_\omega^-(0, \mu, \phi)$ is the phonon distribution approaching the cross-plane wall at $z = 0$, $g_\omega^+(d, \mu, \phi)$ is the phonon distribution approaching the cross-plane wall at $z = d$, $g_\omega^-(d, \mu, \phi)$ is the phonon distribution leaving the cross-plane wall at $z = d$, C_ω is the specific heat of a phonon mode

with frequency ω , and p_ω and σ_ω are the phonon specularity parameter and the thermalization parameter for the thin film walls respectively. The specularity parameter represents the fraction of specularly scattered phonons at the boundaries and the thermalization parameter represents the fraction of the phonon distribution that is absorbed and reemitted at the local equilibrium temperature of the thin film walls. For simplicity, we ignore mode conversion for non-thermalizing boundary condition in our analysis. The simulation domain and the boundary conditions (equation 5.2) are pictorially represented in figure 5.1.

The unknown quantities in this problem are the phonon distribution function

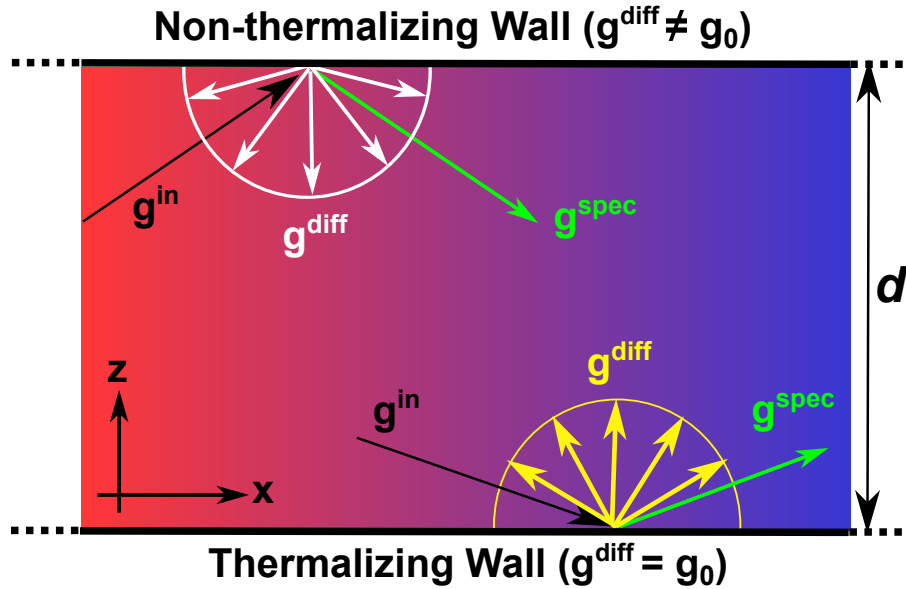


Figure 5.1: Spatial distribution of the temperature profile and pictorial representation of the boundary conditions (equation 5.2) used in this work. The thin film is assumed to be infinite in extent along the in-plane (x) direction and has a finite thickness (d) in the cross-plane (z) direction. For steady state transport calculations, the temperature gradient exists only in the in-plane (x) direction. For transient transport, the initial temperature distribution is an in-plane sinusoidal distribution with a period λ , but can develop a cross-plane temperature gradient at later times. In the case of non-thermalizing wall, the diffusely reflected component g^{diff} of the distribution function is isotropic but away from local thermal equilibrium at the boundary while for the thermalizing wall, g^{diff} is equal to the local equilibrium distribution function g_0 . For both thermalizing and non-thermalizing boundary conditions, the specular reflection component (g^{spec}) has its direction reversed compared to the incoming distribution g^{in} and is also away from the local thermal equilibrium. In our work, we consider either thermalizing or non-thermalizing boundary conditions for both walls of the thin films at a time.

$(g_\omega(t, x, z, \mu, \phi))$ and the deviational temperature distribution $(\Delta T(t, x, z))$. They are related to each other through the energy conservation requirement,

$$\int_{\omega=0}^{\omega_m} \int_{\mu=-1}^1 \int_{\phi=0}^{2\pi} \left[\frac{g_\omega}{\tau_\omega} - \frac{1}{4\pi} \frac{C_\omega}{\tau_\omega} \Delta T \right] d\phi d\mu d\omega = 0 \quad (5.3)$$

Due to the high dimensionality of the BTE, analytical or semi-analytical solutions are only available in literature for either semi-infinite domains [89, 102, 103] or domains with simple boundary and transport conditions [104] or with several approximations [105]. For nanostructures with physically realistic boundaries, several numerical solutions of the BTE have been reported [38, 100, 106]. However, computationally efficient analytical or semi-analytical solutions for the in-plane heat conduction along even simple unpatterned films [21, 23] are unavailable. To overcome this problem, we solve the BTE analytically for steady state transport (section 5.2) and semi-analytically for transient transport along thin films in the transient grating (TG) experiment [21, 23] (section 5.2).

Steady State Heat Conduction in Thin Films

In this section, we extend the Fuchs-Sondheimer relation for thermal conductivity suppression due to phonon boundary scattering to the general boundary conditions described in equation 5.2. To simulate steady state transport, Q_ω is set to 0 in the BTE (equation 5.1). Furthermore, we assume that a one-dimensional temperature gradient exists along the thin film (figure 5.1) and $\frac{\partial g_\omega}{\partial x} \approx \frac{\partial g_\omega^0}{\partial x}$. These assumptions are consistent with the conditions under which typical steady state thermal transport measurements are conducted on nanostructures [16, 18, 28]. Under these assumptions, the BTE is simplified as,

$$v_\omega \mu \frac{\partial g_\omega}{\partial z} + v_\omega \sqrt{1 - \mu^2} \cos \phi \frac{\partial g_\omega^0}{\partial x} = -\frac{g_\omega - g_\omega^0}{\tau_\omega} \quad (5.4)$$

For steady state transport, it is convenient to solve the BTE in terms of the deviation from equilibrium distribution ($\bar{g}_\omega = g_\omega - g_\omega^0(\Delta T(x))$). In this case, the BTE transforms into,

$$\frac{\partial \bar{g}_\omega}{\partial z} + \frac{\bar{g}_\omega}{\mu \Lambda_\omega} = -\frac{\cos \phi \sqrt{1 - \mu^2}}{\mu} \frac{\partial g_\omega^0}{\partial x} \quad (5.5)$$

which represents a one-dimensional ODE whose general solution is given by,

For $\mu \in (0, 1]$,

$$\begin{aligned} \bar{g}_\omega^+(z, \mu, \phi) &= \bar{g}_\omega^+(0, \mu, \phi) \exp\left(-\frac{z}{\mu\Lambda_\omega}\right) \\ &\quad - \Lambda_\omega \cos \phi \sqrt{1 - \mu^2} \frac{\partial \bar{g}_\omega^0}{\partial x} \left(1 - \exp\left(-\frac{z}{\mu\Lambda_\omega}\right)\right) \end{aligned} \quad (5.6)$$

For $\mu \in [-1, 0)$,

$$\begin{aligned} \bar{g}_\omega^-(z, \mu, \phi) &= \bar{g}_\omega^-(d, \mu, \phi) \exp\left(\frac{d - z}{\mu\Lambda_\omega}\right) \\ &\quad - \Lambda_\omega \cos \phi \sqrt{1 - \mu^2} \frac{\partial \bar{g}_\omega^0}{\partial x} \left(1 - \exp\left(\frac{d - z}{\mu\Lambda_\omega}\right)\right) \end{aligned}$$

The boundary conditions under the assumptions made in this section now become,

For $\mu \in (0, 1]$,

$$\begin{aligned} \bar{g}_\omega^+(0, \mu, \phi) &= p_\omega \bar{g}_\omega^-(0, -\mu, \phi) \\ &\quad - \frac{(1 - p_\omega)(1 - \sigma_\omega)}{\pi} \int_0^{2\pi} \int_{-1}^0 \bar{g}_\omega^-(0, \mu', \phi) \mu' d\mu' d\phi \end{aligned} \quad (5.7)$$

For $\mu \in [-1, 0)$,

$$\begin{aligned} \bar{g}_\omega^-(d, \mu, \phi) &= p_\omega \bar{g}_\omega^+(d, -\mu, \phi) \\ &\quad + \frac{(1 - p_\omega)(1 - \sigma_\omega)}{\pi} \int_0^{2\pi} \int_0^1 \bar{g}_\omega^+(d, \mu', \phi) \mu' d\mu' d\phi \end{aligned}$$

Since $g_\omega^0(T)|_{z=0}$ and $g_\omega^0(T)|_{z=d}$ are independent of the angular variables μ and ϕ , the boundary conditions can be rewritten as follows:

for $\mu \in (0, 1]$,

$$\begin{aligned}
\bar{g}_\omega^+(0, \mu, \phi) &= p_\omega \bar{g}_\omega^-(d, -\mu, \phi) \exp\left(-\frac{d}{\mu\Lambda_\omega}\right) \\
&\quad - p_\omega \Lambda_\omega \cos \phi \sqrt{1 - \mu^2} \frac{\partial g_\omega^0}{\partial x} \left(1 - \exp\left(-\frac{d}{\mu\Lambda_\omega}\right)\right) \\
&\quad - \frac{(1 - p_\omega)(1 - \sigma_\omega)}{\pi} \int_0^{2\pi} \int_{-1}^0 \bar{g}_\omega^-(d, \mu', \phi) \exp\left(\frac{d}{\mu'\Lambda_\omega}\right) \mu' d\mu' d\phi \\
&\quad + \frac{(1 - p_\omega)(1 - \sigma_\omega)}{\pi} \\
&\quad \times \int_0^{2\pi} \int_{-1}^0 \Lambda_\omega \cos \phi \sqrt{1 - \mu'^2} \frac{\partial g_\omega^0}{\partial x} \left(1 - \exp\left(\frac{d}{\mu'\Lambda_\omega}\right)\right) \mu' d\mu' d\phi \\
&= p_\omega \bar{g}_\omega^-(d, -\mu, \phi) \exp\left(-\frac{d}{\mu\Lambda_\omega}\right) - p_\omega \Lambda_\omega \cos \phi \sqrt{1 - \mu^2} \frac{\partial g_\omega^0}{\partial x} \left(1 - \exp\left(-\frac{d}{\mu\Lambda_\omega}\right)\right) \\
&\quad - \frac{(1 - p_\omega)(1 - \sigma_\omega)}{\pi} \int_0^{2\pi} \int_{-1}^0 \bar{g}_\omega^-(d, \mu', \phi) \exp\left(\frac{d}{\mu'\Lambda_\omega}\right) \mu' d\mu' d\phi
\end{aligned}$$

and for $\mu \in [-1, 0)$,

$$\begin{aligned}
\bar{g}_\omega^-(d, \mu, \phi) &= p_\omega \bar{g}_\omega^+(0, -\mu, \phi) \exp\left(\frac{d}{\mu\Lambda_\omega}\right) \\
&\quad - p_\omega \Lambda_\omega \cos \phi \sqrt{1 - \mu^2} \frac{\partial g_\omega^0}{\partial x} \left(1 - \exp\left(\frac{d}{\mu\Lambda_\omega}\right)\right) \\
&\quad + \frac{(1 - p_\omega)(1 - \sigma_\omega)}{\pi} \int_0^{2\pi} \int_0^1 \bar{g}_\omega^+(0, \mu', \phi) \exp\left(-\frac{d}{\mu'\Lambda_\omega}\right) \mu' d\mu' d\phi \\
&\quad - \frac{(1 - p_\omega)(1 - \sigma_\omega)}{\pi} \\
&\quad \times \int_0^{2\pi} \int_0^1 \Lambda_\omega \cos \phi \sqrt{1 - \mu'^2} \frac{\partial g_\omega^0}{\partial x} \left(1 - \exp\left(-\frac{d}{\mu'\Lambda_\omega}\right)\right) \mu' d\mu' d\phi \\
&= p_\omega \bar{g}_\omega^+(0, -\mu, \phi) \exp\left(\frac{d}{\mu\Lambda_\omega}\right) - p_\omega \Lambda_\omega \cos \phi \sqrt{1 - \mu^2} \frac{\partial g_\omega^0}{\partial x} \left(1 - \exp\left(\frac{d}{\mu\Lambda_\omega}\right)\right) \\
&\quad + \frac{(1 - p_\omega)(1 - \sigma_\omega)}{\pi} \int_0^{2\pi} \int_0^1 \bar{g}_\omega^+(0, \mu', \phi) \exp\left(-\frac{d}{\mu'\Lambda_\omega}\right) \mu' d\mu' d\phi
\end{aligned} \tag{5.8}$$

since $\int_0^{2\pi} \cos \phi d\phi = 0$. For simplicity and convenience, we change the limits of the variables μ and μ' from $[-1, 0)$ to $(0, 1]$ wherever necessary to get,

$$\begin{aligned}\bar{g}_\omega^+(0, \mu, \phi) &= p_\omega \bar{g}_\omega^-(d, -\mu, \phi) \exp\left(-\frac{d}{\mu\Lambda_\omega}\right) \\ &\quad - p_\omega \Lambda_\omega \cos \phi \sqrt{1 - \mu^2} \frac{\partial g_\omega^0}{\partial x} \left(1 - \exp\left(-\frac{d}{\mu\Lambda_\omega}\right)\right) + (1 - p_\omega)(1 - \sigma_\omega) A_\omega^+ \\ \bar{g}_\omega^-(d, -\mu, \phi) &= p_\omega \bar{g}_\omega^+(0, \mu, \phi) \exp\left(-\frac{d}{\mu\Lambda_\omega}\right) \\ &\quad - p_\omega \Lambda_\omega \cos \phi \sqrt{1 - \mu^2} \frac{\partial g_\omega^0}{\partial x} \left(1 - \exp\left(-\frac{d}{\mu\Lambda_\omega}\right)\right) + (1 - p_\omega)(1 - \sigma_\omega) A_\omega^-\end{aligned}\tag{5.9}$$

where A_ω^+ and A_ω^- are constants, independent of the angular variables μ and ϕ , given by,

$$\begin{aligned}A_\omega^+ &= \frac{1}{\pi} \int_0^{2\pi} \int_0^1 \bar{g}_\omega^-(d, -\mu', \phi) \exp\left(-\frac{d}{\mu'\Lambda_\omega}\right) \mu' d\mu' d\phi \\ A_\omega^- &= \frac{1}{\pi} \int_0^{2\pi} \int_0^1 \bar{g}_\omega^+(0, \mu', \phi) \exp\left(-\frac{d}{\mu'\Lambda_\omega}\right) \mu' d\mu' d\phi\end{aligned}$$

Solving these boundary conditions, we get,

$$\begin{aligned}\bar{g}_\omega^+(0, \mu, \phi) &= -p_\omega \Lambda_\omega \cos \phi \sqrt{1 - \mu^2} \frac{\partial g_\omega^0}{\partial x} \frac{\left(1 - \exp\left(-\frac{d}{\mu\Lambda_\omega}\right)\right)}{1 - p_\omega \exp\left(-\frac{d}{\mu\Lambda_\omega}\right)} \\ &\quad + \frac{(1 - p_\omega)(1 - \sigma_\omega) \left[A_\omega^+ + p_\omega \exp\left(-\frac{d}{\mu\Lambda_\omega}\right) A_\omega^-\right]}{1 - p_\omega^2 \exp\left(-\frac{2d}{\mu\Lambda_\omega}\right)} \\ \bar{g}_\omega^-(d, -\mu, \phi) &= -p_\omega \Lambda_\omega \cos \phi \sqrt{1 - \mu^2} \frac{\partial g_\omega^0}{\partial x} \frac{\left(1 - \exp\left(-\frac{d}{\mu\Lambda_\omega}\right)\right)}{1 - p_\omega \exp\left(-\frac{d}{\mu\Lambda_\omega}\right)} \\ &\quad + \frac{(1 - p_\omega)(1 - \sigma_\omega) \left[A_\omega^- + p_\omega \exp\left(-\frac{d}{\mu\Lambda_\omega}\right) A_\omega^+\right]}{1 - p_\omega^2 \exp\left(-\frac{2d}{\mu\Lambda_\omega}\right)}\end{aligned}\tag{5.10}$$

Using these boundary conditions, the general solution (equation 5.6) can now be written as,

$$\begin{aligned}
\bar{g}_\omega^+(z, \mu, \phi) &= -\Lambda_\omega \cos \phi \sqrt{1 - \mu^2} \frac{\partial g_\omega^0}{\partial x} \left[\frac{p_\omega \left(1 - \exp\left(-\frac{d}{\mu\Lambda_\omega}\right)\right) \exp\left(-\frac{z}{\mu\Lambda_\omega}\right)}{1 - p_\omega \exp\left(-\frac{d}{\mu\Lambda_\omega}\right)} \right. \\
&\quad \left. + \left(1 - \exp\left(-\frac{z}{\mu\Lambda_\omega}\right)\right) \right] \\
&\quad + \frac{(1 - p_\omega)(1 - \sigma_\omega) \left[A_\omega^+ + p_\omega \exp\left(-\frac{d}{\mu\Lambda_\omega}\right) A_\omega^-\right]}{1 - p_\omega^2 \exp\left(-\frac{2d}{\mu\Lambda_\omega}\right)} \exp\left(-\frac{z}{\mu\Lambda_\omega}\right) \\
\bar{g}_\omega^-(z, -\mu, \phi) &= -\Lambda_\omega \cos \phi \sqrt{1 - \mu^2} \frac{\partial g_\omega^0}{\partial x} \left[\frac{p_\omega \left(1 - \exp\left(-\frac{d}{\mu\Lambda_\omega}\right)\right) \exp\left(-\frac{(d-z)}{\mu\Lambda_\omega}\right)}{1 - p_\omega \exp\left(-\frac{d}{\mu\Lambda_\omega}\right)} \right. \\
&\quad \left. + \left(1 - \exp\left(-\frac{(d-z)}{\mu\Lambda_\omega}\right)\right) \right] \\
&\quad + \frac{(1 - p_\omega)(1 - \sigma_\omega) \left[A_\omega^- + p_\omega \exp\left(-\frac{d}{\mu\Lambda_\omega}\right) A_\omega^+\right]}{1 - p_\omega^2 \exp\left(-\frac{2d}{\mu\Lambda_\omega}\right)} \exp\left(-\frac{(d-z)}{\mu\Lambda_\omega}\right)
\end{aligned} \tag{5.11}$$

which simplifies into:

$$\begin{aligned}
\bar{g}_\omega^+(z, \mu, \phi) &= -\Lambda_\omega \cos \phi \sqrt{1 - \mu^2} \frac{\partial g_\omega^0}{\partial x} \left[1 - \frac{\exp\left(-\frac{z}{\mu\Lambda_\omega}\right) (1 - p_\omega)}{1 - p_\omega \exp\left(-\frac{d}{\mu\Lambda_\omega}\right)} \right] \\
&\quad + \underbrace{\frac{(1 - p_\omega)(1 - \sigma_\omega) \left[A_\omega^+ + p_\omega \exp\left(-\frac{d}{\mu\Lambda_\omega}\right) A_\omega^-\right]}{1 - p_\omega^2 \exp\left(-\frac{2d}{\mu\Lambda_\omega}\right)} \exp\left(-\frac{z}{\mu\Lambda_\omega}\right)}_I \\
\bar{g}_\omega^-(z, -\mu, \phi) &= -\Lambda_\omega \cos \phi \sqrt{1 - \mu^2} \frac{\partial g_\omega^0}{\partial x} \left[1 - \frac{\exp\left(-\frac{(d-z)}{\mu\Lambda_\omega}\right) (1 - p_\omega)}{1 - p_\omega \exp\left(-\frac{d}{\mu\Lambda_\omega}\right)} \right] \\
&\quad + \underbrace{\frac{(1 - p_\omega)(1 - \sigma_\omega) \left[A_\omega^- + p_\omega \exp\left(-\frac{d}{\mu\Lambda_\omega}\right) A_\omega^+\right]}{1 - p_\omega^2 \exp\left(-\frac{2d}{\mu\Lambda_\omega}\right)} \exp\left(-\frac{(d-z)}{\mu\Lambda_\omega}\right)}_{II}
\end{aligned} \tag{5.12}$$

for $\mu \in (0, 1]$. Here, the terms A_ω^+ and A_ω^- only depend on phonon frequency. In particular, they are independent of the angular coordinates μ and ϕ . The expression

for the in-plane (x direction) spectral heat flux is given by,

$$\begin{aligned}
 q_{x,\omega} &= \frac{1}{d} \int_{z=0}^d \int_{\mu=-1}^1 \int_{\phi=0}^{2\pi} v_x \bar{g}_\omega \frac{D(\omega)}{4\pi} d\phi d\mu dz \\
 &= - \left[\frac{1}{3} C_\omega v_\omega \Lambda_\omega \right] \frac{\partial T}{\partial x} \left[1 - \frac{3(1-p_\omega)\Lambda_\omega}{2d} \int_0^1 (\mu - \mu^3) \frac{1 - \exp\left(-\frac{d}{\mu\Lambda_\omega}\right)}{1 - p_\omega \exp\left(-\frac{d}{\mu\Lambda_\omega}\right)} d\mu \right]
 \end{aligned} \tag{5.13}$$

since the diffuse contributions to the distribution functions given by $\bar{g}_\omega^+(z, \mu, \phi)$ and $\bar{g}_\omega^-(z, -\mu, \phi)$ (terms I and II in equation 5.12) are independent of the azimuthal angle ϕ and integrate out to 0. Comparing equation 5.13 with the expression for heat flux from the Fourier's law, the spectral effective thermal conductivity of the thin film is obtained as a product of the bulk spectral thermal conductivity and the well-known Fuchs-Sondheimer reduction factor due to phonon boundary scattering given by,

$$k_{\omega,\text{eff}}(d) = \underbrace{\left[\frac{1}{3} C_\omega v_\omega \Lambda_\omega \right]}_{k_{\omega,\text{bulk}}} \underbrace{\left[1 - \frac{3(1-p_\omega)\Lambda_\omega}{2d} \int_0^1 (\mu - \mu^3) \frac{1 - \exp\left(-\frac{d}{\mu\Lambda_\omega}\right)}{1 - p_\omega \exp\left(-\frac{d}{\mu\Lambda_\omega}\right)} d\mu \right]}_{\text{Fuchs-Sondheimer reduction factor } -F\left(\frac{\Lambda_\omega}{d}\right)} \tag{5.14}$$

It is interesting to observe from equation 5.14 that the spectral effective thermal conductivity is independent of the thermalization parameter σ_ω even though a general boundary condition (equation 5.2) has been used in this derivation. Thus, the steady state thermal conductivity suppression due to boundary scattering is only influenced by the relative extent of specular and diffuse scattering (parameterized by the specular parameter p_ω) and does not depend on the type of diffuse scattering process (parameterized by the thermalization parameter σ_ω). We explicitly demonstrate this result using numerical simulations in section 5.3.

Transient Heat Conduction in Thin Films

In this section, we solve the BTE (equation 5.1) for transient thermal transport along a thin film. The initial temperature profile considered in this work is identical to that of the TG experiment, which has been used extensively to study heat conduction in suspended thin films [21, 23]. In the TG experiment, the thermal transport properties of the sample are obtained by observing the transient decay of a one-dimensional impulsive sinusoidal temperature grating on the sample at different grating periods. In the large grating period limit of heat diffusion, the temporal

decay is a single exponential. Since the initial temperature distribution is an infinite one-dimensional sinusoid in the x direction, the temperature distribution remains spatially sinusoidal at all later times. Therefore, each wave vector q in the spatially Fourier transformed BTE directly corresponds to a unique grating period $\lambda = 2\pi/q$. Unlike in the steady state case, here we solve for the absolute phonon distribution g_ω rather than the deviation $\bar{g}_\omega = g_\omega - g_\omega^0$. Furthermore, the BTE is solved in the frequency domain (η) by Fourier transforming equation 5.1 in the time variable t . With these transformations, the BTE reduces to,

$$i\eta G_\omega + \mu v_\omega \frac{\partial G_\omega}{\partial z} + iq v_\omega \sqrt{1 - \mu^2} \cos \phi G_\omega = -\frac{G_\omega}{\tau_\omega} + \frac{1}{4\pi} \frac{C_\omega}{\tau_\omega} \Delta \bar{T} + \frac{\bar{Q}_\omega}{4\pi} \quad (5.15)$$

where the substitution $G_0(T) = \frac{1}{4\pi} C_\omega \Delta \bar{T}$ has been made and G_ω represents the spatial (in-plane axis) and temporal Fourier transform of absolute phonon energy distribution function g_ω .

The outline of the solution methodology for equation 5.15 is as follows. The general solution is given by,

$$\begin{aligned} \text{For } \mu \in (0, 1], \quad G_\omega^+(z, \mu, \phi) &= G_\omega^+(0, \mu, \phi) \exp\left(-\frac{\gamma_{\mu\phi}^{\text{FS}}}{\mu\Lambda_\omega} z\right) \\ &+ \frac{\exp\left(-\frac{\gamma_{\mu\phi}^{\text{FS}}}{\mu\Lambda_\omega} z\right)}{4\pi\mu\Lambda_\omega} \int_0^z (C_\omega \Delta \bar{T} + \bar{Q}_\omega \tau_\omega) \exp\left(\frac{\gamma_{\mu\phi}^{\text{FS}}}{\mu\Lambda_\omega} z'\right) dz' \\ \text{For } \mu \in [-1, 0), \quad G_\omega^-(z, \mu, \phi) &= G_\omega^-(d, \mu, \phi) \exp\left(\frac{\gamma_{\mu\phi}^{\text{FS}}}{\mu\Lambda_\omega} (d - z)\right) \\ &- \frac{\exp\left(-\frac{\gamma_{\mu\phi}^{\text{FS}}}{\mu\Lambda_\omega} z\right)}{4\pi\mu\Lambda_\omega} \int_z^d (C_\omega \Delta \bar{T} + \bar{Q}_\omega \tau_\omega) \exp\left(\frac{\gamma_{\mu\phi}^{\text{FS}}}{\mu\Lambda_\omega} z'\right) dz' \\ \text{where, } \gamma_{\mu\phi}^{\text{FS}} &= (1 + i\eta\tau_\omega) + i\Lambda_\omega q \sqrt{1 - \mu^2} \cos \phi \end{aligned} \quad (5.16)$$

Here, $G_\omega^+(0, \mu, \phi)$ and $G_\omega^-(d, \mu, \phi)$ are determined by solving the boundary conditions (equation 5.2) with the following procedure. First, the angular integrals in the boundary conditions are discretized using Gauss quadrature, which results in the following set of linear equations in the variables $G_\omega^+(0, \mu_i, \phi_j)$ and $G_\omega^-(d, -\mu_i, \phi_j)$

for every $\{\mu_i, \phi_j\} \in (0, 1] \times [0, 2\pi]$ doublet from the discretization:

$$\begin{aligned}
G_\omega^+(0, \mu_i, \phi_j) &= p_\omega G_\omega^-(d, -\mu_i, \phi_j) \exp\left(-\frac{\gamma_{ij}^{\text{FS}}}{\mu_i \Lambda_\omega} d\right) \\
&+ \frac{p_\omega}{4\pi \mu_i \Lambda_\omega} \int_0^d (C_\omega \Delta \bar{T} + \bar{Q}_\omega \tau_\omega) \exp\left(-\frac{\gamma_{ij}^{\text{FS}}}{\mu_i \Lambda_\omega} z'\right) dz' \\
&+ (1 - p_\omega) \left[\sigma_\omega \frac{C_\omega \Delta \bar{T}(z=0)}{4\pi} \right. \\
&+ \frac{(1 - \sigma_\omega)}{\pi} \sum_{i'j'} G_\omega^-(d, -\mu_{i'}, \phi_{j'}) \exp\left(-\frac{\gamma_{i'j'}^{\text{FS}}}{\mu_{i'} \Lambda_\omega} d\right) \mu_{i'} w_{\mu_{i'} w_{\phi_{j'}}} \\
&+ \left. \frac{(1 - \sigma_\omega)}{4\pi^2 \Lambda_\omega} \sum_{i'j'} \int_0^d (C_\omega \Delta \bar{T} + \bar{Q}_\omega \tau_\omega) \exp\left(-\frac{\gamma_{i'j'}^{\text{FS}}}{\mu_{i'} \Lambda_\omega} z'\right) dz' w_{\mu_{i'} w_{\phi_{j'}}} \right] \\
G_\omega^-(d, -\mu_i, \phi_j) &= p_\omega G_\omega^+(0, \mu_i, \phi_j) \exp\left(-\frac{\gamma_{ij}^{\text{FS}}}{\mu_i \Lambda_\omega} d\right) \\
&+ \frac{p_\omega}{4\pi \mu_i \Lambda_\omega} \int_0^d (C_\omega \Delta \bar{T} + \bar{Q}_\omega \tau_\omega) \exp\left(-\frac{\gamma_{ij}^{\text{FS}}}{\mu_i \Lambda_\omega} (d - z')\right) dz' \\
&+ (1 - p_\omega) \left[\sigma_\omega \frac{C_\omega \Delta \bar{T}(z=d)}{4\pi} \right. \\
&+ \frac{(1 - \sigma_\omega)}{\pi} \sum_{i'j'} G_\omega^+(0, \mu_{i'}, \phi_{j'}) \exp\left(-\frac{\gamma_{i'j'}^{\text{FS}}}{\mu_{i'} \Lambda_\omega} d\right) \mu_{i'} w_{\mu_{i'} w_{\phi_{j'}}} \\
&+ \left. \frac{(1 - \sigma_\omega)}{4\pi^2 \Lambda_\omega} \sum_{i'j'} \int_0^d (C_\omega \Delta \bar{T} + \bar{Q}_\omega \tau_\omega) \exp\left(-\frac{\gamma_{i'j'}^{\text{FS}}}{\mu_{i'} \Lambda_\omega} (d - z')\right) dz' w_{\mu_{i'} w_{\phi_{j'}}} \right]
\end{aligned} \tag{5.17}$$

To obtain equation 5.17, we have substituted the general BTE solution into the boundary conditions to eliminate $G_\omega^-(0, \mu, \phi)$ and $G_\omega^+(d, \mu, \phi)$. Therefore, the only unknowns in the set of linear equations (equation 5.17) are given by $G_\omega^+(0, \mu, \phi)$ and $G_\omega^-(d, \mu, \phi)$. By bringing the terms containing $G_\omega^+(0, \mu, \phi)$ and $G_\omega^-(d, \mu, \phi)$ to the left hand side, equation 5.17 can be written in a concise matrix form:

$$\begin{bmatrix} U_{kk'}^+ & U_{kk'}^- \\ D_{kk'}^+ & D_{kk'}^- \end{bmatrix} \begin{pmatrix} G_\omega^+(0, \mu_i, \phi_j) \\ G_\omega^-(d, -\mu_i, \phi_j) \end{pmatrix} = \begin{pmatrix} \bar{c}_\omega^+(0, \mu_{i'}, \phi_{j'}) \\ \bar{c}_\omega^-(d, \mu_{i'}, \phi_{j'}) \end{pmatrix} \tag{5.18}$$

where $\bar{c}_\omega^+(0, \mu_{i'}, \phi_{j'})$ and $\bar{c}_\omega^-(d, \mu_{i'}, \phi_{j'})$ are analytical functions of the unknown temperature distribution function $\Delta \bar{T}$ obtained from the right hand side of equa-

tion 5.17. The solution to this set of linear equations can be represented as,

$$\begin{pmatrix} G_{\omega}^{+}(0, \mu_i, \phi_j) \\ G_{\omega}^{-}(d, -\mu_i, \phi_j) \end{pmatrix} = \begin{bmatrix} T_{kk'}^{+} & T_{kk'}^{-} \\ B_{kk'}^{+} & B_{kk'}^{-} \end{bmatrix} \begin{pmatrix} \bar{c}_{\omega}^{+}(0, \mu_{i'}, \phi_{j'}) \\ \bar{c}_{\omega}^{-}(d, \mu_{i'}, \phi_{j'}) \end{pmatrix} \quad (5.19)$$

where k is the index which represents the doublet $\{\mu_i, \phi_j\}$. To close the problem, the expressions for $G_{\omega}^{+}(z, \mu, \phi)$ and $G_{\omega}^{-}(z, \mu, \phi)$ (equation 5.16) and the boundary conditions (equation 5.19) are substituted into the energy conservation equation (equation 5.3) and an integral equation in the variable z for $\Delta\bar{T}(z)$ at each η and q is obtained, which has the form,

$$\Delta\bar{T}(z) = h(z) + f(z) + \int_0^d [K(z', z) \Delta\bar{T}(z')] dz' \quad (5.20)$$

where the functions $f(z)$ and $h(z)$ are dependent only on the variable z , and the kernel $K(z', z)$ is dependent only on the variables z and z' . Specifically, these functions are independent of the angular variables μ and ϕ . This integral equation (equation 5.20) is then solved using the method of degenerate kernels for each η and q to obtain the frequency domain solution $\Delta\bar{T}(z)$ for every η and q . Finally, the solution $\Delta\bar{T}(z)$ is substituted into equation 5.16 to obtain expressions for $G_{\omega}(z, \mu, \phi)$ and also the thickness-averaged in-plane heat flux $j_{x,\omega}$ given by,

$$\begin{aligned} j_{x,\omega} &= \frac{1}{4\pi d} \int_0^d \int_0^{2\pi} \int_{-1}^1 G_{\omega} v_{\omega} \sqrt{1-\mu^2} \cos\phi d\mu d\phi dz \\ &= \frac{1}{4\pi} \sum_{ij} \left[\frac{\mu_i \text{Kn}_{\omega}^d}{\gamma_{ij}^{\text{FS}}} \sum_{i'j'} \left[(T_{kk'}^{+} + B_{kk'}^{+}) \bar{c}_{\omega}^{+}(0, \mu_{i'}, \phi_{j'}) \right. \right. \\ &\quad \left. \left. + (T_{kk'}^{-} + B_{kk'}^{-}) \bar{c}_{\omega}^{-}(d, \mu_{i'}, \phi_{j'}) \right] \left(1 - \exp\left(-\frac{\gamma_{ij}^{\text{FS}}}{\mu_i \text{Kn}_{\omega}^d}\right) \right) \right. \\ &\quad \left. + \frac{2}{4\pi \gamma_{ij}^{\text{FS}}} \left(C_{\omega} \frac{t_0}{2} + \bar{Q}_{\omega} \tau_{\omega} \right) \left[1 - \frac{\mu_i \text{Kn}_{\omega}^d}{\gamma_{ij}^{\text{FS}}} \left(1 - \exp\left(-\frac{\gamma_{ij}^{\text{FS}}}{\mu_i \text{Kn}_{\omega}^d}\right) \right) \right] \right. \\ &\quad \left. - \frac{C_{\omega} \left(1 - \exp\left(-\frac{\gamma_{ij}^{\text{FS}}}{\mu_i \text{Kn}_{\omega}^d}\right) \right)}{4\pi \mu_i \text{Kn}_{\omega}^d} \sum_{m=1}^N t_m \frac{1 + (-1)^m}{m^2 \pi^2 + \left(\frac{\gamma_{ij}^{\text{FS}}}{\mu_i \text{Kn}_{\omega}^d}\right)^2} \right] v_{\omega} \sqrt{1-\mu_i^2} w_{\mu_i} w_{\phi_j} \end{aligned} \quad (5.21)$$

where t_i 's are the Fourier coefficients for the expansion of $\Delta\bar{T}$ in the cross-plane (z) direction and $\text{Kn}_{\omega}^d = \Lambda_{\omega}/d$ is the Knudsen number.

The details of the simplification of the boundary conditions and the evaluation of $T_{kk'}^+$, $T_{kk'}^-$, $B_{kk'}^+$, $B_{kk'}^-$, $\bar{c}_\omega^+(0, \mu_{i'}, \phi_{j'})$ and $\bar{c}_\omega^-(d, \mu_{i'}, \phi_{j'})$, the functional forms of $f(z)$, $h(z)$ and the kernel $K(z', z)$, and the description of the method of degenerate kernels used to solve equation 5.20 are described in the following three subsections.

Numerical Discretization of the Boundary Conditions

In this section, the discretization and the symbolic solution of the boundary conditions are discussed. The general boundary conditions at the boundaries of the thin film considered in this article are given by,

For $\mu \in (0, 1]$,

$$\begin{aligned} g_\omega^+(0, \mu, \phi) &= p_\omega g_\omega^-(0, -\mu, \phi) \\ &+ (1 - p_\omega) \left(\sigma_\omega g_\omega^0(\Delta T(z=0)) - \frac{(1 - \sigma_\omega)}{\pi} \int_0^{2\pi} \int_{-1}^0 g_\omega^-(0, \mu', \phi') \mu' d\mu' d\phi' \right) \\ &= p_\omega g_\omega^-(0, -\mu, \phi) \\ &+ (1 - p_\omega) \left(\sigma_\omega \frac{C_\omega \Delta T(z=0)}{4\pi} - \frac{(1 - \sigma_\omega)}{\pi} \int_0^{2\pi} \int_{-1}^0 g_\omega^-(0, \mu', \phi') \mu' d\mu' d\phi' \right) \end{aligned}$$

For $\mu \in [-1, 0)$,

$$\begin{aligned} g_\omega^-(d, \mu, \phi) &= p_\omega g_\omega^+(d, -\mu, \phi) \\ &+ (1 - p_\omega) \left(\sigma_\omega g_\omega^0(\Delta T(z=d)) + \frac{(1 - \sigma_\omega)}{\pi} \int_0^{2\pi} \int_0^1 g_\omega^+(d, \mu', \phi') \mu' d\mu' d\phi' \right) \\ &= p_\omega g_\omega^+(d, -\mu, \phi) \\ &+ (1 - p_\omega) \left(\sigma_\omega \frac{C_\omega \Delta T(z=d)}{4\pi} + \frac{(1 - \sigma_\omega)}{\pi} \int_0^{2\pi} \int_0^1 g_\omega^+(d, \mu', \phi') \mu' d\mu' d\phi' \right) \end{aligned} \tag{5.22}$$

In the frequency domain,

For $\mu \in (0, 1]$,

$$G_{\omega}^{+}(0, \mu, \phi) = p_{\omega} G_{\omega}^{-}(0, -\mu, \phi) + (1 - p_{\omega}) \left(\sigma_{\omega} \frac{C_{\omega} \Delta \bar{T}(z=0)}{4\pi} - \frac{(1 - \sigma_{\omega})}{\pi} \int_0^{2\pi} \int_{-1}^0 G_{\omega}^{-}(0, \mu', \phi') \mu' d\mu' d\phi' \right)$$

For $\mu \in [-1, 0)$,

$$G_{\omega}^{-}(d, \mu, \phi) = p_{\omega} G_{\omega}^{+}(d, -\mu, \phi) + (1 - p_{\omega}) \left(\sigma_{\omega} \frac{C_{\omega} \Delta \bar{T}(z=d)}{4\pi} + \frac{(1 - \sigma_{\omega})}{\pi} \int_0^{2\pi} \int_0^1 G_{\omega}^{+}(d, \mu', \phi') \mu' d\mu' d\phi' \right) \quad (5.23)$$

For any given μ and ϕ , there are four unknown quantities to be determined at the thin film boundaries: $G_{\omega}^{+}(0, \mu, \phi)$, $G_{\omega}^{-}(0, -\mu, \phi)$, $G_{\omega}^{+}(d, -\mu, \phi)$, and $G_{\omega}^{-}(d, \mu, \phi)$, while there are only two equations which are directly evident (equation 5.23). However, closed-form relations for these four unknown quantities can be obtained in terms of the unknown temperature distribution at the thin film boundaries in the frequency domain ($\Delta \bar{T}(z=0)$ and $\Delta \bar{T}(z=d)$) by substituting the general solution of the BTE

into boundary conditions (equation 5.23) to get the following:

for $\mu \in (0, 1]$,

$$\begin{aligned}
G_{\omega}^{+}(0, \mu, \phi) &= p_{\omega} G_{\omega}^{-}(d, -\mu, \phi) \exp\left(-\frac{\gamma_{\mu\phi}^{\text{FS}}}{\mu\Lambda_{\omega}} d\right) \\
&+ \frac{p_{\omega}}{4\pi\mu\Lambda_{\omega}} \int_0^d (C_{\omega}\Delta\bar{T} + \bar{Q}_{\omega}\tau_{\omega}) \exp\left(-\frac{\gamma_{\mu\phi}^{\text{FS}}}{\mu\Lambda_{\omega}} z'\right) dz' \\
&+ (1 - p_{\omega}) \left[\sigma_{\omega} \frac{C_{\omega}\Delta\bar{T}(z=0)}{4\pi} \right. \\
&- \frac{(1 - \sigma_{\omega})}{\pi} \int_0^{2\pi} \int_{-1}^0 G_{\omega}^{-}(d, \mu', \phi') \exp\left(\frac{\gamma_{\mu'\phi'}^{\text{FS}}}{\mu'\Lambda_{\omega}} d\right) \mu' d\mu' d\phi' \\
&\left. + \frac{(1 - \sigma_{\omega})}{4\pi^2\Lambda_{\omega}} \int_0^{2\pi} \int_{-1}^0 \int_0^d (C_{\omega}\Delta\bar{T} + \bar{Q}_{\omega}\tau_{\omega}) \exp\left(\frac{\gamma_{\mu'\phi'}^{\text{FS}}}{\mu'\Lambda_{\omega}} z'\right) dz' d\mu' d\phi' \right]
\end{aligned}$$

and for $\mu \in [-1, 0)$,

$$\begin{aligned}
G_{\omega}^{-}(d, \mu, \phi) &= p_{\omega} G_{\omega}^{+}(0, -\mu, \phi) \exp\left(\frac{\gamma_{\mu\phi}^{\text{FS}}}{\mu\Lambda_{\omega}} d\right) \\
&- \frac{p_{\omega} \exp\left(\frac{\gamma_{\mu\phi}^{\text{FS}}}{\mu\Lambda_{\omega}} d\right)}{4\pi\mu\Lambda_{\omega}} \int_0^d (C_{\omega}\Delta\bar{T} + \bar{Q}_{\omega}\tau_{\omega}) \exp\left(-\frac{\gamma_{\mu\phi}^{\text{FS}}}{\mu\Lambda_{\omega}} z'\right) dz' \\
&+ (1 - p_{\omega}) \left[\sigma_{\omega} \frac{C_{\omega}\Delta\bar{T}(z=d)}{4\pi} \right. \\
&+ \frac{(1 - \sigma_{\omega})}{\pi} \int_0^{2\pi} \int_0^1 G_{\omega}^{+}(0, \mu', \phi') \exp\left(-\frac{\gamma_{\mu'\phi'}^{\text{FS}}}{\mu'\Lambda_{\omega}} d\right) \mu' d\mu' d\phi' \\
&+ \frac{(1 - \sigma_{\omega})}{4\pi^2\Lambda_{\omega}} \int_0^{2\pi} \int_0^1 \exp\left(-\frac{\gamma_{\mu'\phi'}^{\text{FS}}}{\mu'\Lambda_{\omega}} d\right) \int_0^d (C_{\omega}\Delta\bar{T} + \bar{Q}_{\omega}\tau_{\omega}) \\
&\quad \times \exp\left(\frac{\gamma_{\mu'\phi'}^{\text{FS}}}{\mu'\Lambda_{\omega}} z'\right) dz' d\mu' d\phi' \left. \right]
\end{aligned}$$

(5.24)

For convenience, the limits on variables μ and μ' are changed from $[-1, 1]$ to $(0, 1]$ in equation 5.24 wherever necessary to obtain

$$\begin{aligned}
G_{\omega}^{+}(0, \mu, \phi) &= p_{\omega} G_{\omega}^{-}(d, -\mu, \phi) \exp\left(-\frac{\gamma_{\mu\phi}^{\text{FS}}}{\mu\Lambda_{\omega}} d\right) \\
&+ \frac{p_{\omega}}{4\pi\mu\Lambda_{\omega}} \int_0^d (C_{\omega}\Delta\bar{T} + \bar{Q}_{\omega}\tau_{\omega}) \exp\left(-\frac{\gamma_{\mu\phi}^{\text{FS}}}{\mu\Lambda_{\omega}} z'\right) dz' \\
&+ (1 - p_{\omega}) \left[\sigma_{\omega} \frac{C_{\omega}\Delta\bar{T}(z=0)}{4\pi} \right. \\
&+ \frac{(1 - \sigma_{\omega})}{\pi} \int_0^{2\pi} \int_0^1 G_{\omega}^{-}(d, -\mu', \phi') \exp\left(-\frac{\gamma_{\mu'\phi'}^{\text{FS}}}{\mu'\Lambda_{\omega}} d\right) \mu' d\mu' d\phi' \\
&+ \left. \frac{(1 - \sigma_{\omega})}{4\pi^2\Lambda_{\omega}} \int_0^{2\pi} \int_0^1 \int_0^d (C_{\omega}\Delta\bar{T} + \bar{Q}_{\omega}\tau_{\omega}) \exp\left(-\frac{\gamma_{\mu'\phi'}^{\text{FS}}}{\mu'\Lambda_{\omega}} z'\right) dz' d\mu' d\phi' \right] \\
G_{\omega}^{-}(d, -\mu, \phi) &= p_{\omega} G_{\omega}^{+}(0, \mu, \phi) \exp\left(-\frac{\gamma_{\mu\phi}^{\text{FS}}}{\mu\Lambda_{\omega}} d\right) \\
&+ \frac{p_{\omega}}{4\pi\mu\Lambda_{\omega}} \int_0^d (C_{\omega}\Delta\bar{T} + \bar{Q}_{\omega}\tau_{\omega}) \exp\left(-\frac{\gamma_{\mu\phi}^{\text{FS}}}{\mu\Lambda_{\omega}} (d - z')\right) dz' \\
&+ (1 - p_{\omega}) \left[\sigma_{\omega} \frac{C_{\omega}\Delta\bar{T}(z=d)}{4\pi} \right. \\
&+ \frac{(1 - \sigma_{\omega})}{\pi} \int_0^{2\pi} \int_0^1 G_{\omega}^{+}(0, \mu', \phi') \exp\left(-\frac{\gamma_{\mu'\phi'}^{\text{FS}}}{\mu'\Lambda_{\omega}} d\right) \mu' d\mu' d\phi' \\
&+ \left. \frac{(1 - \sigma_{\omega})}{4\pi^2\Lambda_{\omega}} \int_0^{2\pi} \int_0^1 \int_0^d (C_{\omega}\Delta\bar{T} + \bar{Q}_{\omega}\tau_{\omega}) \exp\left(-\frac{\gamma_{\mu'\phi'}^{\text{FS}}}{\mu'\Lambda_{\omega}} (d - z')\right) dz' d\mu' d\phi' \right]
\end{aligned} \tag{5.25}$$

Equation 5.25 represents a system of integral equations to solve for the two unknown quantities $G_{\omega}^{+}(0, \mu, \phi)$ and $G_{\omega}^{-}(d, -\mu, \phi)$ for every μ and ϕ . In order to solve this system of equations, the integrals in μ' and ϕ' variables are first discretized using Gauss quadrature,

$$\int_0^{2\pi} \int_0^1 f(\mu', \phi') d\mu' d\phi' = \sum_{ij} f(\mu_i, \phi_j) w_{\mu_i} w_{\phi_j} \tag{5.26}$$

where μ_i and ϕ_j are the quadrature points and w_{μ_i} and w_{ϕ_j} are the corresponding

weights. Therefore, equation 5.25 transforms into,

$$\begin{aligned}
G_{\omega}^{+}(0, \mu_i, \phi_j) &= p_{\omega} G_{\omega}^{-}(d, -\mu_i, \phi_j) \exp\left(-\frac{\gamma_{ij}^{\text{FS}}}{\mu_i \Lambda_{\omega}} d\right) \\
&+ \frac{p_{\omega}}{4\pi \mu_i \Lambda_{\omega}} \int_0^d (C_{\omega} \Delta \bar{T} + \bar{Q}_{\omega} \tau_{\omega}) \exp\left(-\frac{\gamma_{ij}^{\text{FS}}}{\mu_i \Lambda_{\omega}} z'\right) dz' \\
&+ (1 - p_{\omega}) \left[\sigma_{\omega} \frac{C_{\omega} \Delta \bar{T}(z=0)}{4\pi} \right. \\
&+ \frac{(1 - \sigma_{\omega})}{\pi} \sum_{i'j'} G_{\omega}^{-}(d, -\mu_{i'}, \phi_{j'}) \exp\left(-\frac{\gamma_{i'j'}^{\text{FS}}}{\mu_{i'} \Lambda_{\omega}} d\right) \mu_{i'} w_{\mu_{i'} w_{\phi_{j'}}} \\
&+ \left. \frac{(1 - \sigma_{\omega})}{4\pi^2 \Lambda_{\omega}} \sum_{i'j'} \int_0^d (C_{\omega} \Delta \bar{T} + \bar{Q}_{\omega} \tau_{\omega}) \exp\left(-\frac{\gamma_{i'j'}^{\text{FS}}}{\mu_{i'} \Lambda_{\omega}} z'\right) dz' w_{\mu_{i'} w_{\phi_{j'}}} \right] \\
G_{\omega}^{-}(d, -\mu_i, \phi_j) &= p_{\omega} G_{\omega}^{+}(0, \mu_i, \phi_j) \exp\left(-\frac{\gamma_{ij}^{\text{FS}}}{\mu_i \Lambda_{\omega}} d\right) \\
&+ \frac{p_{\omega}}{4\pi \mu_i \Lambda_{\omega}} \int_0^d (C_{\omega} \Delta \bar{T} + \bar{Q}_{\omega} \tau_{\omega}) \exp\left(-\frac{\gamma_{ij}^{\text{FS}}}{\mu_i \Lambda_{\omega}} (d - z')\right) dz' \\
&+ (1 - p_{\omega}) \left[\sigma_{\omega} \frac{C_{\omega} \Delta \bar{T}(z=d)}{4\pi} \right. \\
&+ \frac{(1 - \sigma_{\omega})}{\pi} \sum_{i'j'} G_{\omega}^{+}(0, \mu_{i'}, \phi_{j'}) \exp\left(-\frac{\gamma_{i'j'}^{\text{FS}}}{\mu_{i'} \Lambda_{\omega}} d\right) \mu_{i'} w_{\mu_{i'} w_{\phi_{j'}}} \\
&+ \left. \frac{(1 - \sigma_{\omega})}{4\pi^2 \Lambda_{\omega}} \sum_{i'j'} \int_0^d (C_{\omega} \Delta \bar{T} + \bar{Q}_{\omega} \tau_{\omega}) \exp\left(-\frac{\gamma_{i'j'}^{\text{FS}}}{\mu_{i'} \Lambda_{\omega}} (d - z')\right) dz' w_{\mu_{i'} w_{\phi_{j'}}} \right]
\end{aligned} \tag{5.27}$$

To simplify these expressions, the following substitutions into equation 5.27 are made:

$$\begin{aligned}
I_{\mu\phi}^{+} &= \int_0^d (C_{\omega} \Delta \bar{T} + \bar{Q}_{\omega} \tau_{\omega}) \exp\left(-\frac{\gamma_{\mu\phi}^{\text{FS}}}{\mu \Lambda_{\omega}} z'\right) dz' \\
&= C_{\omega} \int_0^d \Delta \bar{T} \exp\left(-\frac{\gamma_{\mu\phi}^{\text{FS}}}{\mu \Lambda_{\omega}} z'\right) dz' + \bar{Q}_{\omega} \tau_{\omega} \Lambda_{\omega} \frac{\mu}{\gamma_{\mu\phi}^{\text{FS}}} \left(1 - \exp\left(-\frac{\gamma_{\mu\phi}^{\text{FS}}}{\mu \Lambda_{\omega}} d\right)\right) \\
I_{\mu\phi}^{-} &= \int_0^d (C_{\omega} \Delta \bar{T} + \bar{Q}_{\omega} \tau_{\omega}) \exp\left(-\frac{\gamma_{\mu\phi}^{\text{FS}}}{\mu \Lambda_{\omega}} (d - z')\right) dz' \\
&= C_{\omega} \int_0^d \Delta \bar{T} \exp\left(-\frac{\gamma_{\mu\phi}^{\text{FS}}}{\mu \Lambda_{\omega}} (d - z')\right) dz' + \bar{Q}_{\omega} \tau_{\omega} \Lambda_{\omega} \frac{\mu}{\gamma_{\mu\phi}^{\text{FS}}} \left(1 - \exp\left(-\frac{\gamma_{\mu\phi}^{\text{FS}}}{\mu \Lambda_{\omega}} d\right)\right)
\end{aligned} \tag{5.28}$$

which transform equation 5.27 into

$$\begin{aligned}
G_{\omega}^{+}(0, \mu_i, \phi_j) &= p_{\omega} G_{\omega}^{-}(d, -\mu_i, \phi_j) \exp\left(-\frac{\gamma_{ij}^{\text{FS}}}{\mu_i \Lambda_{\omega}} d\right) + \frac{p_{\omega}}{4\pi \mu_i \Lambda_{\omega}} I_{ij}^{+} \\
&+ (1 - p_{\omega}) \left[\sigma_{\omega} \frac{C_{\omega} \Delta \bar{T}(z=0)}{4\pi} \right. \\
&+ \frac{(1 - \sigma_{\omega})}{\pi} \sum_{i'j'} G_{\omega}^{-}(d, -\mu_{i'}, \phi_{j'}) \exp\left(-\frac{\gamma_{i'j'}^{\text{FS}}}{\mu_{i'} \Lambda_{\omega}} d\right) \mu_{i'} w_{\mu_{i'}} w_{\phi_{j'}} \\
&\left. + \frac{(1 - \sigma_{\omega})}{4\pi^2 \Lambda_{\omega}} \sum_{i'j'} w_{\mu_{i'}} w_{\phi_{j'}} I_{i'j'}^{+} \right] \\
G_{\omega}^{-}(d, -\mu_i, \phi_j) &= p_{\omega} G_{\omega}^{+}(0, \mu_i, \phi_j) \exp\left(-\frac{\gamma_{ij}^{\text{FS}}}{\mu_i \Lambda_{\omega}} d\right) + \frac{p_{\omega}}{4\pi \mu_i \Lambda_{\omega}} I_{ij}^{-} \\
&+ (1 - p_{\omega}) \left[\sigma_{\omega} \frac{C_{\omega} \Delta \bar{T}(z=d)}{4\pi} \right. \\
&+ \frac{(1 - \sigma_{\omega})}{\pi} \sum_{i'j'} G_{\omega}^{+}(0, \mu_{i'}, \phi_{j'}) \exp\left(-\frac{\gamma_{i'j'}^{\text{FS}}}{\mu_{i'} \Lambda_{\omega}} d\right) \mu_{i'} w_{\mu_{i'}} w_{\phi_{j'}} \\
&\left. + \frac{(1 - \sigma_{\omega})}{4\pi^2 \Lambda_{\omega}} \sum_{i'j'} w_{\mu_{i'}} w_{\phi_{j'}} I_{i'j'}^{+} \right]
\end{aligned} \tag{5.29}$$

These discretized boundary conditions (equation 5.29) can be written in a concise matrix form as

$$[A] \mathbf{G}_{\text{BC}} = \bar{\mathbf{c}} \tag{5.30}$$

with the solution of the form

$$\mathbf{G}_{\text{BC}} = [A]^{-1} \bar{\mathbf{c}} \tag{5.31}$$

where,

$$\begin{aligned}
\mathbf{G}_{\text{BC}} &= \begin{pmatrix} G_{\omega}^{+}(0, \mu_i, \phi_j) \\ G_{\omega}^{-}(d, -\mu_i, \phi_j) \end{pmatrix}_{[2N \times 1]} \\
[A]^{-1} &= \begin{bmatrix} T_{kk'}^{+} & T_{kk'}^{-} \\ B_{kk'}^{+} & B_{kk'}^{-} \end{bmatrix}_{[2N \times 2N]}
\end{aligned}$$

and

$$\bar{\mathbf{c}} = \begin{pmatrix} \bar{c}_{\omega}^{+}(0, \mu_{i'}, \phi_{j'}) \\ \bar{c}_{\omega}^{-}(d, \mu_{i'}, \phi_{j'}) \end{pmatrix}_{[2N \times 1]}$$

Here, k is the index for the combination $\{\mu_i, \phi_j\}$, N is the total number of combinations of $\{\mu_i, \phi_j\}$ and

$$\begin{aligned}
\bar{c}_\omega^+(0, \mu'_i, \phi'_j) &= \frac{p_\omega}{4\pi\mu'_i\Lambda_\omega} I_{\mu'_i\phi'_j}^+ \\
&\quad + (1 - p_\omega) \left(\frac{\sigma_\omega}{4\pi} C_\omega \Delta \bar{T}(z=0) + \frac{(1 - \sigma_\omega)}{4\pi^2\Lambda_\omega} \sum_{i''j''} w_{\mu_{i''}} w_{\phi_{j''}} I_{i''j''}^+ \right) \\
\bar{c}_\omega^-(d, \mu'_i, \phi'_j) &= \frac{p_\omega}{4\pi\mu'_i\Lambda_\omega} I_{\mu'_i\phi'_j}^- \\
&\quad + (1 - p_\omega) \left(\frac{\sigma_\omega}{4\pi} C_\omega \Delta \bar{T}(z=d) + \frac{(1 - \sigma_\omega)}{4\pi^2\Lambda_\omega} \sum_{i''j''} w_{\mu_{i''}} w_{\phi_{j''}} I_{i''j''}^- \right)
\end{aligned} \tag{5.32}$$

After substituting equation 5.31 into general BTE solution,

$$\begin{aligned}
G_{\omega}^{+}(z, \mu_i, \phi_j) &= \left(\sum_{i'j'} [T_{kk'}^{+} \bar{c}_{\omega}^{+}(0, \mu_{i'}, \phi_{j'}) + T_{kk'}^{-} \bar{c}_{\omega}^{-}(d, \mu_{i'}, \phi_{j'})] \right) \exp\left(-\frac{\gamma_{ij}^{\text{FS}}}{\mu_i \Lambda_{\omega}} z\right) \\
&\quad + \frac{\exp\left(-\frac{\gamma_{ij}^{\text{FS}}}{\mu_i \Lambda_{\omega}} z\right)}{4\pi \mu_i \Lambda_{\omega}} \int_0^z (C_{\omega} \Delta \bar{T} + \bar{Q}_{\omega} \tau_{\omega}) \exp\left(\frac{\gamma_{ij}^{\text{FS}}}{\mu_i \Lambda_{\omega}} z'\right) dz' \\
&= \left(\sum_{i'j'} [T_{kk'}^{+} \bar{c}_{\omega}^{+}(0, \mu_{i'}, \phi_{j'}) + T_{kk'}^{-} \bar{c}_{\omega}^{-}(d, \mu_{i'}, \phi_{j'})] \right) \exp\left(-\frac{\gamma_{ij}^{\text{FS}}}{\mu_i \Lambda_{\omega}} z\right) \\
&\quad + \frac{1}{4\pi \mu_i \Lambda_{\omega}} \int_0^z (C_{\omega} \Delta \bar{T} + \bar{Q}_{\omega} \tau_{\omega}) \exp\left(-\frac{\gamma_{ij}^{\text{FS}}}{\mu_i \Lambda_{\omega}} |z' - z|\right) dz' \\
G_{\omega}^{-}(z, -\mu_i, \phi_j) &= \left(\sum_{i'j'} [B_{kk'}^{+} \bar{c}_{\omega}^{+}(0, \mu_{i'}, \phi_{j'}) + B_{kk'}^{-} \bar{c}_{\omega}^{-}(d, \mu_{i'}, \phi_{j'})] \right) \\
&\quad \times \exp\left(-\frac{\gamma_{ij}^{\text{FS}}}{\mu_i \Lambda_{\omega}} (d - z)\right) \\
&\quad + \frac{\exp\left(\frac{\gamma_{ij}^{\text{FS}}}{\mu_i \Lambda_{\omega}} z\right)}{4\pi \mu_i \Lambda_{\omega}} \int_z^d (C_{\omega} \Delta \bar{T} + \bar{Q}_{\omega} \tau_{\omega}) \exp\left(-\frac{\gamma_{ij}^{\text{FS}}}{\mu_i \Lambda_{\omega}} z'\right) dz' \\
&= \left(\sum_{i'j'} [B_{kk'}^{+} \bar{c}_{\omega}^{+}(0, \mu_{i'}, \phi_{j'}) + B_{kk'}^{-} \bar{c}_{\omega}^{-}(d, \mu_{i'}, \phi_{j'})] \right) \exp\left(-\frac{\gamma_{ij}^{\text{FS}}}{\mu_i \Lambda_{\omega}} (d - z)\right) \\
&\quad + \frac{1}{4\pi \mu_i \Lambda_{\omega}} \int_z^d (C_{\omega} \Delta \bar{T} + \bar{Q}_{\omega} \tau_{\omega}) \exp\left(-\frac{\gamma_{ij}^{\text{FS}}}{\mu_i \Lambda_{\omega}} |z' - z|\right) dz'
\end{aligned} \tag{5.33}$$

where the unknown quantities $G_{\omega}^{+}(z, \mu_i, \phi_j)$, $G_{\omega}^{-}(z, -\mu_i, \phi_j)$ and $\Delta \bar{T}$ are related through the energy conservation requirement.

Formulation of the Integral Equation for $\Delta \bar{T}$

In order to solve for the unknown quantities ($G_{\omega}^{+}(z, \mu_i, \phi_j)$, $G_{\omega}^{-}(z, -\mu_i, \phi_j)$ and $\Delta \bar{T}$), the energy conservation equation is first discretized in the angular variables (μ and ϕ) using Gauss quadrature (equation 5.26). Next, the general solution (equation 5.33) is substituted into the discretized energy conservation equation to obtain

the following integral equation for $\Delta\bar{T}$:

$$\begin{aligned}
\Delta\bar{T}(z) &= \frac{1}{\int_{\omega=0}^{\omega_m} \frac{C_\omega}{\tau_\omega} d\omega} \int_{\omega=0}^{\omega_m} \left[\frac{1}{\tau_\omega} \sum_{ij} (G_\omega^+(z, \mu_i, \phi_j) + G_\omega^-(z, -\mu_i, \phi_j)) w_{\mu_i} w_{\phi_j} \right] d\omega \\
&= \frac{1}{\int_{\omega=0}^{\omega_m} \frac{C_\omega}{\tau_\omega} d\omega} \int_{\omega=0}^{\omega_m} \frac{1}{\tau_\omega} \\
&\quad \times \left[\sum_{ij} \left(\int_0^d (C_\omega \Delta\bar{T} + \bar{Q}_\omega \tau_\omega) \exp\left(-\frac{\gamma_{ij}^{\text{FS}}}{\mu_i \Lambda_\omega} |z' - z|\right) dz' \right) \frac{w_{\mu_i} w_{\phi_j}}{4\pi \mu_i \Lambda_\omega} \right. \\
&\quad + \sum_{ij} \sum_{i'j'} (T_{kk}^+ \bar{c}_\omega^+(0, \mu_{i'}, \phi_{j'}) + T_{kk}^- \bar{c}_\omega^-(d, \mu_{i'}, \phi_{j'})) w_{\mu_i} w_{\phi_j} \exp\left(-\frac{\gamma_{ij}^{\text{FS}}}{\mu_i \Lambda_\omega} z\right) \\
&\quad \left. + \sum_{ij} \sum_{i'j'} (B_{kk}^+ \bar{c}_\omega^+(0, \mu_{i'}, \phi_{j'}) + B_{kk}^- \bar{c}_\omega^-(d, \mu_{i'}, \phi_{j'})) w_{\mu_i} w_{\phi_j} \right. \\
&\quad \left. \times \exp\left(-\frac{\gamma_{ij}^{\text{FS}}}{\mu_i \Lambda_\omega} (d - z)\right) \right] d\omega
\end{aligned} \tag{5.34}$$

Let us analyze the RHS of this equation term-by-term. For simplicity, let $\Omega = \int_{\omega=0}^{\omega_m} \frac{C_\omega}{\tau_\omega} d\omega$. The first term in the RHS of equation 5.34 becomes,

$$\begin{aligned}
&\frac{1}{\Omega} \int_{\omega=0}^{\omega_m} \frac{1}{\tau_\omega} \left[\sum_{ij} \left(\int_0^d (C_\omega \Delta\bar{T} + \bar{Q}_\omega \tau_\omega) \exp\left(-\frac{\gamma_{ij}^{\text{FS}}}{\mu_i \Lambda_\omega} |z' - z|\right) dz' \right) \frac{w_{\mu_i} w_{\phi_j}}{4\pi \mu_i \Lambda_\omega} d\omega \right] \\
&= \frac{1}{\Omega} \int_0^d \Delta\bar{T} \left[\int_{\omega=0}^{\omega_m} \left(\frac{C_\omega}{4\pi \tau_\omega \Lambda_\omega} \sum_{ij} \frac{w_{\mu_i} w_{\phi_j}}{\mu_i} \exp\left(-\frac{\gamma_{ij}^{\text{FS}}}{\mu_i \Lambda_\omega} |z' - z|\right) \right) d\omega \right] dz' \\
&\quad + \frac{1}{\Omega} \int_{\omega=0}^{\omega_m} \bar{Q}_\omega \left[\sum_{ij} \left(\int_0^z \exp\left(-\frac{\gamma_{ij}^{\text{FS}}}{\mu_i \Lambda_\omega} |z' - z|\right) dz' \right. \right. \\
&\quad \left. \left. + \int_z^d \exp\left(-\frac{\gamma_{ij}^{\text{FS}}}{\mu_i \Lambda_\omega} |z' - z|\right) dz' \right) \frac{w_{\mu_i} w_{\phi_j}}{4\pi \mu_i \Lambda_\omega} \right] \\
&= \frac{1}{\Omega} \int_0^d \Delta\bar{T} \left[\int_{\omega=0}^{\omega_m} \left(\frac{C_\omega}{4\pi \tau_\omega \Lambda_\omega} \sum_{ij} \frac{w_{\mu_i} w_{\phi_j}}{\mu_i} \exp\left(-\frac{\gamma_{ij}^{\text{FS}}}{\mu_i \Lambda_\omega} |z' - z|\right) \right) d\omega \right] dz' \\
&\quad + \frac{1}{\Omega} \int_{\omega=0}^{\omega_m} \bar{Q}_\omega \left[\sum_{ij} \left(2 - \exp\left(-\frac{\gamma_{ij}^{\text{FS}}}{\mu_i \Lambda_\omega} z\right) - \exp\left(-\frac{\gamma_{ij}^{\text{FS}}}{\mu_i \Lambda_\omega} (d - z)\right) \right) \frac{w_{\mu_i} w_{\phi_j}}{4\pi \gamma_{ij}^{\text{FS}}} \right] d\omega \\
&= \int_0^d \Delta\bar{T} [K_1^1(z', z)] dz' + f_1^1(z)
\end{aligned} \tag{5.35}$$

Similarly, the second term in the RHS of equation 5.34 becomes,

$$\begin{aligned}
& \frac{1}{\Omega} \int_{\omega=0}^{\omega_m} \frac{1}{\tau_\omega} \left[\sum_{ij} \sum_{i'j'} \left(T_{kk'}^+ \bar{c}_\omega^+ (0, \mu_{i'}, \phi_{j'}) + T_{kk'}^- \bar{c}_\omega^- (d, \mu_{i'}, \phi_{j'}) \right) \right. \\
& \quad \left. \times w_{\mu_i} w_{\phi_j} \exp \left(-\frac{\gamma_{ij}^{\text{FS}}}{\mu_i \Lambda_\omega} z \right) \right] d\omega \\
&= \frac{1}{\Omega} \int_{\omega=0}^{\omega_m} \frac{1}{\tau_\omega} \left[\sum_{ij} \sum_{i'j'} \left(\frac{p_\omega}{4\pi \mu_{i'} \Lambda_\omega} \left(I_{i'j'}^+ T_{kk'}^+ + I_{i'j'}^- T_{kk'}^- \right) w_{\mu_i} w_{\phi_j} \exp \left(-\frac{\gamma_{ij}^{\text{FS}}}{\mu_i \Lambda_\omega} z \right) \right) \right. \\
& \quad \left. + (1 - p_\omega) (1 - \sigma_\omega) \right. \\
& \quad \left. \times \sum_{ij} \sum_{i'j'} \sum_{i''j''} \left(\frac{w_{\mu_{i''}} w_{\phi_{j''}}}{4\pi^2 \Lambda_\omega} \left(I_{i''j''}^+ T_{kk'}^+ + I_{i''j''}^- T_{kk'}^- \right) w_{\mu_i} w_{\phi_j} \exp \left(-\frac{\gamma_{ij}^{\text{FS}}}{\mu_i \Lambda_\omega} z \right) \right) \right. \\
& \quad \left. + (1 - p_\omega) \sigma_\omega \right. \\
& \quad \left. \times \sum_{ij} \sum_{i'j'} \left(\frac{C_\omega}{4\pi} \left(T_{kk'}^+ \Delta \bar{T} (z=0) + T_{kk'}^- \Delta \bar{T} (z=d) \right) w_{\mu_i} w_{\phi_j} \exp \left(-\frac{\gamma_{ij}^{\text{FS}}}{\mu_i \Lambda_\omega} z \right) \right) \right] d\omega \\
&= f_2^1(z) + f_2^2(z) + h_2(z) + \int_0^d \Delta \bar{T} \left[K_2^1(z', z) + K_2^2(z', z) \right] dz'
\end{aligned} \tag{5.36}$$

where,

$$\begin{aligned}
f_2^1(z) &= \frac{1}{\Omega} \int_{\omega=0}^{\omega_m} \left[\sum_{ij} \sum_{i'j'} \left(\frac{\bar{Q}_\omega p_\omega (T_{kk'}^+ + T_{kk'}^-)}{4\pi \gamma_{\mu_i \phi_j}^{\text{FS}}} \right) \right. \\
& \quad \left. \times \left(1 - \exp \left(-\frac{\gamma_{i'j'}^{\text{FS}}}{\mu_{i'} \Lambda_\omega} d \right) \right) \exp \left(-\frac{\gamma_{ij}^{\text{FS}}}{\mu_i \Lambda_\omega} z \right) w_{\mu_i} w_{\phi_j} \right] d\omega
\end{aligned} \tag{5.37}$$

$$\begin{aligned}
f_2^2(z) &= \frac{1}{\Omega} \int_{\omega=0}^{\omega_m} \left[\sum_{ij} \sum_{i'j'} \sum_{i''j''} \left(\frac{\bar{Q}_\omega (1 - p_\omega) (1 - \sigma_\omega) (T_{kk'}^+ + T_{kk'}^-) \mu_{i''} w_{\mu_{i''}} w_{\phi_{j''}}}{4\pi^2 \gamma_{i''j''}^{\text{FS}}} \right) \right. \\
& \quad \left. \times \left(1 - \exp \left(-\frac{\gamma_{i''j''}^{\text{FS}}}{\mu_{i''} \Lambda_\omega} d \right) \right) w_{\mu_i} w_{\phi_j} \exp \left(-\frac{\gamma_{ij}^{\text{FS}}}{\mu_i \Lambda_\omega} z \right) \right] d\omega
\end{aligned} \tag{5.38}$$

$$\begin{aligned}
h_2(z) &= \frac{1}{\Omega} \int_{\omega=0}^{\omega_m} \frac{1}{\tau_\omega} \left[\sum_{ij} \sum_{i'j'} \left(\frac{C_\omega (1 - p_\omega) \sigma_\omega}{4\pi} \left(T_{kk'}^+ \Delta \bar{T} (z=0) + T_{kk'}^- \Delta \bar{T} (z=d) \right) \right) \right. \\
& \quad \left. \times w_{\mu_i} w_{\phi_j} \exp \left(-\frac{\gamma_{ij}^{\text{FS}}}{\mu_i \Lambda_\omega} z \right) \right]
\end{aligned} \tag{5.39}$$

$$\begin{aligned}
K_2^1(z', z) &= \frac{1}{\Omega} \int_{\omega=0}^{\omega_m} \frac{C_\omega}{\tau_\omega} \left[\sum_{ij} \sum_{i'j'} \left(\frac{p_\omega}{4\pi\mu_{i'}\Lambda_\omega} \left(\exp\left(-\frac{\gamma_{i'j'}^{\text{FS}}}{\mu_{i'}\Lambda_\omega} z'\right) T_{kk'}^+ \right. \right. \right. \\
&\quad \left. \left. \left. + \exp\left(-\frac{\gamma_{i'j'}^{\text{FS}}}{\mu_{i'}\Lambda_\omega} (d-z')\right) T_{kk'}^- \right) w_{\mu_i} w_{\phi_j} \exp\left(-\frac{\gamma_{ij}^{\text{FS}}}{\mu_i\Lambda_\omega} z\right) \right] d\omega \quad (5.40)
\end{aligned}$$

$$\begin{aligned}
K_2^2(z', z) &= \frac{1}{\Omega} \int_{\omega=0}^{\omega_m} \frac{C_\omega (1-p_\omega) (1-\sigma_\omega)}{\tau_\omega} \\
&\quad \times \left[\sum_{ij} \sum_{i'j'} \sum_{i''j''} \left(\frac{w_{\mu_{i''}} w_{\phi_{j''}}}{4\pi^2\Lambda_\omega} \left(\exp\left(-\frac{\gamma_{i''j''}^{\text{FS}}}{\mu_{i''}\Lambda_\omega} z'\right) T_{kk'}^+ \right. \right. \right. \\
&\quad \left. \left. \left. + \exp\left(-\frac{\gamma_{i''j''}^{\text{FS}}}{\mu_{i''}\Lambda_\omega} (d-z')\right) T_{kk'}^- \right) w_{\mu_i} w_{\phi_j} \exp\left(-\frac{\gamma_{ij}^{\text{FS}}}{\mu_i\Lambda_\omega} z\right) \right] d\omega \quad (5.41)
\end{aligned}$$

and the third term in the RHS of equation 5.34 becomes

$$\begin{aligned}
&\frac{1}{\Omega} \int_{\omega=0}^{\omega_m} \frac{1}{\tau_\omega} \left[\sum_{ij} \sum_{i'j'} \left(B_{kk'}^+ \bar{c}_\omega^+ (0, \mu_{i'}, \phi_{j'}) + B_{kk'}^- \bar{c}_\omega^- (d, \mu_{i'}, \phi_{j'}) \right) \right. \\
&\quad \left. \times w_{\mu_i} w_{\phi_j} \exp\left(-\frac{\gamma_{ij}^{\text{FS}}}{\mu_i\Lambda_\omega} (d-z)\right) \right] d\omega \\
&= \frac{1}{\Omega} \int_{\omega=0}^{\omega_m} \frac{1}{\tau_\omega} \\
&\quad \times \left[\sum_{ij} \sum_{i'j'} \left(\frac{p_\omega}{4\pi\mu_{i'}\Lambda_\omega} \left(I_{i'j'}^+ B_{kk'}^+ + I_{i'j'}^- B_{kk'}^- \right) w_{\mu_i} w_{\phi_j} \exp\left(-\frac{\gamma_{ij}^{\text{FS}}}{\mu_i\Lambda_\omega} (d-z)\right) \right) \right. \\
&\quad + \sum_{ij} \sum_{i'j'} \sum_{i''j''} \left(\frac{w_{\mu_{i''}} w_{\phi_{j''}} (1-p_\omega) (1-\sigma_\omega)}{4\pi^2\Lambda_\omega} \right. \\
&\quad \left. \times \left(I_{i''j''}^+ B_{kk'}^+ + I_{i''j''}^- B_{kk'}^- \right) w_{\mu_i} w_{\phi_j} \exp\left(-\frac{\gamma_{ij}^{\text{FS}}}{\mu_i\Lambda_\omega} (d-z)\right) \right) \\
&\quad + \sum_{ij} \sum_{i'j'} \left(\frac{C_\omega (1-p_\omega) \sigma_\omega}{4\pi} \left(B_{kk'}^+ \Delta\bar{T}(z=0) + B_{kk'}^- \Delta\bar{T}(z=d) \right) \right. \\
&\quad \left. \times w_{\mu_i} w_{\phi_j} \exp\left(-\frac{\gamma_{ij}^{\text{FS}}}{\mu_i\Lambda_\omega} (d-z)\right) \right] d\omega \\
&= f_3^1(z) + f_3^2(z) + h_3(z) + \int_0^d \Delta\bar{T} \left[K_3^1(z', z) + K_3^2(z', z) \right] dz' \quad (5.42)
\end{aligned}$$

where,

$$f_3^1(z) = \frac{1}{\Omega} \int_{\omega=0}^{\omega_m} \left[\sum_{ij} \sum_{i'j'} \left(\frac{\bar{Q}_\omega p_\omega}{4\pi \gamma_{\mu_i' \phi_j'}^{\text{FS}}} \left(1 - \exp\left(-\frac{\gamma_{i'j'}^{\text{FS}}}{\mu_{i'} \Lambda_\omega} d\right) \right) \left(B_{kk'}^+ + B_{kk'}^- \right) \right. \right. \\ \left. \left. w_{\mu_i} w_{\phi_j} \exp\left(-\frac{\gamma_{ij}^{\text{FS}}}{\mu_i \Lambda_\omega} (d-z)\right) \right) \right] d\omega \quad (5.43)$$

$$f_3^2(z) = \frac{1}{\Omega} \int_{\omega=0}^{\omega_m} \left[\sum_{ij} \sum_{i'j'} \sum_{i''j''} \left(\frac{\bar{Q}_\omega \mu_{i''} w_{\mu_{i''}} w_{\phi_{k''}} (1-p_\omega) (1-\sigma_\omega)}{4\pi^2 \gamma_{i''j''}^{\text{FS}}} \right. \right. \\ \left. \left. \times \left(1 - \exp\left(-\frac{\gamma_{i''j''}^{\text{FS}}}{\mu_{i''} \Lambda_\omega} d\right) \right) \left(B_{kk'}^+ + B_{kk'}^- \right) w_{\mu_i} w_{\phi_j} \exp\left(-\frac{\gamma_{ij}^{\text{FS}}}{\mu_i \Lambda_\omega} (d-z)\right) \right) \right] d\omega \quad (5.44)$$

$$h_3(z) = \frac{1}{\Omega} \int_{\omega=0}^{\omega_m} \frac{1}{\tau_\omega} \left[\sum_{ij} \sum_{i'j'} \left(\frac{C_\omega (1-p_\omega) \sigma_\omega}{4\pi} \left(B_{kk'}^+ \Delta \bar{T}(z=0) \right. \right. \right. \\ \left. \left. \left. + B_{kk'}^- \Delta \bar{T}(z=d) \right) w_{\mu_i} w_{\phi_j} \exp\left(-\frac{\gamma_{ij}^{\text{FS}}}{\mu_i \Lambda_\omega} (d-z)\right) \right) \right] \quad (5.45)$$

$$K_3^1(z', z) = \frac{1}{\Omega} \int_{\omega=0}^{\omega_m} \frac{C_\omega}{\tau_\omega} \left[\sum_{ij} \sum_{i'j'} \left(\frac{p_\omega}{4\pi \mu_{i'} \Lambda_\omega} \left(\exp\left(-\frac{\gamma_{i'j'}^{\text{FS}}}{\mu_{i'} \Lambda_\omega} z'\right) B_{kk'}^+ \right. \right. \right. \\ \left. \left. \left. + \exp\left(-\frac{\gamma_{i'j'}^{\text{FS}}}{\mu_{i'} \Lambda_\omega} (d-z')\right) B_{kk'}^- \right) w_{\mu_i} w_{\phi_j} \exp\left(-\frac{\gamma_{ij}^{\text{FS}}}{\mu_i \Lambda_\omega} (d-z)\right) \right) \right] d\omega \quad (5.46)$$

$$K_3^2(z', z) = \frac{1}{\Omega} \int_{\omega=0}^{\omega_m} \frac{C_\omega}{\tau_\omega} \left[\sum_{ij} \sum_{i'j'} \sum_{i''j''} \left(\frac{w_{\mu_{i''}} w_{\phi_{j''}} (1-p_\omega) (1-\sigma_\omega)}{4\pi^2 \Lambda_\omega} \right. \right. \\ \left. \left. \times \left(\exp\left(-\frac{\gamma_{i''j''}^{\text{FS}}}{\mu_{i''} \Lambda_\omega} z'\right) B_{kk'}^+ + \exp\left(-\frac{\gamma_{i''j''}^{\text{FS}}}{\mu_{i''} \Lambda_\omega} (d-z')\right) B_{kk'}^- \right) \right. \right. \\ \left. \left. \times w_{\mu_i} w_{\phi_j} \exp\left(-\frac{\gamma_{ij}^{\text{FS}}}{\mu_i \Lambda_\omega} (d-z)\right) \right) \right] d\omega \quad (5.47)$$

Finally, the system to solve (equation 5.34) for can be represented as an integral equation of the form:

$$\Delta \bar{T}(z) - h(z) = f(z) + \int_0^d [K(z', z) \Delta \bar{T}(z')] dz' \quad (5.48)$$

where,

$$f(z) = f_1^1(z) + f_2^1(z) + f_2^2(z) + f_3^1(z) + f_3^2(z) \quad (5.49)$$

$$K(z', z) = K_1^1(z', z) + K_2^1(z', z) + K_2^2(z', z) + K_3^1(z', z) + K_3^2(z', z) \quad (5.50)$$

and

$$h(z) = h_2(z) + h_3(z) \quad (5.51)$$

There are several important properties of the integral equation 5.48.

1. The kernel $K(z', z)$ is singular for $z = z'$ due to the singularity of $K_1^1(z', z)$ at $z = z'$.
2. Unlike the term $f(z)$, the term $h(z)$ is a function of $\Delta\bar{T}$ and can be represented as $h(z) = H(z', z)\Delta\bar{T}$, where $H(z', z)$ is independent of $\Delta\bar{T}$.

There are several approaches available in the literature to solve such singular integral equations. In this work, this integral equation is solved using the method of degenerate kernels, the details of which are described in the following section.

The Method of Degenerate Kernels

The integral equation (equation 5.48) can be solved using the method of degenerate kernels. First, the integral equation is rewritten as,

$$\Delta\bar{T}(\hat{z}) - h(\hat{z}) = f(\hat{z}) + \int_0^1 [\bar{K}(\hat{z}', \hat{z}) \Delta\bar{T}(\hat{z}')] d\hat{z}' \quad (5.52)$$

where $\hat{z} = z/d$ and $\bar{K}(\hat{z}', \hat{z}) = d \times K(z', z)$. Then the functions $\Delta\bar{T}(\hat{z})$, $f(\hat{z})$ and $K(\hat{z}', \hat{z})$ are expanded in Fourier series :

$$\Delta\bar{T}_{(N)}(\hat{z}) = \frac{1}{2}t_0 + \sum_{m=1}^N t_m \cos(m\pi\hat{z}) \quad (5.53)$$

$$f_{(N)}(\hat{z}) = \frac{1}{2}f_0 + \sum_{m=1}^N f_n \cos(m\pi\hat{z}) \quad (5.54)$$

$$h_{(N)}(\hat{z}) = \frac{1}{2}h_0 + \sum_{m=1}^N h_n \cos(m\pi\hat{z})$$

$$\begin{aligned}\bar{K}_{(N)}(\hat{z}', \hat{z}) &= \frac{1}{4}K_{00} + \frac{1}{2} \sum_{m=1}^N K_{m0} \cos(m\pi\hat{z}') + \frac{1}{2} \sum_{n=1}^N K_{0n} \cos(n\pi\hat{z}) \\ &+ \sum_{m=1}^N \sum_{n=1}^N K_{mn} \cos(m\pi\hat{z}') \cos(n\pi\hat{z})\end{aligned}$$

where the Fourier coefficients are given by,

$$f_m = 2 \int_0^1 f(\hat{z}) \cos(m\pi\hat{z}) d\hat{z} \quad (5.55)$$

$$h_m = 2 \int_0^1 h(\hat{z}) \cos(m\pi\hat{z}) d\hat{z} \quad (5.56)$$

and

$$K_{mn} = 4 \int_0^1 \int_0^1 K(\hat{z}', \hat{z}) \cos(m\pi\hat{z}') \cos(n\pi\hat{z}) d\hat{z}' d\hat{z} \quad (5.57)$$

Here, a Fourier cosine series has been used for all the functions by assuming that all the functions are even with respect to \hat{z} and \hat{z}' . This assumption is valid since the integral equation (equation 5.48) has been solved only in the domain $\hat{z} \in [0, 1]$. After several algebraic simplifications, the expressions for the Fourier coefficients (equations 5.55, 5.56, and 5.57) simplify into the following concise forms:

$$f_{1,m}^1 = -\frac{2}{\Omega} \int_{\omega=0}^{\omega_m} \bar{Q}_\omega \left[\sum_{ij} (I_1(m) + I_2(m)) \frac{w_{\mu_i} w_{\phi_j}}{4\pi\gamma_{ij}^{\text{FS}}} \right] d\omega \quad (5.58)$$

$$\begin{aligned}f_{2,m}^1 &= \frac{2}{\Omega} \int_{\omega=0}^{\omega_m} \left[\sum_{ij} \sum_{i'j'} \left(\frac{\bar{Q}_\omega p_\omega}{4\pi\gamma_{\mu_i' \phi_j'}^{\text{FS}}} \left(1 - \exp\left(-\frac{\gamma_{i'j'}^{\text{FS}}}{\mu_i' \Lambda_\omega} d\right) \right) \right. \right. \\ &\quad \left. \left. \times (T_{kk'}^+ + T_{kk'}^-) w_{\mu_i} w_{\phi_j} I_1(m) \right) \right] d\omega\end{aligned} \quad (5.59)$$

$$\begin{aligned}f_{2,m}^2 &= \frac{2}{\Omega} \int_{\omega=0}^{\omega_m} \left[\sum_{ij} \sum_{i'j'} \sum_{i''j''} \left(\frac{\bar{Q}_\omega \mu_{i''} w_{\mu_{i''}} w_{\phi_{j''}} (1-p_\omega) (1-\sigma_\omega)}{4\pi^2 \gamma_{i''j''}^{\text{FS}}} \right. \right. \\ &\quad \left. \left. \times \left(1 - \exp\left(-\frac{\gamma_{i''j''}^{\text{FS}}}{\mu_{i''} \Lambda_\omega} d\right) \right) (T_{kk'}^+ + T_{kk'}^-) w_{\mu_i} w_{\phi_j} I_1(m) \right) \right] d\omega\end{aligned} \quad (5.60)$$

$$\begin{aligned}h_{2,m} &= \frac{2}{\Omega} \int_{\omega=0}^{\omega_m} \frac{1}{\tau_\omega} \left[\sum_{ij} \sum_{i'j'} \left(\frac{C_\omega (1-p_\omega) \sigma_\omega}{4\pi} \right. \right. \\ &\quad \left. \left. \times (T_{kk'}^+ \Delta \bar{T}(z=0) + T_{kk'}^- \Delta \bar{T}(z=d)) w_{\mu_i} w_{\phi_j} I_1(m) \right) \right] d\omega\end{aligned} \quad (5.61)$$

$$f_{3,m}^1 = \frac{2}{\Omega} \int_{\omega=0}^{\omega_m} \left[\sum_{ij} \sum_{i'j'} \left(\frac{\bar{Q}_\omega p_\omega}{4\pi \gamma_{\mu_i' \phi_j'}^{\text{FS}}} \left(1 - \exp\left(-\frac{\gamma_{i'j'}^{\text{FS}}}{\mu_{i'} \Lambda_\omega} d\right) \right) \right) \right. \\ \left. \times \left(B_{kk'}^+ + B_{kk'}^- \right) w_{\mu_i} w_{\phi_j} I_2(m) \right] d\omega \quad (5.62)$$

$$f_{3,m}^2 = \frac{2}{\Omega} \int_{\omega=0}^{\omega_m} \left[\sum_{ij} \sum_{i'j'} \sum_{i''j''} \left(\frac{\bar{Q}_\omega (1-p_\omega) (1-\sigma_\omega) \mu_{i''} w_{\mu_{i''}} w_{\phi_{j''}}}{4\pi^2 \gamma_{i''j''}^{\text{FS}}} \right) \right. \\ \left. \times \left(1 - \exp\left(-\frac{\gamma_{i''j''}^{\text{FS}}}{\mu_{i''} \Lambda_\omega} d\right) \right) \left(B_{kk'}^+ + B_{kk'}^- \right) w_{\mu_i} w_{\phi_j} I_2(m) \right] d\omega \quad (5.63)$$

$$h_{3,m} = \frac{2}{\Omega} \int_{\omega=0}^{\omega_m} \frac{1}{\tau_\omega} \left[\sum_{ij} \sum_{i'j'} \left(\frac{C_\omega (1-p_\omega) \sigma_\omega}{4\pi} \right) \right. \\ \left. \times \left(B_{kk'}^+ \Delta \bar{T}(z=0) + B_{kk'}^- \Delta \bar{T}(z=d) \right) w_{\mu_i} w_{\phi_j} I_2(m) \right] \quad (5.64)$$

$$K_{1,mn}^1 = \frac{4d}{\Omega} \left[\int_{\omega=0}^{\omega_m} \left(\frac{C_\omega}{4\pi \tau_\omega \Lambda_\omega} \sum_{ij} \frac{w_{\mu_i} w_{\phi_j}}{\mu_i} I_3(m,n) \right) d\omega \right] \quad (5.65)$$

$$K_{2,mn}^1 = \frac{4d}{\Omega} \int_{\omega=0}^{\omega_m} \frac{C_\omega}{\tau_\omega} \left[\sum_{ij} \sum_{i'j'} \left(\frac{p_\omega}{4\pi \mu_{i'} \Lambda_\omega} \left(I_1'(m) T_{kk'}^+ + I_2'(m) T_{kk'}^- \right) \right) \right. \\ \left. \times w_{\mu_i} w_{\phi_j} I_1(n) \right] d\omega \quad (5.66)$$

$$K_{2,mn}^2 = \frac{4d}{\Omega} \int_{\omega=0}^{\omega_m} \frac{C_\omega}{\tau_\omega} \left[\sum_{ij} \sum_{i'j'} \sum_{i''j''} \left(\frac{w_{\mu_{i''}} w_{\phi_{j''}} (1-p_\omega) (1-\sigma_\omega)}{4\pi^2 \Lambda_\omega} \left(I_1''(m) T_{kk'}^+ \right. \right. \right. \\ \left. \left. \left. + I_2''(m) T_{kk'}^- \right) w_{\mu_i} w_{\phi_j} I_1(n) \right) \right] d\omega \quad (5.67)$$

$$K_{3,mn}^1 = \frac{4d}{\Omega} \int_{\omega=0}^{\omega_m} \frac{C_\omega}{\tau_\omega} \left[\sum_{ij} \sum_{i'j'} \left(\frac{p_\omega}{4\pi \mu_{i'} \Lambda_\omega} \left(I_1'(m) B_{kk'}^+ + I_2'(m) B_{kk'}^- \right) \right) \right. \\ \left. \times w_{\mu_i} w_{\phi_j} I_2(n) \right] d\omega \quad (5.68)$$

$$\begin{aligned}
K_{3,mn}^2 = & \frac{4d}{\Omega} \int_{\omega=0}^{\omega_m} \frac{C_\omega}{\tau_\omega} \left[\sum_{ij} \sum_{i'j'} \sum_{i''j''} \left(\frac{w_{\mu_i''} w_{\phi_{j''}} (1-p_\omega) (1-\sigma_\omega)}{4\pi^2 \Lambda_\omega} \left(I_1''(m) B_{kk'}^+ \right. \right. \right. \\
& \left. \left. \left. + I_2''(m) B_{kk'}^- \right) w_{\mu_i} w_{\phi_j} I_2(n) \right) \right] d\omega
\end{aligned} \tag{5.69}$$

where,

$$\begin{aligned}
I_1(m) &= \int_0^1 \exp\left(-\frac{\gamma_{ij}^{\text{FS}}}{\mu_i \text{Kn}_\omega^d} \hat{z}\right) \cos(m\pi \hat{z}) d\hat{z} \\
&= \frac{\frac{\gamma_{ij}^{\text{FS}}}{\mu_i \text{Kn}_\omega^d}}{m^2 \pi^2 + \left(\frac{\gamma_{ij}^{\text{FS}}}{\mu_i \text{Kn}_\omega^d}\right)^2} \left[1 - (-1)^m \exp\left(-\frac{\gamma_{ij}^{\text{FS}}}{\mu_i \text{Kn}_\omega^d}\right) \right]
\end{aligned}$$

$$\begin{aligned}
I_2(m) &= \int_0^1 \exp\left(-\frac{\gamma_{ij}^{\text{FS}}}{\mu_i \text{Kn}_\omega^d} (1-\hat{z})\right) \cos(m\pi \hat{z}) d\hat{z} \\
&= \frac{\frac{\gamma_{ij}^{\text{FS}}}{\mu_i \text{Kn}_\omega^d}}{m^2 \pi^2 + \left(\frac{\gamma_{ij}^{\text{FS}}}{\mu_i \text{Kn}_\omega^d}\right)^2} \left[(-1)^m - \exp\left(-\frac{\gamma_{ij}^{\text{FS}}}{\mu_i \text{Kn}_\omega^d}\right) \right]
\end{aligned}$$

$$\begin{aligned}
I_3(m, n) &= \int_0^1 \int_0^1 \exp\left(-\frac{\gamma_{ij}^{\text{FS}}}{\mu_i \text{Kn}_\omega^d} |\hat{z}' - \hat{z}|\right) \cos(m\pi \hat{z}) \cos(n\pi \hat{z}') d\hat{z} d\hat{z}' \\
&= \begin{cases} \frac{\frac{\gamma_{ij}^{\text{FS}}}{\mu_i \text{Kn}_\omega^d}}{m^2 \pi^2 + \left(\frac{\gamma_{ij}^{\text{FS}}}{\mu_i \text{Kn}_\omega^d}\right)^2} [\delta_{mn} - (I_1(n) + (-1)^m I_2(n))] & \text{for } m \neq 0 \\ \frac{\frac{\gamma_{ij}^{\text{FS}}}{\mu_i \text{Kn}_\omega^d}}{m^2 \pi^2 + \left(\frac{\gamma_{ij}^{\text{FS}}}{\mu_i \text{Kn}_\omega^d}\right)^2} [2\delta_{mn} - (I_1(n) + (-1)^m I_2(n))] & \text{for } m = 0 \end{cases}
\end{aligned}$$

and primes (' and '') on I_1, I_2 , and I_3 indicate that these functions are evaluated for $\{\mu', \phi'\}$ and $\{\mu'', \phi''\}$ respectively. These Fourier coefficients are substituted into the cosine series for the corresponding functions in the integral equation (equation 5.48)

to get,

$$\begin{aligned}
& \frac{1}{2}t_0 + \sum_{m=1}^N t_m \cos(m\pi\hat{z}) - \frac{1}{2}h_0 - \sum_{m=1}^N h_m \cos(m\pi\hat{z}) \\
&= \frac{1}{2}f_0 + \sum_{m=1}^N f_n \cos(m\pi\hat{z}) + \frac{1}{8}t_0K_{00} + \frac{1}{4} \sum_{n=1}^N t_0K_{0n} \cos(n\pi\hat{z}) \\
&\quad + \sum_{m=1}^N \left(\frac{t_0K_{m0}}{4} + \frac{K_{00}t_m}{4} + \sum_{n=1}^N \frac{t_0K_{mn} + t_mK_{0n}}{2} \cos(n\pi\hat{z}) \right) \int_0^1 \cos(m\pi\hat{z}') d\hat{z}' \\
&\quad + \sum_{m=1}^N \sum_{n=1}^N \left(\frac{t_mK_{n0}}{2} + \sum_{p=1}^N t_mK_{np} \cos(p\pi\hat{z}) \right) \int_0^1 \cos(m\pi\hat{z}') \cos(n\pi\hat{z}') d\hat{z}' \\
&= \frac{1}{2}f_0 + \sum_{m=1}^N f_n \cos(m\pi\hat{z}) + \frac{1}{8}t_0K_{00} + \frac{1}{4} \sum_{n=1}^N t_0K_{0n} \cos(n\pi\hat{z}) \\
&\quad + \frac{1}{2} \sum_{m=1}^N \left(\frac{t_mK_{m0}}{2} + \sum_{n=1}^N t_mK_{mn} \cos(n\pi\hat{z}) \right)
\end{aligned}$$

Due to the orthogonality of $\cos(m\pi\hat{z})$ in the interval $\hat{z} \in [0, 1]$, it is sufficient to solve for the Fourier coefficients (t_m) by grouping together the coefficients with the same index, which results in a system of linear equations in t_m :

$$\begin{aligned}
& \left(\frac{1}{2} - \frac{1}{8}K_{00} \right) t_0 - \frac{1}{4} \sum_{n=1}^N K_{n0}t_n - \frac{1}{2}h_0 = \frac{1}{2}f_0 \\
& \sum_{n=1}^N \left(\delta_{nm} - \frac{1}{2}K_{nm} \right) t_n - \frac{1}{4}K_{0m}t_0 - h_m = f_m \quad \text{for } m = 1, \dots, N
\end{aligned} \tag{5.70}$$

Noting that h_i 's are linear combinations of t_j 's, the system of linear equations (equation 5.70) can be written in a concise matrix form as:

$$Ft = f$$

which can be solved by standard matrix inversion techniques. The resulting solution (t_m) is used to calculate the temperature profile $\Delta\bar{T}(\eta, \zeta_x, \zeta_y, z)$ and the phonon energy distribution functions $G_\omega^+(z, \mu_i, \phi_j)$ and $G_\omega^-(z, -\mu_i, \phi_j)$ for each η and ζ_x as follows:

First, the expressions for $I_{\mu\phi}^+$ and $I_{\mu\phi}^-$ are simplified as

$$\begin{aligned}
I_{\mu\phi}^+ &= C_\omega \int_0^d \Delta \bar{T} \exp\left(-\frac{\gamma_{\mu\phi}^{\text{FS}}}{\mu\Lambda_\omega} z'\right) dz' + \bar{Q}_\omega \tau_\omega \Lambda_\omega \frac{\mu}{\gamma_{\mu\phi}^{\text{FS}}} \left(1 - \exp\left(-\frac{\gamma_{\mu\phi}^{\text{FS}}}{\mu\Lambda_\omega} d\right)\right) \\
&= C_\omega d \left(\frac{1}{2} t_0 \frac{\mu \text{Kn}_\omega^d}{\gamma_{\mu\phi}^{\text{FS}}} \left(1 - \exp\left(-\frac{\gamma_{\mu\phi}^{\text{FS}}}{\mu \text{Kn}_\omega^d}\right)\right) + \sum_{m=1}^N t_m I_1(m)\right) \\
&\quad + \bar{Q}_\omega \tau_\omega d \frac{\mu \text{Kn}_\omega^d}{\gamma_{\mu\phi}^{\text{FS}}} \left(1 - \exp\left(-\frac{\gamma_{\mu\phi}^{\text{FS}}}{\mu \text{Kn}_\omega^d}\right)\right)
\end{aligned}$$

$$\begin{aligned}
I_{\mu\phi}^- &= C_\omega \int_0^d \Delta \bar{T} \exp\left(-\frac{\gamma_{\mu\phi}^{\text{FS}}}{\mu\Lambda_\omega} z'\right) dz' + \bar{Q}_\omega \tau_\omega \Lambda_\omega \frac{\mu}{\gamma_{\mu\phi}^{\text{FS}}} \left(1 - \exp\left(-\frac{\gamma_{\mu\phi}^{\text{FS}}}{\mu\Lambda_\omega} d\right)\right) \\
&= C_\omega d \left(\frac{1}{2} t_0 \frac{\mu \text{Kn}_\omega^d}{\gamma_{\mu\phi}^{\text{FS}}} \left(1 - \exp\left(-\frac{\gamma_{\mu\phi}^{\text{FS}}}{\mu \text{Kn}_\omega^d}\right)\right) + \sum_{m=1}^N t_m I_2(m)\right) \\
&\quad + \bar{Q}_\omega \tau_\omega d \frac{\mu \text{Kn}_\omega^d}{\gamma_{\mu\phi}^{\text{FS}}} \left(1 - \exp\left(-\frac{\gamma_{\mu\phi}^{\text{FS}}}{\mu \text{Kn}_\omega^d}\right)\right)
\end{aligned}$$

where $\text{Kn}_\omega^d = \Lambda_\omega/d$ is the Knudsen number of a phonon mode defined based on the thickness of the thin film. Next, using the expressions for $I_{\mu\phi}^+$ and $I_{\mu\phi}^-$, the expressions for $\bar{c}_\omega^+(0, \mu'_i, \phi'_j)$ and $\bar{c}_\omega^-(d, \mu'_i, \phi'_j)$ are evaluated and finally, the expressions

for $G_\omega^+(\hat{z}, \mu_i, \phi_j)$ and $G_\omega^-(\hat{z}, -\mu_i, \phi_j)$ are evaluated as,

$$\begin{aligned}
G_\omega^+(\hat{z}, \mu_i, \phi_j) &= \left(\sum_{i'j'} [T_{kk'}^+ \bar{c}_\omega^+(0, \mu_{i'}, \phi_{j'}) + T_{kk'}^- \bar{c}_\omega^-(d, \mu_{i'}, \phi_{j'})] \right) \exp\left(-\frac{\gamma_{ij}^{\text{FS}}}{\mu_i \text{Kn}_\omega^d} \hat{z}\right) \\
&\quad + \frac{1}{4\pi\gamma_{ij}^{\text{FS}}} \left(C_\omega \frac{t_0}{2} + \bar{Q}_\omega \tau_\omega\right) \left[1 - \exp\left(-\frac{\gamma_{ij}^{\text{FS}}}{\mu_i \text{Kn}_\omega^d} \hat{z}\right)\right] \\
&\quad + \frac{C_\omega}{4\pi\mu_i \text{Kn}_\omega^d} \sum_{m=1}^N t_m I_3^1(m; \hat{z}) \\
G_\omega^-(\hat{z}, -\mu_i, \phi_j) &= \left(\sum_{i'j'} [B_{kk'}^+ \bar{c}_\omega^+(0, \mu_{i'}, \phi_{j'}) + B_{kk'}^- \bar{c}_\omega^-(d, \mu_{i'}, \phi_{j'})] \right) \\
&\quad \times \exp\left(-\frac{\gamma_{ij}^{\text{FS}}}{\mu_i \text{Kn}_\omega^d} (1 - \hat{z})\right) \\
&\quad + \frac{1}{4\pi\gamma_{ij}^{\text{FS}}} \left(C_\omega \frac{t_0}{2} + \bar{Q}_\omega \tau_\omega\right) \left[1 - \exp\left(-\frac{\gamma_{ij}^{\text{FS}}}{\mu_i \text{Kn}_\omega^d} [1 - \hat{z}]\right)\right] \\
&\quad + \frac{C_\omega}{4\pi\mu_i \text{Kn}_\omega^d} \sum_{m=1}^N t_m I_3^2(m; \hat{z})
\end{aligned} \tag{5.71}$$

where,

$$\begin{aligned}
I_3^1(m; \hat{z}) &= \int_0^{\hat{z}'} \exp\left(-\frac{\gamma_{ij}^{\text{FS}}}{\mu_i \text{Kn}_\omega^d} [\hat{z}' - \hat{z}]\right) \cos(m\pi\hat{z}) d\hat{z} \\
&= \frac{1}{m^2\pi^2 + \left(\frac{\gamma_{ij}^{\text{FS}}}{\mu_i \text{Kn}_\omega^d}\right)^2} \left[\left(\frac{\gamma_{ij}^{\text{FS}}}{\mu_i \text{Kn}_\omega^d} \cos(m\pi\hat{z}') + m\pi \sin(m\pi\hat{z}')\right) \right. \\
&\quad \left. - \frac{\gamma_{ij}^{\text{FS}}}{\mu_i \text{Kn}_\omega^d} \exp\left(-\frac{\gamma_{ij}^{\text{FS}}}{\mu_i \text{Kn}_\omega^d} \hat{z}'\right) \right] \\
I_3^2(m; \hat{z}) &= \int_{\hat{z}'}^1 \exp\left(\frac{\gamma_{ij}^{\text{FS}}}{\mu_i \text{Kn}_\omega^d} [\hat{z}' - \hat{z}]\right) \cos(m\pi\hat{z}) d\hat{z} \\
&= \frac{1}{m^2\pi^2 + \left(\frac{\gamma_{ij}^{\text{FS}}}{\mu_i \text{Kn}_\omega^d}\right)^2} \left[\left(-\frac{\gamma_{ij}^{\text{FS}}}{\mu_i \text{Kn}_\omega^d} (-1)^m\right) \exp\left(-\frac{\gamma_{ij}^{\text{FS}}}{\mu_i \text{Kn}_\omega^d} (1 - \hat{z}')\right) \right. \\
&\quad \left. - \left(-\frac{\gamma_{ij}^{\text{FS}}}{\mu_i \text{Kn}_\omega^d} \cos(m\pi\hat{z}') + m\pi \sin(m\pi\hat{z}')\right) \right]
\end{aligned}$$

Finally, the solution $\Delta\bar{T}(z)$ obtained from equation 5.53 is substituted into equation 5.16 to obtain expressions for $G_\omega(z, \mu, \phi)$ and also the thickness-averaged in-plane heat flux $j_{x,\omega}$ given by,

$$\begin{aligned}
j_{x,\omega} &= \frac{1}{4\pi d} \int_0^d \int_0^{2\pi} \int_{-1}^1 G_\omega v_\omega \sqrt{1-\mu^2} \cos\phi d\mu d\phi dz \\
&= \frac{1}{4\pi} \sum_{ij} \left[\frac{\mu_i \text{Kn}_\omega^d}{\gamma_{ij}^{\text{FS}}} \sum_{i'j'} \left[(T_{kk'}^+ + B_{kk'}^+) \bar{c}_\omega^+(0, \mu_{i'}, \phi_{j'}) \right. \right. \\
&\quad \left. \left. + (T_{kk'}^- + B_{kk'}^-) \bar{c}_\omega^-(d, \mu_{i'}, \phi_{j'}) \right] \left(1 - \exp\left(-\frac{\gamma_{ij}^{\text{FS}}}{\mu_i \text{Kn}_\omega^d}\right) \right) \right. \\
&\quad \left. + \frac{2}{4\pi \gamma_{ij}^{\text{FS}}} \left(C_\omega \frac{t_0}{2} + \bar{Q}_\omega \tau_\omega \right) \left[1 - \frac{\mu_i \text{Kn}_\omega^d}{\gamma_{ij}^{\text{FS}}} \left(1 - \exp\left(-\frac{\gamma_{ij}^{\text{FS}}}{\mu_i \text{Kn}_\omega^d}\right) \right) \right] \right. \\
&\quad \left. - \frac{C_\omega \left(1 - \exp\left(-\frac{\gamma_{ij}^{\text{FS}}}{\mu_i \text{Kn}_\omega^d}\right) \right)}{4\pi \mu_i \text{Kn}_\omega^d} \sum_{m=1}^N t_m \frac{1 + (-1)^m}{m^2 \pi^2 + \left(\frac{\gamma_{ij}^{\text{FS}}}{\mu_i \text{Kn}_\omega^d}\right)^2} \right] v_\omega \sqrt{1-\mu_i^2} w_{\mu_i} w_{\phi_j}
\end{aligned} \tag{5.72}$$

where t_i 's are the Fourier coefficients for the expansion of $\Delta\bar{T}$ in the cross-plane (z) direction and $\text{Kn}_\omega^d = \Lambda_\omega/d$ is the Knudsen number. The conventional approach to describe the thermal transport properties of the thin film is to compare the expression for heat flux from the BTE solution with that expected for heat diffusion, as was done in equation 5.13 for the steady state Fuchs-Sondheimer theory. However, in practice, equation 5.72 is not easily reduced into the form of Fourier's law. To overcome this problem, the following strategy is adopted. The solution of the Fourier heat equation to a one-dimensional heat conduction with an instantaneous spatially sinusoidal heat source is a simple exponential decay $\Delta T(t, x=0) = \Delta T_0 \exp(-\gamma t)$, where the decay rate (γ) is related to the effective thermal conductivity (k_{eff}) and the volumetric heat capacity of the solid (C) as, $\gamma = k_{\text{eff}} q^2 / C$. Therefore, to obtain the effective thermal conductivity from our calculations, we perform an inverse Fourier transform of the temperature distribution averaged in the z -direction ($\int_0^d \Delta\bar{T}(\eta, q, z) dz$) with respect to the variable η , fit the resulting solution to an exponentially decaying function $\Delta T_0 \exp(-\gamma t)$ and extract the thermal conductivity from the fit. If the fitting fails, the transport is in the strongly quasi-ballistic regime [89] and we conclude that the Fourier law description of the heat conduction with an effective thermal conductivity k_{eff} is not valid for that case.

The semi-analytical solution of the BTE for transient transport presented in this work is computationally very efficient, taking only a few seconds on a single computer processor, while the direct Monte Carlo simulation of the BTE takes up to a few days on a high-performance computer cluster executed in parallel mode. Moreover, it is computationally challenging to extract the heat flux distribution directly from the Monte Carlo solution, while in our semi-analytical solution, the evaluation of heat flux distribution is a single step process (equation 5.72).

5.3 Results & Discussion

We now present the results of the calculations for free-standing silicon thin films. To obtain these results, we use an isotropic dispersion and intrinsic scattering rates calculated using a Gaussian kernel-based regression [107] from the *ab-initio* phonon properties of isotopically pure silicon. The first principles phonon properties are calculated by *J. Carrete & N. Mingo* using ShengBTE [108, 109] and Phonopy [110] from the inter-atomic force constants calculated using VASP [111–114].

Steady State Transport in Thin Films

Comparison with Monte Carlo Solution

We first examine steady state heat condition along thin films. Figures 5.2 (a) and (b) show the cross-plane distribution of the in-plane heat flux and the effective thermal conductivity respectively, for steady state transport through thin films computed using the MC technique described in chapter 2 and the analytical solution from this work. For both fully diffuse and partially specular boundary conditions, the heat flux distribution and the effective thermal conductivity of the thin film show excellent agreement between the Monte Carlo solutions and the analytical solution from this work over a range of temperatures and film thicknesses. In particular, both solutions predict identical heat flux and thermal conductivities for thermalizing and non-thermalizing boundary conditions at the thin film walls since the steady state transport is insensitive to the type of diffuse boundary scattering of phonons, as discussed in section 5.2. This observation can be generalized further to state that in steady state thermal transport experiments on thin films, it is impossible to distinguish between non-thermalizing and *any* type of inelastic diffuse scattering of phonons at boundaries.

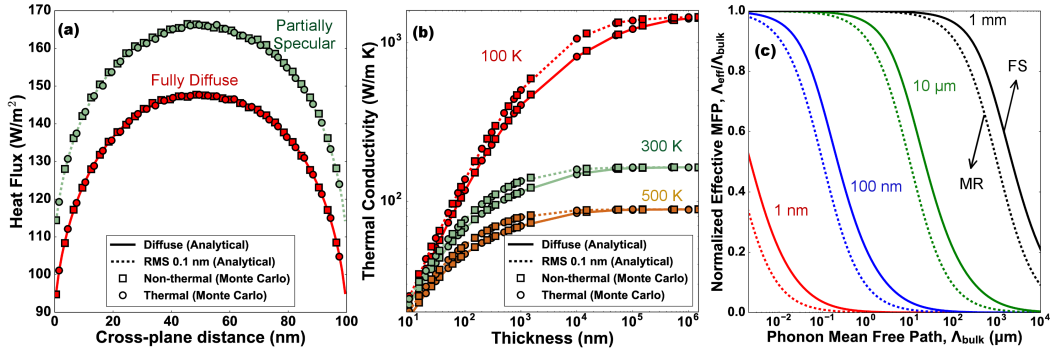


Figure 5.2: (a) Comparison of the cross-plane distribution of the in-plane steady state heat flux between analytical and Monte Carlo solutions of the BTE at 300 K and film thickness of 100 nm for different boundary conditions. The geometry of the thin film and the coordinate axes used in this work are the same as shown in figure 5.1. (b) Comparison of the steady state thermal conductivity between analytical and Monte Carlo solutions of the BTE at different temperatures and thin film thicknesses. For both (a) and (b), the Monte Carlo solutions are identical for thermalizing and non-thermalizing boundary scattering and agree well with the analytical solution derived in this work for both fully diffuse and partially specular boundary conditions (RMS 0.1 nm). For the partially specular boundary condition, the specularity parameter (p_ω) is calculated from Ziman's specularity model [6] for a surface RMS roughness of 0.1 nm. (c) Effective MFPs of phonons computed using the Matthiessen's rule (MR) and the Fuchs-Sondheimer (FS) theory for different film thicknesses and fully diffuse boundary scattering. Matthiessen's rule underpredicts the effective phonon MFPs in thin films compared to the Fuchs-Sondheimer theory, which is a rigorous BTE solution.

Effective Phonon Mean Free Path

We also examine the effective mean free path (MFP) of phonons within the thin film for various film thicknesses. An approach to estimate the effective phonon mean free path in thin films is by using the Matthiessen's rule [6] given by,

$$\frac{1}{\Lambda_{\omega,\text{eff}}} = \frac{1}{\Lambda_{\omega,\text{bulk}}} + \frac{1 - p_\omega}{1 + p_\omega} \frac{1}{d} \quad (5.73)$$

where d is the thickness of the thin film and $\Lambda_{\omega,\text{bulk}}$ is the intrinsic phonon mean free path in the bulk material. Although the Matthiessen's rule has been used in the past for computational [72] and experimental [4] investigations of phonon boundary scattering, the mathematical rigor of such an expression for effective mean free path is unclear. On the other hand, the effective mean free path of phonons in thin films

can also be determined rigorously from the Fuchs-Sondheimer factor ($F(\Lambda_\omega/d)$), since by definition, $F(\Lambda_\omega/d) = k_{\omega,\text{eff}}/k_{\omega,\text{bulk}} = \Lambda_{\omega,\text{eff}}/\Lambda_{\omega,\text{bulk}}$. Figure 5.2 (c) shows the comparison of the normalized effective phonon mean free paths obtained from the Fuchs-Sondheimer factor and Matthiessen's rule for different film thicknesses. Matthiessen's rule underpredicts phonon MFPs comparable to the thickness of the film. Even for phonons with intrinsic mean free path an order of magnitude smaller than the film thickness, Matthiessen's rule predicts a shorter effective phonon mean free path compared to the predictions of the Fuchs-Sondheimer factor from the rigorous solution of the BTE, which is consistent with the findings of another work based on Monte Carlo sampling [40]. This result highlights the importance of using the rigorous BTE solution to estimate the extent of diffuse phonon boundary scattering even in simple nanostructures.

Transient Transport in Thin Films

We now examine transient thermal conduction along thin films observed in the TG experiment. To perform this calculation, we solve the integral equation (equation 5.20) semi-analytically using the same isotropic phonon properties used in steady state transport calculations. The source term in the BTE (equation 5.15) is assumed to follow a thermal distribution given by $Q_\omega = C_\omega \Delta T_0$, where C_ω is the volumetric specific heat of the phonon mode.

Difference between Thermalizing and Non-thermalizing Boundary Scattering

Figure 5.3 (a) shows a comparison of the time traces calculated from the degenerate kernel method and the Monte Carlo method for a grating period of $20 \mu\text{m}$. To obtain the thickness averaged time traces using the degenerate kernels method, we used 6 Gauss quadrature points for μ variable, 10 Gauss quadrature points for ϕ variable, and 1 term in the Fourier cosine expansion to achieve a convergence threshold of 10^{-6} on the relative change in the solution for an increase in the number of discretization points. The transient decays are in good agreement between the degenerate kernel and the Monte Carlo solutions over a wide range of temperatures and different boundary conditions. As expected, the solution for the specular boundary condition results in a faster transient decay than the diffuse boundary conditions since a specularly reflecting wall does not resist the flow of heat in the in-plane direction. However, the transient decay for the non-thermalizing diffuse boundary condition is faster than the thermalizing diffuse boundary condition, indicating that the thermalizing boundary condition offers higher resistance to heat flow

than the non-thermalizing diffuse scattering.

This observation is also evident from figure 5.3 (b), which shows the thermal conductivities obtained by fitting the time traces to an exponential decay for different temperatures, different grating periods, and different boundary conditions. The observed thermal conductivity of the thin film decreases with decreasing grating period due to the breakdown of the Fourier's law of heat conduction and the onset of quasiballistic thermal transport [89] when the grating period is comparable to phonon MFPs. Consistent with the findings from the time traces, the thermal conductivity of the thin film with specular walls is higher than that of the thin film with diffuse walls. Moreover, even for very long grating periods compared to phonon MFPs, where the thermal transport is diffusive and obeys Fourier's law, the thermal conductivity of thin film with non-thermalizing diffuse walls is higher than that of the thin films with thermalizing diffuse walls. This observation is in stark contrast with the steady state condition, where there was no difference in thermal conductivity between thermalizing and non-thermalizing boundary conditions.

Validity of the Thermalizing and Non-thermalizing Boundary Conditions

At this point, it is important to investigate the validity of the thermalizing and non-thermalizing boundary condition for the thin film walls. The non-thermalizing boundary scattering condition can be naturally derived from the conservation of heat flux at the boundary [105]. However, the thermalizing boundary condition is not derived from the heat flux conservation at the boundary. Therefore, in the absence of any external scattering mechanisms, phonons cannot reach the local thermal equilibrium and simultaneously conserve heat flux at the boundary in general, due to the following reason.

Consider a boundary at $z = 0$ separating a solid at $z > 0$ from vacuum in $z < 0$. The incoming phonon distribution at $z = 0$ is $g_{\omega}^{-}(0, \mu, \phi)$, which is a general phonon distribution, not necessarily at the local thermal equilibrium. According to the formulation of the thermalizing diffuse boundary condition, the outgoing phonon distribution, in the case of fully diffuse boundary scattering, is given by $g_{\omega}(\Delta T(z = 0)) \approx \frac{C_{\omega}}{4\pi} \Delta T(z = 0)$, where C_{ω} is the heat capacity of the phonon mode and $\Delta T(z = 0)$ is the local equilibrium temperature at the boundary $z = 0$. Since the boundary separates a solid from vacuum, all of the heat flux incident on the

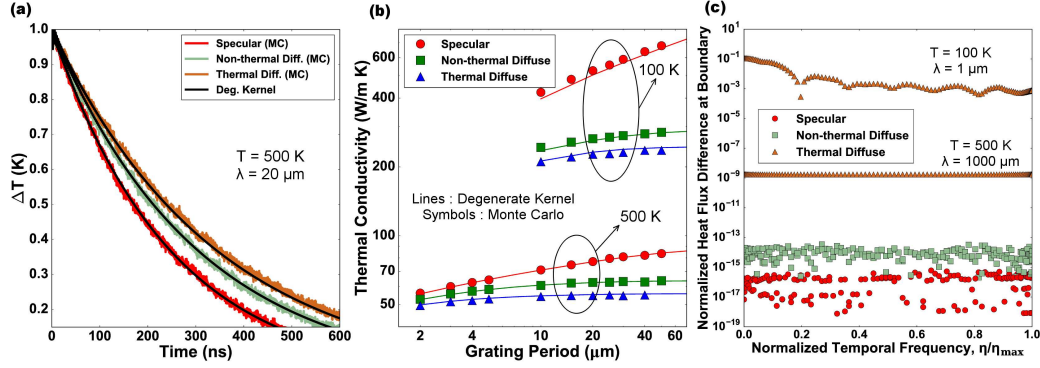


Figure 5.3: (a) Comparison between time traces from the Monte Carlo (colored noisy lines) and the degenerate kernels solutions (black lines) of the BTE for a grating period of $20 \mu\text{m}$ at 500 K. (b) Comparison of the thermal conductivity predictions from the Monte Carlo (symbols) and the degenerate kernels solutions (black lines) of the BTE for different temperatures and grating periods. For both (a) and (b), the Monte Carlo solutions and the BTE solutions from this work are in very good agreement. (c) Plot showing the difference between the incoming and outgoing heat flux normalized by the incoming heat flux at the thin film boundaries as a function of the temporal frequency normalized by the maximum temporal frequency at which the simulations were performed (η_{max}). Specular and non-thermalizing diffuse boundary conditions conserve heat flux to numerical precision while thermalizing diffuse boundary condition violates heat flux conservation at the film wall under quasiballistic ($T = 100$ K, grating period = $1 \mu\text{m}$) and diffusive ($T = 500$ K, grating period = $1000 \mu\text{m}$) transport regimes.

boundary has to be reflected back into the solid. This constraint on the incident and reflected heat flux at the thermalizing diffuse boundary leads to the following relation for ΔT ($z = 0$):

$$\Delta T (z = 0) = 4 \frac{\sum_p \int_{\omega=0}^{\omega_{\text{max}}} \int_{\mu=-1}^0 \int_{\phi=0}^{2\pi} g_{\omega}^{-}(0, \mu, \phi) v_{\omega} \mu d\mu d\phi d\omega}{\sum_p \int_{\omega=0}^{\omega_{\text{max}}} C_{\omega} v_{\omega} d\omega} \quad (5.74)$$

Additionally, energy conservation (equation 5.3) has to be satisfied at all locations including the boundaries in the absence of any other source or sink of phonons. This requirement further adds constraints on ΔT ($z = 0$) through the relation,

$$\Delta T (z = 0) = 2 \frac{\sum_p \int_{\omega=0}^{\omega_{\text{max}}} \int_{\mu=-1}^0 \int_{\phi=0}^{2\pi} \frac{g_{\omega}^{-}(0, \mu, \phi)}{\tau_{\omega}} d\mu d\phi d\omega}{\sum_p \int_{\omega=0}^{\omega_{\text{max}}} \frac{C_{\omega}}{\tau_{\omega}} d\omega} \quad (5.75)$$

For the assumptions made in the Fuchs-Sondheimer theory under steady state transport conditions, the integrals of the incoming and the outgoing distribution func-

tions (equation 5.12) over the azimuthal angle ϕ are 0. Therefore, there is no heat flux towards or away from the boundary and the constraints on $\Delta T(z=0)$ (given by equations 5.74 and 5.75) are trivially satisfied. However, in general, these two expressions for $\Delta T(z=0)$ are not equal, indicating phonons cannot thermalize at the boundaries in the absence of any external source or sink of phonons.

Figure 5.3 (c) shows the difference between the incoming and outgoing total heat flux at the thin film wall ($z=0$) as a function of the temporal frequency η . The specular and non-thermalizing diffuse boundary conditions satisfy heat flux conservation to numerical precision. However, there is a significant difference between the incoming and the outgoing heat flux for the thermalizing diffuse boundary condition under quasiballistic ($T=100$ K, grating period = $1 \mu\text{m}$) and diffusive ($T=500$ K, grating period = $1000 \mu\text{m}$) transport regimes. Nevertheless, it is still possible for inelastic (but not thermalizing) diffuse boundary scattering to take place as long as the following conditions for heat flux are met at the thin film boundaries:

$$\begin{aligned} \sum_p \int_{\omega=0}^{\omega_{\max}} g_{\omega}^{+}(z=0) v_{\omega} d\omega &= \\ & - \frac{1}{\pi} \sum_p \int_{\omega=0}^{\omega_{\max}} \int_{\mu=-1}^0 \int_{\phi=0}^{2\pi} g_{\omega}^{-}(z=0, \mu, \phi) v_{\omega} \mu d\mu d\phi d\omega \\ \sum_p \int_{\omega=0}^{\omega_{\max}} g_{\omega}^{-}(z=d) v_{\omega} d\omega &= \\ & \frac{1}{\pi} \sum_p \int_{\omega=0}^{\omega_{\max}} \int_{\mu=0}^1 \int_{\phi=0}^{2\pi} g_{\omega}^{+}(z=d, \mu, \phi) v_{\omega} \mu d\mu d\phi d\omega \end{aligned}$$

Comparison with Fuchs-Sondheimer Theory at Different Grating Periods

We now examine if the Fuchs-Sondheimer theory can be used to explain transient heat conduction in the TG experiment along thin films. If the suppression in thermal conductivity of thin films due to phonon boundary scattering and quasiballistic effects in the TG experiment are assumed to be independent, Fuchs-Sondheimer theory can be employed to describe quasiballistic transport in the TG experiment using the following expression:

$$k(q, d) = \sum_p \int_0^{\omega_{\max}} F\left(p_{\omega}, \frac{\Lambda_{\omega}}{d}\right) S(q\Lambda_{\omega}) \left[\frac{1}{3} C_{\omega} v_{\omega} \Lambda_{\omega}\right] d\omega \quad (5.76)$$

where $F\left(p_{\omega}, \frac{\Lambda_{\omega}}{d}\right)$ is the Fuchs-Sondheimer suppression function from the steady state transport condition and $S(q\Lambda_{\omega})$ is the quasiballistic suppression function [89]

for a grating period q . Recent works [21] have used a similar expression for the thermal conductivity suppression of the form:

$$k(q, d) = \sum_p \int_0^{\omega_{\max}} F\left(p_\omega, \frac{\Lambda_\omega}{d}\right) S\left(q\Lambda_\omega F\left(p_\omega, \frac{\Lambda_\omega}{d}\right)\right) \left[\frac{1}{3}C_\omega v_\omega \Lambda_\omega\right] d\omega \quad (5.77)$$

Henceforth, equation 5.76 is referred to as FS I and equation 5.77 is referred to as FS II. Figure 5.4 (a) shows the comparison of thermal conductivity obtained by fitting the BTE solution for temperature decay, and thermal conductivities from FS I and FS II models for fully diffuse boundary scattering. We only consider non-thermalizing diffuse scattering as we have shown that thermalizing diffuse scattering is unphysical for the problem considered here. At very long grating periods, when the transport is primarily diffusive, the thermal conductivity predictions from FS I and FS II match well with the BTE solution from this work, as expected. However, at the shorter grating periods comparable to phonon MFPs, where the transport is in the quasiballistic regime, FS I underpredicts the thin film thermal conductivity while FS II overpredicts it.

This observation is also evident from the magnitude of the suppression function plotted at $\eta = 0$ for fully diffuse boundary conditions shown in figures 5.4 (b) and (c). The suppression function for the thin film geometry is defined as

$$S(q\Lambda_\omega, \Lambda_\omega/d, \eta\tau_\omega, p_\omega) = \frac{\kappa_{\omega, \text{BTE}}}{\kappa_{\omega, \text{Fourier}}} \quad (5.78)$$

where $\kappa_\omega = j_{x,\omega}/\Delta\bar{T}$ is the conductance per phonon mode and $j_{x,\omega}$ is the thickness-averaged in-plane heat flux defined in equation 5.72. In figures 5.4 (b) and 5.4 (c), the magnitude of the suppression function at $\eta = 0$ is plotted against phonon MFP non-dimensionalized with respect to the grating period q . The suppression functions from the complete BTE solution and the models FS I and FS II are identical at high temperatures and long grating periods, when the transport is primarily diffusive, governed by the Fourier's law of heat conduction. However, for low temperatures and short grating periods, FS I underpredicts the heat flux and FS II overpredicts the heat flux carried by phonons with very long MFPs. Moreover, the difference between the models FS I and FS II, and the BTE solution is smaller for thinner films indicating that enhanced boundary scattering in thinner films delays the onset of quasiballistic heat conduction. These observations emphasize the importance of using the complete BTE solution to accurately investigate boundary scattering when grating periods are comparable to phonon MFPs.

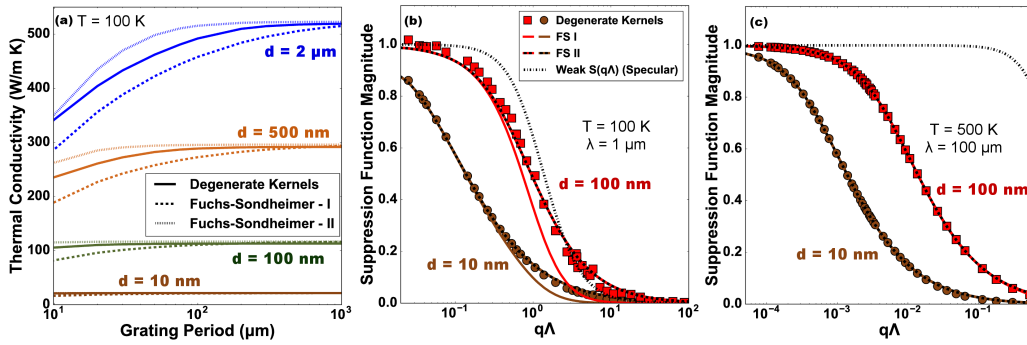


Figure 5.4: Comparison of the thermal conductivity (a) and the suppression functions ((b) and (c)) calculated from the models FS I, FS II and by solving the BTE for non-thermalizing diffuse boundary conditions at different temperatures, grating periods (λ) and film thicknesses. In figures (b) and (c), the symbols correspond to the degenerate kernel solution, the solid lines correspond to FS I model and the dashed solid lines correspond to FS II model. For very thin films and long grating periods, the models FS I and FS II are in good agreement with the BTE predictions. For thicker films and shorter grating periods, FS I underpredicts and FS II overpredicts the thermal conductivity at short grating periods (a) and the contribution of phonons with long MFP ((b) and (c)) compared to the complete BTE solution.

5.4 Extension to Finite Pump-Probe Penetration Depth

Till now, we discussed the solution of the BTE for the TG experiment on a suspended membrane, when the initial temperature distribution is a one-dimensional sinusoid in the in-plane (x) direction. However, in reality, the intensity of the pump laser, which sets up the instantaneous temperature distribution on the sample, decays exponentially in the cross-plane (z) direction as it passes through the membrane. Here, we investigate the effect of the two dimensional initial temperature profile on the final BTE solution. The sample geometry considered in this study is shown in figure 5.5 (a). We first obtain the penetration depth of the pump and probe laser used in the TG experiment at different temperatures from ref. [115, 116] shown in figure 5.5 (b). The derivation of the BTE solution proceeds similar to the uniform cross-plane heating case, with the only difference being the source term, \bar{Q}_ω is replaced by $\bar{Q}_\omega^0 \exp(-\beta_p z)$, where β_p is the absorption coefficient of the pump laser. Once again, the complete mathematical derivation is provided in the appendix C. The final semi-analytical solution for the temperature profile measured

by the probe laser is given by,

$$\begin{aligned}\Delta\bar{T}_{\text{Expt}} &= \int_0^d \Delta\bar{T}(z) \exp(-\beta_{pr}z) dz \\ &= d \left[\frac{t_0}{2d\beta_{pr}} (1 - \exp(-d\beta_{pr})) \right. \\ &\quad \left. + d\beta_{pr} \sum_{m=1}^{\infty} \frac{t_m}{m^2\pi^2 + d^2\beta_{pr}^2} (1 - (-1)^m \exp(-d\beta_{pr})) \right]\end{aligned}$$

where β_{pr} is the absorption coefficient of the probe laser and t_i 's are functions of the pump absorption coefficient β_p . Figure 5.5 (c) shows the comparison of the temperature profiles obtained from the semi-analytical solution and the MC technique described in chapter 2 for fully specular boundary scattering in a suspended membrane of 1518 nm thickness at room temperature and a grating period of 11.5 μm , considering finite penetration depth of light from figure (b). The semi-analytical BTE solution agrees well with the MC solution. Also shown for comparison is the semi-analytical solution for the same parameters, but with uniform cross-plane temperature distribution. The BTE solutions are very different initially for the uniform and exponentially decaying initial cross-plane temperature distribution, when cross-plane conduction is important. At later times, where only in-plane conduction occurs, the two solutions overlap. This difference between the BTE solution with finite penetration depth and uniform cross-plane temperature profile is observed irrespective of whether the membrane boundaries are specularly scattering or diffuse scattering, as shown in figure 5.6. However, as shown in figure 5.7, the difference between the BTE solution with finite penetration depth and uniform cross-section temperature profile for the membrane thicknesses used in our experiments vanishes as the grating period increases and the temperature decreases. Therefore, it is sufficient to use the BTE solution with uniform cross-section temperature profile to interpret our experiments. However, while performing measurements on thicker membranes, the BTE solution for finite penetration depth has to be used, as using the BTE solution with uniform cross-section temperature profile will overpredict the thermal conductivity of the membrane.

5.5 Conclusion

We have studied the effect of thermalizing and non-thermalizing boundary scattering of phonons in steady state and transient heat conduction along thin films by solving the BTE using analytical and computationally efficient semi-analytical techniques. From our analysis, we reach the following conclusions. First, under

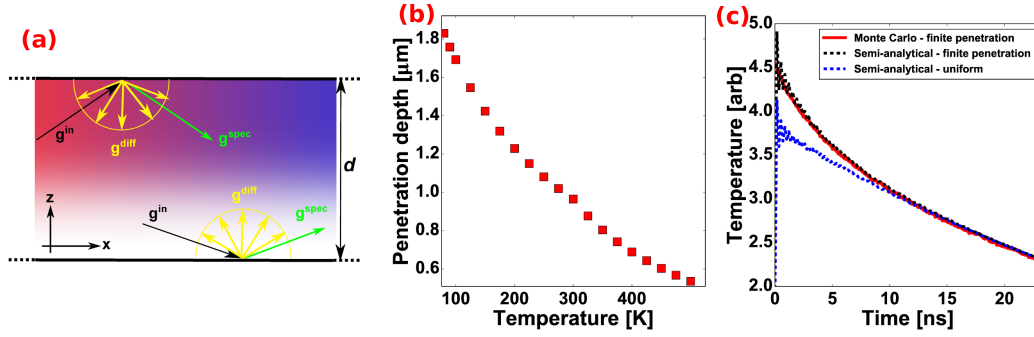


Figure 5.5: (a) The sample heating geometry with finite laser penetration depth considered in this chapter. Along with a sinusoidal in-plane (x) distribution, an exponentially decaying initial temperature profile in the cross-plane (z) direction due to the finite penetration depth of the pump laser is also considered. Moreover, the finite penetration depth of the probe laser is also considered while solving the BTE for the experimentally measured signal. (b) Optical penetration depth of silicon from 80 K to 500 K for pump laser with a wavelength of 532 nm. The penetration depth of silicon for 532 nm light is $\sim 1 \mu\text{m}$, which is comparable to the membrane thicknesses in our experiments. (c) Validation of the BTE solution with simulations using the MC technique described in chapter 2 for fully specular boundary scattering in a suspended membrane of 1518 nm thickness at room temperature and a grating period of $11.5 \mu\text{m}$, considering finite penetration depth of light from figure (b). The semi-analytical BTE solution agrees well with the MC solution. Also shown for comparison is the semi-analytical solution for the same parameters, but with uniform cross-plane temperature distribution. The BTE solutions are very different initially for the uniform and exponentially decaying initial cross-plane temperature distributions, when cross-plane conduction is important. At later times, where only in-plane conduction occurs, the two solutions overlap.

steady state transport conditions, we find that the thermal transport is governed by the Fuchs-Sondheimer theory and is insensitive to whether the boundaries are thermalizing or not. In contrast, under transient conditions, the decay rates are significantly different for thermalizing and non-thermalizing walls and the Fuchs-Sondheimer theory is only applicable in the heat diffusion regime. We also show that, for transient transport, the thermalizing wall boundary condition is unphysical due to violation of heat flux conservation. Our results provide insights into the boundary scattering process of thermal phonons over a wide range of heating length scales that are useful for interpreting thermal measurements on nanostructures.

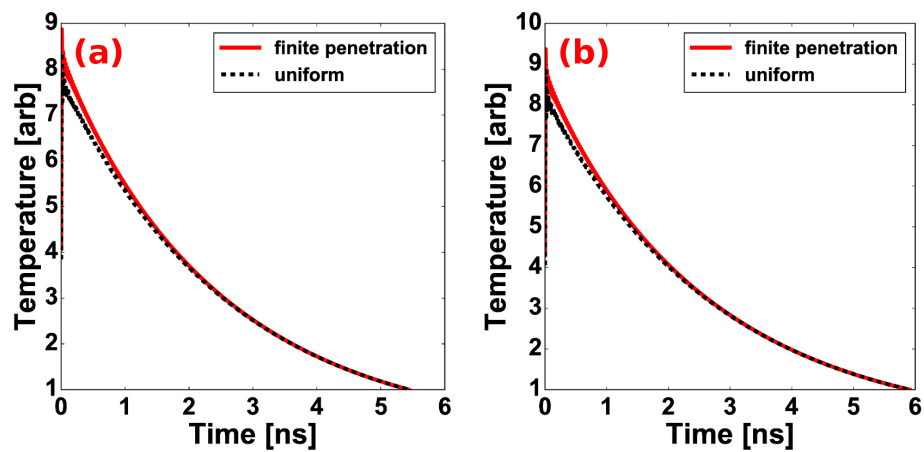


Figure 5.6: Comparison of the temperature decay profiles between the BTE solutions considering finite penetration depth and uniform initial cross-plane temperature excitations for a 600 nm suspended membrane, a grating period of $2 \mu\text{m}$ and a mean temperature of 400 K while considering (a) fully specular boundary scattering (b) fully diffuse boundary scattering. In both cases, similar difference is observed between the BTE solutions considering finite penetration depth and uniform initial cross-plane temperature excitations.

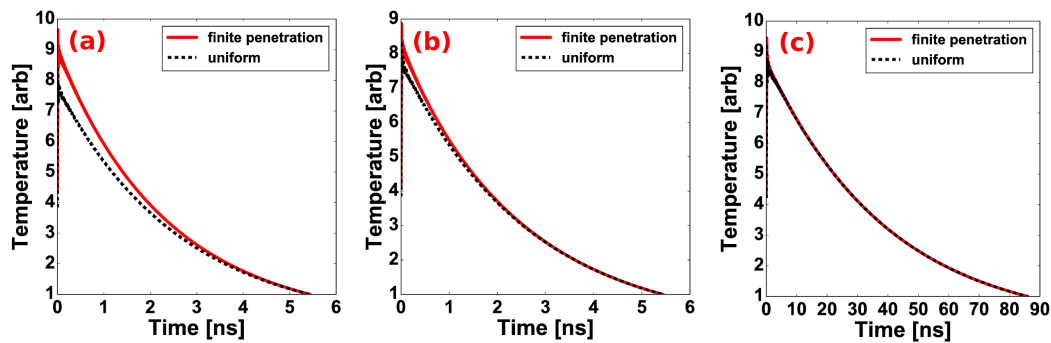


Figure 5.7: Comparison of the temperature decay profiles between the BTE solutions considering finite penetration depth and uniform initial cross-plane temperature distributions for (a) a 600 nm suspended membrane, a grating period of $2 \mu\text{m}$ and a mean temperature of 400 K (b) a 1150 nm suspended membrane, a grating period of $2 \mu\text{m}$ and a mean temperature of 400 K (c) a 1150 nm suspended membrane, a grating period of $60 \mu\text{m}$ and a mean temperature of 80 K. In all three figures, specular boundary scattering is considered. In the case of the 600 nm membrane, there is very little difference in the time decay between the two cases even at a high temperature (short penetration depth, see figure 5.5 (b)) and a short grating period. For the 1150 nm membrane, the difference between the BTE solutions with finite penetration depth and uniform temperature distribution is larger than the 600 nm case, but the difference vanishes at lower temperatures and longer grating periods.

Chapter 6

PHONON SPECULARITY PARAMETER MEASUREMENT

In the previous chapters, we introduced the TG technique and demonstrated the measurement of grating period-dependent thermal conductivity of free-standing silicon membranes. We also derived a transfer function $k^{\text{Expt}} = H(\Lambda, p_\lambda)$ from the BTE relating the phonon specularity parameter to the grating period-dependent thermal conductivity measured in the TG experiment. In this chapter, we present our methodology to extract the phonon specularity parameter by inverting the BTE transfer function H derived in chapter 4 using the experimental measurements in chapter 3, and also investigate the validity of Ziman's specularity model in our thin silicon membranes.

6.1 Ab-initio Bulk Phonon Properties for Silicon

To interpret our experiments, the solutions of the BTE presented in chapter 5 require *ab-initio* phonon properties of Si projected onto an equivalent isotropic crystal. We use a Gaussian kernel-based regression method to obtain the isotropic phonon properties for silicon from a complete set of phonon properties in reciprocal space (full Brillouin zone) calculated by *J. Carrete & N. Mingo* using ShengBTE [108, 109] and Phonopy [110], using the inter-atomic force constants calculated from VASP [111–114].

In the equivalent isotropic dataset, all phonon properties are represented only as functions of phonon frequency. In particular, for any property $I_n(\mathbf{k})$, where \mathbf{k} is the wave vector of the reciprocal space and n is the mode number, we are interested in obtaining:

$$\bar{I}_n(\omega) = \int_{\text{BZ}} \frac{d\mathbf{k}}{(2\pi)^3} I_n(\mathbf{k}) \delta(\omega - \omega_{\mathbf{k}}) \approx \sum_{\mathbf{k}} I_n(\mathbf{k}) w(\mathbf{k}) \delta(\omega - \omega_{\mathbf{k}}) \quad (6.1)$$

where V is the volume of the supercell and $w(\mathbf{k})$ are the weights on the discrete Brillouin zone grid. In order to evaluate the sum/integral in equation 6.1, we use the following approximation for the δ -function:

$$\delta(\omega - \omega_{\mathbf{k}}) \approx \frac{1}{W\sqrt{2\pi}} \exp\left(-\frac{(\omega - \omega_{\mathbf{k}})^2}{2W^2}\right)$$

with W being a smearing parameter. However, an important decision has to be made about the choice of the smearing parameter W in the approximation of the δ -function. If $W \gg$ frequency grid spacing $\Delta\omega_{\mathbf{k}}$, then the δ -function is poorly approximated and the isotropic phonon properties will produce very different macroscopic thermal properties upon evaluation. If $W \ll \Delta\omega_{\mathbf{k}}$, then there will be a number of zeros in the evaluation of $I_n(\omega)$ resulting in a number of unrealistic jumps in the isotropic phonon properties. To overcome these problems, it is clear that we require $W \sim \Delta\omega_{\mathbf{k}}$.

Now, since phonons are dispersive in semiconductors, $\Delta\omega_{\mathbf{k}}$ varies from one \mathbf{k} point to another. In order to choose $W \sim \Delta\omega_{\mathbf{k}}$, we follow the adaptive broadening scheme for \mathbf{k} -space integration introduced in [117]. In this technique, the parameter W is adaptively chosen according to,

$$W_{n\mathbf{k}} = a \left| \frac{\partial\omega}{\partial\mathbf{k}} \right| \Delta k = a |v_g(n, \mathbf{k})| \Delta k$$

where a is a constant on the order of 1 and $v_g(n, \mathbf{k})$ is the group velocity of the phonon mode n at a wave vector \mathbf{k} . Note that in this scheme, W is a function of the phonon mode number n and the wave vector \mathbf{k} . Intuitively, when the phonon group velocity is small, a large number of points gets clustered in the dispersion. The adaptive broadening scheme balances this effect by including a fewer number of points in the average (equation 6.1).

Using this technique, we obtain the isotropic phonon properties such as phonon density of states, phonon group velocities, phonon lifetimes, and phonon MFPs on a phonon frequency grid. Figures 6.1 to 6.4 show the agreement obtained between the spectral phonon specific heat and the spectral phonon thermal conductivity accumulation functions computed using the *ab-initio* phonon data and the equivalent-isotropic properties obtained using the above described method at two different temperatures.

6.2 Impurity Scattering Rate in Thin Membranes

The first principles phonon data provided by *J. Carrete & N. Mingo* was evaluated for isotopically pure silicon. However, the device layer on the SOI wafers, from which the suspended membranes have been fabricated, is lightly p-doped. Therefore, the suspended membranes in our experiments contains Boron and isotopic

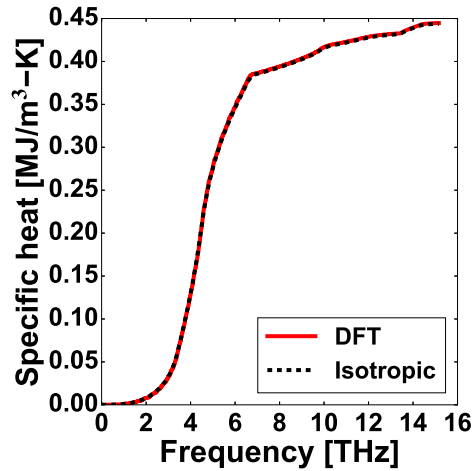


Figure 6.1: Comparison between spectral phonon specific heat accumulation computed using the *ab-initio* and equivalent isotropic phonon properties at **80 K**

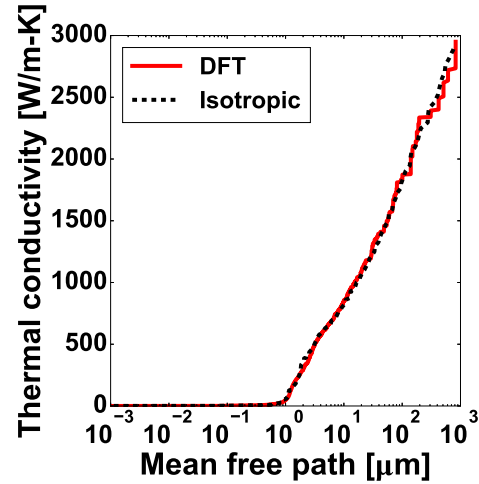


Figure 6.2: Comparison between spectral phonon thermal conductivity accumulation computed using the *ab-initio* and equivalent isotropic phonon properties at **80 K**

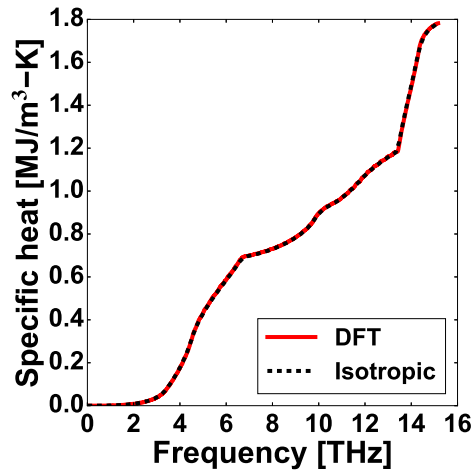


Figure 6.3: Comparison between spectral phonon specific heat accumulation computed using the *ab-initio* and equivalent isotropic phonon properties at **400 K**

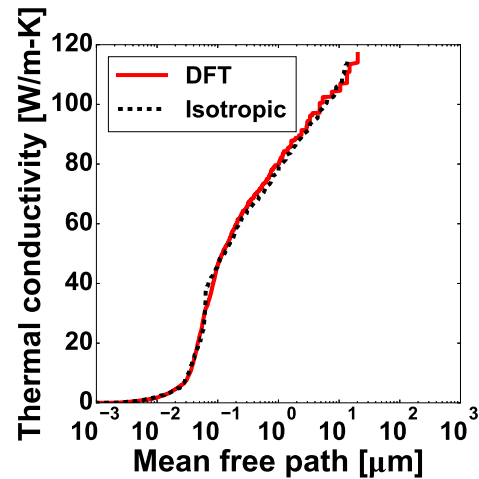


Figure 6.4: Comparison between spectral phonon thermal conductivity accumulation computed using the *ab-initio* and equivalent isotropic phonon properties at **400 K**

silicon impurities. Our estimates of the impurity concentration varied by an order of magnitude for the highest and lowest electrical resistivity reported by the SOI wafer manufacturers. To avoid using the impurity concentration with such a large

uncertainty, we perform a direct measurement of the impurity scattering rate in our experiment.

Phonon isotope scattering is conventionally treated in the BTE using the Tamura's formula [118], which holds exactly for a cubic crystal like silicon. Tamura's formula for impurity scattering rate is of the form:

$$\tau_{\omega}^{-1} = \frac{\pi V_{\text{at}}}{6} \left[\sum_i f_i \left(\frac{(\delta M)_i}{M} \right)^2 \right] \omega^2 D(\omega) = A \omega^2 D(\omega) \quad (6.2)$$

where τ_{ω}^{-1} is the impurity scattering rate, V_{at} is the volume occupied by a single atom in the unit cell, f_i is the volume fraction and $(\delta M)_i$ is the mass difference of species i , M is the average mass of the atoms, and $D(\omega)$ is the density of states of phonons with frequency ω . If we can determine the parameter A from the experiment, we would have determined the phonon-impurity scattering rate unambiguously.

In general, at large grating periods or low temperatures, the measured thermal conductivity depends on the impurity scattering rate and also on whether boundary scattering is specular or diffuse at the suspended membrane walls, since the phonon MFP is very long compared to the thickness of the membrane (figure 6.2). However, at higher temperatures, phonon MFP is significantly reduced (figure 6.2), thereby minimizing the effect of boundary scattering on the thermal conductivity of the membrane. Therefore, the membrane thermal conductivity measured at high temperatures like 400 K and at short grating periods, where any available long MFP phonons are quasiballistically suppressed, depends only on the phonon-impurity scattering rate. Since Tamura's formula (equation 6.2) for phonon-impurity scattering rate is independent of temperature, we can fit the rate coefficient A with the thermal conductivity measurements at high temperatures and short grating periods, and use it to interpret the measurements at low temperatures.

Figure 6.5 (a) shows the difference in the membrane thermal conductivity predicted by the BTE between fully specular and fully diffuse boundary scattering limits. At low temperatures of 100 K, the difference between the specular and diffuse limits is $\geq 60\%$, while at high temperatures of 400 K and short grating periods, the difference between the specular and diffuse limits is less than 10%. Therefore, we use these measurements to fit the impurity scattering rate coefficient A in Tamura's

formula (equation 6.2), as shown in figure 6.5 (b).

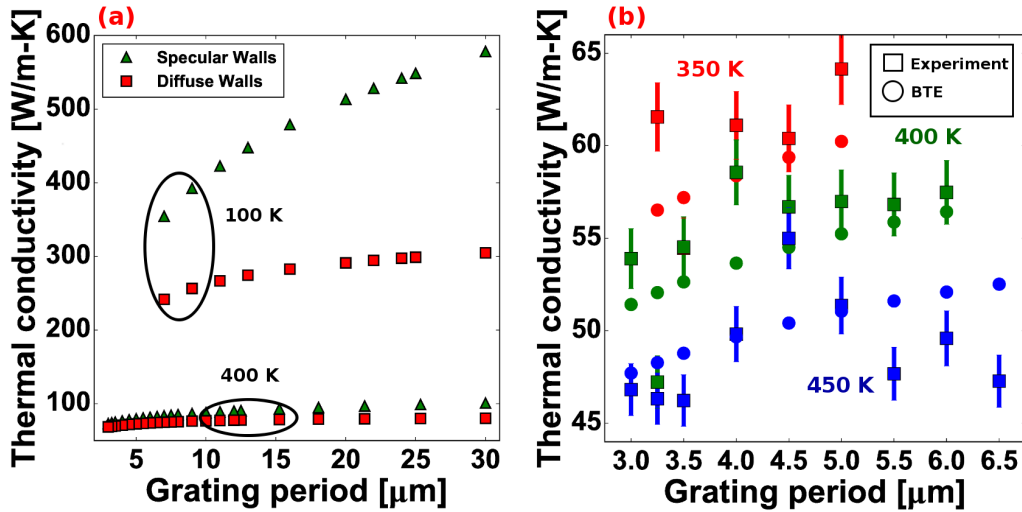


Figure 6.5: (a) Difference in the membrane thermal conductivity predicted by the BTE between fully specular and fully diffuse boundary scattering limits. At low temperatures of 100 K, the difference between the specular and diffuse limits is $\geq 60\%$, while at high temperatures of 400 K and short grating periods, the difference between the specular and diffuse limits is less than 10%. (b) Comparison between the experiments and the BTE solution that produced the best fit with the experiments. The impurity scattering rate coefficient A in Tamura's formula (equation 6.2) was extracted from this fit.

At this point, it is important to address the necessity to solve the BTE rigorously for the TG experiment. As explained in chapter 4, the conventional Fuchs-Sondheimer theory fails to accurately predict the grating period-dependence of thermal conductivity at short grating periods. Since we obtain the phonon-impurity scattering rate using the thermal conductivities at short grating periods, using the Fuchs-Sondheimer theory will result in erroneous interpretation of the experimental measurements.

6.3 Failure of Ziman's Specularity Model

Now that we have a complete description of the intrinsic phonon properties in our membrane samples, we investigate the validity of Ziman's specularity model to explain the measured thermal conductivity of the suspended membranes. As described earlier, performing measurements over a range of temperatures and grating periods

allows us to probe different parts of the phonon spectrum separately. Therefore, by comparing the absolute values and grating period-dependent trends of the predicted and observed thermal conductivity of the membranes, we can check the validity of Ziman's specularity over a large portion of the phonon spectrum in the material, unlike in previous works.

Figures 6.6 to 6.8 show the measured thermal conductivity of 3 different suspended membranes with different thicknesses as a function of grating period at different temperatures compared with the BTE predictions for fully specular, fully diffuse, and partially specular boundary scattering based on Ziman's specularity model (equation 1.1). It is evident from these figures that Ziman's model neither predicts the absolute thermal conductivity values nor the observed trends with grating periods and temperature correctly. Even for the smallest surface roughness value estimated from AFM and TEM images on our sample surfaces (RMS: 0.28 nm), we find that Ziman's theory predicts almost fully diffuse scattering of phonons for all temperatures and grating periods in this study, while our experiments lie far above the diffuse limit, with the difference increasing with decreasing temperature.

6.4 Bayesian Inference to Extract Specularity Parameter

Next, we explore the possibility of extracting the phonon specularity parameter from our experimental measurements, by inverting the thermal conductivity transfer function derived from the BTE ($H(\Lambda, p_\lambda) = k^{\text{BTE}}(p_\lambda)$) over the experimentally measured grating-period dependent thermal conductivities of the thin membranes. To rigorously quantify the uncertainty in our experimental measurements, we use the method of Bayesian inference to fit our experimental measurements to the BTE model and obtain the optimal specularity profile that produces the best fit. Bayesian inference is a statistical method of uncertainty quantification, which helps us rigorously combine our prior expected features of the final solution, in this case, the specularity parameter, with information from experiments. Bayesian inference is based on Bayes theorem, which can be mathematically represented as,

$$\pi_{\text{post}}(p_\lambda | k^{\text{expt}}) \propto \mathcal{N}(k^{\text{expt}} - k^{\text{BTE}}(p_\lambda), \sigma^2 I) \times \pi_{\text{prior}}(p_\lambda) \quad (6.3)$$

In this equation, $\pi_{\text{prior}}(p_\lambda)$ represents the prior probability density of the specularity parameter. Prior probability density helps us rigorously add our prior knowledge about the specularity profile. For this work, the only prior knowledge we incorporate is the smoothness of the specularity profile with respect to phonon wave-

length. $\mathcal{N}(k^{\text{expt}} - k^{\text{BTE}}(p_\lambda), \sigma^2 I)$ represents the normal distribution function for the difference between our measurements and the prediction from the BTE solution for a given specularly parameter, p_λ , with an experimental variance σ . The result of Bayesian inference is a posterior probability density for the specularly parameter, which is proportional to the product of the prior probability distribution $\pi_{\text{prior}}(p_\lambda)$ and the extent to which p_λ explains our measurements, given by $\mathcal{N}(k^{\text{expt}} - k^{\text{BTE}}(p_\lambda), \sigma^2 I)$. Intuitively, the Bayes theorem (equation 6.3) states that a specularly profile $\{p_\lambda\}_i$ has a higher posterior probability density if (a) it is a smooth function of phonon wavelength, and (b) the BTE solution with $\{p_\lambda\}_i$ matches well with our experiments.

The first challenge in this procedure is to construct a prior distribution function, which reflects our knowledge about the smoothness of the specularly profile. In order to derive a smooth prior distribution, we start with the definition of smoothness of the specularly profile p_λ (where $\lambda = 1, 2, \dots$ represents the different phonon modes) as,

$$p_i = \frac{1}{2} (p_{i-1} + p_{i+1})$$

In order to admit some uncertainty in our prior knowledge, we add perturbations to the definition of smoothness as,

$$p_i = \frac{1}{2} (p_{i-1} + p_{i+1}) + W_i$$

where $\{W_i\} \sim \mathcal{N}(0, \gamma^2 I)$ is a new random variable with variance γ . In matrix formulation, we get

$$Lp = W$$

where L is given by,

$$L = \frac{1}{2} \begin{bmatrix} -1 & 2 & -1 & \ddots & & & \vdots \\ 0 & -1 & 2 & -1 & \ddots & & \vdots \\ \vdots & \ddots & \ddots & \ddots & \ddots & \ddots & \vdots \\ \vdots & & \ddots & \ddots & \ddots & \ddots & \vdots \\ \vdots & & & \ddots & -1 & 2 & -1 & 0 \\ \vdots & & & & \ddots & -1 & 2 & -1 \end{bmatrix}$$

Now, the distribution of Lp is the same as the distribution of the random variable W . Since W is normally distributed, the prior distribution of the specularly profile $\{p_\lambda\}$ is given by,

$$\pi_{\text{prior}} \propto \exp\left(-\frac{1}{\gamma^2}\|Lp\|^2\right) \quad (6.4)$$

The next step in the Bayesian uncertainty estimation is to select sample specularly profiles from the prior probability distribution (equation 6.4) and compute the posterior probability estimate from Bayes theorem (equation 6.3). There are two difficulties that we have to address at this point.

1. We only know the prior probability density up to a constant factor (due to the proportionality in equation 6.4).
2. The prior distribution couples p_i with p_{i+1} and p_{i-1} through the matrix L . Therefore, the individual elements of the vector $\{p\}_i$ are not independent random variables.

We overcome these challenges by utilizing a Metropolis Hastings Markov Chain Monte Carlo (MH-MCMC) algorithm [119] to sample $\{p_\lambda\}$ from the prior probability distribution. MH-MCMC algorithm is similar to a rejection-acceptance sampling algorithm, which does not require the knowledge of the sampling distribution accurate to a proportionality constant. This algorithm proceeds as follows:

Algorithm 1 Metropolis Hastings Markov Chain Monte Carlo algorithm

- 1: Choose a proposal density $q(m, p) = \frac{1}{\sqrt{2\pi\gamma^2}} \exp\left(-\frac{1}{2\gamma^2}\|m - p\|^2\right)$.
- 2: Choose initial sample p_0 at random.
- 3: **for** $k = 0, \dots, N$ **do**
- 4: Draw a sample m from the proposal density $q(p_k, m)$
- 5: Compute $\pi_{\text{prior}}(m)$
- 6: Compute the acceptance probability

$$\alpha(p_k, m) = \mathbf{min} \left[1, \frac{\pi(m)}{\pi(p_k)} \right]$$

- 7: Accept and set $p_{k+1} = m$ with probability $\alpha(p_k, m)$. Otherwise, reject and set $p_{k+1} = p_k$.
-

Since we only deal with ratios of $\pi(p)$'s in this technique, there is no need to know the proportionality constant in equation 6.4. Moreover, since the samples m are

generated from a proposal distribution $q(m, p)$ for an independent and identically distributed normal random variable, standard sampling techniques developed for a multivariate normal distribution can be employed. The information about the coupling between different components of $\{p_\lambda\}$ are included in the expression for the acceptance probability $\alpha(p_k, m)$.

Once we have these random samples ($\{p_\lambda\}_j$) drawn according to the prior distribution function (equation 6.4), we can compute the residual $\mathcal{N}(k^{\text{expt}} - k^{\text{BTE}}(\{p_\lambda\}_j), \sigma^2 I)$ by solving the BTE and finally invoke the Bayes theorem to obtain the posterior probability density ($\pi_{\text{posterior}}(\{p_\lambda\}_j)$) for every sample specular profile $\{p_\lambda\}_j$.

6.5 Optimal Profile for the Specularity Parameter

We used Bayesian inference to extract the posterior probability density of the phonon specularity parameter that best explains all of our experimental measurements over a range of temperatures and grating periods. The Bayesian inference algorithm converged to an optimal specularity profile for one of our membranes with a thickness of 525 nm. The posterior probability density for the specularity parameter that we obtained for this membrane is shown in figure 6.9 (b). The entire phonon spectrum is partially specularly scattered at the boundaries of this membrane. The specularity of phonons increases with increasing phonon wavelength, since a surface RMS roughness of about 0.3 nm, which is the smallest RMS surface roughness amplitude measured on our membranes (figure 6.9 (a)), is likely to scatter phonons with comparable wavelength diffusely but is unlikely to scatter phonons with wavelength much longer than 1 nm. Interestingly, even phonons with wavelength comparable to unit cell size in silicon (~ 0.5 nm) is partially specularly scattered at the membrane walls. Most importantly, the specularity of phonons in this membrane is much higher than the predictions from Ziman's theory (equation 1.1) using the same RMS surface roughness found on the membrane.

In figure 6.10, we compare our thermal conductivity predictions from the posterior probability density of optimal specularity profiles with the experimental measurements for the 525 nm thick membrane. The measured thermal conductivity values lie between the fully specular and fully diffuse boundary scattering limits obtained from the BTE at all temperatures and grating periods, confirming partial specular scattering of phonons. The grating period trends and the absolute values of

the thermal conductivity estimates from the Bayesian inference procedure are in good agreement with the experiment, thereby validating our approach to extract the phonon specularity parameter from the TG experiment.

6.6 Possibility of Phonon Mode Conversion at the Membrane Boundaries

The Bayesian inference approach failed to converge to an optimal posterior probability density for the specularity profile for the other two membranes. Even though all 3 free-standing membranes were fabricated using the same procedure described in chapter 3, the thermal conductivity of the thicker membranes start at the fully diffuse limit and move farther away towards the fully specular limit as the temperature is decreased (figures 6.7 and 6.8). We have characterized the surface quality of these two membranes using AFM and reflectometry measurements and found them to be similar to the 525 nm thick membrane.

One possible explanation for the failure of the Bayesian inference method is that we do not consider phonon mode conversion at the membrane boundaries while solving the BTE. Even though boundary scattering of phonons is expected to be an elastic process, a longitudinal (transverse) polarized phonon can get converted into a transverse (longitudinal) phonon of the same energy at a boundary. In fact, mode conversion naturally occurs for very long wavelength elastic waves at a stress-free boundary and solutions have been found for the mode conversion probability of seismic waves interacting with the rough earth's crust [120, 121]. To investigate if mode conversion at the membrane boundary can explain the discrepancies, we solve the BTE with a modified boundary condition to allow for conversion of phonon modes with the same frequency between each other. The modified bound-

ary conditions for the BTE are given by,

For $\mu \in (0, 1]$,

$$v_{\omega,s'} g_{\omega,s'}^+(0, \mu, \phi) = \sum_s \left(\alpha_{\omega,s's}^{\text{spec}} p_{\omega,s} v_{\omega,s} g_{\omega,s}^-(0, -\mu, \phi) - \alpha_{\omega,s's}^{\text{diff}} \frac{(1-p_{\omega,s})}{\pi} v_{\omega,s} \int_0^{2\pi} \int_{-1}^0 g_{\omega,s}^-(0, \mu', \phi') \mu' d\mu' d\phi' \right)$$

For $\mu \in [-1, 0)$,

$$v_{\omega,s'} g_{\omega,s'}^-(d, \mu, \phi) = \sum_s \left(\alpha_{\omega,s's}^{\text{spec}} p_{\omega,s} v_{\omega,s} g_{\omega,s}^+(d, -\mu, \phi) + \alpha_{\omega,s's}^{\text{diff}} \frac{(1-p_{\omega,s})}{\pi} v_{\omega,s} \int_0^{2\pi} \int_0^1 g_{\omega,s}^+(d, \mu', \phi') \mu' d\mu' d\phi' \right)$$

where $\alpha_{\omega,s's}^{\text{spec/diff}}$ is the probability with which a phonon mode s gets converted into another phonon mode s' of the same frequency ω . These $\alpha_{s's}$'s are constrained by the fact that the sum of the probabilities of a particular mode s converting into one of the other modes with the same frequency (including itself) is 1, i.e., $\sum_{s'} \alpha_{\omega,s's}^{\text{spec/diff}} = 1$ separately for specular and diffuse phonon scattering. In this work, we have neglected the angular dependence of the mode conversion probabilities $\alpha_{\omega,s's}^{\text{spec/diff}}$. Moreover, the mode conversion probabilities $\alpha_{\omega,s's}^{\text{spec/diff}}$ have to obey the following detailed balance relation,

$$\alpha_{\omega,s's}^{\text{spec/diff}} D(\omega, s) = \alpha_{\omega,s's'}^{\text{spec/diff}} D(\omega, s') \quad (6.5)$$

in order to preserve the microscopic reversibility of the system at equilibrium. In this equation, $D(\omega, s)$ is the density of states of a mode with frequency ω and a polarization s . Similar to the chapter 4, the mathematics behind the derivation of the BTE solution is tedious and therefore has been described in appendix D.

The choice of the mode conversion parameters $\alpha_{\omega,s's}^{\text{spec/diff}}$ determines the final solution of the BTE for a given temperature and grating period. However, these mode conversion parameters are only known for an isotropic continuum elastic solid with a rough surface. Moreover, since continuum elasticity is assumed in ref. [120, 121], these results do not describe the mode conversion behavior of heat carrying phonons which have a wavelength of a few nanometers in an elastically anisotropic material like silicon. We overcome this problem in this work by choosing random samples of the mode conversion probabilities $\alpha_{\omega,s's}^{\text{spec/diff}}$ uniformly from the interval (0, 1) with

the constraints $0 \leq \alpha_{\omega,s's}^{\text{spec/diff}} \leq 1$, $\sum_{s'} \alpha_{\omega,s's}^{\text{spec/diff}} = 1$ (phonon conservation) and the detailed balance equation (equation 6.5).

Figure 6.11 (a) and (b) show the comparison of experiments with BTE simulations using random mode conversion parameters $\alpha_{\omega,s's}^{\text{spec/diff}}$ for the 1150 nm thick membrane studied in this work at 400 K and 125 K respectively. Although the spread in the BTE solutions with mode conversion does not enclose the experimental data, the mode conversion cases show a reduction in thermal conductivity compared to the solution without mode conversion at long grating periods and low temperatures, similar to the experimental trend. Although at this point we cannot conclude that mode conversion explains all of the experimental results, getting accurate mode conversion parameters from ab-initio phonon transport calculations using atomistic green's function method and including them in the analysis can give us more insights into the phonon boundary scattering in our membranes.

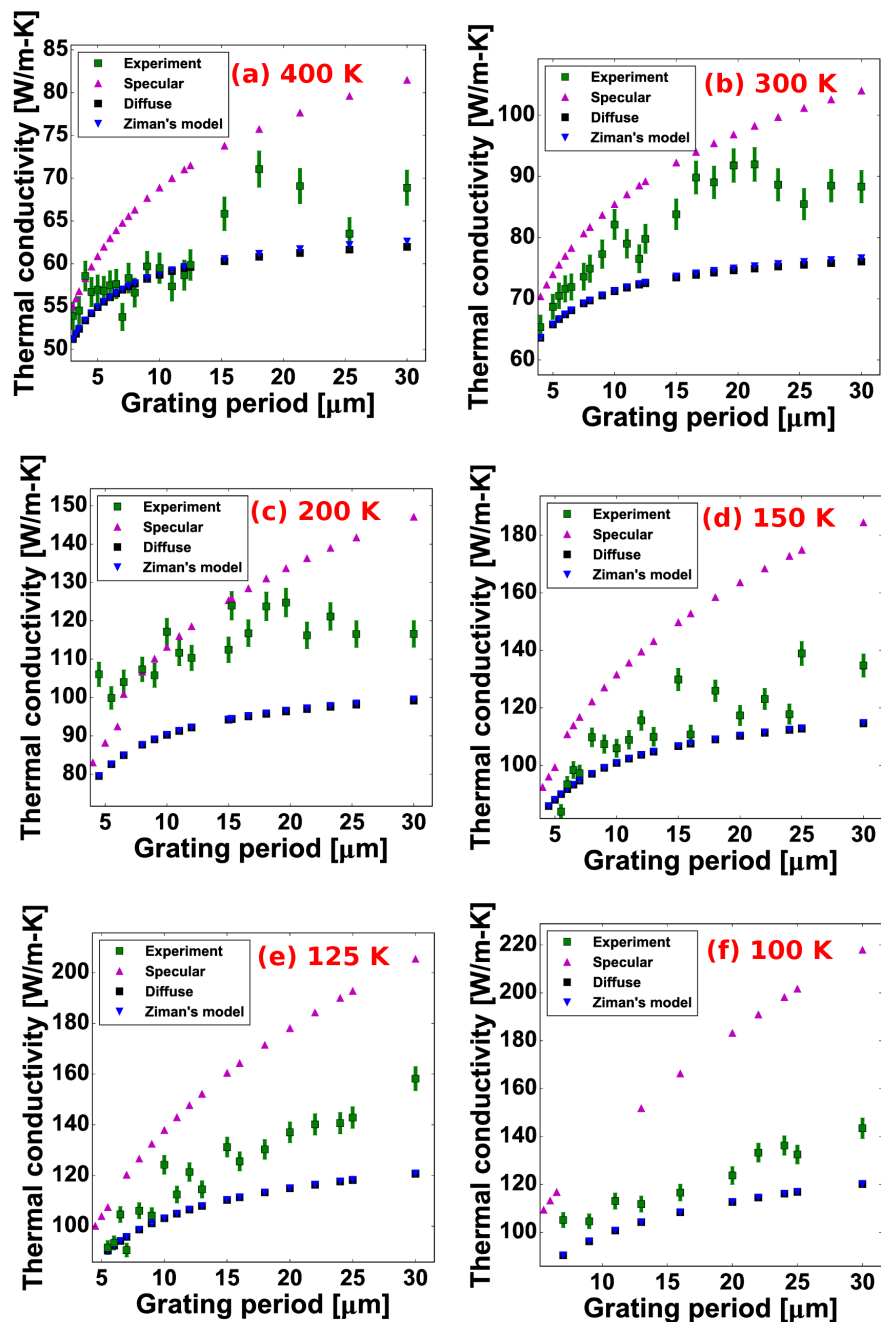


Figure 6.6: Measured thermal conductivity of a 525 nm thick membrane as a function of grating period at different temperatures. Also shown are the BTE predictions for fully specular, fully diffuse, and partially specular boundary scattering based on Ziman's specular model (equation 1.1). Ziman's specular model is unable to explain the experimental measurements over a range of temperatures and grating periods.

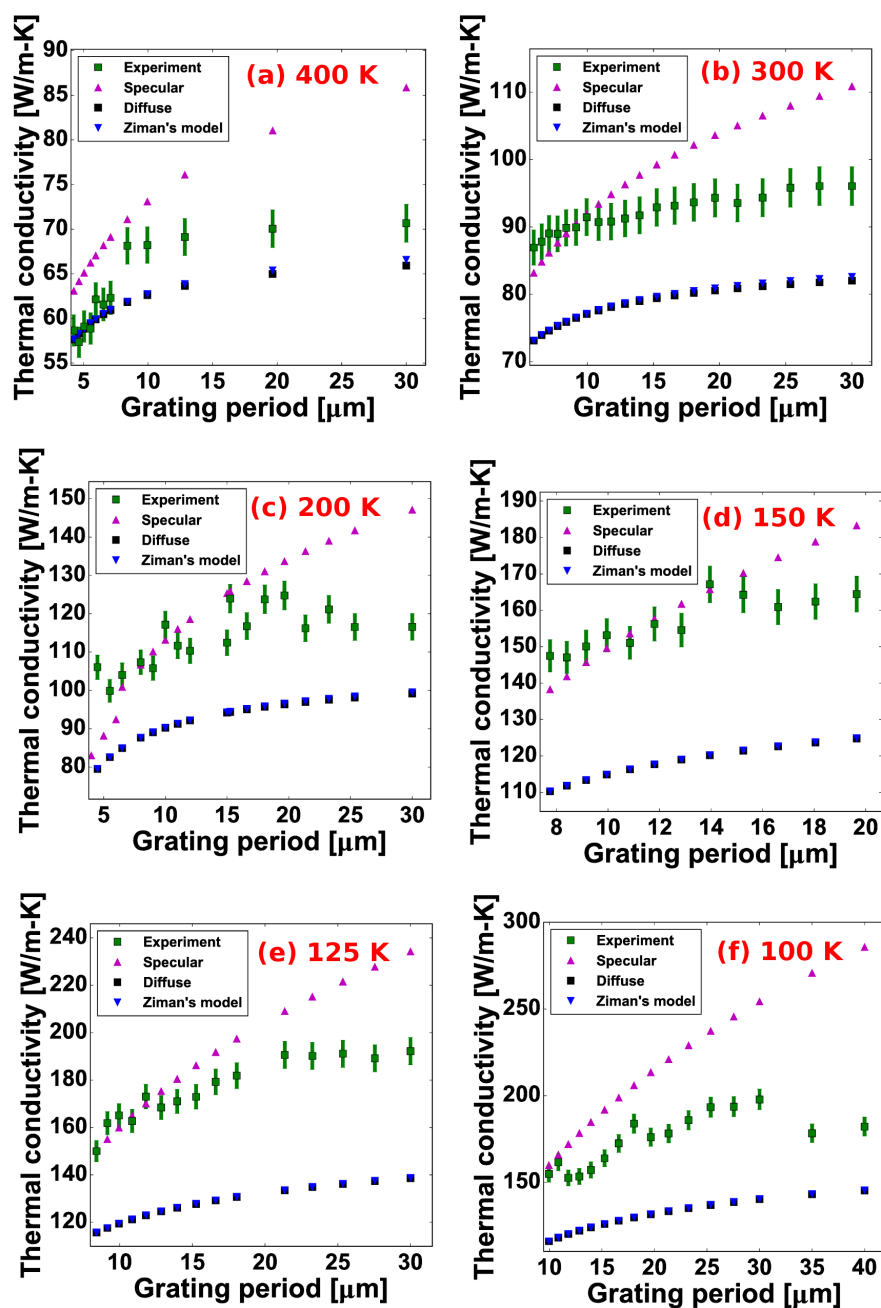


Figure 6.7: Measured thermal conductivity of a 610 nm thick membrane as a function of grating period at different temperatures. Also shown are the BTE predictions for fully specular, fully diffuse, and partially specular boundary scattering based on Ziman's specular model (equation 1.1). Ziman's specular model is unable to explain the experimental measurements over a range of temperatures and grating periods.

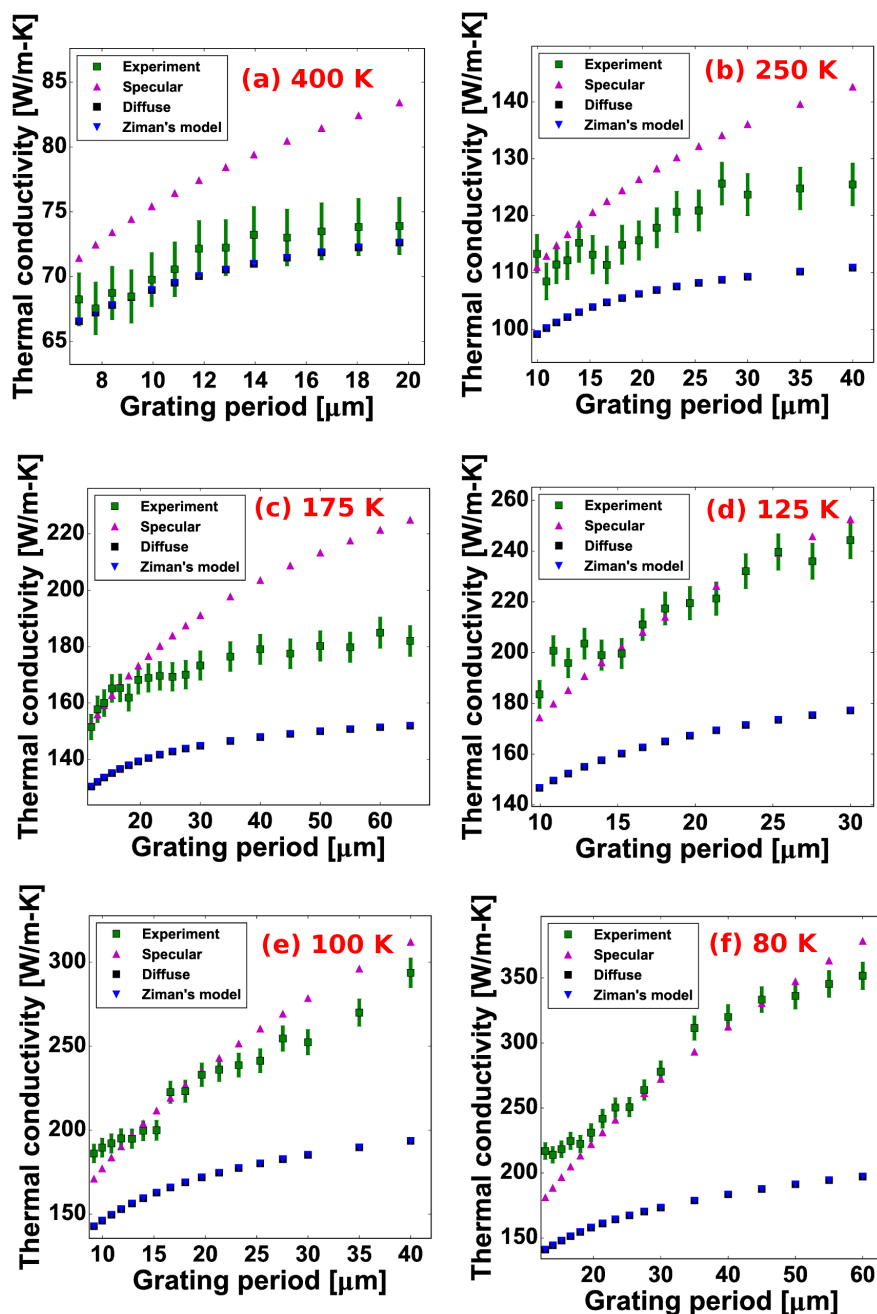


Figure 6.8: Measured thermal conductivity of a 1150 nm thick membrane as a function of grating period at different temperatures. Also shown are the BTE predictions for fully specular, fully diffuse, and partially specular boundary scattering based on Ziman's specular model (equation 1.1). Ziman's specular model is unable to explain the experimental measurements over a range of temperatures and grating periods.

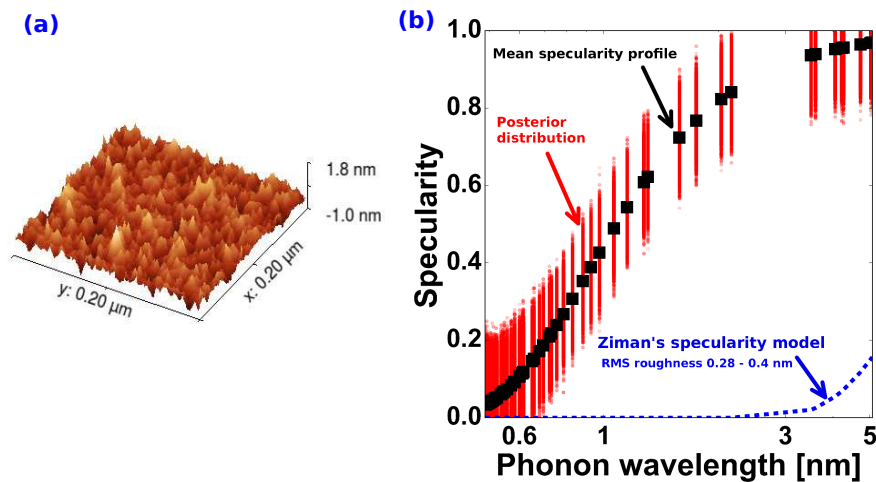


Figure 6.9: (a) Atomic force microscope (AFM) image of the surface roughness profile for one of our membranes. The measured surface RMS roughness varied between $\sim 0.3 - 0.4$ nm. All of our membranes had RMS surface roughness amplitude in this range. (b) Phonon specularity parameter obtained using the Bayesian inference procedure that best fits with the thermal conductivity measurements on a 525 nm thick membrane. The black symbols represent the mean of all the specularity profiles sampled in the Bayesian procedure and the red region has an intensity proportional to the posterior probability density of the specularity profile obtained from Bayes' theorem (equation 6.3). Phonons are more specularly scattered compared to Ziman's predictions (equation 1.1) for the smallest RMS roughness (~ 0.3 nm) measured on the membrane surface.

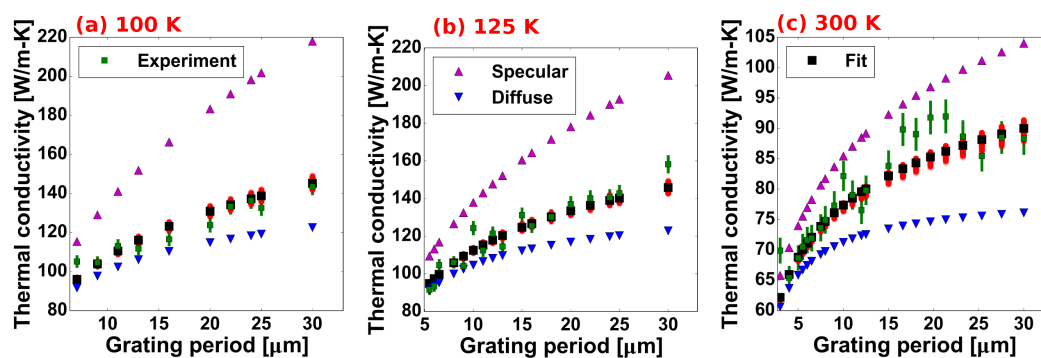


Figure 6.10: Comparison of thermal conductivity obtained from the TG experiments with the BTE fits obtained using the Bayesian inference approach. Similar to figure 6.9, the black symbols represent the mean of all the specularity profiles sampled in the Bayesian procedure and the red region has an intensity proportional to the posterior probability density of the specularity profile obtained from Bayes' theorem (equation 6.3). The measured thermal conductivity values lie between the fully specular and fully diffuse boundary scattering limits obtained from the BTE at all temperatures and grating periods, indicating partial specular scattering of phonons.

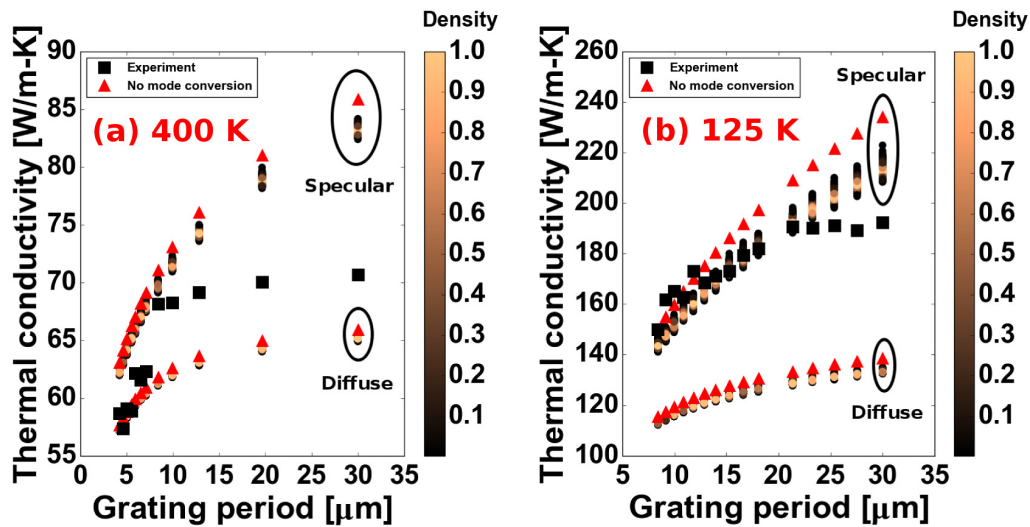


Figure 6.11: Comparison of thermal conductivity measured in experiments with the thermal conductivity from the BTE simulations using random mode conversion parameters $\alpha_{\omega,s's}^{\text{spec/diff}}$ for the 1150 nm thick membrane studied in this work at (a) 400 K and (b) 125 K. The mode conversion parameters ($\alpha_{\omega,s's}^{\text{spec/diff}}$) are drawn from a uniform distribution and the thin film thermal conductivity is calculated by solving the BTE using every one of these random mode conversion parameters. The density of points is a measure of the number of mode conversion parameters resulting in the same thermal conductivity. The triangular symbols are the BTE calculations for the case of no mode conversion.

Chapter 7

SUMMARY AND OUTLOOK

Controlling the thermal phonon properties without disturbing the electronic properties of nanoscale devices is a new and exciting topic driving research in the nanoscale heat transfer community. This dissertation sheds light on the microscopic phonon boundary interactions that contribute to a significant fraction of thermal boundary resistance in the nanoscale systems and provide an elegant method to control the heat carrying capacity of phonons without significantly affecting the electrons. After a detailed review of the past work in this field, we started this thesis in chapter 2 by discussing the impact of diffuse boundary scattering on the thermal conductivity of the semiconductor nanostructures using efficient variance reduced MC solutions of the BTE. We demonstrated how diffuse phonon boundary scattering can reduce the thermal conductivity of nanostructures by over two orders of magnitude compared to the thermal conductivity of the constituent materials, and showed that the lack of microscopic understanding of the phonon boundary scattering processes could lead to inconclusive interpretation of the observed thermal conductivity of nanostructures in terms of whether phonons scatter coherently or incoherently at the material boundaries. We also motivated the need to measure the mode-dependent phonon specularity parameter at material boundaries to better understand the connection between the nature of surface irregularities with the resulting thermal boundary resistance in the nanostructures.

In chapter 3, we describe the phenomenon of quasiballistic heat conduction which enables the measurement of spectral phonon properties in semiconductor materials. We showed that, in the quasiballistic heat transfer regime, by changing the length scale across which heat transfer takes place, we can change the distribution of phonons carrying heat in semiconductors, thereby using the quasiballistic effect as a knob to isolate and probe different parts of the thermal phonon spectrum. We demonstrated the experimental manifestation of quasiballistic heat conduction by observing thermal length scale dependent thermal conductivity, using the MC solutions of the BTE in a two-layer simulation geometry. Finally, we introduced the non-contact optical pump probe technique, the TG experiment, as a natural choice to measure heating length scale-dependent thermal conductivity in a single layer

membrane sample, which is ideal to study phonon scattering at free material boundaries.

In chapter 4, we described the design and construction of the TG experiment used in this study. We described the working principle of the experiment in detail, followed by some discussion on the alignment of optics to achieve the desired temperature rise on the sample. Next, we validated the TG experiment by measuring the speed of sound in water and by measuring thermal transport in single crystal GaAs wafer. We described the protocol adopted to fabricate free-standing suspended silicon thin membranes used in our study and reported very good signal to noise ratio in our experiments on the thin membranes. Finally, we demonstrated the observation of quasiballistic heat conduction in our thin silicon membranes and motivated the requirement for a rigorous analysis of the BTE to understand the observed quasiballistic, boundary scattering-dominated thermal transport in the thin membranes.

In chapter 5, we described our computationally efficient semi-analytical solution for the BTE in the exact same heating geometry of the thin membrane in the TG experiment. We showed that the conventional treatment of boundaries as thermalizing walls violate the conservation of heat flux in the quasiballistic heat conduction regime within the membranes, and also showed that the conventional Fuchs-Sondheimer model for reduction in thermal conductivity of thin membrane due to boundary scattering cannot accurately describe the membrane thermal conductivity in the quasiballistic heat transfer regime. Through this work, we derived a transfer function connecting the mode-dependent phonon specular parameter at the membrane boundaries and the observed grating period-dependent thermal conductivity in the TG experiments.

In chapter 6, we discussed our measurements and interpretation of the thermal conductivity of the free-standing membranes at different temperatures and grating periods in the quasiballistic heat conduction regime. We described our methodology to obtain the intrinsic phonon properties and impurity scattering rates in bulk silicon required to accurately extract the only unknown quantity in this problem - the phonon specular parameter. We showed that the 50 year old Ziman's model for phonon specular parameter failed to explain the magnitude and the trends of the observed thermal conductivity as a function of grating periods and temperature in our ex-

periments. Next, we elucidated our experimental uncertainty estimation procedure based on Bayesian inference to rigorously invert the BTE transfer function developed in chapter 5 and extract the posterior probability density of the specular parameter, which quantifies the likelihood of a given specular profile to explain our experiments. We showed that our extracted specular profile from one of our membranes predicts a significantly higher specular scattering of phonons compared to the conventional Ziman's model for the phonon specular parameter. We also showed that a simple partially specular boundary scattering picture cannot adequately describe the observed thermal conductivity trends in a few membranes, and discuss the possibility of phonon mode conversion at the boundaries of these membranes.

7.1 Outlook

The first main contribution of this thesis is demonstrating computationally efficient semi-analytical and numerical solutions of the governing equation for phonon transport in nanostructures — the BTE. These solutions have enabled the interpretation of macroscopic thermal conductivity measurements in terms of microscopic phonon properties and educated us about several new heat transfer regimes that we do not usually observe in our macroscopic world view. While we have only considered phonon-phonon and phonon-impurity interactions in the BTE solution, our solution methodology can be extended to study interactions of phonons with other particles like electrons and magnons and help resolve the mysteries in the heat conduction properties of several unique materials demonstrating strong electron-phonon and magnon-phonon interactions. [122–124]

Chapter 3 of this thesis provides a very detailed description of how to use the TG technique to measure the thermal conductivity of bulk and thin film semiconductor devices, synthesizing the work of many previous authors, particularly Prof. Keith Nelson's group at MIT. We have learnt the power of this experiment in unambiguously measuring thermal phonon properties in thin crystalline semiconductor membranes while figuring out the working principle and the underlying heat transfer physics in this experiment. The TG experiment has already provided conclusive evidence for the presence of phonons with MFP longer than $1 \mu\text{m}$ in silicon at room temperature, thereby putting to rest a decade long argument about the presence of long MFP phonons in silicon [85]. However, the scope of this experimen-

tal technique extends far beyond just measuring thermal transport in silicon thin membranes. In fact, efforts have already begun to extend this technique to measure thermal transport in crystalline polymers and amorphous semiconductors, and ambipolar diffusion of carriers in silicon in our group. There are also reports of exploring phonon-magnon dynamics in magnetic materials using the TG technique elsewhere [125]. Exploring transport in these new materials could lead to new technological inventions and TG will be a front runner in aiding the study of these new and interesting transport phenomena.

Finally, chapter 6 of this thesis has shown us a clear future research direction to further our understanding of phonon boundary scattering. Until recently, experiments have not been able to measure the microscopic interactions of phonons in nanoscale semiconductor materials. Therefore, predictions from theorists on different phonon boundary interactions using *ab-initio* modeling approaches have been treated partly as speculative and therefore have not accelerated improvements in the thermal performance of devices like LEDs. Our ability to perform phonon mode-dependent measurements using the TG technique over a wide range of the experimental parameter space should give enough information for the theorists to confirm or reject their new proposals. In particular, ab-initio modeling of phonon mode conversion at the membrane boundaries using atomistic green's function method and solutions of the elastic wave equation can help explain the observed thermal conductivity trends and can eventually lead to achieving better control over the thermal boundary resistance in thin membrane devices by just engineering their nanoscale surface features.

BIBLIOGRAPHY

- [1] M. Wienold et al. “Optical and thermal characteristics of narrow-ridge quantum-cascade lasers”. In: *Journal of Applied Physics* 103.8 (Apr. 2008), p. 083113. ISSN: 0021-8979, 1089-7550. DOI: 10.1063/1.2907862. URL: <http://scitation.aip.org.clsproxy.library.caltech.edu/content/aip/journal/jap/103/8/10.1063/1.2907862>.
- [2] Denzil Roberts and Gregory Triplett. “Tuning nonlinear susceptibility in strained AlGaAs/InGaAs quantum cascade lasers”. In: *Solid-State Electronics*. Papers Selected from the International Semiconductor Device Research Symposium 2007 – ISDRS 2007 52.10 (Oct. 2008), pp. 1669–1673. ISSN: 0038-1101. DOI: 10.1016/j.sse.2008.06.040. URL: <http://www.sciencedirect.com/science/article/pii/S0038110108001950>.
- [3] Y.-L. Li, Y.-R. Huang, and Y.-H. Lai. “Efficiency droop behaviors of InGaNGaN multiple-quantum-well light-emitting diodes with varying quantum well thickness”. In: *Applied Physics Letters* 91.18 (Oct. 2007), p. 181113. ISSN: 0003-6951, 1077-3118. DOI: 10.1063/1.2805197. URL: <http://scitation.aip.org.clsproxy.library.caltech.edu/content/aip/journal/apl/91/18/10.1063/1.2805197>.
- [4] Allon I. Hochbaum et al. “Enhanced thermoelectric performance of rough silicon nanowires”. en. In: *Nature* 451.7175 (Jan. 2008), pp. 163–167. ISSN: 0028-0836. DOI: 10.1038/nature06381. URL: <http://www.nature.com.clsproxy.library.caltech.edu/nature/journal/v451/n7175/abs/nature06381.html>.
- [5] Katsuhiko Tomioka, Masatoshi Yoshimura, and Takashi Fukui. “A III-V nanowire channel on silicon for high-performance vertical transistors”. en. In: *Nature* 488.7410 (Aug. 2012), pp. 189–192. ISSN: 0028-0836. DOI: 10.1038/nature11293. URL: <http://www.nature.com.clsproxy.library.caltech.edu/nature/journal/v488/n7410/full/nature11293.html>.
- [6] John M Ziman. *Electrons and phonons: the theory of transport phenomena in solids*. Oxford University Press, 1960.
- [7] R. O. Pohl and B. Stritzker. “Phonon scattering at crystal surfaces”. In: *Physical Review B* 25.6 (Mar. 1982), pp. 3608–3614. DOI: 10.1103/PhysRevB.25.3608. URL: <http://link.aps.org/doi/10.1103/PhysRevB.25.3608>.
- [8] Tom Klitsner and R. O. Pohl. “Phonon scattering at a crystal surface from {in situ} -deposited thin films”. In: *Physical Review B* 34.8 (Oct. 1986), pp. 6045–6048. DOI: 10.1103/PhysRevB.34.6045. URL: <http://link.aps.org/doi/10.1103/PhysRevB.34.6045>.

- [9] E. T. Swartz and R. O. Pohl. “Thermal Boundary Resistance from 0.5–300K”. en. In: *Phonon Scattering in Condensed Matter V*. Ed. by Professor Ansel C. Anderson and Professor James P. Wolfe. Springer Series in Solid-State Sciences 68. DOI: 10.1007/978-3-642-82912-3_65. Springer Berlin Heidelberg, 1986, pp. 228–230. ISBN: 978-3-642-82914-7 978-3-642-82912-3. URL: http://link.springer.com/chapter/10.1007/978-3-642-82912-3_65.
- [10] Tom Klitsner et al. “Phonon radiative heat transfer and surface scattering”. In: *Physical Review B* 38.11 (Oct. 1988), pp. 7576–7594. doi: 10.1103/PhysRevB.38.7576. URL: <http://link.aps.org/doi/10.1103/PhysRevB.38.7576>.
- [11] E. T. Swartz and R. O. Pohl. “Thermal boundary resistance”. In: *Reviews of Modern Physics* 61.3 (July 1989), pp. 605–668. doi: 10.1103/RevModPhys.61.605. URL: <http://link.aps.org/doi/10.1103/RevModPhys.61.605>.
- [12] Dunwei Wang et al. “Two-Dimensional Single-Crystal Nanowire Arrays”. en. In: *Small* 3.12 (2007), pp. 2043–2047. ISSN: 1613-6829. doi: 10.1002/sml1.200700279. URL: <http://onlinelibrary.wiley.com/doi/10.1002/sml1.200700279/abstract>.
- [13] James R. Heath. “Superlattice Nanowire Pattern Transfer (SNAP)”. In: *Accounts of Chemical Research* 41.12 (Dec. 2008), pp. 1609–1617. ISSN: 0001-4842. doi: 10.1021/ar800015y. URL: <http://dx.doi.org/10.1021/ar800015y>.
- [14] A. Shchepetov et al. “Ultra-thin free-standing single crystalline silicon membranes with strain control”. In: *Applied Physics Letters* 102.19 (May 2013), p. 192108. ISSN: 0003-6951, 1077-3118. doi: 10.1063/1.4807130. URL: <http://scitation.aip.org.clsproxy.library.caltech.edu/content/aip/journal/apl/102/19/10.1063/1.4807130>.
- [15] M. Asheghi et al. “Phonon-boundary scattering in thin silicon layers”. In: *Applied Physics Letters* 71.13 (Sept. 1997), pp. 1798–1800. ISSN: 0003-6951, 1077-3118. doi: 10.1063/1.119402. URL: <http://scitation.aip.org.clsproxy.library.caltech.edu/content/aip/journal/apl/71/13/10.1063/1.119402>.
- [16] Y. S. Ju and K. E. Goodson. “Phonon scattering in silicon films with thickness of order 100 nm”. In: *Applied Physics Letters* 74.20 (May 1999), pp. 3005–3007. ISSN: 0003-6951, 1077-3118. doi: 10.1063/1.123994. URL: <http://scitation.aip.org.clsproxy.library.caltech.edu/content/aip/journal/apl/74/20/10.1063/1.123994>.
- [17] M. Asheghi et al. “Thermal conduction in doped single-crystal silicon films”. In: *Journal of Applied Physics* 91.8 (Apr. 2002), pp. 5079–5088. ISSN: 0021-8979, 1089-7550. doi: 10.1063/1.1458057. URL: <http://scitation>.

aip.org.clsproxy.library.caltech.edu/content/aip/journal/jap/91/8/10.1063/1.1458057.

- [18] W. Liu and M. Asheghi. “Phonon–boundary scattering in ultrathin single-crystal silicon layers”. In: *Applied Physics Letters* 84.19 (May 2004), pp. 3819–3821. ISSN: 0003-6951, 1077-3118. DOI: 10.1063/1.1741039. URL: <http://scitation.aip.org.clsproxy.library.caltech.edu/content/aip/journal/apl/84/19/10.1063/1.1741039>.
- [19] Wenjun Liu and Mehdi Asheghi. “Thermal conduction in ultrathin pure and doped single-crystal silicon layers at high temperatures”. In: *Journal of Applied Physics* 98.12 (Dec. 2005), p. 123523. ISSN: 0021-8979, 1089-7550. DOI: 10.1063/1.2149497. URL: <http://scitation.aip.org.clsproxy.library.caltech.edu/content/aip/journal/jap/98/12/10.1063/1.2149497>.
- [20] A. J. Minnich. “Determining Phonon Mean Free Paths from Observations of Quasiballistic Thermal Transport”. In: *Physical Review Letters* 109.20 (Nov. 2012), p. 205901. DOI: 10.1103/PhysRevLett.109.205901. URL: <http://link.aps.org/doi/10.1103/PhysRevLett.109.205901>.
- [21] Jeremy A. Johnson et al. “Direct Measurement of Room-Temperature Non-diffusive Thermal Transport Over Micron Distances in a Silicon Membrane”. In: *Physical Review Letters* 110.2 (Jan. 2013), p. 025901. DOI: 10.1103/PhysRevLett.110.025901. URL: <http://link.aps.org/doi/10.1103/PhysRevLett.110.025901>.
- [22] A. A. Maznev et al. “Lifetime of high-order thickness resonances of thin silicon membranes”. In: *Ultrasonics* 56 (Feb. 2015), pp. 116–121. ISSN: 0041-624X. DOI: 10.1016/j.ultras.2014.02.016. URL: <http://www.sciencedirect.com/science/article/pii/S0041624X1400047X>.
- [23] John Cuffe et al. “Reconstructing phonon mean-free-path contributions to thermal conductivity using nanoscale membranes”. In: *Physical Review B* 91.24 (June 2015), p. 245423. DOI: 10.1103/PhysRevB.91.245423. URL: <http://link.aps.org/doi/10.1103/PhysRevB.91.245423>.
- [24] T. S. Tighe, J. M. Worlock, and M. L. Roukes. “Direct thermal conductance measurements on suspended monocrystalline nanostructures”. In: *Applied Physics Letters* 70.20 (May 1997), pp. 2687–2689. ISSN: 0003-6951, 1077-3118. DOI: 10.1063/1.118994. URL: <http://scitation.aip.org.clsproxy.library.caltech.edu/content/aip/journal/apl/70/20/10.1063/1.118994>.
- [25] K. Schwab et al. “Measurement of the quantum of thermal conductance”. In: *Nature* 404.6781 (Apr. 2000), pp. 974–977. ISSN: 0028-0836. DOI: 10.1038/35010065. URL: <http://www.nature.com.clsproxy.library.caltech.edu/nature/journal/v404/n6781/abs/404974a0.html>.

- [26] Kedar Hippalgaonkar et al. “Fabrication of Microdevices with Integrated Nanowires for Investigating Low-Dimensional Phonon Transport”. In: *Nano Letters* 10.11 (Nov. 2010), pp. 4341–4348. ISSN: 1530-6984. DOI: 10.1021/nl101671r. URL: <http://dx.doi.org/10.1021/nl101671r>.
- [27] Jongwoo Lim et al. “Quantifying surface roughness effects on phonon transport in silicon nanowires”. In: *Nano letters* 12.5 (2012), pp. 2475–2482.
- [28] Renkun Chen et al. “Thermal Conductance of Thin Silicon Nanowires”. In: *Physical Review Letters* 101.10 (Sept. 2008), p. 105501. DOI: 10.1103/PhysRevLett.101.105501. URL: <http://link.aps.org/doi/10.1103/PhysRevLett.101.105501>.
- [29] Jen-Kan Yu et al. “Reduction of thermal conductivity in phononic nanomesh structures”. en. In: *Nature Nanotechnology* 5.10 (Oct. 2010), pp. 718–721. ISSN: 1748-3387. DOI: 10.1038/nnano.2010.149. URL: <http://www.nature.com/nano/journal/v5/n10/full/nnano.2010.149.html>.
- [30] Akram I. Boukai et al. “Silicon nanowires as efficient thermoelectric materials”. en. In: *Nature* 451.7175 (Jan. 2008), pp. 168–171. ISSN: 0028-0836. DOI: 10.1038/nature06458. URL: <http://www.nature.com/nature/journal/v451/n7175/full/nature06458.html>.
- [31] H.B.G. Casimir. “Note on the conduction of heat in crystals”. In: *Physica* 5.6 (June 1938), pp. 495–500. ISSN: 0031-8914. DOI: 10.1016/S0031-8914(38)80162-2. URL: <http://www.sciencedirect.com/science/article/pii/S0031891438801622>.
- [32] Joseph Callaway. “Model for Lattice Thermal Conductivity at Low Temperatures”. In: *Physical Review* 113.4 (Feb. 1959), pp. 1046–1051. DOI: 10.1103/PhysRev.113.1046. URL: <http://link.aps.org/doi/10.1103/PhysRev.113.1046>.
- [33] M. G. Holland. “Analysis of Lattice Thermal Conductivity”. In: *Physical Review* 132.6 (Dec. 1963), pp. 2461–2471. DOI: 10.1103/PhysRev.132.2461. URL: <http://link.aps.org/doi/10.1103/PhysRev.132.2461>.
- [34] P. G. Klemens. “The Scattering of Low-Frequency Lattice Waves by Static Imperfections”. en. In: *Proceedings of the Physical Society. Section A* 68.12 (1955), p. 1113. ISSN: 0370-1298. DOI: 10.1088/0370-1298/68/12/303. URL: <http://stacks.iop.org/0370-1298/68/i=12/a=303>.
- [35] K. Fuchs. “The conductivity of thin metallic films according to the electron theory of metals”. In: *Mathematical Proceedings of the Cambridge Philosophical Society* 34.01 (Jan. 1938), pp. 100–108. ISSN: 1469-8064. DOI: 10.1017/S0305004100019952. URL: http://journals.cambridge.org/article_S0305004100019952.

- [36] G. E. H. Reuter and E. H. Sondheimer. “The Theory of the Anomalous Skin Effect in Metals”. In: *Proceedings of the Royal Society of London. Series A, Mathematical and Physical Sciences* 195.1042 (Dec. 1948), pp. 336–364. ISSN: 0080-4630. URL: <http://www.jstor.org/stable/98333>.
- [37] Gang Chen. *Nanoscale Heat Transfer and Energy Conversion*. 2007.
- [38] J. E. Turney, A. J. H. McGaughey, and C. H. Amon. “In-plane phonon transport in thin films”. In: *Journal of Applied Physics* 107.2 (Jan. 2010), pages. ISSN: 00218979. DOI: doi:10.1063/1.3296394. URL: http://jap.aip.org/resource/1/japiau/v107/i2/p024317_s1.
- [39] D. P. Sellan et al. “Cross-plane phonon transport in thin films”. In: *Journal of Applied Physics* 108.11 (Dec. 2010), pages. ISSN: 00218979. DOI: doi:10.1063/1.3517158. URL: http://jap.aip.org/resource/1/japiau/v108/i11/p113524_s1.
- [40] Alan J. H. McGaughey and Ankit Jain. “Nanostructure thermal conductivity prediction by Monte Carlo sampling of phonon free paths”. In: *Applied Physics Letters* 100.6 (Feb. 2012), pages. ISSN: 00036951. DOI: doi:10.1063/1.3683539. URL: http://apl.aip.org/resource/1/applab/v100/i6/p061911_s1.
- [41] Ankit Jain, Ying-Ju Yu, and Alan J. H. McGaughey. “Phonon transport in periodic silicon nanoporous films with feature sizes greater than 100 nm”. In: *Physical Review B* 87.19 (May 2013), p. 195301. DOI: 10.1103/PhysRevB.87.195301. URL: <http://link.aps.org/doi/10.1103/PhysRevB.87.195301>.
- [42] Jean-Philippe M. Péraud and Nicolas G. Hadjiconstantinou. “Efficient simulation of multidimensional phonon transport using energy-based variance-reduced Monte Carlo formulations”. In: *Physical Review B* 84.20 (Nov. 2011), p. 205331. DOI: 10.1103/PhysRevB.84.205331. URL: <http://link.aps.org/doi/10.1103/PhysRevB.84.205331>.
- [43] Jean-Philippe M. Péraud and Nicolas G. Hadjiconstantinou. “An alternative approach to efficient simulation of micro/nanoscale phonon transport”. In: *Applied Physics Letters* 101.15 (2012), pages. ISSN: 0003-6951. DOI: 10.1063/1.4757607.
- [44] Colin D. Landon and Nicolas G. Hadjiconstantinou. “Deviational simulation of phonon transport in graphene ribbons with ab initio scattering”. In: *Journal of Applied Physics* 116.16 (Oct. 2014), p. 163502. ISSN: 0021-8979, 1089-7550. DOI: 10.1063/1.4898090. URL: <http://scitation.aip.org.clsproxy.library.caltech.edu/content/aip/journal/jap/116/16/10.1063/1.4898090>.
- [45] Z. Aksamija and I. Knezevic. “Anisotropy and boundary scattering in the lattice thermal conductivity of silicon nanomembranes”. In: *Physical Re-*

- view B* 82.4 (July 2010), p. 045319. doi: 10.1103/PhysRevB.82.045319. URL: <http://link.aps.org/doi/10.1103/PhysRevB.82.045319>.
- [46] Sanghamitra Neogi et al. “Tuning thermal transport in ultrathin silicon membranes by surface nanoscale engineering”. In: *ACS nano* 9.4 (2015), pp. 3820–3828.
- [47] Pierre Martin et al. “Impact of Phonon-Surface Roughness Scattering on Thermal Conductivity of Thin Si Nanowires”. In: *Physical Review Letters* 102.12 (Mar. 2009), p. 125503. doi: 10.1103/PhysRevLett.102.125503. URL: <http://link.aps.org/doi/10.1103/PhysRevLett.102.125503>.
- [48] Jie Zou and Alexander Balandin. “Phonon heat conduction in a semiconductor nanowire”. In: *Journal of Applied Physics* 89.5 (Mar. 2001), pp. 2932–2938. ISSN: 0021-8979, 1089-7550. doi: 10.1063/1.1345515. URL: <http://scitation.aip.org.clsproxy.library.caltech.edu/content/aip/journal/jap/89/5/10.1063/1.1345515>.
- [49] Jyothi Sadhu and Sanjiv Sinha. “Room-temperature phonon boundary scattering below the Casimir limit”. In: *Physical Review B* 84.11 (Sept. 2011), p. 115450. doi: 10.1103/PhysRevB.84.115450. URL: <http://link.aps.org/doi/10.1103/PhysRevB.84.115450>.
- [50] A. A. Maznev. “Boundary scattering of phonons: Specularity of a randomly rough surface in the small-perturbation limit”. In: *Physical Review B* 91.13 (Apr. 2015), p. 134306. doi: 10.1103/PhysRevB.91.134306. URL: <http://link.aps.org/doi/10.1103/PhysRevB.91.134306>.
- [51] Jared B. Hertzberg et al. *Direct Measurements of Surface Scattering in Si Nanosheets Using a Microscale Phonon Spectrometer: Implications for Casimir-Limit Predicted by Ziman Theory*. EN. rapid-communication. Jan. 2014. URL: <http://pubs.acs.org.clsproxy.library.caltech.edu/doi/abs/10.1021/nl402701a>.
- [52] David G. Cahill et al. “Nanoscale thermal transport”. In: *Journal of Applied Physics* 93.2 (Jan. 2003), p. 793. ISSN: 00218979. doi: doi:10.1063/1.1524305. URL: http://jap.aip.org/resource/1/japiau/v93/i2/p793_s1.
- [53] M. Zebarjadi et al. “Perspectives on thermoelectrics: from fundamentals to device applications”. en. In: *Energy Environ. Sci.* 5.1 (2012), pp. 5147–5162. ISSN: 1754-5692, 1754-5706. doi: 10.1039/C1EE02497C. URL: <http://xlink.rsc.org/?DOI=C1EE02497C>.
- [54] Joseph P. Heremans et al. “When thermoelectrics reached the nanoscale”. en. In: *Nature Nanotechnology* 8.7 (July 2013), pp. 471–473. ISSN: 1748-3387. doi: 10.1038/nnano.2013.129. URL: <http://www.nature.com.clsproxy.library.caltech.edu/nnano/journal/v8/n7/full/nnano.2013.129.html>.

- [55] Ihtesham Chowdhury et al. “On-chip cooling by superlattice-based thin-film thermoelectrics”. en. In: *Nature Nanotechnology* 4.4 (Apr. 2009), pp. 235–238. ISSN: 1748-3387. DOI: 10.1038/nnano.2008.417. URL: <http://www.nature.com.clsproxy.library.caltech.edu/nnano/journal/v4/n4/abs/nnano.2008.417.html>.
- [56] Bed Poudel et al. “High-Thermoelectric Performance of Nanostructured Bismuth Antimony Telluride Bulk Alloys”. en. In: *Science* 320.5876 (May 2008), pp. 634–638. ISSN: 0036-8075, 1095-9203. DOI: 10.1126/science.1156446. URL: <http://www.sciencemag.org/content/320/5876/634>.
- [57] Rutvik J. Mehta et al. “A new class of doped nanobulk high-figure-of-merit thermoelectrics by scalable bottom-up assembly”. en. In: *Nature Materials* 11.3 (Mar. 2012), pp. 233–240. ISSN: 1476-1122. DOI: 10.1038/nmat3213. URL: <http://www.nature.com.clsproxy.library.caltech.edu/nmat/journal/v11/n3/full/nmat3213.html>.
- [58] J. Ma et al. “Glass-like phonon scattering from a spontaneous nanostructure in AgSbTe₂”. en. In: *Nature Nanotechnology* 8.6 (June 2013), pp. 445–451. ISSN: 1748-3387. DOI: 10.1038/nnano.2013.95. URL: <http://www.nature.com.clsproxy.library.caltech.edu/nnano/journal/v8/n6/full/nnano.2013.95.html>.
- [59] Kanishka Biswas et al. “High-performance bulk thermoelectrics with all-scale hierarchical architectures”. en. In: *Nature* 489.7416 (Sept. 2012), pp. 414–418. ISSN: 0028-0836. DOI: 10.1038/nature11439. URL: <http://www.nature.com.clsproxy.library.caltech.edu/nature/journal/v489/n7416/abs/nature11439.html>.
- [60] Kanishka Biswas et al. “Strained endotaxial nanostructures with high thermoelectric figure of merit”. en. In: *Nature Chemistry* 3.2 (Feb. 2011), pp. 160–166. ISSN: 1755-4330. DOI: 10.1038/nchem.955. URL: <http://www.nature.com.clsproxy.library.caltech.edu/nchem/journal/v3/n2/full/nchem.955.html>.
- [61] Maria N. Luckyanova et al. “Coherent Phonon Heat Conduction in Superlattices”. en. In: *Science* 338.6109 (Nov. 2012), pp. 936–939. ISSN: 0036-8075, 1095-9203. DOI: 10.1126/science.1225549. URL: <http://www.sciencemag.org/content/338/6109/936>.
- [62] Jyothi Sadhu, Myunghoon Seong, and Sanjiv Sinha. “Partially coherent phonon transport in two-dimensionally rough nanowires”. en. In: *Journal of Computational Electronics* 11.1 (Jan. 2012), pp. 1–7. ISSN: 1569-8025, 1572-8137. DOI: 10.1007/s10825-012-0382-2. URL: <http://link.springer.com/article/10.1007/s10825-012-0382-2>.

- [63] Martin Maldovan. “Narrow Low-Frequency Spectrum and Heat Management by Thermocrystals”. In: *Physical Review Letters* 110.2 (Jan. 2013), p. 025902. doi: 10.1103/PhysRevLett.110.025902. URL: <http://link.aps.org/doi/10.1103/PhysRevLett.110.025902>.
- [64] Martin Maldovan. “Sound and heat revolutions in phononics”. en. In: *Nature* 503.7475 (Nov. 2013), pp. 209–217. ISSN: 0028-0836. doi: 10.1038/nature12608. URL: <http://www.nature.com.clsproxy.library.caltech.edu/nature/journal/v503/n7475/full/nature12608.html>.
- [65] Jayakanth Ravichandran et al. “Crossover from incoherent to coherent phonon scattering in epitaxial oxide superlattices”. en. In: *Nature Materials* 13.2 (Feb. 2014), pp. 168–172. ISSN: 1476-1122. doi: 10.1038/nmat3826. URL: <http://www.nature.com.clsproxy.library.caltech.edu/nmat/journal/v13/n2/full/nmat3826.html>.
- [66] C. Colvard et al. “Observation of Folded Acoustic Phonons in a Semiconductor Superlattice”. In: *Physical Review Letters* 45.4 (July 1980), pp. 298–301. doi: 10.1103/PhysRevLett.45.298. URL: <http://link.aps.org/doi/10.1103/PhysRevLett.45.298>.
- [67] Alexander Balandin and Kang L. Wang. “Significant decrease of the lattice thermal conductivity due to phonon confinement in a free-standing semiconductor quantum well”. In: *Physical Review B* 58.3 (July 1998), pp. 1544–1549. doi: 10.1103/PhysRevB.58.1544. URL: <http://link.aps.org/doi/10.1103/PhysRevB.58.1544>.
- [68] B. Yang and G. Chen. “Partially coherent phonon heat conduction in superlattices”. In: *Physical Review B* 67.19 (May 2003), p. 195311. doi: 10.1103/PhysRevB.67.195311. URL: <http://link.aps.org/doi/10.1103/PhysRevB.67.195311>.
- [69] Patrick E. Hopkins et al. “Reduction in the Thermal Conductivity of Single Crystalline Silicon by Phononic Crystal Patterning”. In: *Nano Letters* 11.1 (Jan. 2011), pp. 107–112. ISSN: 1530-6984. doi: 10.1021/nl102918q. URL: <http://dx.doi.org/10.1021/nl102918q>.
- [70] Qing Hao, Gang Chen, and Ming-Shan Jeng. “Frequency-dependent Monte Carlo simulations of phonon transport in two-dimensional porous silicon with aligned pores”. In: *Journal of Applied Physics* 106.11 (Dec. 2009), p. 114321. ISSN: 00218979. doi: doi:10.1063/1.3266169. URL: http://jap.aip.org/resource/1/japiau/v106/i11/p114321_s1.
- [71] Yuping He et al. “Thermal Transport in Nanoporous Silicon: Interplay between Disorder at Mesoscopic and Atomic Scales”. In: *ACS Nano* 5.3 (Mar. 2011), pp. 1839–1844. ISSN: 1936-0851. doi: 10.1021/nn2003184. URL: <http://dx.doi.org/10.1021/nn2003184>.

- [72] Edward Dechaumphai and Renkun Chen. “Thermal transport in phononic crystals: The role of zone folding effect”. In: *Journal of Applied Physics* 111.7 (Apr. 2012), p. 073508. ISSN: 00218979. DOI: doi : 10 . 1063 / 1 . 3699056. URL: http://jap.aip.org/resource/1/japiau/v111/i7/p073508_s1.
- [73] A. Majumdar. “Microscale Heat Conduction in Dielectric Thin Films”. In: *Journal of Heat Transfer* 115.1 (Feb. 1993), pp. 7–16. ISSN: 0022-1481. DOI: 10.1115/1.2910673. URL: <http://dx.doi.org/10.1115/1.2910673>.
- [74] Ming-Shan Jeng et al. “Modeling the Thermal Conductivity and Phonon Transport in Nanoparticle Composites Using Monte Carlo Simulation”. In: *Journal of Heat Transfer* 130.4 (Mar. 2008), pp. 042410–042410. ISSN: 0022-1481. DOI: 10 . 1115 / 1 . 2818765. URL: <http://dx.doi.org/10.1115/1.2818765>.
- [75] Sreekant V. Narumanchi, Jayathi Y. Murthy, and Cristina H. Amon. “Comparison of Different Phonon Transport Models for Predicting Heat Conduction in Silicon-on-Insulator Transistors”. In: *Journal of Heat Transfer* 127.7 (Mar. 2005), pp. 713–723. ISSN: 0022-1481. DOI: 10 . 1115 / 1 . 1924571. URL: <http://dx.doi.org/10.1115/1.1924571>.
- [76] James M. Loy, Sanjay R. Mathur, and Jayathi Y. Murthy. “A Coupled Ordinates Method for Convergence Acceleration of the Phonon Boltzmann Transport Equation”. In: (Nov. 2012), pp. 2897–2911. DOI: 10 . 1115 / IMECE2012-89352. URL: <http://dx.doi.org/10.1115/IMECE2012-89352>.
- [77] A. J. Minnich et al. “Quasiballistic heat transfer studied using the frequency-dependent Boltzmann transport equation”. In: *Physical Review B* 84.23 (Dec. 2011), p. 235207. DOI: 10.1103/PhysRevB.84.235207. URL: <http://link.aps.org/doi/10.1103/PhysRevB.84.235207>.
- [78] A. A. Maznev et al. “Lifetime of sub-THz coherent acoustic phonons in a GaAs-AlAs superlattice”. In: *Applied Physics Letters* 102.4 (Jan. 2013), p. 041901. ISSN: 0003-6951, 1077-3118. DOI: 10 . 1063 / 1 . 4789520. URL: <http://scitation.aip.org.clsproxy.library.caltech.edu/content/aip/journal/apl/102/4/10.1063/1.4789520>.
- [79] Jinyao Tang et al. “Holey Silicon as an Efficient Thermoelectric Material”. In: *Nano Letters* 10.10 (Oct. 2010), pp. 4279–4283. ISSN: 1530-6984, 1530-6992. DOI: 10 . 1021 / nl102931z. URL: <http://pubs.acs.org/doi/abs/10.1021/nl102931z>.
- [80] David Song and Gang Chen. “Thermal conductivity of periodic microporous silicon films”. In: *Applied Physics Letters* 84.5 (Feb. 2004), pp. 687–689. ISSN: 0003-6951, 1077-3118. DOI: 10 . 1063 / 1 . 1642753. URL: <http://scitation.aip.org.clsproxy.library.caltech.edu/content/aip/journal/apl/84/5/10.1063/1.1642753>.

- [81] E. Lampin et al. “Thermal boundary resistance at silicon-silica interfaces by molecular dynamics simulations”. In: *Applied Physics Letters* 100.13 (Mar. 2012), p. 131906. ISSN: 00036951. DOI: doi : 10 . 1063 / 1 . 3698325. URL: http://apl.aip.org/resource/1/applab/v100/i13/p131906_s1.
- [82] Arden L. Moore et al. “Phonon backscattering and thermal conductivity suppression in sawtooth nanowires”. In: *Applied Physics Letters* 93.8 (2008), p. 083112. ISSN: 00036951. DOI: 10 . 1063 / 1 . 2970044. URL: <http://link.aip.org/link/APPLAB/v93/i8/p083112/s1&Agg=doi>.
- [83] Aaron J. Schmidt. *Optical characterization of thermal transport from the nanoscale to the macroscale*. 2008.
- [84] Kathleen M. Hoogeboom-Pot et al. “A new regime of nanoscale thermal transport: Collective diffusion increases dissipation efficiency”. en. In: *Proceedings of the National Academy of Sciences* 112.16 (Apr. 2015), pp. 4846–4851. ISSN: 0027-8424, 1091-6490. DOI: 10 . 1073 / pnas . 1503449112. URL: <http://www.pnas.org/content/112/16/4846>.
- [85] Jeremy A. Johnson. *Optical characterization of complex mechanical and thermal transport properties*. 2011.
- [86] Andrea Taschin et al. “Supercooled water relaxation dynamics probed with heterodyne transient grating experiments”. In: *Physical Review E* 74.3 (Sept. 2006), p. 031502. DOI: 10 . 1103 / PhysRevE . 74 . 031502. URL: <http://link.aps.org/doi/10.1103/PhysRevE.74.031502>.
- [87] Alexei A. Maznev, Jeremy A. Johnson, and Keith A. Nelson. “Onset of nondiffusive phonon transport in transient thermal grating decay”. In: *Physical Review B* 84.19 (2011), p. 195206. URL: <http://journals.aps.org/clsproxy.library.caltech.edu/prb/abstract/10.1103/PhysRevB.84.195206>.
- [88] Kimberlee C. Collins et al. “Non-diffusive relaxation of a transient thermal grating analyzed with the Boltzmann transport equation”. In: *Journal of Applied Physics* 114.10 (2013), p. 104302. URL: <http://scitation.aip.org/clsproxy.library.caltech.edu/content/aip/journal/jap/114/10/10.1063/1.4820572>.
- [89] Chengyun Hua and Austin J. Minnich. “Transport regimes in quasiballistic heat conduction”. In: *Physical Review B* 89.9 (Mar. 2014), p. 094302. DOI: 10 . 1103 / PhysRevB . 89 . 094302. URL: <http://link.aps.org/doi/10.1103/PhysRevB.89.094302>.
- [90] Jeremy A. Johnson et al. “Non-diffusive thermal transport in GaAs at micron length scales”. In: *Journal of Applied Physics* 118.15 (Oct. 2015), p. 155104. ISSN: 0021-8979, 1089-7550. DOI: 10 . 1063 / 1 . 4933285. URL: <http://scitation.aip.org/clsproxy.library.caltech.edu/content/aip/journal/jap/118/15/10.1063/1.4933285>.

- [91] R. O. Carlson, G. A. Slack, and S. J. Silverman. “Thermal Conductivity of GaAs and GaAs_{1-x}P_x Laser Semiconductors”. In: *Journal of Applied Physics* 36.2 (Feb. 1965), pp. 505–507. ISSN: 0021-8979, 1089-7550. DOI: 10.1063/1.1714018. URL: <http://scitation.aip.org.clsproxy.library.caltech.edu/content/aip/journal/jap/36/2/10.1063/1.1714018>.
- [92] Xiren Zhang, Bincheng Li, and Chunming Gao. “Electronic transport characterization of silicon wafers by laterally resolved free-carrier absorption and multiparameter fitting”. In: *Applied Physics Letters* 89.11 (Sept. 2006), p. 112120. ISSN: 0003-6951, 1077-3118. DOI: 10.1063/1.2354006. URL: <http://scitation.aip.org.clsproxy.library.caltech.edu/content/aip/journal/apl/89/11/10.1063/1.2354006>.
- [93] Jan Linnros and Vytautas Grivickas. “Carrier-diffusion measurements in silicon with a Fourier-transient-grating method”. In: *Physical Review B* 50.23 (Dec. 1994), pp. 16943–16955. DOI: 10.1103/PhysRevB.50.16943. URL: <http://link.aps.org/doi/10.1103/PhysRevB.50.16943>.
- [94] Chun-Mao Li, Theodore Sjodin, and Hai-Lung Dai. “Photoexcited carrier diffusion near a Si(111) surface: Non-negligible consequence of carrier-carrier scattering”. In: *Physical Review B* 56.23 (Dec. 1997), pp. 15252–15255. DOI: 10.1103/PhysRevB.56.15252. URL: <http://link.aps.org/doi/10.1103/PhysRevB.56.15252>.
- [95] David G. Cahill et al. “Nanoscale thermal transport. II. 2003–2012”. In: *Applied Physics Reviews* 1.1 (Mar. 2014), p. 011305. ISSN: 1931-9401. DOI: 10.1063/1.4832615. URL: <http://scitation.aip.org/content/aip/journal/apr2/1/1/10.1063/1.4832615>.
- [96] Jungwan Cho et al. “Phonon scattering in strained transition layers for GaN heteroepitaxy”. In: *Physical Review B* 89.11 (Mar. 2014), p. 115301. DOI: 10.1103/PhysRevB.89.115301. URL: <http://link.aps.org/doi/10.1103/PhysRevB.89.115301>.
- [97] Zhong Yan et al. “Graphene quilts for thermal management of high-power GaN transistors”. en. In: *Nature Communications* 3 (May 2012), p. 827. DOI: 10.1038/ncomms1828. URL: <http://www.nature.com/ncomms/journal/v3/n5/full/ncomms1828.html>.
- [98] Yee Kan Koh et al. “Heat-Transport Mechanisms in Superlattices”. en. In: *Advanced Functional Materials* 19.4 (Feb. 2009), pp. 610–615. ISSN: 1616-3028. DOI: 10.1002/adfm.200800984. URL: <http://onlinelibrary.wiley.com/doi/10.1002/adfm.200800984/abstract>.
- [99] Sandip Mazumder and Arunava Majumdar. “Monte Carlo Study of Phonon Transport in Solid Thin Films Including Dispersion and Polarization”. In: *Journal of Heat Transfer* 123.4 (Jan. 2001), pp. 749–759. ISSN: 0022-1481.

- doi: 10.1115/1.1377018. URL: <http://dx.doi.org/10.1115/1.1377018>.
- [100] Navaneetha K. Ravichandran and Austin J. Minnich. “Coherent and incoherent thermal transport in nanomeshes”. In: *Physical Review B* 89.20 (May 2014), p. 205432. doi: 10.1103/PhysRevB.89.205432. URL: <http://link.aps.org/doi/10.1103/PhysRevB.89.205432>.
- [101] Deyu Li et al. “Thermal conductivity of individual silicon nanowires”. In: *Applied Physics Letters* 83.14 (Oct. 2003), pp. 2934–2936. ISSN: 0003-6951, 1077-3118. doi: 10.1063/1.1616981. URL: <http://scitation.aip.org.clsproxy.library.caltech.edu/content/aip/journal/apl/83/14/10.1063/1.1616981>.
- [102] A. J. Minnich. “Multidimensional quasiballistic thermal transport in transient grating spectroscopy”. In: *Physical Review B* 92.8 (Aug. 2015), p. 085203. doi: 10.1103/PhysRevB.92.085203. URL: <http://link.aps.org/doi/10.1103/PhysRevB.92.085203>.
- [103] Chengyun Hua and Austin J. Minnich. “Analytical Green’s function of the multidimensional frequency-dependent phonon Boltzmann equation”. In: *Physical Review B* 90.21 (Dec. 2014), p. 214306. doi: 10.1103/PhysRevB.90.214306. URL: <http://link.aps.org/doi/10.1103/PhysRevB.90.214306>.
- [104] Chengyun Hua and Austin J. Minnich. “Semi-analytical solution to the frequency-dependent Boltzmann transport equation for cross-plane heat conduction in thin films”. In: *Journal of Applied Physics* 117.17 (May 2015), p. 175306. ISSN: 0021-8979, 1089-7550. doi: 10.1063/1.4919432. URL: <http://scitation.aip.org/content/aip/journal/jap/117/17/10.1063/1.4919432>.
- [105] Taofang Zeng and Gang Chen. “Phonon Heat Conduction in Thin Films: Impacts of Thermal Boundary Resistance and Internal Heat Generation”. In: *Journal of Heat Transfer* 123.2 (Nov. 2000), pp. 340–347. ISSN: 0022-1481. doi: 10.1115/1.1351169. URL: <http://dx.doi.org/10.1115/1.1351169>.
- [106] Jean-Philippe M. Peraud, Colin D. Landon, and Nicolas G. Hadjiconstantinou. “MONTE CARLO METHODS FOR SOLVING THE BOLTZMANN TRANSPORT EQUATION”. en. In: *Annual Review of Heat Transfer* 17.N/A (2014), pp. 205–265. ISSN: 1049-0787. doi: 10.1615/AnnualRevHeatTransfer.2014007381. URL: <http://www.dl.begellhouse.com/references/5756967540dd1b03,7deb9f2f1087a9e3,1d883b612ccfafde.html>.
- [107] N. Mingo et al. “Ab Initio Thermal Transport”. en. In: *Length-Scale Dependent Phonon Interactions*. Ed. by Subhash L. Shindé and Gyaneshwar P. Srivastava. Topics in Applied Physics 128. DOI: 10.1007/978-1-4614-8651-0_5. Springer New York, 2014, pp. 137–173. ISBN: 978-1-4614-8650-

- 3 978-1-4614-8651-0. URL: http://link.springer.com/chapter/10.1007/978-1-4614-8651-0_5.
- [108] Wu Li et al. “Thermal conductivity of diamond nanowires from first principles”. In: *Physical Review B* 85.19 (May 2012), p. 195436. DOI: 10.1103/PhysRevB.85.195436. URL: <http://link.aps.org/doi/10.1103/PhysRevB.85.195436>.
- [109] Wu Li et al. “ShengBTE: A solver of the Boltzmann transport equation for phonons”. In: *Computer Physics Communications* 185.6 (June 2014), pp. 1747–1758. ISSN: 0010-4655. DOI: 10.1016/j.cpc.2014.02.015. URL: <http://www.sciencedirect.com/science/article/pii/S0010465514000484>.
- [110] *Welcome to phonopy — Phonopy v.1.9.7*. URL: <http://phonopy.sourceforge.net/>.
- [111] G. Kresse and J. Hafner. “{Ab initio} molecular dynamics for open-shell transition metals”. In: *Physical Review B* 48.17 (Nov. 1993), pp. 13115–13118. DOI: 10.1103/PhysRevB.48.13115. URL: <http://link.aps.org/doi/10.1103/PhysRevB.48.13115>.
- [112] G. Kresse and J. Hafner. “{Ab initio} molecular-dynamics simulation of the liquid-metal-{}amorphous-semiconductor transition in germanium”. In: *Physical Review B* 49.20 (May 1994), pp. 14251–14269. DOI: 10.1103/PhysRevB.49.14251. URL: <http://link.aps.org/doi/10.1103/PhysRevB.49.14251>.
- [113] G. Kresse and J. Furthmüller. “Efficiency of ab-initio total energy calculations for metals and semiconductors using a plane-wave basis set”. In: *Computational Materials Science* 6.1 (July 1996), pp. 15–50. ISSN: 0927-0256. DOI: 10.1016/0927-0256(96)00008-0. URL: <http://www.sciencedirect.com/science/article/pii/0927025696000080>.
- [114] G. Kresse and J. Furthmüller. “Efficient iterative schemes for {ab initio} total-energy calculations using a plane-wave basis set”. In: *Physical Review B* 54.16 (Oct. 1996), pp. 11169–11186. DOI: 10.1103/PhysRevB.54.11169. URL: <http://link.aps.org/doi/10.1103/PhysRevB.54.11169>.
- [115] G. E. Jellison Jr and F. A. Modine. “Optical absorption of silicon between 1.6 and 4.7 eV at elevated temperatures”. In: *Applied Physics Letters* 41.2 (July 1982), pp. 180–182. ISSN: 0003-6951, 1077-3118. DOI: 10.1063/1.93454. URL: <http://scitation.aip.org.clsproxy.library.caltech.edu/content/aip/journal/apl/41/2/10.1063/1.93454>.
- [116] Simon M Sze and Kwok K Ng. *Physics of semiconductor devices*. John Wiley & sons, 2006.

- [117] Jonathan R. Yates et al. “Spectral and Fermi surface properties from Wannier interpolation”. In: *Physical Review B* 75.19 (May 2007), p. 195121. doi: 10.1103/PhysRevB.75.195121. URL: <http://link.aps.org/doi/10.1103/PhysRevB.75.195121>.
- [118] Shin-ichiro Tamura. “Isotope scattering of dispersive phonons in Ge”. In: *Physical Review B* 27.2 (Jan. 1983), pp. 858–866. doi: 10.1103/PhysRevB.27.858. URL: <http://link.aps.org/doi/10.1103/PhysRevB.27.858>.
- [119] Houman Owhadi. *Lecture notes on Introduction to Stochastic Processes and Modeling*. California Institute of Technology, 2014.
- [120] Freeman Gilbert and Leon Knopoff. “Seismic scattering from topographic irregularities”. en. In: *Journal of Geophysical Research* 65.10 (Oct. 1960), pp. 3437–3444. ISSN: 2156-2202. doi: 10.1029/JZ065i010p03437. URL: <http://onlinelibrary.wiley.com.clsproxy.library.caltech.edu/doi/10.1029/JZ065i010p03437/abstract>.
- [121] J. A. Ogilvy. “Wave scattering from rough surfaces”. en. In: *Reports on Progress in Physics* 50.12 (1987), p. 1553. ISSN: 0034-4885. doi: 10.1088/0034-4885/50/12/001. URL: <http://stacks.iop.org/0034-4885/50/i=12/a=001>.
- [122] Hyungyu Jin et al. “Phonon-induced diamagnetic force and its effect on the lattice thermal conductivity”. en. In: *Nature Materials* 14.6 (June 2015), pp. 601–606. ISSN: 1476-1122. doi: 10.1038/nmat4247. URL: <http://www.nature.com.clsproxy.library.caltech.edu/nmat/journal/v14/n6/abs/nmat4247.html>.
- [123] K. Gofryk et al. “Anisotropic thermal conductivity in uranium dioxide”. en. In: *Nature Communications* 5 (Aug. 2014), p. 4551. doi: 10.1038/ncomms5551. URL: <http://www.nature.com/ncomms/2014/140801/ncomms5551/full/ncomms5551.html>.
- [124] Bolin Liao et al. “Significant Reduction of Lattice Thermal Conductivity by the Electron-Phonon Interaction in Silicon with High Carrier Concentrations: A First-Principles Study”. In: *Physical Review Letters* 114.11 (Mar. 2015), p. 115901. doi: 10.1103/PhysRevLett.114.115901. URL: <http://link.aps.org/doi/10.1103/PhysRevLett.114.115901>.
- [125] J Janušonis et al. “Transient Grating Spectroscopy in Magnetic Thin Films: Simultaneous Detection of Elastic and Magnetic Dynamics”. In: *Scientific Reports* 6 (2016).

Appendix A

**THE EFFECT OF FINITE LASER PENETRATION DEPTH ON
THE THERMAL TRANSPORT THROUGH THIN FILMS**

In this appendix, we describe the derivation for transient thermal transport in the TG experiment through thin membranes, considering finite penetration depth of the pump and probe lasers through the membrane.

A.1 Numerical Discretization of the Boundary Conditions

The general boundary conditions at the thin film walls are given by the following:

For $\mu \in (0, 1]$,

$$\begin{aligned} g_{\omega}^{+}(0, \mu, \phi) &= p_{\omega} g_{\omega}^{-}(0, -\mu, \phi) \\ &+ (1 - p_{\omega}) \left(\sigma_{\omega} g_{\omega}^0(\Delta T(z = 0)) - \frac{(1 - \sigma_{\omega})}{\pi} \int_0^{2\pi} \int_{-1}^0 g_{\omega}^{-}(0, \mu', \phi') \mu' d\mu' d\phi' \right) \\ &= p_{\omega} g_{\omega}^{-}(0, -\mu, \phi) \\ &+ (1 - p_{\omega}) \left(\sigma_{\omega} \frac{C_{\omega} \Delta T(z = 0)}{4\pi} - \frac{(1 - \sigma_{\omega})}{\pi} \int_0^{2\pi} \int_{-1}^0 g_{\omega}^{-}(0, \mu', \phi') \mu' d\mu' d\phi' \right) \end{aligned}$$

and for $\mu \in [-1, 0)$,

$$\begin{aligned} g_{\omega}^{-}(d, \mu, \phi) &= p_{\omega} g_{\omega}^{+}(d, -\mu, \phi) \\ &+ (1 - p_{\omega}) \left(\sigma_{\omega} g_{\omega}^0(\Delta T(z = d)) + \frac{(1 - \sigma_{\omega})}{\pi} \int_0^{2\pi} \int_0^1 g_{\omega}^{+}(d, \mu', \phi') \mu' d\mu' d\phi' \right) \\ &= p_{\omega} g_{\omega}^{+}(d, -\mu, \phi) \\ &+ (1 - p_{\omega}) \left(\sigma_{\omega} \frac{C_{\omega} \Delta T(z = d)}{4\pi} + \frac{(1 - \sigma_{\omega})}{\pi} \int_0^{2\pi} \int_0^1 g_{\omega}^{+}(d, \mu', \phi') \mu' d\mu' d\phi' \right) \end{aligned} \tag{A.1}$$

In the frequency domain, the boundary conditions (equation A.1) can be written as follows:

$$\begin{aligned}
 & \text{For } \mu \in (0, 1], \\
 & G_{\omega}^{+}(0, \mu, \phi) = p_{\omega} G_{\omega}^{-}(0, -\mu, \phi) \\
 & \quad + (1 - p_{\omega}) \left(\sigma_{\omega} \frac{C_{\omega} \Delta \bar{T}(z=0)}{4\pi} - \frac{(1 - \sigma_{\omega})}{\pi} \int_0^{2\pi} \int_{-1}^0 G_{\omega}^{-}(0, \mu', \phi') \mu' d\mu' d\phi' \right) \\
 & \text{and for } \mu \in [-1, 0), \\
 & G_{\omega}^{-}(d, \mu, \phi) = p_{\omega} G_{\omega}^{+}(d, -\mu, \phi) \\
 & \quad + (1 - p_{\omega}) \left(\sigma_{\omega} \frac{C_{\omega} \Delta \bar{T}(z=d)}{4\pi} + \frac{(1 - \sigma_{\omega})}{\pi} \int_0^{2\pi} \int_0^1 G_{\omega}^{+}(d, \mu', \phi') \mu' d\mu' d\phi' \right)
 \end{aligned} \tag{A.2}$$

For any given μ and ϕ , there are four unknown quantities to be determined at the thin film boundaries: $G_{\omega}^{+}(0, \mu, \phi)$, $G_{\omega}^{-}(0, -\mu, \phi)$, $G_{\omega}^{+}(d, -\mu, \phi)$, and $G_{\omega}^{-}(d, \mu, \phi)$, while there are only two equations which are directly evident (equation A.2). However, closed-form relations for these four unknown quantities can be obtained in terms of the unknown temperature distribution at the thin film boundaries in the frequency domain ($\Delta \bar{T}(z=0)$ and $\Delta \bar{T}(z=d)$) by substituting the general solution of the BTE (equation 5.16 in the main article) into boundary conditions (equation A.2) to get

the following:

For $\mu \in (0, 1]$,

$$\begin{aligned}
G_{\omega}^{+}(0, \mu, \phi) &= p_{\omega} G_{\omega}^{-}(d, -\mu, \phi) \exp\left(-\frac{\gamma_{\mu\phi}^{\text{FS}}}{\mu\Lambda_{\omega}} d\right) \\
&+ \frac{p_{\omega}}{4\pi\mu\Lambda_{\omega}} \int_0^d (C_{\omega}\Delta\bar{T} + \bar{Q}_{\omega}\tau_{\omega}) \exp\left(-\frac{\gamma_{\mu\phi}^{\text{FS}}}{\mu\Lambda_{\omega}} z'\right) dz' \\
&+ (1 - p_{\omega}) \left[\sigma_{\omega} \frac{C_{\omega}\Delta\bar{T}(z=0)}{4\pi} \right. \\
&- \frac{(1 - \sigma_{\omega})}{\pi} \int_0^{2\pi} \int_{-1}^0 G_{\omega}^{-}(d, \mu', \phi') \exp\left(\frac{\gamma_{\mu'\phi'}^{\text{FS}}}{\mu'\Lambda_{\omega}} d\right) \mu' d\mu' d\phi' \\
&\left. + \frac{(1 - \sigma_{\omega})}{4\pi^2\Lambda_{\omega}} \int_0^{2\pi} \int_{-1}^0 \int_0^d (C_{\omega}\Delta\bar{T} + \bar{Q}_{\omega}\tau_{\omega}) \exp\left(\frac{\gamma_{\mu'\phi'}^{\text{FS}}}{\mu'\Lambda_{\omega}} z'\right) dz' d\mu' d\phi' \right]
\end{aligned}$$

and for $\mu \in [-1, 0)$,

$$\begin{aligned}
G_{\omega}^{-}(d, \mu, \phi) &= p_{\omega} G_{\omega}^{+}(0, -\mu, \phi) \exp\left(\frac{\gamma_{\mu\phi}^{\text{FS}}}{\mu\Lambda_{\omega}} d\right) \\
&- \frac{p_{\omega} \exp\left(\frac{\gamma_{\mu\phi}^{\text{FS}}}{\mu\Lambda_{\omega}} d\right)}{4\pi\mu\Lambda_{\omega}} \int_0^d (C_{\omega}\Delta\bar{T} + \bar{Q}_{\omega}\tau_{\omega}) \exp\left(-\frac{\gamma_{\mu\phi}^{\text{FS}}}{\mu\Lambda_{\omega}} z'\right) dz' \\
&+ (1 - p_{\omega}) \left[\sigma_{\omega} \frac{C_{\omega}\Delta\bar{T}(z=d)}{4\pi} \right. \\
&+ \frac{(1 - \sigma_{\omega})}{\pi} \int_0^{2\pi} \int_0^1 G_{\omega}^{+}(0, \mu', \phi') \exp\left(-\frac{\gamma_{\mu'\phi'}^{\text{FS}}}{\mu'\Lambda_{\omega}} d\right) \mu' d\mu' d\phi' \\
&+ \frac{(1 - \sigma_{\omega})}{4\pi^2\Lambda_{\omega}} \int_0^{2\pi} \int_0^1 \exp\left(-\frac{\gamma_{\mu'\phi'}^{\text{FS}}}{\mu'\Lambda_{\omega}} d\right) \int_0^d (C_{\omega}\Delta\bar{T} + \bar{Q}_{\omega}\tau_{\omega}) \\
&\quad \times \exp\left(\frac{\gamma_{\mu'\phi'}^{\text{FS}}}{\mu'\Lambda_{\omega}} z'\right) dz' d\mu' d\phi' \left. \right]
\end{aligned}$$

(A.3)

For convenience, the limits on variables μ and μ' are changed from $[-1, 1]$ to $(0, 1]$ in equation A.3 wherever necessary to obtain

$$\begin{aligned}
G_{\omega}^{+}(0, \mu, \phi) &= p_{\omega} G_{\omega}^{-}(d, -\mu, \phi) \exp\left(-\frac{\gamma_{\mu\phi}^{\text{FS}}}{\mu\Lambda_{\omega}} d\right) \\
&+ \frac{p_{\omega}}{4\pi\mu\Lambda_{\omega}} \int_0^d (C_{\omega}\Delta\bar{T} + \bar{Q}_{\omega}\tau_{\omega}) \exp\left(-\frac{\gamma_{\mu\phi}^{\text{FS}}}{\mu\Lambda_{\omega}} z'\right) dz' \\
&+ (1 - p_{\omega}) \left[\sigma_{\omega} \frac{C_{\omega}\Delta\bar{T}(z=0)}{4\pi} \right. \\
&+ \frac{(1 - \sigma_{\omega})}{\pi} \int_0^{2\pi} \int_0^1 G_{\omega}^{-}(d, -\mu', \phi') \exp\left(-\frac{\gamma_{\mu'\phi'}^{\text{FS}}}{\mu'\Lambda_{\omega}} d\right) \mu' d\mu' d\phi' \\
&+ \left. \frac{(1 - \sigma_{\omega})}{4\pi^2\Lambda_{\omega}} \int_0^{2\pi} \int_0^1 \int_0^d (C_{\omega}\Delta\bar{T} + \bar{Q}_{\omega}\tau_{\omega}) \exp\left(-\frac{\gamma_{\mu'\phi'}^{\text{FS}}}{\mu'\Lambda_{\omega}} z'\right) dz' d\mu' d\phi' \right] \\
G_{\omega}^{-}(d, -\mu, \phi) &= p_{\omega} G_{\omega}^{+}(0, \mu, \phi) \exp\left(-\frac{\gamma_{\mu\phi}^{\text{FS}}}{\mu\Lambda_{\omega}} d\right) \\
&+ \frac{p_{\omega}}{4\pi\mu\Lambda_{\omega}} \int_0^d (C_{\omega}\Delta\bar{T} + \bar{Q}_{\omega}\tau_{\omega}) \exp\left(-\frac{\gamma_{\mu\phi}^{\text{FS}}}{\mu\Lambda_{\omega}} (d - z')\right) dz' \\
&+ (1 - p_{\omega}) \left[\sigma_{\omega} \frac{C_{\omega}\Delta\bar{T}(z=d)}{4\pi} \right. \\
&+ \frac{(1 - \sigma_{\omega})}{\pi} \int_0^{2\pi} \int_0^1 G_{\omega}^{+}(0, \mu', \phi') \exp\left(-\frac{\gamma_{\mu'\phi'}^{\text{FS}}}{\mu'\Lambda_{\omega}} d\right) \mu' d\mu' d\phi' \\
&+ \left. \frac{(1 - \sigma_{\omega})}{4\pi^2\Lambda_{\omega}} \int_0^{2\pi} \int_0^1 \int_0^d (C_{\omega}\Delta\bar{T} + \bar{Q}_{\omega}\tau_{\omega}) \exp\left(-\frac{\gamma_{\mu'\phi'}^{\text{FS}}}{\mu'\Lambda_{\omega}} (d - z')\right) dz' d\mu' d\phi' \right]
\end{aligned} \tag{A.4}$$

Equation A.4 represents a system of integral equations to solve for the two unknown quantities $G_{\omega}^{+}(0, \mu, \phi)$ and $G_{\omega}^{-}(d, -\mu, \phi)$ for every μ and ϕ . To solve this system of equations, the integrals in μ' and ϕ' variables are first discretized using Gauss quadrature,

$$\int_0^{2\pi} \int_0^1 f(\mu', \phi') d\mu' d\phi' = \sum_{ij} f(\mu_i, \phi_j) w_{\mu_i} w_{\phi_j} \tag{A.5}$$

where μ_i and ϕ_j are the quadrature points and w_{μ_i} and w_{ϕ_j} are the corresponding weights. Therefore, equation A.4 transforms into,

$$\begin{aligned}
G_{\omega}^{+}(0, \mu_i, \phi_j) &= p_{\omega} G_{\omega}^{-}(d, -\mu_i, \phi_j) \exp\left(-\frac{\gamma_{ij}^{\text{FS}}}{\mu_i \Lambda_{\omega}} d\right) \\
&+ \frac{p_{\omega}}{4\pi \mu_i \Lambda_{\omega}} \int_0^d (C_{\omega} \Delta \bar{T} + \bar{Q}_{\omega} \tau_{\omega}) \exp\left(-\frac{\gamma_{ij}^{\text{FS}}}{\mu_i \Lambda_{\omega}} z'\right) dz' \\
&+ (1 - p_{\omega}) \left[\sigma_{\omega} \frac{C_{\omega} \Delta \bar{T}(z=0)}{4\pi} \right. \\
&+ \frac{(1 - \sigma_{\omega})}{\pi} \sum_{i'j'} G_{\omega}^{-}(d, -\mu_{i'}, \phi_{j'}) \exp\left(-\frac{\gamma_{i'j'}^{\text{FS}}}{\mu_{i'} \Lambda_{\omega}} d\right) \mu_{i'} w_{\mu_{i'}} w_{\phi_{j'}} \\
&+ \left. \frac{(1 - \sigma_{\omega})}{4\pi^2 \Lambda_{\omega}} \sum_{i'j'} \int_0^d (C_{\omega} \Delta \bar{T} + \bar{Q}_{\omega} \tau_{\omega}) \exp\left(-\frac{\gamma_{i'j'}^{\text{FS}}}{\mu_{i'} \Lambda_{\omega}} z'\right) dz' w_{\mu_{i'}} w_{\phi_{j'}} \right] \\
G_{\omega}^{-}(d, -\mu_i, \phi_j) &= p_{\omega} G_{\omega}^{+}(0, \mu_i, \phi_j) \exp\left(-\frac{\gamma_{ij}^{\text{FS}}}{\mu_i \Lambda_{\omega}} d\right) \\
&+ \frac{p_{\omega}}{4\pi \mu_i \Lambda_{\omega}} \int_0^d (C_{\omega} \Delta \bar{T} + \bar{Q}_{\omega} \tau_{\omega}) \exp\left(-\frac{\gamma_{ij}^{\text{FS}}}{\mu_i \Lambda_{\omega}} (d - z')\right) dz' \\
&+ (1 - p_{\omega}) \left[\sigma_{\omega} \frac{C_{\omega} \Delta \bar{T}(z=d)}{4\pi} \right. \\
&+ \frac{(1 - \sigma_{\omega})}{\pi} \sum_{i'j'} G_{\omega}^{+}(0, \mu_{i'}, \phi_{j'}) \exp\left(-\frac{\gamma_{i'j'}^{\text{FS}}}{\mu_{i'} \Lambda_{\omega}} d\right) \mu_{i'} w_{\mu_{i'}} w_{\phi_{j'}} \\
&+ \frac{(1 - \sigma_{\omega})}{4\pi^2 \Lambda_{\omega}} \sum_{i'j'} \int_0^d (C_{\omega} \Delta \bar{T} + \bar{Q}_{\omega} \tau_{\omega}) \exp\left(-\frac{\gamma_{i'j'}^{\text{FS}}}{\mu_{i'} \Lambda_{\omega}} (d - z')\right) dz' \\
&\left. \times w_{\mu_{i'}} w_{\phi_{j'}} \right] \tag{A.6}
\end{aligned}$$

To simplify these expressions, we substitute the following into equation A.6:

$$\begin{aligned}
I_{\mu\phi}^+ &= \int_0^d (C_\omega \Delta \bar{T} + \bar{Q}_\omega \tau_\omega) \exp\left(-\frac{\gamma_{\mu\phi}^{\text{FS}}}{\mu\Lambda_\omega} z'\right) dz' \\
&= C_\omega \int_0^d \Delta \bar{T} \exp\left(-\frac{\gamma_{\mu\phi}^{\text{FS}}}{\mu\Lambda_\omega} z'\right) dz' + \frac{\bar{Q}_\omega^0 \tau_\omega}{\beta_p + \frac{\gamma_{\mu\phi}^{\text{FS}}}{\mu\Lambda_\omega}} \left(1 - \exp\left(-\left[\beta_p + \frac{\gamma_{\mu\phi}^{\text{FS}}}{\mu\Lambda_\omega}\right] d\right)\right) \\
I_{\mu\phi}^- &= \int_0^d (C_\omega \Delta \bar{T} + \bar{Q}_\omega \tau_\omega) \exp\left(-\frac{\gamma_{\mu\phi}^{\text{FS}}}{\mu\Lambda_\omega} (d - z')\right) dz' \\
&= C_\omega \int_0^d \Delta \bar{T} \exp\left(-\frac{\gamma_{\mu\phi}^{\text{FS}}}{\mu\Lambda_\omega} (d - z')\right) dz' \\
&\quad + \frac{\bar{Q}_\omega^0 \tau_\omega}{\beta_p - \frac{\gamma_{\mu\phi}^{\text{FS}}}{\mu\Lambda_\omega}} \left(\exp\left(-\frac{\gamma_{\mu\phi}^{\text{FS}}}{\mu\Lambda_\omega} d\right) - \exp(-\beta_p d)\right)
\end{aligned} \tag{A.7}$$

which transform equation A.6 into

$$\begin{aligned}
G_\omega^+(0, \mu_i, \phi_j) &= p_\omega G_\omega^-(d, -\mu_i, \phi_j) \exp\left(-\frac{\gamma_{ij}^{\text{FS}}}{\mu_i \Lambda_\omega} d\right) + \frac{p_\omega}{4\pi \mu_i \Lambda_\omega} I_{ij}^+ \\
&\quad + (1 - p_\omega) \left[\sigma_\omega \frac{C_\omega \Delta \bar{T}(z=0)}{4\pi} \right. \\
&\quad + \frac{(1 - \sigma_\omega)}{\pi} \sum_{i'j'} G_\omega^-(d, -\mu_{i'}, \phi_{j'}) \exp\left(-\frac{\gamma_{i'j'}^{\text{FS}}}{\mu_{i'} \Lambda_\omega} d\right) \mu_{i'} w_{\mu_{i'}} w_{\phi_{j'}} \\
&\quad \left. + \frac{(1 - \sigma_\omega)}{4\pi^2 \Lambda_\omega} \sum_{i'j'} w_{\mu_{i'}} w_{\phi_{j'}} I_{i'j'}^+ \right] \\
G_\omega^-(d, -\mu_i, \phi_j) &= p_\omega G_\omega^+(0, \mu_i, \phi_j) \exp\left(-\frac{\gamma_{ij}^{\text{FS}}}{\mu_i \Lambda_\omega} d\right) + \frac{p_\omega}{4\pi \mu_i \Lambda_\omega} I_{ij}^- \\
&\quad + (1 - p_\omega) \left[\sigma_\omega \frac{C_\omega \Delta \bar{T}(z=d)}{4\pi} \right. \\
&\quad + \frac{(1 - \sigma_\omega)}{\pi} \sum_{i'j'} G_\omega^+(0, \mu_{i'}, \phi_{j'}) \exp\left(-\frac{\gamma_{i'j'}^{\text{FS}}}{\mu_{i'} \Lambda_\omega} d\right) \mu_{i'} w_{\mu_{i'}} w_{\phi_{j'}} \\
&\quad \left. + \frac{(1 - \sigma_\omega)}{4\pi^2 \Lambda_\omega} \sum_{i'j'} w_{\mu_{i'}} w_{\phi_{j'}} I_{i'j'}^+ \right]
\end{aligned} \tag{A.8}$$

These discretized boundary conditions (equation A.8) can be written in a concise matrix form as

$$[A] \mathbf{G}_{\text{BC}} = \bar{\mathbf{c}} \tag{A.9}$$

with the solution of the form

$$\mathbf{G}_{\text{BC}} = [\mathbf{A}]^{-1} \bar{\mathbf{c}} \quad (\text{A.10})$$

where,

$$\mathbf{G}_{\text{BC}} = \begin{pmatrix} G_{\omega}^{+}(0, \mu_i, \phi_j) \\ G_{\omega}^{-}(d, -\mu_i, \phi_j) \end{pmatrix}_{[2N \times 1]}$$

$$[\mathbf{A}]^{-1} = \begin{bmatrix} T_{kk'}^{+} & T_{kk'}^{-} \\ B_{kk'}^{+} & B_{kk'}^{-} \end{bmatrix}_{[2N \times 2N]}$$

and

$$\bar{\mathbf{c}} = \begin{pmatrix} \bar{c}_{\omega}^{+}(0, \mu_{i'}, \phi_{j'}) \\ \bar{c}_{\omega}^{-}(d, \mu_{i'}, \phi_{j'}) \end{pmatrix}_{[2N \times 1]}$$

Here, k is the index for the combination $\{\mu_i, \phi_j\}$, N is the total number of combinations of $\{\mu_i, \phi_j\}$, and

$$\begin{aligned} \bar{c}_{\omega}^{+}(0, \mu_{i'}, \phi_{j'}) &= \frac{p_{\omega}}{4\pi\mu_{i'}\Lambda_{\omega}} I_{\mu_{i'}\phi_{j'}}^{+} \\ &+ (1 - p_{\omega}) \left(\frac{\sigma_{\omega}}{4\pi} C_{\omega} \Delta \bar{T}(z=0) + \frac{(1 - \sigma_{\omega})}{4\pi^2 \Lambda_{\omega}} \sum_{i''j''} w_{\mu_{i''}} w_{\phi_{j''}} I_{i''j''}^{+} \right) \\ \bar{c}_{\omega}^{-}(d, \mu_{i'}, \phi_{j'}) &= \frac{p_{\omega}}{4\pi\mu_{i'}\Lambda_{\omega}} I_{\mu_{i'}\phi_{j'}}^{-} \\ &+ (1 - p_{\omega}) \left(\frac{\sigma_{\omega}}{4\pi} C_{\omega} \Delta \bar{T}(z=d) + \frac{(1 - \sigma_{\omega})}{4\pi^2 \Lambda_{\omega}} \sum_{i''j''} w_{\mu_{i''}} w_{\phi_{j''}} I_{i''j''}^{-} \right) \end{aligned} \quad (\text{A.11})$$

With the substitution of equation A.10, the general BTE solution (equation 5.16 in the main article) becomes,

$$\begin{aligned}
G_{\omega}^{+}(z, \mu_i, \phi_j) &= \left(\sum_{i'j'} [T_{kk'}^{+} \bar{c}_{\omega}^{+}(0, \mu_{i'}, \phi_{j'}) + T_{kk'}^{-} \bar{c}_{\omega}^{-}(d, \mu_{i'}, \phi_{j'})] \right) \exp\left(-\frac{\gamma_{ij}^{\text{FS}}}{\mu_i \Lambda_{\omega}} z\right) \\
&\quad + \frac{\exp\left(-\frac{\gamma_{ij}^{\text{FS}}}{\mu_i \Lambda_{\omega}} z\right)}{4\pi \mu_i \Lambda_{\omega}} \int_0^z (C_{\omega} \Delta \bar{T} + \bar{Q}_{\omega} \tau_{\omega}) \exp\left(\frac{\gamma_{ij}^{\text{FS}}}{\mu_i \Lambda_{\omega}} z'\right) dz' \\
&= \left(\sum_{i'j'} [T_{kk'}^{+} \bar{c}_{\omega}^{+}(0, \mu_{i'}, \phi_{j'}) + T_{kk'}^{-} \bar{c}_{\omega}^{-}(d, \mu_{i'}, \phi_{j'})] \right) \exp\left(-\frac{\gamma_{ij}^{\text{FS}}}{\mu_i \Lambda_{\omega}} z\right) \\
&\quad + \frac{1}{4\pi \mu_i \Lambda_{\omega}} \int_0^z (C_{\omega} \Delta \bar{T} + \bar{Q}_{\omega} \tau_{\omega}) \exp\left(-\frac{\gamma_{ij}^{\text{FS}}}{\mu_i \Lambda_{\omega}} |z' - z|\right) dz' \\
G_{\omega}^{-}(z, -\mu_i, \phi_j) &= \left(\sum_{i'j'} [B_{kk'}^{+} \bar{c}_{\omega}^{+}(0, \mu_{i'}, \phi_{j'}) + B_{kk'}^{-} \bar{c}_{\omega}^{-}(d, \mu_{i'}, \phi_{j'})] \right) \\
&\quad \exp\left(-\frac{\gamma_{ij}^{\text{FS}}}{\mu_i \Lambda_{\omega}} (d - z)\right) \\
&\quad + \frac{\exp\left(\frac{\gamma_{ij}^{\text{FS}}}{\mu_i \Lambda_{\omega}} z\right)}{4\pi \mu_i \Lambda_{\omega}} \int_z^d (C_{\omega} \Delta \bar{T} + \bar{Q}_{\omega} \tau_{\omega}) \exp\left(-\frac{\gamma_{ij}^{\text{FS}}}{\mu_i \Lambda_{\omega}} z'\right) dz' \\
&= \left(\sum_{i'j'} [B_{kk'}^{+} \bar{c}_{\omega}^{+}(0, \mu_{i'}, \phi_{j'}) + B_{kk'}^{-} \bar{c}_{\omega}^{-}(d, \mu_{i'}, \phi_{j'})] \right) \exp\left(-\frac{\gamma_{ij}^{\text{FS}}}{\mu_i \Lambda_{\omega}} (d - z)\right) \\
&\quad + \frac{1}{4\pi \mu_i \Lambda_{\omega}} \int_z^d (C_{\omega} \Delta \bar{T} + \bar{Q}_{\omega} \tau_{\omega}) \exp\left(-\frac{\gamma_{ij}^{\text{FS}}}{\mu_i \Lambda_{\omega}} |z' - z|\right) dz'
\end{aligned} \tag{A.12}$$

where the unknown quantities $G_{\omega}^{+}(z, \mu_i, \phi_j)$, $G_{\omega}^{-}(z, -\mu_i, \phi_j)$, and $\Delta \bar{T}$ are related through the energy conservation requirement.

A.2 Formulation of the Integral Equation for $\Delta \bar{T}$

To solve for the unknown quantities ($G_{\omega}^{+}(z, \mu_i, \phi_j)$, $G_{\omega}^{-}(z, -\mu_i, \phi_j)$ and $\Delta \bar{T}$), the energy conservation equation is first discretized in the angular variables (μ and ϕ) using Gauss quadrature (equation A.5). Next, the general solution (equation A.12) is substituted into the discretized energy conservation equation to obtain the follow-

ing integral equation for $\Delta\bar{T}$:

$$\begin{aligned}
\Delta\bar{T}(z) &= \frac{1}{\int_{\omega=0}^{\omega_m} \frac{C_\omega}{\tau_\omega} d\omega} \int_{\omega=0}^{\omega_m} \left[\frac{1}{\tau_\omega} \sum_{ij} (G_\omega^+(z, \mu_i, \phi_j) + G_\omega^-(z, -\mu_i, \phi_j)) w_{\mu_i} w_{\phi_j} \right] d\omega \\
&= \frac{1}{\int_{\omega=0}^{\omega_m} \frac{C_\omega}{\tau_\omega} d\omega} \int_{\omega=0}^{\omega_m} \frac{1}{\tau_\omega} \\
&\quad \times \left[\sum_{ij} \left(\int_0^d (C_\omega \Delta\bar{T} + \bar{Q}_\omega \tau_\omega) \exp\left(-\frac{\gamma_{ij}^{\text{FS}}}{\mu_i \Lambda_\omega} |z' - z|\right) dz' \right) \frac{w_{\mu_i} w_{\phi_j}}{4\pi \mu_i \Lambda_\omega} \right. \\
&\quad + \sum_{ij} \sum_{i'j'} (T_{kk'}^+ \bar{c}_\omega^+(0, \mu_{i'}, \phi_{j'}) + T_{kk'}^- \bar{c}_\omega^-(d, \mu_{i'}, \phi_{j'})) w_{\mu_i} w_{\phi_j} \\
&\quad \times \exp\left(-\frac{\gamma_{ij}^{\text{FS}}}{\mu_i \Lambda_\omega} z\right) \\
&\quad + \sum_{ij} \sum_{i'j'} (B_{kk'}^+ \bar{c}_\omega^+(0, \mu_{i'}, \phi_{j'}) + B_{kk'}^- \bar{c}_\omega^-(d, \mu_{i'}, \phi_{j'})) w_{\mu_i} w_{\phi_j} \\
&\quad \left. \times \exp\left(-\frac{\gamma_{ij}^{\text{FS}}}{\mu_i \Lambda_\omega} (d - z)\right) \right] d\omega
\end{aligned}$$

(A.13)

Let us analyze the right hand side (RHS) of this equation term-by-term. For simplicity, let $\Omega = \int_{\omega=0}^{\omega_m} \frac{C_\omega}{\tau_\omega} d\omega$. The first term in the RHS of equation A.13 becomes:

$$\begin{aligned}
& \frac{1}{\Omega} \int_{\omega=0}^{\omega_m} \frac{1}{\tau_\omega} \left[\sum_{ij} \left(\int_0^d (C_\omega \Delta \bar{T} + \bar{Q}_\omega \tau_\omega) \exp\left(-\frac{\gamma_{ij}^{\text{FS}}}{\mu_i \Lambda_\omega} |z' - z|\right) dz' \right) \frac{w_{\mu_i} w_{\phi_j}}{4\pi \mu_i \Lambda_\omega} d\omega \right] \\
&= \frac{1}{\Omega} \int_0^d \Delta \bar{T} \left[\int_{\omega=0}^{\omega_m} \left(\frac{C_\omega}{4\pi \tau_\omega \Lambda_\omega} \sum_{ij} \frac{w_{\mu_i} w_{\phi_j}}{\mu_i} \exp\left(-\frac{\gamma_{ij}^{\text{FS}}}{\mu_i \Lambda_\omega} |z' - z|\right) \right) d\omega \right] dz' \\
&\quad + \frac{1}{\Omega} \int_{\omega=0}^{\omega_m} \bar{Q}_\omega \left[\sum_{ij} \left(\int_0^z \exp\left(-\frac{\gamma_{ij}^{\text{FS}}}{\mu_i \Lambda_\omega} |z' - z|\right) dz' \right. \right. \\
&\quad \left. \left. + \int_z^d \exp\left(-\frac{\gamma_{ij}^{\text{FS}}}{\mu_i \Lambda_\omega} |z' - z|\right) dz' \right) \frac{w_{\mu_i} w_{\phi_j}}{4\pi \mu_i \Lambda_\omega} \right] \\
&= \frac{1}{\Omega} \int_0^d \Delta \bar{T} \left[\int_{\omega=0}^{\omega_m} \left(\frac{C_\omega}{4\pi \tau_\omega \Lambda_\omega} \sum_{ij} \frac{w_{\mu_i} w_{\phi_j}}{\mu_i} \exp\left(-\frac{\gamma_{ij}^{\text{FS}}}{\mu_i \Lambda_\omega} |z' - z|\right) \right) d\omega \right] dz' \\
&\quad + \frac{1}{\Omega} \int_{\omega=0}^{\omega_m} \bar{Q}_\omega \left[\sum_{ij} \left(2 - \exp\left(-\frac{\gamma_{ij}^{\text{FS}}}{\mu_i \Lambda_\omega} z\right) - \exp\left(-\frac{\gamma_{ij}^{\text{FS}}}{\mu_i \Lambda_\omega} (d - z)\right) \right) \frac{w_{\mu_i} w_{\phi_j}}{4\pi \gamma_{ij}^{\text{FS}}} \right] d\omega \\
&= \frac{1}{\Omega} \int_0^d \Delta \bar{T} \left[\int_{\omega=0}^{\omega_m} \left(\frac{C_\omega}{4\pi \tau_\omega \Lambda_\omega} \sum_{ij} \frac{w_{\mu_i} w_{\phi_j}}{\mu_i} \exp\left(-\frac{\gamma_{ij}^{\text{FS}}}{\mu_i \Lambda_\omega} |z' - z|\right) \right) d\omega \right] dz' \\
&\quad + \frac{1}{\Omega} \int_{\omega=0}^{\omega_m} \bar{Q}_\omega^0 \exp(-\beta_p z) \\
&\quad \times \left[\sum_{ij} \left(2 - \exp\left(-\frac{\gamma_{ij}^{\text{FS}}}{\mu_i \Lambda_\omega} z\right) - \exp\left(-\frac{\gamma_{ij}^{\text{FS}}}{\mu_i \Lambda_\omega} (d - z)\right) \right) \frac{w_{\mu_i} w_{\phi_j}}{4\pi \gamma_{ij}^{\text{FS}}} \right] d\omega \\
&= \int_0^d \Delta \bar{T} [K_1^1(z', z)] dz' + f_1^1(z)
\end{aligned}$$

(A.14)

Similarly, the second term in the RHS of equation A.13 becomes:

$$\begin{aligned}
& \frac{1}{\Omega} \int_{\omega=0}^{\omega_m} \frac{1}{\tau_\omega} \\
& \times \left[\sum_{ij} \sum_{i'j'} \left(T_{kk'}^+ \bar{c}_\omega^+ (0, \mu_{i'}, \phi_{j'}) + T_{kk'}^- \bar{c}_\omega^- (d, \mu_{i'}, \phi_{j'}) \right) w_{\mu_i} w_{\phi_j} \exp\left(-\frac{\gamma_{ij}^{\text{FS}}}{\mu_i \Lambda_\omega} z\right) \right] d\omega \\
& = \frac{1}{\Omega} \int_{\omega=0}^{\omega_m} \frac{1}{\tau_\omega} \left[\sum_{ij} \sum_{i'j'} \left(\frac{p_\omega}{4\pi \mu_{i'} \Lambda_\omega} (I_{i'j'}^+ T_{kk'}^+ + I_{i'j'}^- T_{kk'}^-) w_{\mu_i} w_{\phi_j} \exp\left(-\frac{\gamma_{ij}^{\text{FS}}}{\mu_i \Lambda_\omega} z\right) \right) \right. \\
& \quad + (1 - p_\omega) (1 - \sigma_\omega) \\
& \quad \times \sum_{ij} \sum_{i'j'} \sum_{i''j''} \left(\frac{w_{\mu_{i''}} w_{\phi_{j''}}}{4\pi^2 \Lambda_\omega} (I_{i''j''}^+ T_{kk'}^+ + I_{i''j''}^- T_{kk'}^-) w_{\mu_i} w_{\phi_j} \exp\left(-\frac{\gamma_{ij}^{\text{FS}}}{\mu_i \Lambda_\omega} z\right) \right) \\
& \quad + (1 - p_\omega) \sigma_\omega \\
& \quad \times \left. \sum_{ij} \sum_{i'j'} \left(\frac{C_\omega}{4\pi} (T_{kk'}^+ \Delta \bar{T}(z=0) + T_{kk'}^- \Delta \bar{T}(z=d)) w_{\mu_i} w_{\phi_j} \exp\left(-\frac{\gamma_{ij}^{\text{FS}}}{\mu_i \Lambda_\omega} z\right) \right) \right] d\omega \\
& = f_2^1(z) + f_2^2(z) + h_2(z) + \int_0^d \Delta \bar{T} [K_2^1(z', z) + K_2^2(z', z)] dz'
\end{aligned} \tag{A.15}$$

where,

$$\begin{aligned}
f_2^1(z) &= \frac{1}{\Omega} \int_{\omega=0}^{\omega_m} \left[\sum_{ij} \sum_{i'j'} \left(\frac{\bar{Q}_\omega^0 p_\omega (T_{kk'}^+ + T_{kk'}^-)}{4\pi \gamma_{\mu_{i'} \phi_{j'}}^{\text{FS}}} \left(1 - \exp\left(-\frac{\gamma_{i'j'}^{\text{FS}}}{\mu_{i'} \Lambda_\omega} d\right) \right) \right. \right. \\
& \quad \left. \left. \exp\left(-\left[\beta_p + \frac{\gamma_{ij}^{\text{FS}}}{\mu_i \Lambda_\omega}\right] z\right) w_{\mu_i} w_{\phi_j} \right) \right] d\omega
\end{aligned} \tag{A.16}$$

$$\begin{aligned}
f_2^2(z) &= \frac{1}{\Omega} \int_{\omega=0}^{\omega_m} \left[\sum_{ij} \sum_{i'j'} \sum_{i''j''} \left(\frac{\bar{Q}_\omega^0 (1 - p_\omega) (1 - \sigma_\omega) (T_{kk'}^+ + T_{kk'}^-) \mu_{i''} w_{\mu_{i''}} w_{\phi_{k''}}}{4\pi^2 \gamma_{i''j''}^{\text{FS}}} \right. \right. \\
& \quad \left. \left. \times \left(1 - \exp\left(-\frac{\gamma_{i''j''}^{\text{FS}}}{\mu_{i''} \Lambda_\omega} d\right) \right) w_{\mu_i} w_{\phi_j} \exp\left(-\left[\beta_p + \frac{\gamma_{ij}^{\text{FS}}}{\mu_i \Lambda_\omega}\right] z\right) \right) \right] d\omega
\end{aligned} \tag{A.17}$$

$$\begin{aligned}
h_2(z) &= \frac{1}{\Omega} \int_{\omega=0}^{\omega_m} \frac{1}{\tau_\omega} \left[\sum_{ij} \sum_{i'j'} \left(\frac{C_\omega (1 - p_\omega) \sigma_\omega}{4\pi} (T_{kk'}^+ \Delta \bar{T}(z=0) + T_{kk'}^- \Delta \bar{T}(z=d)) \right) \right. \\
& \quad \left. \times w_{\mu_i} w_{\phi_j} \exp\left(-\frac{\gamma_{ij}^{\text{FS}}}{\mu_i \Lambda_\omega} z\right) \right]
\end{aligned} \tag{A.18}$$

$$\begin{aligned}
K_2^1(z', z) = & \frac{1}{\Omega} \int_{\omega=0}^{\omega_m} \frac{C_\omega}{\tau_\omega} \left[\sum_{ij} \sum_{i'j'} \left(\frac{p_\omega}{4\pi\mu_{i'}\Lambda_\omega} \left(\exp\left(-\frac{\gamma_{i'j'}^{\text{FS}}}{\mu_{i'}\Lambda_\omega} z'\right) T_{kk'}^+ \right. \right. \right. \\
& \left. \left. \left. + \exp\left(-\frac{\gamma_{i'j'}^{\text{FS}}}{\mu_{i'}\Lambda_\omega} (d-z')\right) T_{kk'}^- \right) w_{\mu_i} w_{\phi_j} \exp\left(-\frac{\gamma_{ij}^{\text{FS}}}{\mu_i\Lambda_\omega} z\right) \right] d\omega \quad (\text{A.19})
\end{aligned}$$

$$\begin{aligned}
K_2^2(z', z) = & \frac{1}{\Omega} \int_{\omega=0}^{\omega_m} \frac{C_\omega (1-p_\omega) (1-\sigma_\omega)}{\tau_\omega} \left[\sum_{ij} \sum_{i'j'} \sum_{i''j''} \left(\frac{w_{\mu_{i''}} w_{\phi_{j''}}}{4\pi^2\Lambda_\omega} \right. \right. \\
& \times \left(\exp\left(-\frac{\gamma_{i''j''}^{\text{FS}}}{\mu_{i''}\Lambda_\omega} z'\right) T_{kk'}^+ + \exp\left(-\frac{\gamma_{i''j''}^{\text{FS}}}{\mu_{i''}\Lambda_\omega} (d-z')\right) T_{kk'}^- \right) \\
& \left. \left. \times w_{\mu_i} w_{\phi_j} \exp\left(-\frac{\gamma_{ij}^{\text{FS}}}{\mu_i\Lambda_\omega} z\right) \right] d\omega \quad (\text{A.20})
\end{aligned}$$

and the third term in the RHS of equation A.13 becomes

$$\begin{aligned}
& \frac{1}{\Omega} \int_{\omega=0}^{\omega_m} \frac{1}{\tau_\omega} \left[\sum_{ij} \sum_{i'j'} \left(B_{kk'}^+ \bar{c}_\omega^+ (0, \mu_{i'}, \phi_{j'}) + B_{kk'}^- \bar{c}_\omega^- (d, \mu_{i'}, \phi_{j'}) \right) \right. \\
& \quad \left. \times w_{\mu_i} w_{\phi_j} \exp\left(-\frac{\gamma_{ij}^{\text{FS}}}{\mu_i\Lambda_\omega} (d-z)\right) \right] d\omega \\
& = \frac{1}{\Omega} \int_{\omega=0}^{\omega_m} \frac{1}{\tau_\omega} \left[\sum_{ij} \sum_{i'j'} \left(\frac{p_\omega}{4\pi\mu_{i'}\Lambda_\omega} \left(I_{i'j'}^+ B_{kk'}^+ + I_{i'j'}^- B_{kk'}^- \right) \right. \right. \\
& \quad \left. \left. \times w_{\mu_i} w_{\phi_j} \exp\left(-\frac{\gamma_{ij}^{\text{FS}}}{\mu_i\Lambda_\omega} (d-z)\right) \right) \right. \\
& \quad + \sum_{ij} \sum_{i'j'} \sum_{i''j''} \left(\frac{w_{\mu_{i''}} w_{\phi_{j''}} (1-p_\omega) (1-\sigma_\omega)}{4\pi^2\Lambda_\omega} \left(I_{i''j''}^+ B_{kk'}^+ + I_{i''j''}^- B_{kk'}^- \right) \right. \\
& \quad \left. \left. \times w_{\mu_i} w_{\phi_j} \exp\left(-\frac{\gamma_{ij}^{\text{FS}}}{\mu_i\Lambda_\omega} (d-z)\right) \right) \right. \\
& \quad + \sum_{ij} \sum_{i'j'} \left(\frac{C_\omega (1-p_\omega) \sigma_\omega}{4\pi} \left(B_{kk'}^+ \Delta\bar{T}(z=0) + B_{kk'}^- \Delta\bar{T}(z=d) \right) \right. \\
& \quad \left. \left. \times w_{\mu_i} w_{\phi_j} \exp\left(-\frac{\gamma_{ij}^{\text{FS}}}{\mu_i\Lambda_\omega} (d-z)\right) \right) \right] d\omega \\
& = f_3^1(z) + f_3^2(z) + h_3(z) + \int_0^d \Delta\bar{T} \left[K_3^1(z', z) + K_3^2(z', z) \right] dz' \quad (\text{A.21})
\end{aligned}$$

where,

$$f_3^1(z) = \frac{1}{\Omega} \int_{\omega=0}^{\omega_m} \left[\sum_{ij} \sum_{i'j'} \left(\frac{\bar{Q}_\omega^0 p_\omega}{4\pi \gamma_{\mu_i' \phi_j'}^{\text{FS}}} \left(1 - \exp\left(-\frac{\gamma_{i'j'}^{\text{FS}}}{\mu_{i'} \Lambda_\omega} d\right) \right) \left(B_{kk'}^+ + B_{kk'}^- \right) \right. \right. \\ \left. \left. w_{\mu_i} w_{\phi_j} \exp\left(-\frac{\gamma_{ij}^{\text{FS}}}{\mu_i \Lambda_\omega} (d-z) - \beta_p z\right) \right) \right] d\omega \quad (\text{A.22})$$

$$f_3^2(z) = \frac{1}{\Omega} \int_{\omega=0}^{\omega_m} \left[\sum_{ij} \sum_{i'j'} \sum_{i''j''} \left(\frac{\bar{Q}_\omega^0 \mu_{i''} w_{\mu_{i''}} w_{\phi_{k''}} (1-p_\omega) (1-\sigma_\omega)}{4\pi^2 \gamma_{i''j''}^{\text{FS}}} \right. \right. \\ \times \left(1 - \exp\left(-\frac{\gamma_{i''j''}^{\text{FS}}}{\mu_{i''} \Lambda_\omega} d\right) \right) \\ \left. \times \left(B_{kk'}^+ + B_{kk'}^- \right) w_{\mu_i} w_{\phi_j} \exp\left(-\frac{\gamma_{ij}^{\text{FS}}}{\mu_i \Lambda_\omega} (d-z) - \beta_p z\right) \right] d\omega \quad (\text{A.23})$$

$$h_3(z) = \frac{1}{\Omega} \int_{\omega=0}^{\omega_m} \frac{1}{\tau_\omega} \left[\sum_{ij} \sum_{i'j'} \left(\frac{C_\omega (1-p_\omega) \sigma_\omega}{4\pi} \left(B_{kk'}^+ \Delta \bar{T}(z=0) \right. \right. \right. \\ \left. \left. + B_{kk'}^- \Delta \bar{T}(z=d) \right) w_{\mu_i} w_{\phi_j} \exp\left(-\frac{\gamma_{ij}^{\text{FS}}}{\mu_i \Lambda_\omega} (d-z)\right) \right] d\omega \quad (\text{A.24})$$

$$K_3^1(z', z) = \frac{1}{\Omega} \int_{\omega=0}^{\omega_m} \frac{C_\omega}{\tau_\omega} \left[\sum_{ij} \sum_{i'j'} \left(\frac{p_\omega}{4\pi \mu_{i'} \Lambda_\omega} \left(\exp\left(-\frac{\gamma_{i'j'}^{\text{FS}}}{\mu_{i'} \Lambda_\omega} z'\right) B_{kk'}^+ \right. \right. \right. \\ \left. \left. + \exp\left(-\frac{\gamma_{i'j'}^{\text{FS}}}{\mu_{i'} \Lambda_\omega} (d-z')\right) B_{kk'}^- \right) w_{\mu_i} w_{\phi_j} \exp\left(-\frac{\gamma_{ij}^{\text{FS}}}{\mu_i \Lambda_\omega} (d-z)\right) \right] d\omega \quad (\text{A.25})$$

$$K_3^2(z', z) = \frac{1}{\Omega} \int_{\omega=0}^{\omega_m} \frac{C_\omega}{\tau_\omega} \left[\sum_{ij} \sum_{i'j'} \sum_{i''j''} \left(\frac{w_{\mu_{i''}} w_{\phi_{j''}} (1-p_\omega) (1-\sigma_\omega)}{4\pi^2 \Lambda_\omega} \right. \right. \\ \times \left(\exp\left(-\frac{\gamma_{i''j''}^{\text{FS}}}{\mu_{i''} \Lambda_\omega} z'\right) B_{kk'}^+ + \exp\left(-\frac{\gamma_{i''j''}^{\text{FS}}}{\mu_{i''} \Lambda_\omega} (d-z')\right) B_{kk'}^- \right) \\ \left. \times w_{\mu_i} w_{\phi_j} \exp\left(-\frac{\gamma_{ij}^{\text{FS}}}{\mu_i \Lambda_\omega} (d-z)\right) \right] d\omega \quad (\text{A.26})$$

Finally, the system to solve for (equation A.13) can be represented as an integral equation of the form:

$$\Delta \bar{T}(z) - h(z) = f(z) + \int_0^d [K(z', z) \Delta \bar{T}(z')] dz' \quad (\text{A.27})$$

where,

$$f(z) = f_1^1(z) + f_2^1(z) + f_2^2(z) + f_3^1(z) + f_3^2(z) \quad (\text{A.28})$$

$$K(z', z) = K_1^1(z', z) + K_2^1(z', z) + K_2^2(z', z) + K_3^1(z', z) + K_3^2(z', z) \quad (\text{A.29})$$

and

$$h(z) = h_2(z) + h_3(z) \quad (\text{A.30})$$

There are several important properties of the integral equation A.27.

1. The kernel $K(z', z)$ is singular for $z = z'$ due to the singularity of $K_1^1(z', z)$ at $z = z'$.
2. Unlike the term $f(z)$, the term $h(z)$ is a function of $\Delta\bar{T}$ and can be represented as $h(z) = H(z', z)\Delta\bar{T}$ where $H(z', z)$ is independent of $\Delta\bar{T}$.

There are several approaches available in the literature to solve such singular integral equations. In this work, this integral equation is solved using the method of degenerate kernels, the details of which are described in section A.3.

A.3 The Method of Degenerate Kernels

The integral equation (equation A.27) can be solved using the method of degenerate kernels. First, the integral equation is rewritten as,

$$\Delta\bar{T}(\hat{z}) - h(\hat{z}) = f(\hat{z}) + \int_0^1 [\bar{K}(\hat{z}', \hat{z}) \Delta\bar{T}(\hat{z}')] d\hat{z}' \quad (\text{A.31})$$

where $\hat{z} = z/d$ and $\bar{K}(\hat{z}', \hat{z}) = d \times K(z', z)$. Then the functions $\Delta\bar{T}(\hat{z})$, $f(\hat{z})$ and $K(\hat{z}', \hat{z})$ are expanded in a Fourier series:

$$\Delta\bar{T}_{(N)}(\hat{z}) = \frac{1}{2}t_0 + \sum_{m=1}^N t_m \cos(m\pi\hat{z}) \quad (\text{A.32})$$

$$f_{(N)}(\hat{z}) = \frac{1}{2}f_0 + \sum_{m=1}^N f_m \cos(m\pi\hat{z}) \quad (\text{A.33})$$

$$h_{(N)}(\hat{z}) = \frac{1}{2}h_0 + \sum_{m=1}^N h_m \cos(m\pi\hat{z})$$

$$\begin{aligned} \bar{K}_{(N)}(\hat{z}', \hat{z}) &= \frac{1}{4}K_{00} + \frac{1}{2} \sum_{m=1}^N K_{m0} \cos(m\pi\hat{z}') + \frac{1}{2} \sum_{n=1}^N K_{0n} \cos(n\pi\hat{z}) \\ &+ \sum_{m=1}^N \sum_{n=1}^N K_{mn} \cos(m\pi\hat{z}') \cos(n\pi\hat{z}) \end{aligned}$$

where the Fourier coefficients are given by,

$$f_m = 2 \int_0^1 f(\hat{z}) \cos(m\pi\hat{z}) d\hat{z} \quad (\text{A.34})$$

$$h_m = 2 \int_0^1 h(\hat{z}) \cos(m\pi\hat{z}) d\hat{z} \quad (\text{A.35})$$

and

$$K_{mn} = 4 \int_0^1 \int_0^1 K(\hat{z}', \hat{z}) \cos(m\pi\hat{z}') \cos(n\pi\hat{z}) d\hat{z}' d\hat{z} \quad (\text{A.36})$$

Here, a Fourier cosine series has been used for all of the functions by assuming that all the functions are even with respect to \hat{z} and \hat{z}' . This assumption is valid since the integral equation (equation A.27) has been solved only in the domain $\hat{z} \in [0, 1]$. After several algebraic simplifications, the expressions for the Fourier coefficients (equations A.34, A.35, and A.36) simplify into the following concise forms:

$$f_{1,m}^1 = \frac{2}{\Omega} \int_{\omega=0}^{\omega_m} \bar{Q}_\omega^0 \left[\sum_{ij} (2J_0(m) - J_1(m) - J_2(m)) \frac{w_{\mu_i} w_{\phi_j}}{4\pi\gamma_{ij}^{\text{FS}}} \right] d\omega \quad (\text{A.37})$$

$$f_{2,m}^1 = \frac{2}{\Omega} \int_{\omega=0}^{\omega_m} \left[\sum_{ij} \sum_{i'j'} \left(\frac{\bar{Q}_\omega^0 p_\omega}{4\pi\gamma_{\mu_i' \phi_j'}^{\text{FS}}} \left(1 - \exp\left(-\frac{\gamma_{i'j'}^{\text{FS}}}{\mu_{i'} \Lambda_\omega} d\right) \right) (T_{kk'}^+ + T_{kk'}^-) \right. \right. \\ \left. \left. \times w_{\mu_i} w_{\phi_j} J_1(m) \right) \right] d\omega \quad (\text{A.38})$$

$$f_{2,m}^2 = \frac{2}{\Omega} \int_{\omega=0}^{\omega_m} \left[\sum_{ij} \sum_{i'j'} \sum_{i''j''} \left(\frac{\bar{Q}_\omega^0 \mu_{i''} w_{\mu_{i''}} w_{\phi_{k''}} (1-p_\omega) (1-\sigma_\omega)}{4\pi^2 \gamma_{i''j''}^{\text{FS}}} \right. \right. \\ \left. \left. \times \left(1 - \exp\left(-\frac{\gamma_{i''j''}^{\text{FS}}}{\mu_{i''} \Lambda_\omega} d\right) \right) (T_{kk'}^+ + T_{kk'}^-) w_{\mu_i} w_{\phi_j} J_1(m) \right) \right] d\omega \quad (\text{A.39})$$

$$h_{2,m} = \frac{2}{\Omega} \int_{\omega=0}^{\omega_m} \frac{1}{\tau_\omega} \left[\sum_{ij} \sum_{i'j'} \left(\frac{C_\omega (1-p_\omega) \sigma_\omega}{4\pi} (T_{kk'}^+ \Delta \bar{T}(z=0) + T_{kk'}^- \Delta \bar{T}(z=d)) \right) \right. \\ \left. \times w_{\mu_i} w_{\phi_j} I_1(m) \right] \quad (\text{A.40})$$

$$f_{3,m}^1 = \frac{2}{\Omega} \int_{\omega=0}^{\omega_m} \left[\sum_{ij} \sum_{i'j'} \left(\frac{\bar{Q}_\omega^0 p_\omega}{4\pi\gamma_{\mu_i' \phi_j'}^{\text{FS}}} \left(1 - \exp\left(-\frac{\gamma_{i'j'}^{\text{FS}}}{\mu_{i'} \Lambda_\omega} d\right) \right) (B_{kk'}^+ + B_{kk'}^-) \right. \right. \\ \left. \left. \times w_{\mu_i} w_{\phi_j} J_2(m) \right) \right] d\omega \quad (\text{A.41})$$

$$f_{3,m}^2 = \frac{2}{\Omega} \int_{\omega=0}^{\omega_m} \left[\sum_{ij} \sum_{i'j'} \sum_{i''j''} \left(\frac{\bar{Q}_\omega^0 (1-p_\omega) (1-\sigma_\omega) \mu_{i''} w_{\mu_{i''}} w_{\phi_{k''}}}{4\pi^2 \gamma_{i''j''}^{\text{FS}}} \right) \right. \\ \left. \times \left(1 - \exp\left(-\frac{\gamma_{i''j''}^{\text{FS}}}{\mu_{i''} \Lambda_\omega} d\right) \right) (B_{kk'}^+ + B_{kk'}^-) w_{\mu_i} w_{\phi_j} J_2(m) \right] d\omega \quad (\text{A.42})$$

$$h_{3,m} = \frac{2}{\Omega} \int_{\omega=0}^{\omega_m} \frac{1}{\tau_\omega} \left[\sum_{ij} \sum_{i'j'} \left(\frac{C_\omega (1-p_\omega) \sigma_\omega}{4\pi} \left(B_{kk'}^+ \Delta \bar{T}(z=0) + B_{kk'}^- \Delta \bar{T}(z=d) \right) \right) \right. \\ \left. \times w_{\mu_i} w_{\phi_j} I_2(m) \right] \quad (\text{A.43})$$

$$K_{1,mn}^1 = \frac{4d}{\Omega} \left[\int_{\omega=0}^{\omega_m} \left(\frac{C_\omega}{4\pi \tau_\omega \Lambda_\omega} \sum_{ij} \frac{w_{\mu_i} w_{\phi_j}}{\mu_i} I_3(m, n) \right) d\omega \right] \quad (\text{A.44})$$

$$K_{2,mn}^1 = \frac{4d}{\Omega} \int_{\omega=0}^{\omega_m} \frac{C_\omega}{\tau_\omega} \\ \times \left[\sum_{ij} \sum_{i'j'} \left(\frac{P_\omega}{4\pi \mu_{i'} \Lambda_\omega} \left(I_1'(m) T_{kk'}^+ + I_2'(m) T_{kk'}^- \right) w_{\mu_i} w_{\phi_j} I_1(n) \right) \right] d\omega \quad (\text{A.45})$$

$$K_{2,mn}^2 = \frac{4d}{\Omega} \int_{\omega=0}^{\omega_m} \frac{C_\omega}{\tau_\omega} \left[\sum_{ij} \sum_{i'j'} \sum_{i''j''} \left(\frac{w_{\mu_{i''}} w_{\phi_{j''}} (1-p_\omega) (1-\sigma_\omega)}{4\pi^2 \Lambda_\omega} \right) \right. \\ \left. \times \left(I_1''(m) T_{kk'}^+ + I_2''(m) T_{kk'}^- \right) w_{\mu_i} w_{\phi_j} I_1(n) \right] d\omega \quad (\text{A.46})$$

$$K_{3,mn}^1 = \frac{4d}{\Omega} \int_{\omega=0}^{\omega_m} \frac{C_\omega}{\tau_\omega} \left[\sum_{ij} \sum_{i'j'} \left(\frac{P_\omega}{4\pi \mu_{i'} \Lambda_\omega} \left(I_1'(m) B_{kk'}^+ + I_2'(m) B_{kk'}^- \right) \right) \right. \\ \left. \times w_{\mu_i} w_{\phi_j} I_2(n) \right] d\omega \quad (\text{A.47})$$

$$K_{3,mn}^2 = \frac{4d}{\Omega} \int_{\omega=0}^{\omega_m} \frac{C_\omega}{\tau_\omega} \left[\sum_{ij} \sum_{i'j'} \sum_{i''j''} \left(\frac{w_{\mu_{i''}} w_{\phi_{j''}} (1-p_\omega) (1-\sigma_\omega)}{4\pi^2 \Lambda_\omega} \right) \right. \\ \left. \times \left(I_1''(m) B_{kk'}^+ + I_2''(m) B_{kk'}^- \right) w_{\mu_i} w_{\phi_j} I_2(n) \right] d\omega \quad (\text{A.48})$$

where,

$$\begin{aligned} J_0(m) &= \int_0^1 \exp(-d\beta_p \hat{z}) \cos(m\pi \hat{z}) d\hat{z} \\ &= \frac{d\beta_p}{m^2\pi^2 + d^2\beta_p^2} \left[1 - (-1)^m \exp(-d\beta_p) \right] \end{aligned}$$

$$\begin{aligned} J_1(m) &= \int_0^1 \exp\left(-\left[\frac{\gamma_{ij}^{\text{FS}}}{\mu_i \text{Kn}_\omega^d} + d\beta_p\right] \hat{z}\right) \cos(m\pi \hat{z}) d\hat{z} \\ &= \frac{\left[\frac{\gamma_{ij}^{\text{FS}}}{\mu_i \text{Kn}_\omega^d} + d\beta_p\right]}{m^2\pi^2 + \left(\frac{\gamma_{ij}^{\text{FS}}}{\mu_i \text{Kn}_\omega^d} + d\beta_p\right)^2} \left[1 - (-1)^m \exp\left(-\left[\frac{\gamma_{ij}^{\text{FS}}}{\mu_i \text{Kn}_\omega^d} + d\beta_p\right]\right) \right] \end{aligned}$$

$$\begin{aligned} J_2(m) &= \int_0^1 \exp\left(-\frac{\gamma_{ij}^{\text{FS}}}{\mu_i \text{Kn}_\omega^d} (1 - \hat{z}) - d\beta_p \hat{z}\right) \cos(m\pi \hat{z}) d\hat{z} \\ &= \exp\left(-\frac{\gamma_{ij}^{\text{FS}}}{\mu_i \text{Kn}_\omega^d}\right) \frac{\left[d\beta_p - \frac{\gamma_{ij}^{\text{FS}}}{\mu_i \text{Kn}_\omega^d}\right]}{m^2\pi^2 + \left(d\beta_p - \frac{\gamma_{ij}^{\text{FS}}}{\mu_i \text{Kn}_\omega^d}\right)^2} \\ &\quad \times \left[1 - (-1)^m \exp\left(-\left[d\beta_p - \frac{\gamma_{ij}^{\text{FS}}}{\mu_i \text{Kn}_\omega^d}\right]\right) \right] \end{aligned}$$

$$\begin{aligned} I_1(m) &= \int_0^1 \exp\left(-\frac{\gamma_{ij}^{\text{FS}}}{\mu_i \text{Kn}_\omega^d} \hat{z}\right) \cos(m\pi \hat{z}) d\hat{z} \\ &= \frac{\frac{\gamma_{ij}^{\text{FS}}}{\mu_i \text{Kn}_\omega^d}}{m^2\pi^2 + \left(\frac{\gamma_{ij}^{\text{FS}}}{\mu_i \text{Kn}_\omega^d}\right)^2} \left[1 - (-1)^m \exp\left(-\frac{\gamma_{ij}^{\text{FS}}}{\mu_i \text{Kn}_\omega^d}\right) \right] \end{aligned}$$

$$\begin{aligned} I_2(m) &= \int_0^1 \exp\left(-\frac{\gamma_{ij}^{\text{FS}}}{\mu_i \text{Kn}_\omega^d} (1 - \hat{z})\right) \cos(m\pi \hat{z}) d\hat{z} \\ &= \frac{\frac{\gamma_{ij}^{\text{FS}}}{\mu_i \text{Kn}_\omega^d}}{m^2\pi^2 + \left(\frac{\gamma_{ij}^{\text{FS}}}{\mu_i \text{Kn}_\omega^d}\right)^2} \left[(-1)^m - \exp\left(-\frac{\gamma_{ij}^{\text{FS}}}{\mu_i \text{Kn}_\omega^d}\right) \right] \end{aligned}$$

$$I_3(m, n) = \int_0^1 \int_0^1 \exp\left(-\frac{\gamma_{ij}^{\text{FS}}}{\mu_i \text{Kn}_\omega^d} |\hat{z}' - \hat{z}|\right) \cos(m\pi\hat{z}) \cos(n\pi\hat{z}') d\hat{z}d\hat{z}'$$

$$= \begin{cases} \frac{\frac{\gamma_{ij}^{\text{FS}}}{\mu_i \text{Kn}_\omega^d}}{m^2\pi^2 + \left(\frac{\gamma_{ij}^{\text{FS}}}{\mu_i \text{Kn}_\omega^d}\right)^2} [\delta_{mn} - (I_1(n) + (-1)^m I_2(n))] & \text{for } m \neq 0 \\ \frac{\frac{\gamma_{ij}^{\text{FS}}}{\mu_i \text{Kn}_\omega^d}}{m^2\pi^2 + \left(\frac{\gamma_{ij}^{\text{FS}}}{\mu_i \text{Kn}_\omega^d}\right)^2} [2\delta_{mn} - (I_1(n) + (-1)^m I_2(n))] & \text{for } m = 0 \end{cases}$$

and primes (' and ") on I_1, I_2 , and I_3 indicate that these functions are evaluated for $\{\mu', \phi'\}$ and $\{\mu'', \phi''\}$ respectively. These Fourier coefficients are substituted into the cosine series for the corresponding functions in the integral equation (equation A.27) to get,

$$\begin{aligned} & \frac{1}{2}t_0 + \sum_{m=1}^N t_m \cos(m\pi\hat{z}) - \frac{1}{2}h_0 - \sum_{m=1}^N h_m \cos(m\pi\hat{z}) \\ &= \frac{1}{2}f_0 + \sum_{m=1}^N f_n \cos(m\pi\hat{z}) + \frac{1}{8}t_0 K_{00} + \frac{1}{4} \sum_{n=1}^N t_0 K_{0n} \cos(n\pi\hat{z}) \\ & \quad + \sum_{m=1}^N \left(\frac{t_0 K_{m0}}{4} + \frac{K_{00} t_m}{4} + \sum_{n=1}^N \frac{t_0 K_{mn} + t_m K_{0n}}{2} \cos(n\pi\hat{z}) \right) \int_0^1 \cos(m\pi\hat{z}') d\hat{z}' \\ & \quad + \sum_{m=1}^N \sum_{n=1}^N \left(\frac{t_m K_{n0}}{2} + \sum_{p=1}^N t_m K_{np} \cos(p\pi\hat{z}) \right) \int_0^1 \cos(m\pi\hat{z}') \cos(n\pi\hat{z}') d\hat{z}' \\ &= \frac{1}{2}f_0 + \sum_{m=1}^N f_n \cos(m\pi\hat{z}) + \frac{1}{8}t_0 K_{00} + \frac{1}{4} \sum_{n=1}^N t_0 K_{0n} \cos(n\pi\hat{z}) \\ & \quad + \frac{1}{2} \sum_{m=1}^N \left(\frac{t_m K_{m0}}{2} + \sum_{n=1}^N t_m K_{mn} \cos(n\pi\hat{z}) \right) \end{aligned}$$

Due to the orthogonality of $\cos(m\pi\hat{z})$ in the interval $\hat{z} \in [0, 1]$, it is sufficient to solve for the Fourier coefficients (t_m) by grouping together the coefficients with the same index, which results in a system of linear equations in t_m :

$$\begin{aligned} & \left(\frac{1}{2} - \frac{1}{8}K_{00} \right) t_0 - \frac{1}{4} \sum_{n=1}^N K_{n0} t_n - \frac{1}{2}h_0 = \frac{1}{2}f_0 \\ & \sum_{n=1}^N \left(\delta_{nm} - \frac{1}{2}K_{nm} \right) t_n - \frac{1}{4}K_{0m} t_0 - h_m = f_m \quad \text{for } m = 1, \dots, N \end{aligned} \tag{A.49}$$

Noting that h_i 's are linear combinations of t_j 's, the system of linear equations (equation A.49) can be written in a concise matrix form as:

$$Ft = f$$

which can be solved by standard matrix inversion techniques.

In the TG experiment, the temperature profile that is detected is an average over the varying probe intensity in the cross-plane direction. For unit power on the probe laser, we have,

$$\begin{aligned} \Delta\bar{T}_{\text{Expt}} &= \int_0^d \Delta\bar{T}(z) \exp(-\beta_{pr}z) dz \\ &= d \int_0^1 \Delta\bar{T}(\hat{z}) \exp(-d\beta_{pr}\hat{z}) d\hat{z} \\ &= d \left[\frac{t_0}{2} \int_0^1 \exp(-d\beta_{pr}\hat{z}) d\hat{z} + \sum_{m=1}^{\infty} t_m \int_0^1 \exp(-d\beta_{pr}\hat{z}) \cos(m\pi\hat{z}) d\hat{z} \right] \\ &= d \left[\frac{t_0}{2d\beta_{pr}} (1 - \exp(-d\beta_{pr})) \right. \\ &\quad \left. + d\beta_{pr} \sum_{m=1}^{\infty} \frac{t_m}{m^2\pi^2 + d^2\beta_{pr}^2} (1 - (-1)^m \exp(-d\beta_{pr})) \right] \end{aligned}$$

The resulting solution (t_m) is used to calculate the temperature profile $\Delta\bar{T}(\eta, q, z)$ (equation A.32) and the phonon energy distribution functions $G_{\omega}^{+}(z, \mu_i, \phi_j)$ and $G_{\omega}^{-}(z, -\mu_i, \phi_j)$ (equation A.12) for each η and q as follows:

First, the expressions for $I_{\mu\phi}^{+}$ and $I_{\mu\phi}^{-}$ are simplified as

$$\begin{aligned} I_{\mu\phi}^{+} &= C_{\omega} \int_0^d \Delta\bar{T} \exp\left(-\frac{\gamma_{\mu\phi}^{\text{FS}}}{\mu\Lambda_{\omega}} z'\right) dz' + \frac{\bar{Q}_{\omega}^0 \tau_{\omega}}{\beta_p + \frac{\gamma_{\mu\phi}^{\text{FS}}}{\mu\Lambda_{\omega}}} \left(1 - \exp\left(-\left[\beta_p + \frac{\gamma_{\mu\phi}^{\text{FS}}}{\mu\Lambda_{\omega}}\right] d\right)\right) \\ &= C_{\omega} d \left(\frac{1}{2} t_0 \frac{\mu\text{Kn}_{\omega}^d}{\gamma_{\mu\phi}^{\text{FS}}} \left(1 - \exp\left(-\frac{\gamma_{\mu\phi}^{\text{FS}}}{\mu\text{Kn}_{\omega}^d}\right)\right) + \sum_{m=1}^N t_m I_1(m) \right) \\ &\quad + \frac{\bar{Q}_{\omega}^0 \tau_{\omega}}{\beta_p + \frac{\gamma_{\mu\phi}^{\text{FS}}}{\mu\Lambda_{\omega}}} \left(1 - \exp\left(-\left[\beta_p + \frac{\gamma_{\mu\phi}^{\text{FS}}}{\mu\Lambda_{\omega}}\right] d\right)\right) \end{aligned}$$

$$\begin{aligned}
I_{\mu\phi}^- &= C_\omega \int_0^d \Delta \bar{T} \exp\left(-\frac{\gamma_{\mu\phi}^{\text{FS}}}{\mu\Lambda_\omega} z'\right) dz' + \frac{\bar{Q}_\omega^0 \tau_\omega}{\beta_p - \frac{\gamma_{\mu\phi}^{\text{FS}}}{\mu\Lambda_\omega}} \left(\exp\left(-\frac{\gamma_{\mu\phi}^{\text{FS}}}{\mu\Lambda_\omega} d\right) - \exp(-\beta_p d) \right) \\
&= C_\omega d \left(\frac{1}{2} t_0 \frac{\mu \text{Kn}_\omega^d}{\gamma_{\mu\phi}^{\text{FS}}} \left(1 - \exp\left(-\frac{\gamma_{\mu\phi}^{\text{FS}}}{\mu \text{Kn}_\omega^d} \right) \right) + \sum_{m=1}^N t_m I_2(m) \right) \\
&\quad + \frac{\bar{Q}_\omega^0 \tau_\omega}{\beta_p - \frac{\gamma_{\mu\phi}^{\text{FS}}}{\mu\Lambda_\omega}} \left(\exp\left(-\frac{\gamma_{\mu\phi}^{\text{FS}}}{\mu\Lambda_\omega} d\right) - \exp(-\beta_p d) \right)
\end{aligned}$$

where $\text{Kn}_\omega^d = \Lambda_\omega/d$ is the Knudsen number of a phonon mode defined based on the thickness of the thin film. Next, using the expressions for $I_{\mu\phi}^+$ and $I_{\mu\phi}^-$, the expressions for $\bar{c}_\omega^+(0, \mu'_i, \phi'_j)$ and $\bar{c}_\omega^-(d, \mu'_i, \phi'_j)$ are evaluated and finally, the expressions for $G_\omega^+(\hat{z}, \mu_i, \phi_j)$ and $G_\omega^-(\hat{z}, -\mu_i, \phi_j)$ are evaluated as,

$$\begin{aligned}
G_\omega^+(\hat{z}, \mu_i, \phi_j) &= \left(\sum_{i'j'} [T_{kk'}^+ \bar{c}_\omega^+(0, \mu_{i'}, \phi_{j'}) + T_{kk'}^- \bar{c}_\omega^-(d, \mu_{i'}, \phi_{j'})] \right) \exp\left(-\frac{\gamma_{ij}^{\text{FS}}}{\mu_i \text{Kn}_\omega^d} \hat{z}\right) \\
&\quad + \frac{C_\omega t_0}{8\pi \gamma_{ij}^{\text{FS}}} \left[1 - \exp\left(-\frac{\gamma_{ij}^{\text{FS}}}{\mu_i \text{Kn}_\omega^d} \hat{z}\right) \right] + \frac{C_\omega}{4\pi \mu_i \text{Kn}_\omega^d} \sum_{m=1}^N t_m I_3^1(m; \hat{z}) \\
&\quad + \frac{\bar{Q}_\omega^0 \tau_\omega}{4\pi \mu_i \Lambda_\omega} \left[\frac{\exp\left(-\frac{\gamma_{ij}^{\text{FS}}}{\mu_i \text{Kn}_\omega^d} \hat{z}\right) - \exp(-d\beta_p \hat{z})}{\beta_p - \frac{\gamma_{ij}^{\text{FS}}}{\mu_i \Lambda_\omega}} \right] \\
G_\omega^-(\hat{z}, -\mu_i, \phi_j) &= \left(\sum_{i'j'} [B_{kk'}^+ \bar{c}_\omega^+(0, \mu_{i'}, \phi_{j'}) + B_{kk'}^- \bar{c}_\omega^-(d, \mu_{i'}, \phi_{j'})] \right) \\
&\quad \times \exp\left(-\frac{\gamma_{ij}^{\text{FS}}}{\mu_i \text{Kn}_\omega^d} (1 - \hat{z})\right) \\
&\quad + \frac{C_\omega t_0}{8\pi \gamma_{ij}^{\text{FS}}} \left[1 - \exp\left(-\frac{\gamma_{ij}^{\text{FS}}}{\mu_i \text{Kn}_\omega^d} [1 - \hat{z}]\right) \right] + \frac{C_\omega}{4\pi \mu_i \text{Kn}_\omega^d} \sum_{m=1}^N t_m I_3^2(m; \hat{z}) \\
&\quad + \frac{\bar{Q}_\omega^0 \tau_\omega \exp\left(\frac{\gamma_{ij}^{\text{FS}}}{\mu_i \text{Kn}_\omega^d} \hat{z}\right)}{4\pi \mu_i \Lambda_\omega} \left[\frac{\exp\left(-\left(d\beta_p + \frac{\gamma_{ij}^{\text{FS}}}{\mu_i \text{Kn}_\omega^d}\right) \hat{z}\right) - \exp\left(-\left(d\beta_p + \frac{\gamma_{ij}^{\text{FS}}}{\mu_i \text{Kn}_\omega^d}\right)\right)}{\left[\beta_p + \frac{\gamma_{ij}^{\text{FS}}}{\mu_i \Lambda_\omega}\right]} \right]
\end{aligned} \tag{A.50}$$

where,

$$\begin{aligned}
I_3^1(m; \hat{z}) &= \int_0^{\hat{z}'} \exp\left(-\frac{\gamma_{ij}^{\text{FS}}}{\mu_i \text{Kn}_\omega^d} [\hat{z}' - \hat{z}]\right) \cos(m\pi \hat{z}) \, d\hat{z} \\
&= \frac{1}{m^2 \pi^2 + \left(\frac{\gamma_{ij}^{\text{FS}}}{\mu_i \text{Kn}_\omega^d}\right)^2} \left[\left(\frac{\gamma_{ij}^{\text{FS}}}{\mu_i \text{Kn}_\omega^d} \cos(m\pi \hat{z}') + m\pi \sin(m\pi \hat{z}') \right) \right. \\
&\quad \left. - \frac{\gamma_{ij}^{\text{FS}}}{\mu_i \text{Kn}_\omega^d} \exp\left(-\frac{\gamma_{ij}^{\text{FS}}}{\mu_i \text{Kn}_\omega^d} \hat{z}'\right) \right] \\
I_3^2(m; \hat{z}) &= \int_{\hat{z}'}^1 \exp\left(\frac{\gamma_{ij}^{\text{FS}}}{\mu_i \text{Kn}_\omega^d} [\hat{z}' - \hat{z}]\right) \cos(m\pi \hat{z}) \, d\hat{z} \\
&= \frac{1}{m^2 \pi^2 + \left(\frac{\gamma_{ij}^{\text{FS}}}{\mu_i \text{Kn}_\omega^d}\right)^2} \left[\left(-\frac{\gamma_{ij}^{\text{FS}}}{\mu_i \text{Kn}_\omega^d} (-1)^m \right) \exp\left(-\frac{\gamma_{ij}^{\text{FS}}}{\mu_i \text{Kn}_\omega^d} (1 - \hat{z}')\right) \right. \\
&\quad \left. - \left(-\frac{\gamma_{ij}^{\text{FS}}}{\mu_i \text{Kn}_\omega^d} \cos(m\pi \hat{z}') + m\pi \sin(m\pi \hat{z}') \right) \right]
\end{aligned}$$

Once again, as in the steady state condition, these general solutions for G_ω are substituted into the expression for heat flux and the suppression in thermal conductivity due to phonon boundary scattering is derived for the transient transport condition in the main article.

Appendix B

**THE EFFECT OF PHONON MODE CONVERSION AT
BOUNDARIES ON THE THERMAL TRANSPORT THROUGH
THIN FILMS**

In this appendix, we describe the derivation for transient thermal transport in the TG experiment through thin membranes considering the effect of phonon mode conversion at the material boundaries.

B.1 Numerical Discretization of the Boundary Conditions

The general boundary conditions at the thin film walls are given by the following:

For $\mu \in (0, 1]$,

$$v_{\omega,s'} g_{\omega,s'}^+(0, \mu, \phi) = \sum_s \left(\alpha_{\omega,s's}^{\text{spec}} p_{\omega,s} v_{\omega,s} g_{\omega,s}^-(0, -\mu, \phi) \right. \\ \left. - \alpha_{\omega,s's}^{\text{diff}} \frac{(1 - p_{\omega,s})}{\pi} v_{\omega,s} \int_0^{2\pi} \int_{-1}^0 g_{\omega,s}^-(0, \mu', \phi') \mu' d\mu' d\phi' \right)$$

and for $\mu \in [-1, 0)$,

$$v_{\omega,s'} g_{\omega,s'}^-(d, \mu, \phi) = \sum_s \left(\alpha_{\omega,s's}^{\text{spec}} p_{\omega,s} v_{\omega,s} g_{\omega,s}^+(d, -\mu, \phi) \right. \\ \left. + \alpha_{\omega,s's}^{\text{diff}} \frac{(1 - p_{\omega,s})}{\pi} v_{\omega,s} \int_0^{2\pi} \int_0^1 g_{\omega,s}^+(d, \mu', \phi') \mu' d\mu' d\phi' \right) \quad (\text{B.1})$$

In the frequency domain, the boundary conditions (equation B.1) can be written as follows:

For $\mu \in (0, 1]$,

$$\begin{aligned} \nu_{\omega,s'} G_{\omega,s'}^+(0, \mu, \phi) = & \sum_s \left(\alpha_{\omega,s's}^{\text{spec}} p_{\omega,s} \nu_{\omega,s} G_{\omega,s}^-(0, -\mu, \phi) \right. \\ & \left. - \alpha_{\omega,s's}^{\text{diff}} \frac{(1 - p_{\omega,s})}{\pi} \nu_{\omega,s} \int_0^{2\pi} \int_{-1}^0 G_{\omega,s}^-(0, \mu', \phi') \mu' d\mu' d\phi' \right) \end{aligned}$$

and for $\mu \in [-1, 0)$,

$$\begin{aligned} \nu_{\omega,s'} G_{\omega,s'}^-(d, \mu, \phi) = & \sum_s \left(\alpha_{\omega,s's}^{\text{spec}} p_{\omega,s} \nu_{\omega,s} G_{\omega,s}^+(d, -\mu, \phi) \right. \\ & \left. + \alpha_{\omega,s's}^{\text{diff}} \frac{(1 - p_{\omega,s})}{\pi} \nu_{\omega,s} \int_0^{2\pi} \int_0^1 G_{\omega,s}^+(d, \mu', \phi') \mu' d\mu' d\phi' \right) \end{aligned} \quad (\text{B.2})$$

For any given μ and ϕ , there are four unknown quantities to be determined at the thin film boundaries: $G_{\omega,s}^+(0, \mu, \phi)$, $G_{\omega,s}^-(0, -\mu, \phi)$, $G_{\omega,s}^+(d, -\mu, \phi)$, and $G_{\omega,s}^-(d, \mu, \phi)$, while there are only two equations which are directly evident (equation B.2). However, closed-form relations for these four unknown quantities can be obtained in terms of the unknown temperature distribution at the thin film boundaries in the frequency domain ($\Delta\bar{T}(z=0)$ and $\Delta\bar{T}(z=d)$) by substituting the general solution of the BTE (equation 5.16 in the main article) into boundary conditions to get the

following:

For $\mu \in (0, 1]$,

$$\begin{aligned}
v_{\omega,s'} G_{\omega,s'}^+(0, \mu, \phi) &= \sum_s \left(\alpha_{\omega,s's}^{\text{spec}} p_{\omega,s} v_{\omega,s} G_{\omega,s}^-(d, -\mu, \phi) \exp\left(-\frac{\gamma_{\mu\phi}^{\omega,s}}{\mu\Lambda_{\omega,s}} d\right) \right. \\
&+ \frac{\alpha_{\omega,s's}^{\text{spec}} p_{\omega,s} v_{\omega,s}}{4\pi\mu\Lambda_{\omega,s}} \int_0^d (C_{\omega,s}\Delta\bar{T} + \bar{Q}_{\omega,s}\tau_{\omega,s}) \exp\left(-\frac{\gamma_{\mu\phi}^{\omega,s}}{\mu\Lambda_{\omega,s}} z'\right) dz' \\
&- \frac{\alpha_{\omega,s's}^{\text{diff}} (1-p_{\omega,s}) v_{\omega,s}}{\pi} \int_0^{2\pi} \int_{-1}^0 G_{\omega,s}^-(d, \mu', \phi') \exp\left(\frac{\gamma_{\mu'\phi'}^{\omega,s}}{\mu'\Lambda_{\omega,s}} d\right) \mu' d\mu' d\phi' \\
&+ \frac{\alpha_{\omega,s's}^{\text{diff}} (1-p_{\omega,s}) v_{\omega,s}}{4\pi^2\Lambda_{\omega,s}} \\
&\times \int_0^{2\pi} \int_{-1}^0 \int_0^d (C_{\omega,s}\Delta\bar{T} + \bar{Q}_{\omega,s}\tau_{\omega,s}) \exp\left(\frac{\gamma_{\mu'\phi'}^{\omega,s}}{\mu'\Lambda_{\omega,s}} z'\right) dz' d\mu' d\phi' \Big)
\end{aligned}$$

and for $\mu \in [-1, 0)$,

$$\begin{aligned}
v_{\omega,s'} G_{\omega,s'}^-(d, \mu, \phi) &= \sum_s \left(\alpha_{\omega,s's}^{\text{spec}} p_{\omega,s} v_{\omega,s} G_{\omega,s}^+(0, -\mu, \phi) \exp\left(\frac{\gamma_{\mu\phi}^{\omega,s}}{\mu\Lambda_{\omega,s}} d\right) \right. \\
&- \frac{\alpha_{\omega,s's}^{\text{spec}} p_{\omega,s} v_{\omega,s} \exp\left(\frac{\gamma_{\mu\phi}^{\omega,s}}{\mu\Lambda_{\omega,s}} d\right)}{4\pi\mu\Lambda_{\omega,s}} \int_0^d (C_{\omega,s}\Delta\bar{T} + \bar{Q}_{\omega,s}\tau_{\omega,s}) \exp\left(-\frac{\gamma_{\mu\phi}^{\omega,s}}{\mu\Lambda_{\omega,s}} z'\right) dz' \\
&+ \frac{\alpha_{\omega,s's}^{\text{diff}} (1-p_{\omega,s}) v_{\omega,s}}{\pi} \int_0^{2\pi} \int_0^1 G_{\omega,s}^+(0, \mu', \phi') \exp\left(-\frac{\gamma_{\mu'\phi'}^{\omega,s}}{\mu'\Lambda_{\omega,s}} d\right) \mu' d\mu' d\phi' \\
&+ \frac{\alpha_{\omega,s's}^{\text{diff}} (1-p_{\omega,s}) v_{\omega,s}}{4\pi^2\Lambda_{\omega,s}} \int_0^{2\pi} \int_0^1 \exp\left(-\frac{\gamma_{\mu'\phi'}^{\omega,s}}{\mu'\Lambda_{\omega,s}} d\right) \int_0^d (C_{\omega,s}\Delta\bar{T} + \bar{Q}_{\omega,s}\tau_{\omega,s}) \\
&\times \exp\left(\frac{\gamma_{\mu'\phi'}^{\omega,s}}{\mu'\Lambda_{\omega,s}} z'\right) dz' d\mu' d\phi' \Big)
\end{aligned}$$

(B.3)

For convenience, the limits on variables μ and μ' are changed from $[-1, 1]$ to $(0, 1]$ in equation B.3 wherever necessary to obtain

$$\begin{aligned}
v_{\omega,s'} G_{\omega,s'}^+(0, \mu, \phi) &= \sum_s \left(\alpha_{\omega,s's}^{\text{spec}} p_{\omega,\omega} v_{\omega,s} G_{\omega,s}^-(d, -\mu, \phi) \exp\left(-\frac{\gamma_{\mu\phi}^{\omega,s}}{\mu\Lambda_{\omega,s}} d\right) \right. \\
&+ \frac{\alpha_{\omega,s's}^{\text{spec}} p_{\omega,s} v_{\omega,s}}{4\pi\mu\Lambda_{\omega,s}} \int_0^d (C_{\omega,s}\Delta\bar{T} + \bar{Q}_{\omega,s}\tau_{\omega,s}) \exp\left(-\frac{\gamma_{\mu\phi}^{\omega,s}}{\mu\Lambda_{\omega,s}} z'\right) dz' \\
&+ \frac{\alpha_{\omega,s's}^{\text{diff}} (1-p_{\omega,s}) v_{\omega,s}}{\pi} \int_0^{2\pi} \int_0^1 G_{\omega,s}^-(d, -\mu', \phi') \exp\left(-\frac{\gamma_{\mu'\phi'}^{\omega,s}}{\mu'\Lambda_{\omega,s}} d\right) \mu' d\mu' d\phi' \\
&+ \frac{\alpha_{\omega,m'm}^{\text{diff}} (1-p_{\omega,s}) v_{\omega,s}}{4\pi^2\Lambda_{\omega,s}} \int_0^{2\pi} \int_0^1 \int_0^d (C_{\omega,s}\Delta\bar{T} + \bar{Q}_{\omega,s}\tau_{\omega,s}) \\
&\quad \times \exp\left(-\frac{\gamma_{\mu'\phi'}^{\omega,s}}{\mu'\Lambda_{\omega,s}} z'\right) dz' d\mu' d\phi' \Big) \\
v_{\omega,s'} G_{\omega,s'}^-(d, -\mu, \phi) &= \sum_s \left(\alpha_{\omega,s's}^{\text{spec}} p_{\omega,s} v_{\omega,s} G_{\omega,s}^+(0, \mu, \phi) \exp\left(-\frac{\gamma_{\mu\phi}^{\omega,s}}{\mu\Lambda_{\omega,s}} d\right) \right. \\
&+ \frac{\alpha_{\omega,s's}^{\text{spec}} p_{\omega,s} v_{\omega,s}}{4\pi\mu\Lambda_{\omega,s}} \int_0^d (C_{\omega,s}\Delta\bar{T} + \bar{Q}_{\omega,s}\tau_{\omega,s}) \exp\left(-\frac{\gamma_{\mu\phi}^{\omega,s}}{\mu\Lambda_{\omega,s}} (d-z')\right) dz' \\
&+ \frac{\alpha_{\omega,s's}^{\text{diff}} (1-p_{\omega,s}) v_{\omega,s}}{\pi} \int_0^{2\pi} \int_0^1 G_{\omega,s}^+(0, \mu', \phi') \exp\left(-\frac{\gamma_{\mu'\phi'}^{\omega,s}}{\mu'\Lambda_{\omega,s}} d\right) \mu' d\mu' d\phi' \\
&+ \frac{\alpha_{\omega,s's}^{\text{diff}} (1-p_{\omega,s}) v_{\omega,s}}{4\pi^2\Lambda_{\omega,s}} \int_0^{2\pi} \int_0^1 \int_0^d (C_{\omega,s}\Delta\bar{T} + \bar{Q}_{\omega,s}\tau_{\omega,s}) \\
&\quad \times \exp\left(-\frac{\gamma_{\mu'\phi'}^{\omega,s}}{\mu'\Lambda_{\omega,s}} (d-z')\right) dz' d\mu' d\phi' \Big)
\end{aligned} \tag{B.4}$$

Equation B.4 represents a system of integral equations to solve for the two unknown quantities $G_{\omega,s}^+(0, \mu, \phi)$ and $G_{\omega,s}^-(d, -\mu, \phi)$ for every μ and ϕ . To solve this system of equations, the integrals in μ' and ϕ' variables are first discretized using Gauss quadrature,

$$\int_0^{2\pi} \int_0^1 f(\mu', \phi') d\mu' d\phi' = \sum_{ij} f(\mu_i, \phi_j) w_{\mu_i} w_{\phi_j} \tag{B.5}$$

where μ_i and ϕ_j are the quadrature points and w_{μ_i} and w_{ϕ_j} are the corresponding weights. Therefore, equation B.4 transforms into,

$$\begin{aligned}
v_{\omega,s'} G_{\omega,s'}^+ (0, \mu_i, \phi_j) &= \sum_s \left(\alpha_{\omega,s's}^{\text{spec}} p_{\omega,s} v_{\omega,s} G_{\omega,s}^- (d, -\mu_i, \phi_j) \exp\left(-\frac{\gamma_{ij}^{\omega,s}}{\mu_i \Lambda_{\omega,s}} d\right) \right. \\
&+ \frac{\alpha_{\omega,s's}^{\text{spec}} p_{\omega,s} v_{\omega,s}}{4\pi \mu_i \Lambda_{\omega,s}} \int_0^d (C_{\omega,s} \Delta \bar{T} + \bar{Q}_{\omega,s} \tau_{\omega,s}) \exp\left(-\frac{\gamma_{ij}^{\omega,s}}{\mu_i \Lambda_{\omega,s}} z'\right) dz' \\
&+ \frac{\alpha_{\omega,s's}^{\text{diff}} (1 - p_{\omega,s}) v_{\omega,s}}{\pi} \sum_{i'j'} G_{\omega,s}^- (d, -\mu_{i'}, \phi_{j'}) \exp\left(-\frac{\gamma_{i'j'}^{\omega,s}}{\mu_{i'} \Lambda_{\omega,s}} d\right) \mu_{i'} w_{\mu_{i'}} w_{\phi_{j'}} \\
&+ \frac{\alpha_{\omega,s's}^{\text{diff}} (1 - p_{\omega,s})}{4\pi^2 \Lambda_{\omega,s}} \sum_{i'j'} \int_0^d (C_{\omega,s} \Delta \bar{T} + \bar{Q}_{\omega,s} \tau_{\omega,s}) \exp\left(-\frac{\gamma_{i'j'}^{\omega,s}}{\mu_{i'} \Lambda_{\omega,s}} z'\right) dz' \\
&\left. \times w_{\mu_{i'}} w_{\phi_{j'}} \right) \\
v_{\omega,s'} G_{\omega,s'}^- (d, -\mu_i, \phi_j) &= \sum_s \left(\alpha_{\omega,s's}^{\text{spec}} p_{\omega,s} v_{\omega,s} G_{\omega,s}^+ (0, \mu_i, \phi_j) \exp\left(-\frac{\gamma_{ij}^{\omega,s}}{\mu_i \Lambda_{\omega,s}} d\right) \right. \\
&+ \frac{\alpha_{\omega,s's}^{\text{spec}} p_{\omega,s} v_{\omega,s}}{4\pi \mu_i \Lambda_{\omega,s}} \int_0^d (C_{\omega,s} \Delta \bar{T} + \bar{Q}_{\omega,s} \tau_{\omega,s}) \exp\left(-\frac{\gamma_{ij}^{\omega,s}}{\mu_i \Lambda_{\omega,s}} (d - z')\right) dz' \\
&+ \frac{\alpha_{\omega,s's}^{\text{diff}} (1 - p_{\omega,s}) v_{\omega,s}}{\pi} \sum_{i'j'} G_{\omega,s}^+ (0, \mu_{i'}, \phi_{j'}) \exp\left(-\frac{\gamma_{i'j'}^{\omega,s}}{\mu_{i'} \Lambda_{\omega,s}} d\right) \mu_{i'} w_{\mu_{i'}} w_{\phi_{j'}} \\
&+ \frac{\alpha_{\omega,s's}^{\text{diff}} (1 - p_{\omega,s}) v_{\omega,s}}{4\pi^2 \Lambda_{\omega,s}} \sum_{i'j'} \int_0^d (C_{\omega,s} \Delta \bar{T} + \bar{Q}_{\omega,s} \tau_{\omega,s}) \\
&\left. \times \exp\left(-\frac{\gamma_{i'j'}^{\omega,s}}{\mu_{i'} \Lambda_{\omega,s}} (d - z')\right) dz' w_{\mu_{i'}} w_{\phi_{j'}} \right]
\end{aligned}$$

(B.6)

To simplify these expressions, we substitute the following into equation B.6:

$$\begin{aligned}
I_{\mu\phi,s}^+ &= \int_0^d (C_{\omega,s}\Delta\bar{T} + \bar{Q}_{\omega,s}\tau_{\omega,s}) \exp\left(-\frac{\gamma_{\mu\phi}^{\omega,s}}{\mu\Lambda_{\omega,s}}z'\right) dz' \\
&= C_{\omega,s} \int_0^d \Delta\bar{T} \exp\left(-\frac{\gamma_{\mu\phi}^{\omega,s}}{\mu\Lambda_{\omega,s}}z'\right) dz' + \bar{Q}_{\omega,s}\tau_{\omega,s}\Lambda_{\omega,s}\frac{\mu}{\gamma_{\mu\phi}^{\omega,s}} \left(1 - \exp\left(-\frac{\gamma_{\mu\phi}^{\omega,s}}{\mu\Lambda_{\omega,s}}d\right)\right) \\
I_{\mu\phi,s}^- &= \int_0^d (C_{\omega,s}\Delta\bar{T} + \bar{Q}_{\omega,s}\tau_{\omega,s}) \exp\left(-\frac{\gamma_{\mu\phi}^{\omega,s}}{\mu\Lambda_{\omega,s}}(d-z')\right) dz' \\
&= C_{\omega,s} \int_0^d \Delta\bar{T} \exp\left(-\frac{\gamma_{\mu\phi}^{\omega,s}}{\mu\Lambda_{\omega,s}}(d-z')\right) dz' \\
&\quad + \bar{Q}_{\omega,s}\tau_{\omega,s}\Lambda_{\omega,s}\frac{\mu}{\gamma_{\mu\phi}^{\omega,s}} \left(1 - \exp\left(-\frac{\gamma_{\mu\phi}^{\omega,s}}{\mu\Lambda_{\omega,s}}d\right)\right)
\end{aligned} \tag{B.7}$$

which transform equation B.6 into

$$\begin{aligned}
v_{\omega,s'}G_{\omega,s'}^+(0, \mu_i, \phi_j) &= \sum_s \left(\alpha_{\omega,s's}^{\text{spec}} p_{\omega,s} v_{\omega,s} G_{\omega,s}^-(d, -\mu_i, \phi_j) \exp\left(-\frac{\gamma_{ij}^{\omega,s}}{\mu_i\Lambda_{\omega,s}}d\right) \right. \\
&\quad + \frac{\alpha_{\omega,s's}^{\text{spec}} p_{\omega,s} v_{\omega,s}}{4\pi\mu_i\Lambda_{\omega,s}} I_{ij,\omega s}^+ \\
&\quad + \frac{\alpha_{\omega,s's}^{\text{diff}} (1-p_{\omega,s}) v_{\omega,s}}{\pi} \sum_{i'j'} G_{\omega,s}^-(d, -\mu_{i'}, \phi_{j'}) \exp\left(-\frac{\gamma_{i'j'}^{\omega,s}}{\mu_{i'}\Lambda_{\omega,s}}d\right) \mu_{i'} w_{\mu_{i'}} w_{\phi_{j'}} \\
&\quad \left. + \frac{\alpha_{\omega,s's}^{\text{diff}} (1-p_{\omega,s}) v_{\omega,s}}{4\pi^2\Lambda_{\omega,s}} \sum_{i'j'} w_{\mu_{i'}} w_{\phi_{j'}} I_{i'j',\omega s}^+ \right) \\
v_{\omega,s'}G_{\omega,s'}^-(d, -\mu_i, \phi_j) &= \sum_s \left(\alpha_{\omega,s's}^{\text{spec}} p_{\omega,s} v_{\omega,s} G_{\omega,s}^+(0, \mu_i, \phi_j) \exp\left(-\frac{\gamma_{ij}^{\omega,s}}{\mu_i\Lambda_{\omega,s}}d\right) \right. \\
&\quad + \frac{\alpha_{\omega,s's}^{\text{spec}} p_{\omega,s} v_{\omega,s}}{4\pi\mu_i\Lambda_{\omega,s}} I_{ij,\omega s}^- \\
&\quad + \frac{\alpha_{\omega,s's}^{\text{diff}} (1-p_{\omega,s}) v_{\omega,s}}{\pi} \sum_{i'j'} G_{\omega,s}^+(0, \mu_{i'}, \phi_{j'}) \exp\left(-\frac{\gamma_{i'j'}^{\omega,s}}{\mu_{i'}\Lambda_{\omega,s}}d\right) \mu_{i'} w_{\mu_{i'}} w_{\phi_{j'}} \\
&\quad \left. + \frac{\alpha_{\omega,s's}^{\text{diff}} (1-p_{\omega,s}) v_{\omega,s}}{4\pi^2\Lambda_{\omega,s}} \sum_{i'j'} w_{\mu_{i'}} w_{\phi_{j'}} I_{i'j',\omega s}^+ \right)
\end{aligned} \tag{B.8}$$

These discretized boundary conditions (equation B.8) can be written in a concise matrix form as

$$[A]\mathbf{G}_{\text{BC}} = \bar{\mathbf{c}} \tag{B.9}$$

with the solution of the form

$$\mathbf{G}_{\text{BC}} = [\mathbf{A}]^{-1} \bar{\mathbf{c}} \quad (\text{B.10})$$

where,

$$\mathbf{G}_{\text{BC}} = \begin{pmatrix} G_{\omega,1}^+(0, \mu_i, \phi_j) \\ G_{\omega,1}^-(d, -\mu_i, \phi_j) \\ \dots \\ G_{\omega,s}^+(0, \mu_i, \phi_j) \\ G_{\omega,s}^-(d, -\mu_i, \phi_j) \end{pmatrix}_{[2NM \times 1]}$$

$$[\mathbf{A}]^{-1} = \begin{bmatrix} T_{kk',11}^+ & T_{kk',11}^- & \dots & \dots \\ B_{kk',11}^+ & B_{kk',11}^- & \dots & \dots \\ & & \ddots & \\ \dots & \dots & T_{kk',MM}^+ & T_{kk',MM}^- \\ \dots & \dots & B_{kk',MM}^+ & B_{kk',MM}^- \end{bmatrix}_{[2NM \times 2NM]}$$

and

$$\bar{\mathbf{c}} = \begin{pmatrix} \bar{c}_{\omega,1}^+(0, \mu_{i'}, \phi_{j'}) \\ \bar{c}_{\omega,1}^-(d, \mu_{i'}, \phi_{j'}) \\ \dots \\ \bar{c}_{\omega,s}^+(0, \mu_{i'}, \phi_{j'}) \\ \bar{c}_{\omega,s}^-(d, \mu_{i'}, \phi_{j'}) \end{pmatrix}_{[2NM \times 1]}$$

Here, k is the index for the combination $\{\mu_i, \phi_j\}$, N is the total number of combinations of $\{\mu_i, \phi_j\}$ and

$$\begin{aligned} \bar{c}_{\omega,s'}^+(0, \mu_{i'}, \phi_{j'}) &= \sum_s \left(\frac{\alpha_{\omega,s's}^{\text{spec}} p_{\omega,s} v_{\omega,s}}{4\pi \mu_{i'} \Lambda_{\omega,s}} I_{i'j',\omega s}^+ \right. \\ &\quad \left. + \frac{\alpha_{\omega,s's}^{\text{diff}} (1 - p_{\omega,s}) v_{\omega,s}}{4\pi^2 \Lambda_{\omega,s}} \sum_{i''j''} w_{\mu_{i''}} w_{\phi_{j''}} I_{i''j'',\omega s}^+ \right) \\ \bar{c}_{\omega,s'}^-(d, \mu_{i'}, \phi_{j'}) &= \sum_s \left(\frac{\alpha_{\omega,s's}^{\text{spec}} p_{\omega,s} v_{\omega,s}}{4\pi \mu_{i'} \Lambda_{\omega,s}} I_{i'j',\omega s}^- \right. \\ &\quad \left. + \frac{\alpha_{\omega,s's}^{\text{diff}} (1 - p_{\omega,s}) v_{\omega,s}}{4\pi^2 \Lambda_{\omega,s}} \sum_{i''j''} w_{\mu_{i''}} w_{\phi_{j''}} I_{i''j'',\omega s}^- \right) \end{aligned} \quad (\text{B.11})$$

With the substitution of equation B.10, the general BTE solution becomes,

$$\begin{aligned}
G_{\omega,s'}^+(z, \mu_i, \phi_j) &= \left(\sum_{i'j'} \sum_s [T_{kk',s's}^+ \bar{c}_{\omega,s}^+(0, \mu_{i'}, \phi_{j'}) + T_{kk',s's}^- \bar{c}_{\omega,s}^-(d, \mu_{i'}, \phi_{j'})] \right) \\
&\quad \times \exp\left(-\frac{\gamma_{ij}^{\omega,s'}}{\mu_i \Lambda_{\omega,s'}} z\right) \\
&\quad + \frac{\exp\left(-\frac{\gamma_{ij}^{\omega,s'}}{\mu_i \Lambda_{\omega,s'}} z\right)}{4\pi \mu_i \Lambda_{\omega,s'}} \int_0^z (C_{\omega,s'} \Delta \bar{T} + \bar{Q}_{\omega,s'} \tau_{\omega,s'}) \exp\left(\frac{\gamma_{ij}^{\omega,s'}}{\mu_i \Lambda_{\omega,s'}} z'\right) dz' \\
&= \left(\sum_{i'j'} \sum_s [T_{kk',s's}^+ \bar{c}_{\omega,s}^+(0, \mu_{i'}, \phi_{j'}) + T_{kk',s's}^- \bar{c}_{\omega,s}^-(d, \mu_{i'}, \phi_{j'})] \right) \\
&\quad \times \exp\left(-\frac{\gamma_{ij}^{\omega,s'}}{\mu_i \Lambda_{\omega,s'}} z\right) \\
&\quad + \frac{1}{4\pi \mu_i \Lambda_{\omega,s'}} \int_0^z (C_{\omega,s'} \Delta \bar{T} + \bar{Q}_{\omega,s'} \tau_{\omega,s'}) \exp\left(-\frac{\gamma_{ij}^{\omega,s'}}{\mu_i \Lambda_{\omega,s'}} |z' - z|\right) dz' \\
G_{\omega,s'}^-(z, -\mu_i, \phi_j) &= \left(\sum_{i'j'} \sum_s [B_{kk',s's}^+ \bar{c}_{\omega,s}^+(0, \mu_{i'}, \phi_{j'}) + B_{kk',s's}^- \bar{c}_{\omega,s}^-(d, \mu_{i'}, \phi_{j'})] \right) \\
&\quad \times \exp\left(-\frac{\gamma_{ij}^{\omega,s'}}{\mu_i \Lambda_{\omega,s'}} (d - z)\right) \\
&\quad + \frac{\exp\left(\frac{\gamma_{ij}^{\omega,s'}}{\mu_i \Lambda_{\omega,s'}} z\right)}{4\pi \mu_i \Lambda_{\omega,s'}} \int_z^d (C_{\omega,s'} \Delta \bar{T} + \bar{Q}_{\omega,s'} \tau_{\omega,s'}) \exp\left(-\frac{\gamma_{ij}^{\omega,s'}}{\mu_i \Lambda_{\omega,s'}} z'\right) dz' \\
&= \left(\sum_{i'j'} \sum_s [B_{kk',s's}^+ \bar{c}_{\omega,s}^+(0, \mu_{i'}, \phi_{j'}) + B_{kk',s's}^- \bar{c}_{\omega,s}^-(d, \mu_{i'}, \phi_{j'})] \right) \\
&\quad \times \exp\left(-\frac{\gamma_{ij}^{\omega,s'}}{\mu_i \Lambda_{\omega,s'}} (d - z)\right) \\
&\quad + \frac{1}{4\pi \mu_i \Lambda_{\omega,s'}} \int_z^d (C_{\omega,s'} \Delta \bar{T} + \bar{Q}_{\omega,s'} \tau_{\omega,s'}) \exp\left(-\frac{\gamma_{ij}^{\omega,s'}}{\mu_i \Lambda_{\omega,s'}} |z' - z|\right) dz'
\end{aligned} \tag{B.12}$$

where the unknown quantities $G_{\omega,s}^+(z, \mu_i, \phi_j)$, $G_{\omega,s}^-(z, -\mu_i, \phi_j)$, and $\Delta \bar{T}$ are related through the energy conservation requirement.

B.2 Formulation of the Integral Equation for $\Delta\bar{T}$

To solve for the unknown quantities ($G_{\omega,s}^+(z, \mu_i, \phi_j)$, $G_{\omega,s}^-(z, -\mu_i, \phi_j)$, and $\Delta\bar{T}$), the energy conservation equation is first discretized in the angular variables (μ and ϕ) using Gauss quadrature (equation B.5). Next, the general solution (equation B.12) is substituted into the discretized energy conservation equation to obtain the following integral equation for $\Delta\bar{T}$:

$$\begin{aligned}
\Delta\bar{T}(z) &= \frac{1}{\sum_{s'} \int_{\omega=0}^{\omega_m} \frac{C_{\omega,s'}}{\tau_{\omega,s'}} d\omega} \\
&\quad \times \sum_{s'} \int_{\omega=0}^{\omega'_m} \left[\frac{1}{\tau_{\omega,s'}} \sum_{ij} (G_{\omega,s'}^+(z, \mu_i, \phi_j) + G_{\omega,s'}^-(z, -\mu_i, \phi_j)) w_{\mu_i} w_{\phi_j} \right] d\omega \\
&= \frac{1}{\sum_{s'} \int_{\omega=0}^{\omega_m} \frac{C_{\omega,s'}}{\tau_{\omega,s'}} d\omega} \sum_{s'} \int_{\omega=0}^{\omega_m} \frac{1}{\tau_{\omega,s'}} \\
&\quad \times \left[\sum_{ij} \left(\int_0^d (C_{\omega,s'} \Delta\bar{T} + \bar{Q}_{\omega,s'} \tau_{\omega,s'}) \exp\left(-\frac{\gamma_{ij}^{\omega,s'}}{\mu_i \Lambda_{\omega,s'}} |z' - z|\right) dz' \right) \frac{w_{\mu_i} w_{\phi_j}}{4\pi \mu_i \Lambda_{\omega,s'}} \right. \\
&\quad + \sum_{ij} \sum_{i'j'} \sum_s (T_{kk',s's}^+ \bar{c}_{\omega,s}^+(0, \mu_{i'}, \phi_{j'}) + T_{kk',s's}^- \bar{c}_{\omega,s}^-(d, \mu_{i'}, \phi_{j'})) w_{\mu_i} w_{\phi_j} \\
&\quad \quad \times \exp\left(-\frac{\gamma_{ij}^{\omega,s'}}{\mu_i \Lambda_{\omega,s'}} z\right) \\
&\quad + \sum_{ij} \sum_{i'j'} \sum_s (B_{kk',s's}^+ \bar{c}_{\omega,s}^+(0, \mu_{i'}, \phi_{j'}) + B_{kk',s's}^- \bar{c}_{\omega,s}^-(d, \mu_{i'}, \phi_{j'})) w_{\mu_i} w_{\phi_j} \\
&\quad \quad \left. \times \exp\left(-\frac{\gamma_{ij}^{\omega,s'}}{\mu_i \Lambda_{\omega,s'}} (d - z)\right) \right] d\omega
\end{aligned} \tag{B.13}$$

Let us analyze the right hand side (RHS) of this equation term-by-term. For simplicity, let $\Omega = \sum_{s'} \int_{\omega=0}^{\omega_m} \frac{C_{\omega,s'}}{\tau_{\omega,s'}} d\omega$. The first term in the RHS of equation B.13 becomes:

$$\begin{aligned}
& \frac{1}{\Omega} \sum_{s'} \int_{\omega=0}^{\omega_m} \frac{1}{\tau_{\omega,s'}} \left[\sum_{ij} \left(\int_0^d (C_{\omega,s'} \Delta \bar{T} + \bar{Q}_{\omega,s'} \tau_{\omega,s'}) \exp\left(-\frac{\gamma_{ij}^{\omega,s'}}{\mu_i \Lambda_{\omega,s'}} |z' - z|\right) dz' \right) \right. \\
& \quad \left. \times \frac{w_{\mu_i} w_{\phi_j}}{4\pi \mu_i \Lambda_{\omega,s'}} d\omega \right] \\
&= \frac{1}{\Omega} \sum_{s'} \int_0^d \Delta \bar{T} \left[\int_{\omega=0}^{\omega_m} \left(\frac{C_{\omega,s'}}{4\pi \tau_{\omega,s'} \Lambda_{\omega,s'}} \sum_{ij} \frac{w_{\mu_i} w_{\phi_j}}{\mu_i} \exp\left(-\frac{\gamma_{ij}^{\omega,s'}}{\mu_i \Lambda_{\omega,s'}} |z' - z|\right) \right) d\omega \right] dz' \\
& \quad + \frac{1}{\Omega} \sum_{s'} \int_{\omega=0}^{\omega_m} \bar{Q}_{\omega,s'} \left[\sum_{ij} \left(\int_0^z \exp\left(-\frac{\gamma_{ij}^{\omega,s'}}{\mu_i \Lambda_{\omega,s'}} |z' - z|\right) dz' \right. \right. \\
& \quad \left. \left. + \int_z^d \exp\left(-\frac{\gamma_{ij}^{\omega,s'}}{\mu_i \Lambda_{\omega,s'}} |z' - z|\right) dz' \right) \frac{w_{\mu_i} w_{\phi_j}}{4\pi \mu_i \Lambda_{\omega,s'}} \right] \\
&= \frac{1}{\Omega} \sum_{s'} \int_0^d \Delta \bar{T} \left[\int_{\omega=0}^{\omega_m} \left(\frac{C_{\omega,s'}}{4\pi \tau_{\omega,s'} \Lambda_{\omega,s'}} \sum_{ij} \frac{w_{\mu_i} w_{\phi_j}}{\mu_i} \exp\left(-\frac{\gamma_{ij}^{\omega,s'}}{\mu_i \Lambda_{\omega,s'}} |z' - z|\right) \right) d\omega \right] dz' \\
& \quad + \frac{1}{\Omega} \sum_{s'} \int_{\omega=0}^{\omega_m} \bar{Q}_{\omega,s'} \left[\sum_{ij} \left(2 - \exp\left(-\frac{\gamma_{ij}^{\omega,s'}}{\mu_i \Lambda_{\omega,s'}} z\right) - \exp\left(-\frac{\gamma_{ij}^{\omega,s'}}{\mu_i \Lambda_{\omega,s'}} (d - z)\right) \right) \right. \\
& \quad \left. \times \frac{w_{\mu_i} w_{\phi_j}}{4\pi \gamma_{ij}^{\omega,s'}} \right] d\omega \\
&= \int_0^d \Delta \bar{T} [K_1^1(z', z)] dz' + f_1^1(z)
\end{aligned}$$

(B.14)

Similarly, the second term in the RHS of equation B.13 becomes:

$$\begin{aligned}
& \frac{1}{\Omega} \sum_{s'} \int_{\omega=0}^{\omega_m} \frac{1}{\tau_{\omega,s'}} \left[\sum_{ij} \sum_{i'j'} \sum_s \left(T_{kk',s's}^+ \bar{c}_{\omega,s}^+ (0, \mu_{i'}, \phi_{j'}) + T_{kk',s's}^- \bar{c}_{\omega,s}^- (d, \mu_{i'}, \phi_{j'}) \right) \right. \\
& \quad \left. \times w_{\mu_i} w_{\phi_j} \exp \left(-\frac{\gamma_{ij}^{\omega,s'}}{\mu_i \Lambda_{\omega,s'}} z \right) \right] d\omega \\
& = \frac{1}{\Omega} \sum_{s'} \int_{\omega=0}^{\omega_m} \frac{1}{\tau_{\omega,s'}} \left[\sum_{ij} \sum_{i'j'} \sum_s \sum_{s''} \left(\frac{\alpha_{\omega,s,s''}^{\text{spec}} p_{\omega,s''}}{4\pi \mu_{i'} \Lambda_{\omega,s''}} \right. \right. \\
& \quad \left. \left. \times \left(I_{i'j',\omega s''}^+ T_{kk',s's}^+ + I_{i'j',\omega s''}^- T_{kk',s's}^- \right) w_{\mu_i} w_{\phi_j} \exp \left(-\frac{\gamma_{ij}^{\omega,s'}}{\mu_i \Lambda_{\omega,s'}} z \right) \right) \right. \\
& \quad \left. + \sum_{ij} \sum_{i'j'} \sum_{i''j''} \sum_s \sum_{s''} \left(\frac{\alpha_{\omega,s,s''}^{\text{diff}} (1 - p_{\omega,s''}) w_{\mu_{i''}} w_{\phi_{j''}}}{4\pi^2 \Lambda_{\omega,s''}} \right. \right. \\
& \quad \left. \left. \times \left(I_{i''j'',\omega s''}^+ T_{kk',s's}^+ + I_{i''j'',\omega s''}^- T_{kk',s's}^- \right) w_{\mu_i} w_{\phi_j} \exp \left(-\frac{\gamma_{ij}^{\omega,s'}}{\mu_i \Lambda_{\omega,s'}} z \right) \right) \right] d\omega \\
& = f_2^1(z) + f_2^2(z) + \int_0^d \Delta \bar{T} \left[K_2^1(z', z) + K_2^2(z', z) \right] dz'
\end{aligned} \tag{B.15}$$

where,

$$\begin{aligned}
f_2^1(z) & = \frac{1}{\Omega} \sum_{s'} \int_{\omega=0}^{\omega_m} \frac{1}{\tau_{\omega,s'}} \\
& \quad \times \left[\sum_{ij} \sum_{i'j'} \sum_s \sum_{s''} \left(\frac{\alpha_{\omega,s,s''}^{\text{spec}} \bar{Q}_{\omega,s''} \tau_{\omega,s''} p_{\omega,s''} (T_{kk',s's}^+ + T_{kk',s's}^-)}{4\pi \gamma_{\mu_i \phi_j}^{\omega,s''}} \right) \right. \\
& \quad \left. \times \left(1 - \exp \left(-\frac{\gamma_{i'j'}^{\omega,s''}}{\mu_{i'} \Lambda_{\omega,s''}} d \right) \right) \exp \left(-\frac{\gamma_{ij}^{\omega,s'}}{\mu_i \Lambda_{\omega,s'}} z \right) w_{\mu_i} w_{\phi_j} \right] d\omega
\end{aligned} \tag{B.16}$$

$$\begin{aligned}
f_2^2(z) & = \frac{1}{\Omega} \sum_{s'} \int_{\omega=0}^{\omega_m} \frac{1}{\tau_{\omega,s'}} \\
& \quad \times \left[\sum_{ij} \sum_{i'j'} \sum_{i''j''} \sum_{s''} \left(\frac{\alpha_{\omega,s,s''}^{\text{diff}} \bar{Q}_{\omega,s''} \tau_{\omega,s''} (1 - p_{\omega,s''}) (T_{kk',s's}^+ + T_{kk',s's}^-) \mu_{i''} w_{\mu_{i''}} w_{\phi_{j''}}}{4\pi^2 \gamma_{i''j''}^{\omega,s''}} \right) \right. \\
& \quad \left. \times \left(1 - \exp \left(-\frac{\gamma_{i''j''}^{\omega,s''}}{\mu_{i''} \Lambda_{\omega,s''}} d \right) \right) w_{\mu_i} w_{\phi_j} \exp \left(-\frac{\gamma_{ij}^{\omega,s'}}{\mu_i \Lambda_{\omega,s'}} z \right) \right] d\omega
\end{aligned} \tag{B.17}$$

$$\begin{aligned}
K_2^1(z', z) &= \frac{1}{\Omega} \sum_{s'} \int_{\omega=0}^{\omega_m} \frac{1}{\tau_{\omega, s'}} \\
&\times \left[\sum_{ij} \sum_{i'j'} \sum_s \sum_{s''} \left(\frac{\alpha_{\omega, s, s''}^{\text{spec}} C_{\omega, s''} p_{\omega, s''}}{4\pi \mu_{i'} \Lambda_{\omega, s''}} \left(\exp\left(-\frac{\gamma_{i'j'}^{\omega, s''}}{\mu_{i'} \Lambda_{\omega, s''}} z'\right) T_{kk', s's}^+ \right. \right. \right. \\
&\left. \left. \left. + \exp\left(-\frac{\gamma_{i'j'}^{\omega, s''}}{\mu_{i'} \Lambda_{\omega, s''}} (d - z')\right) T_{kk', s's}^- \right) w_{\mu_i} w_{\phi_j} \exp\left(-\frac{\gamma_{ij}^{\omega, s'}}{\mu_i \Lambda_{\omega, s'}} z\right) \right] d\omega
\end{aligned} \tag{B.18}$$

$$\begin{aligned}
K_2^2(z', z) &= \frac{1}{\Omega} \sum_{s'} \int_{\omega=0}^{\omega_m} \frac{1}{\tau_{\omega, s'}} \left[\sum_{ij} \sum_{i'j'} \sum_{i''j''} \sum_{s's''} \left(\frac{\alpha_{\omega, s, s''}^{\text{diff}} C_{\omega, s''} (1 - p_{\omega, s''}) w_{\mu_{i''}} w_{\phi_{j''}}}{4\pi^2 \Lambda_{\omega, s''}} \right. \right. \\
&\times \left(\exp\left(-\frac{\gamma_{i''j''}^{\omega, s''}}{\mu_{i''} \Lambda_{\omega, s''}} z'\right) T_{kk', s's}^+ + \exp\left(-\frac{\gamma_{i''j''}^{\omega, s''}}{\mu_{i''} \Lambda_{\omega, s''}} (d - z')\right) T_{kk', s's}^- \right) \\
&\left. \left. \times w_{\mu_i} w_{\phi_j} \exp\left(-\frac{\gamma_{ij}^{\omega, s'}}{\mu_i \Lambda_{\omega, s'}} z\right) \right] d\omega
\end{aligned} \tag{B.19}$$

and the third term in the RHS of equation B.13 becomes

$$\begin{aligned}
&\frac{1}{\Omega} \sum_{s'} \int_{\omega=0}^{\omega_m} \frac{1}{\tau_{\omega, s'}} \left[\sum_{ij} \sum_{i'j'} \sum_s \left(B_{kk', s's}^+ \bar{c}_{\omega, s}^+ (0, \mu_{i'}, \phi_{j'}) + B_{kk', s's}^- \bar{c}_{\omega, s}^- (d, \mu_{i'}, \phi_{j'}) \right) \right. \\
&\times \left. w_{\mu_i} w_{\phi_j} \exp\left(-\frac{\gamma_{ij}^{\omega, s'}}{\mu_i \Lambda_{\omega, s'}} (d - z)\right) \right] d\omega \\
&= \frac{1}{\Omega} \sum_{s'} \int_{\omega=0}^{\omega_m} \frac{1}{\tau_{\omega, s'}} \left[\sum_{ij} \sum_{i'j'} \sum_s \sum_{s''} \left(\frac{\alpha_{\omega, s, s''}^{\text{spec}} p_{\omega, s''}}{4\pi \mu_{i'} \Lambda_{\omega, s''}} \right. \right. \\
&\times \left. \left(I_{i'j', \omega s''}^+ B_{kk', s's}^+ + I_{i'j', \omega s''}^- B_{kk', s's}^- \right) w_{\mu_i} w_{\phi_j} \exp\left(-\frac{\gamma_{ij}^{\omega, s'}}{\mu_i \Lambda_{\omega, s'}} (d - z)\right) \right) \\
&+ \sum_{ij} \sum_{i'j'} \sum_{i''j''} \sum_s \sum_{s''} \left(\frac{w_{\mu_{i''}} w_{\phi_{j''}} \alpha_{\omega, s, s''}^{\text{diff}} (1 - p_{\omega, s''})}{4\pi^2 \Lambda_{\omega, s''}} \right. \\
&\times \left. \left(I_{i''j'', \omega s''}^+ B_{kk', s's}^+ + I_{i''j'', \omega s''}^- B_{kk', s's}^- \right) w_{\mu_i} w_{\phi_j} \exp\left(-\frac{\gamma_{ij}^{\omega, s'}}{\mu_i \Lambda_{\omega, s'}} (d - z)\right) \right) \left. \right] d\omega \\
&= f_3^1(z) + f_3^2(z) + \int_0^d \Delta \bar{T} \left[K_3^1(z', z) + K_3^2(z', z) \right] dz'
\end{aligned} \tag{B.20}$$

where,

$$\begin{aligned}
f_3^1(z) &= \frac{1}{\Omega} \sum_{s'} \int_{\omega=0}^{\omega_m} \frac{1}{\tau_{\omega,s'}} \left[\sum_{ij} \sum_{i'j'} \sum_s \sum_{s''} \right. \\
&\quad \times \left(\frac{\alpha_{\omega,s,s''}^{\text{spec}} \bar{Q}_{\omega,s''} \tau_{\omega,s''} p_{\omega,s''}}{4\pi \gamma_{\mu_i' \phi_j'}^{\omega,s''}} \left(1 - \exp\left(-\frac{\gamma_{i'j'}^{\omega,s''}}{\mu_{i'} \Lambda_{\omega,s''}} d\right) \right) \right. \\
&\quad \left. \left. \times \left(B_{kk',s's}^+ + B_{kk',s's}^- \right) w_{\mu_i} w_{\phi_j} \exp\left(-\frac{\gamma_{ij}^{\omega,s'}}{\mu_i \Lambda_{\omega,s'}} (d-z)\right) \right) \right] d\omega
\end{aligned} \tag{B.21}$$

$$\begin{aligned}
f_3^2(z) &= \frac{1}{\Omega} \sum_{s'} \int_{\omega=0}^{\omega_m} \frac{1}{\tau_{\omega,s'}} \\
&\quad \times \left[\sum_{ij} \sum_{i'j'} \sum_{i''j''} \sum_s \sum_{s''} \left(\frac{\alpha_{\omega,s,s''}^{\text{diff}} \bar{Q}_{\omega,s''} \tau_{\omega,s''} \mu_{i''} w_{\mu_{i''}} w_{\phi_{k''}} (1 - p_{\omega,s''})}{4\pi^2 \gamma_{i''j''}^{\omega,s''}} \right) \right. \\
&\quad \times \left(1 - \exp\left(-\frac{\gamma_{i''j''}^{\omega,s''}}{\mu_{i''} \Lambda_{\omega,s''}} d\right) \right) (B_{kk',s's}^+ + B_{kk',s's}^-) \\
&\quad \left. \times w_{\mu_i} w_{\phi_j} \exp\left(-\frac{\gamma_{ij}^{\omega,s'}}{\mu_i \Lambda_{\omega,s'}} (d-z)\right) \right] d\omega
\end{aligned} \tag{B.22}$$

$$\begin{aligned}
K_3^1(z', z) &= \frac{1}{\Omega} \sum_{s'} \int_{\omega=0}^{\omega_m} \frac{1}{\tau_{\omega,s'}} \\
&\quad \times \left[\sum_{ij} \sum_{i'j'} \sum_s \sum_{s''} \left(\frac{\alpha_{\omega,s,s''}^{\text{spec}} C_{\omega,s''} p_{\omega,s''}}{4\pi \mu_{i'} \Lambda_{\omega,s''}} \left(\exp\left(-\frac{\gamma_{i'j'}^{\omega,s''}}{\mu_{i'} \Lambda_{\omega,s''}} z'\right) B_{kk',s's}^+ \right. \right. \right. \\
&\quad \left. \left. + \exp\left(-\frac{\gamma_{i'j'}^{\omega,s''}}{\mu_{i'} \Lambda_{\omega,s''}} (d-z')\right) B_{kk',s's}^- \right) \right. \\
&\quad \left. \left. \times w_{\mu_i} w_{\phi_j} \exp\left(-\frac{\gamma_{ij}^{\omega,s'}}{\mu_i \Lambda_{\omega,s'}} (d-z)\right) \right) \right] d\omega
\end{aligned} \tag{B.23}$$

$$\begin{aligned}
K_3^2(z', z) &= \frac{1}{\Omega} \sum_{s'} \int_{\omega=0}^{\omega_m} \frac{1}{\tau_{\omega, s'}} \\
&\times \left[\sum_{ij} \sum_{i'j'} \sum_{i''j''} \sum_s \sum_{s''} \left(\frac{\alpha_{\omega, s's''}^{\text{diff}} C_{\omega, s''} w_{\mu_{i''}} w_{\phi_{j''}} (1 - p_{\omega, s''})}{4\pi^2 \Lambda_{\omega, s''}} \right. \right. \\
&\times \left(\exp\left(-\frac{\gamma_{i''j''}^{\omega, s''}}{\mu_{i''} \Lambda_{\omega, s''}} z'\right) B_{kk', s's}^+ + \exp\left(-\frac{\gamma_{i''j''}^{\omega, s''}}{\mu_{i''} \Lambda_{\omega, s''}} (d - z')\right) B_{kk', s's}^- \right) \\
&\left. \left. \times w_{\mu_i} w_{\phi_j} \exp\left(-\frac{\gamma_{ij}^{\omega, s'}}{\mu_i \Lambda_{\omega, s'}} (d - z)\right) \right) \right] d\omega
\end{aligned} \tag{B.24}$$

Finally, the system to solve for (equation B.13) can be represented as an integral equation of the form:

$$\Delta\bar{T}(z) = f(z) + \int_0^d [K(z', z) \Delta\bar{T}(z')] dz' \tag{B.25}$$

where,

$$f(z) = f_1^1(z) + f_2^1(z) + f_2^2(z) + f_3^1(z) + f_3^2(z) \tag{B.26}$$

and

$$K(z', z) = K_1^1(z', z) + K_2^1(z', z) + K_2^2(z', z) + K_3^1(z', z) + K_3^2(z', z) \tag{B.27}$$

In this work, this integral equation is solved using the method of degenerate kernels, the details of which are described in section B.3.

B.3 The Method of Degenerate Kernels

The integral equation (equation B.25) can be solved using the method of degenerate kernels. First, the integral equation is rewritten as,

$$\Delta\bar{T}(\hat{z}) = f(\hat{z}) + \int_0^1 [\bar{K}(\hat{z}', \hat{z}) \Delta\bar{T}(\hat{z}')] d\hat{z}' \tag{B.28}$$

where $\hat{z} = z/d$ and $\bar{K}(\hat{z}', \hat{z}) = d \times K(z', z)$. Then the functions $\Delta\bar{T}(\hat{z})$, $f(\hat{z})$ and $K(\hat{z}', \hat{z})$ are expanded in a Fourier series :

$$\Delta\bar{T}_{(N)}(\hat{z}) = \frac{1}{2}t_0 + \sum_{m=1}^N t_m \cos(m\pi\hat{z}) \tag{B.29}$$

$$f_{(N)}(\hat{z}) = \frac{1}{2}f_0 + \sum_{m=1}^N f_n \cos(m\pi\hat{z}) \tag{B.30}$$

$$\begin{aligned} \bar{K}_{(N)}(\hat{z}', \hat{z}) &= \frac{1}{4}K_{00} + \frac{1}{2} \sum_{m=1}^N K_{m0} \cos(m\pi\hat{z}') + \frac{1}{2} \sum_{n=1}^N K_{0n} \cos(n\pi\hat{z}) \\ &+ \sum_{m=1}^N \sum_{n=1}^N K_{mn} \cos(m\pi\hat{z}') \cos(n\pi\hat{z}) \end{aligned}$$

where the Fourier coefficients are given by,

$$f_m = 2 \int_0^1 f(\hat{z}) \cos(m\pi\hat{z}) d\hat{z} \quad (\text{B.31})$$

and

$$K_{mn} = 4 \int_0^1 \int_0^1 K(\hat{z}', \hat{z}) \cos(m\pi\hat{z}') \cos(n\pi\hat{z}) d\hat{z}' d\hat{z} \quad (\text{B.32})$$

Here, a Fourier cosine series has been used for all of the functions by assuming that all the functions are even with respect to \hat{z} and \hat{z}' . This assumption is valid since the integral equation (equation B.25) has been solved only in the domain $\hat{z} \in [0, 1]$. After several algebraic simplifications, the expressions for the Fourier coefficients (equations B.31 and B.32) simplify into the following concise forms:

$$f_{1,m}^1 = -\frac{2}{\Omega} \sum_{s'} \int_{\omega=0}^{\omega_m} \bar{Q}_{\omega,s'} \left[\sum_{ij} (I_{1,s'}(m) + I_{2,s'}(m)) \frac{w_{\mu_i} w_{\phi_j}}{4\pi\gamma_{ij}^{\omega,s'}} \right] d\omega \quad (\text{B.33})$$

$$\begin{aligned} f_{2,m}^1 &= \frac{2}{\Omega} \sum_{s'} \int_{\omega=0}^{\omega_m} \frac{1}{\tau_{\omega,s'}} \\ &\times \left[\sum_{ij} \sum_{i'j'} \sum_s \sum_{s''} \left(\frac{\alpha_{\omega,s,s''}^{\text{spec}} \bar{Q}_{\omega,s''} \tau_{\omega,s''} p_{\omega,s''}}{4\pi\gamma_{\mu_i' \phi_j'}^{\omega,s''}} \left(1 - \exp\left(-\frac{\gamma_{i'j'}^{\omega,s''}}{\mu_{i'} \Lambda_{\omega,s''}} d\right) \right) \right) \right. \\ &\times \left. \left(T_{kk',s's}^+ + T_{kk',s's}^- \right) w_{\mu_i} w_{\phi_j} I_{1,s'}(m) \right] d\omega \end{aligned} \quad (\text{B.34})$$

$$\begin{aligned} f_{2,m}^2 &= \frac{2}{\Omega} \sum_{s'} \int_{\omega=0}^{\omega_m} \frac{1}{\tau_{\omega,s'}} \\ &\times \left[\sum_{ij} \sum_{i'j'} \sum_{i''j''} \sum_s \sum_{s''} \left(\frac{\alpha_{\omega,s,s''}^{\text{diff}} \bar{Q}_{\omega,s''} \tau_{\omega,s''} \mu_{i''} w_{\mu_{i''}} w_{\phi_{k''}} (1 - p_{\omega,s''})}{4\pi^2 \gamma_{i''j''}^{\omega,s''}} \right) \right. \\ &\times \left. \left(1 - \exp\left(-\frac{\gamma_{i''j''}^{\omega,s''}}{\mu_{i''} \Lambda_{\omega,s''}} d\right) \right) \left(T_{kk',s's}^+ + T_{kk',s's}^- \right) w_{\mu_i} w_{\phi_j} I_{1,s'}(m) \right] d\omega \end{aligned} \quad (\text{B.35})$$

$$\begin{aligned}
f_{3,m}^1 &= \frac{2}{\Omega} \sum_{s'} \int_{\omega=0}^{\omega_m} \frac{1}{\tau_{\omega,s'}} \\
&\times \left[\sum_{ij} \sum_{i'j'} \sum_s \sum_{s''} \left(\frac{\alpha_{\omega,s,s''}^{\text{spec}} \bar{Q}_{\omega,s''} \tau_{\omega,s''} p_{\omega,s''}}{4\pi \gamma_{\mu_i' \phi_j'}^{\omega,s''}} \left(1 - \exp \left(-\frac{\gamma_{i'j'}^{\omega,s''}}{\mu_i' \Lambda_{\omega,s''}} d \right) \right) \right) \right. \\
&\times \left. \left(B_{kk',s's}^+ + B_{kk',s's}^- \right) w_{\mu_i} w_{\phi_j} I_{2,s'}(m) \right] d\omega
\end{aligned} \tag{B.36}$$

$$\begin{aligned}
f_{3,m}^2 &= \frac{2}{\Omega} \sum_{s'} \int_{\omega=0}^{\omega_m} \frac{1}{\tau_{\omega,s'}} \\
&\times \left[\sum_{ij} \sum_{i'j'} \sum_{i''j''} \sum_s \sum_{s''} \left(\frac{\alpha_{\omega,s,s''}^{\text{diff}} \bar{Q}_{\omega,s''} \tau_{\omega,s''} (1 - p_{\omega,s''}) \mu_{i''} w_{\mu_{i''}} w_{\phi_{k''}}}{4\pi^2 \gamma_{i''j''}^{\omega,s''}} \right) \right. \\
&\times \left. \left(1 - \exp \left(-\frac{\gamma_{i''j''}^{\omega,s''}}{\mu_{i''} \Lambda_{\omega,s''}} d \right) \right) \left(B_{kk',s's}^+ + B_{kk',s's}^- \right) w_{\mu_i} w_{\phi_j} I_{2,s'}(m) \right] d\omega
\end{aligned} \tag{B.37}$$

$$K_{1,mn}^1 = \frac{4d}{\Omega} \sum_{s'} \left[\int_{\omega=0}^{\omega_m} \left(\frac{C_{\omega,s'}}{4\pi \tau_{\omega,s'} \Lambda_{\omega,s'}} \sum_{ij} \frac{w_{\mu_i} w_{\phi_j}}{\mu_i} I_{3,s'}(m,n) \right) d\omega \right] \tag{B.38}$$

$$\begin{aligned}
K_{2,mn}^1 &= \frac{4d}{\Omega} \sum_{s'} \int_{\omega=0}^{\omega_m} \frac{1}{\tau_{\omega,s'}} \left[\sum_{ij} \sum_{i'j'} \sum_s \sum_{s''} \left(\frac{\alpha_{\omega,s,s''}^{\text{spec}} C_{\omega,s''} p_{\omega,s''}}{4\pi \mu_{i'} \Lambda_{\omega,s''}} \right) \right. \\
&\times \left. \left(I'_{1,s''}(m) T_{kk',s's}^+ + I'_{2,s''}(m) T_{kk',s's}^- \right) w_{\mu_i} w_{\phi_j} I_{1,s'}(n) \right] d\omega
\end{aligned} \tag{B.39}$$

$$\begin{aligned}
K_{2,mn}^2 &= \frac{4d}{\Omega} \sum_{s'} \int_{\omega=0}^{\omega_m} \frac{1}{\tau_{\omega,s'}} \left[\sum_{ij} \sum_{i'j'} \sum_{i''j''} \sum_s \sum_{s''} \left(\frac{\alpha_{\omega,s,s''}^{\text{diff}} C_{\omega,s''} w_{\mu_{i''}} w_{\phi_{j''}} (1 - p_{\omega,s''})}{4\pi^2 \Lambda_{\omega,s''}} \right) \right. \\
&\times \left. \left(I''_{1,s''}(m) T_{kk',s's}^+ + I''_{2,s''}(m) T_{kk',s's}^- \right) w_{\mu_i} w_{\phi_j} I_{1,s'}(n) \right] d\omega
\end{aligned} \tag{B.40}$$

$$\begin{aligned}
K_{3,mn}^1 &= \frac{4d}{\Omega} \sum_{s'} \int_{\omega=0}^{\omega_m} \frac{1}{\tau_{\omega,s'}} \left[\sum_{ij} \sum_{i'j'} \sum_s \sum_{s''} \left(\frac{\alpha_{\omega,s,s''}^{\text{spec}} C_{\omega,s''} p_{\omega,s''}}{4\pi \mu_{i'} \Lambda_{\omega,s''}} \right) \right. \\
&\times \left. \left(I'_{1,s''}(m) B_{kk',s's}^+ + I'_{2,s''}(m) B_{kk',s's}^- \right) w_{\mu_i} w_{\phi_j} I_{2,s'}(n) \right] d\omega
\end{aligned} \tag{B.41}$$

$$\begin{aligned}
K_{3,mn}^2 &= \frac{4d}{\Omega} \sum_{s'} \int_{\omega=0}^{\omega_m} \frac{1}{\tau_{\omega,s'}} \left[\sum_{ij} \sum_{i'j'} \sum_{i''j''} \sum_s \sum_{s''} \left(\frac{\alpha_{\omega,s s''}^{\text{spec}} C_{\omega,s''} w_{\mu_i''} w_{\phi_{j''}} (1 - p_{\omega,s''})}{4\pi^2 \Lambda_{\omega,s''}} \right. \right. \\
&\quad \left. \left. \times \left(I_{1,s''}''(m) B_{kk',s's}^+ + I_{2,s''}''(m) B_{kk',s's}^- \right) w_{\mu_i} w_{\phi_j} I_{2,s'}(n) \right) \right] d\omega
\end{aligned} \tag{B.42}$$

where,

$$\begin{aligned}
I_{1,s}(m) &= \int_0^1 \exp\left(-\frac{\gamma_{ij}^{\omega,s}}{\mu_i \text{Kn}_{\omega,s}^d} \hat{z}\right) \cos(m\pi \hat{z}) d\hat{z} \\
&= \frac{\frac{\gamma_{ij}^{\omega,s}}{\mu_i \text{Kn}_{\omega,s}^d}}{m^2 \pi^2 + \left(\frac{\gamma_{ij}^{\omega,s}}{\mu_i \text{Kn}_{\omega,s}^d}\right)^2} \left[1 - (-1)^m \exp\left(-\frac{\gamma_{ij}^{\omega,s}}{\mu_i \text{Kn}_{\omega,s}^d}\right) \right]
\end{aligned}$$

$$\begin{aligned}
I_{2,s}(m) &= \int_0^1 \exp\left(-\frac{\gamma_{ij}^{\omega,s}}{\mu_i \text{Kn}_{\omega,s}^d} (1 - \hat{z})\right) \cos(m\pi \hat{z}) d\hat{z} \\
&= \frac{\frac{\gamma_{ij}^{\omega,s}}{\mu_i \text{Kn}_{\omega,s}^d}}{m^2 \pi^2 + \left(\frac{\gamma_{ij}^{\omega,s}}{\mu_i \text{Kn}_{\omega,s}^d}\right)^2} \left[(-1)^m - \exp\left(-\frac{\gamma_{ij}^{\omega,s}}{\mu_i \text{Kn}_{\omega,s}^d}\right) \right]
\end{aligned}$$

$$\begin{aligned}
I_{3,s}(m,n) &= \int_0^1 \int_0^1 \exp\left(-\frac{\gamma_{ij}^{\omega,s}}{\mu_i \text{Kn}_{\omega,s}^d} |\hat{z}' - \hat{z}|\right) \cos(m\pi \hat{z}) \cos(n\pi \hat{z}') d\hat{z} d\hat{z}' \\
&= \begin{cases} \frac{\frac{\gamma_{ij}^{\omega,s}}{\mu_i \text{Kn}_{\omega,s}^d}}{m^2 \pi^2 + \left(\frac{\gamma_{ij}^{\omega,s}}{\mu_i \text{Kn}_{\omega,s}^d}\right)^2} [\delta_{mn} - (I_1(n) + (-1)^m I_2(n))] & \text{for } m \neq 0 \\ \frac{\frac{\gamma_{ij}^{\omega,s}}{\mu_i \text{Kn}_{\omega,s}^d}}{m^2 \pi^2 + \left(\frac{\gamma_{ij}^{\omega,s}}{\mu_i \text{Kn}_{\omega,s}^d}\right)^2} [2\delta_{mn} - (I_1(n) + (-1)^m I_2(n))] & \text{for } m = 0 \end{cases}
\end{aligned}$$

and primes (' and '') on I_1 , I_2 , and I_3 indicate that these functions are evaluated for $\{\mu', \phi'\}$ and $\{\mu'', \phi''\}$ respectively. These Fourier coefficients are substituted into the cosine series for the corresponding functions in the integral equation (equa-

tion B.25) to get,

$$\begin{aligned}
\frac{1}{2}t_0 + \sum_{m=1}^N t_m \cos(m\pi\hat{z}) &= \frac{1}{2}f_0 + \sum_{m=1}^N f_n \cos(m\pi\hat{z}) + \frac{1}{8}t_0K_{00} + \frac{1}{4}\sum_{n=1}^N t_0K_{0n} \cos(n\pi\hat{z}) \\
&+ \sum_{m=1}^N \left(\frac{t_0K_{m0}}{4} + \frac{K_{00}t_m}{4} + \sum_{n=1}^N \frac{t_0K_{mn} + t_mK_{0n}}{2} \cos(n\pi\hat{z}) \right) \int_0^1 \cos(m\pi\hat{z}') d\hat{z}' \\
&+ \sum_{m=1}^N \sum_{n=1}^N \left(\frac{t_mK_{n0}}{2} + \sum_{p=1}^N t_mK_{np} \cos(p\pi\hat{z}) \right) \int_0^1 \cos(m\pi\hat{z}') \cos(n\pi\hat{z}') d\hat{z}' \\
&= \frac{1}{2}f_0 + \sum_{m=1}^N f_n \cos(m\pi\hat{z}) + \frac{1}{8}t_0K_{00} + \frac{1}{4}\sum_{n=1}^N t_0K_{0n} \cos(n\pi\hat{z}) \\
&+ \frac{1}{2}\sum_{m=1}^N \left(\frac{t_mK_{m0}}{2} + \sum_{n=1}^N t_mK_{mn} \cos(n\pi\hat{z}) \right)
\end{aligned}$$

Due to the orthogonality of $\cos(m\pi\hat{z})$ in the interval $\hat{z} \in [0, 1]$, it is sufficient to solve for the Fourier coefficients (t_m) by grouping together the coefficients with the same index, which results in a system of linear equations in t_m :

$$\begin{aligned}
\left(\frac{1}{2} - \frac{1}{8}K_{00} \right) t_0 - \frac{1}{4} \sum_{n=1}^N K_{n0} t_n &= \frac{1}{2}f_0 \\
\sum_{n=1}^N \left(\delta_{nm} - \frac{1}{2}K_{nm} \right) t_n - \frac{1}{4}K_{0m}t_0 &= f_m \quad \text{for } m = 1, \dots, N
\end{aligned} \tag{B.43}$$

which can be written in a concise matrix form as:

$$Ft = f$$

which can be solved by standard matrix inversion techniques. The resulting solution (t_m) is used to calculate the temperature profile $\Delta\bar{T}(\eta, q, z)$ (equation B.29) and the phonon energy distribution functions $G_{\omega,s}^+(z, \mu_i, \phi_j)$ and $G_{\omega,s}^-(z, -\mu_i, \phi_j)$ (equation B.12) for each η and q as follows:

First, the expressions for $I_{\mu\phi,s}^+$ and $I_{\mu\phi,s}^-$ are simplified as,

$$\begin{aligned}
I_{\mu\phi,s}^+ &= C_{\omega,s} \int_0^d \Delta\bar{T} \exp\left(-\frac{\gamma_{\mu\phi}^{\omega,s}}{\mu\Lambda_{\omega,s}} z'\right) dz' + \bar{Q}_{\omega,s} \tau_{\omega,s} \Lambda_{\omega,s} \frac{\mu}{\gamma_{\mu\phi}^{\omega,s}} \left(1 - \exp\left(-\frac{\gamma_{\mu\phi}^{\omega,s}}{\mu\Lambda_{\omega,s}} d\right)\right) \\
&= C_{\omega,s} d \left(\frac{1}{2} t_0 \frac{\mu \text{Kn}_{\omega,s}^d}{\gamma_{\mu\phi}^{\omega,s}} \left(1 - \exp\left(-\frac{\gamma_{\mu\phi}^{\omega,s}}{\mu \text{Kn}_{\omega,s}^d}\right)\right) + \sum_{m=1}^N t_m I_{1,s}(m) \right) \\
&\quad + \bar{Q}_{\omega,s} \tau_{\omega,s} d \frac{\mu \text{Kn}_{\omega,s}^d}{\gamma_{\mu\phi}^{\omega,s}} \left(1 - \exp\left(-\frac{\gamma_{\mu\phi}^{\omega,s}}{\mu \text{Kn}_{\omega,s}^d}\right)\right)
\end{aligned}$$

$$\begin{aligned}
I_{\mu\phi,s}^- &= C_{\omega,s} \int_0^d \Delta\bar{T} \exp\left(-\frac{\gamma_{\mu\phi}^{\omega,s}}{\mu\Lambda_{\omega,s}} z'\right) dz' + \bar{Q}_{\omega,s} \tau_{\omega,s} \Lambda_{\omega,s} \frac{\mu}{\gamma_{\mu\phi}^{\omega,s}} \left(1 - \exp\left(-\frac{\gamma_{\mu\phi}^{\omega,s}}{\mu\Lambda_{\omega,s}} d\right)\right) \\
&= C_{\omega,s} d \left(\frac{1}{2} t_0 \frac{\mu \text{Kn}_{\omega,s}^d}{\gamma_{\mu\phi}^{\omega,s}} \left(1 - \exp\left(-\frac{\gamma_{\mu\phi}^{\omega,s}}{\mu \text{Kn}_{\omega,s}^d}\right)\right) + \sum_{m=1}^N t_m I_{2,s}(m) \right) \\
&\quad + \bar{Q}_{\omega,s} \tau_{\omega,s} d \frac{\mu \text{Kn}_{\omega,s}^d}{\gamma_{\mu\phi}^{\omega,s}} \left(1 - \exp\left(-\frac{\gamma_{\mu\phi}^{\omega,s}}{\mu \text{Kn}_{\omega,s}^d}\right)\right)
\end{aligned}$$

where $\text{Kn}_{\omega,s}^d = \Lambda_{\omega,s}/d$ is the Knudsen number of a phonon mode defined based on the thickness of the thin film. Next, using the expressions for $I_{\mu\phi,s}^+$ and $I_{\mu\phi,s}^-$, the expressions for $\bar{c}_{\omega,s}^+(0, \mu'_i, \phi'_j)$ and $\bar{c}_{\omega,s}^-(d, \mu'_i, \phi'_j)$ are evaluated, and finally the

expressions for $G_{\omega,s'}^+(\hat{z}, \mu_i, \phi_j)$ and $G_{\omega,s'}^-(\hat{z}, -\mu_i, \phi_j)$ are evaluated as,

$$\begin{aligned}
G_{\omega,s'}^+(\hat{z}, \mu_i, \phi_j) &= \left(\sum_{i'j'} \sum_s [T_{kk',s's}^+ \bar{c}_{\omega,s}^+(0, \mu_{i'}, \phi_{j'}) + T_{kk',s's}^- \bar{c}_{\omega,s}^-(d, \mu_{i'}, \phi_{j'})] \right) \\
&\quad \times \exp\left(-\frac{\gamma_{ij}^{\omega,s'}}{\mu_i \text{Kn}_{\omega,s'}^d} \hat{z}\right) \\
&\quad + \frac{1}{4\pi\gamma_{ij}^{\omega,s'}} \left(C_{\omega,s'} \frac{t_0}{2} + \bar{Q}_{\omega,s'} \tau_{\omega,s'} \right) \left[1 - \exp\left(-\frac{\gamma_{ij}^{\omega,s'}}{\mu_i \text{Kn}_{\omega,s'}^d} \hat{z}\right) \right] \\
&\quad + \frac{C_{\omega,s'}}{4\pi\mu_i \text{Kn}_{\omega,s'}^d} \sum_{m=1}^N t_m I_{3,s'}^1(m; \hat{z}) \\
G_{\omega,s'}^-(\hat{z}, -\mu_i, \phi_j) &= \left(\sum_{i'j'} \sum_s [B_{kk',s's}^+ \bar{c}_{\omega,s}^+(0, \mu_{i'}, \phi_{j'}) + B_{kk',s's}^- \bar{c}_{\omega,s}^-(d, \mu_{i'}, \phi_{j'})] \right) \\
&\quad \times \exp\left(-\frac{\gamma_{ij}^{\omega,s'}}{\mu_i \text{Kn}_{\omega,s'}^d} (1 - \hat{z})\right) \\
&\quad + \frac{1}{4\pi\gamma_{ij}^{\omega,s'}} \left(C_{\omega,s'} \frac{t_0}{2} + \bar{Q}_{\omega,s'} \tau_{\omega,s'} \right) \left[1 - \exp\left(-\frac{\gamma_{ij}^{\omega,s'}}{\mu_i \text{Kn}_{\omega,s'}^d} [1 - \hat{z}]\right) \right] \\
&\quad + \frac{C_{\omega,s'}}{4\pi\mu_i \text{Kn}_{\omega,s'}^d} \sum_{m=1}^N t_m I_{3,s'}^2(m; \hat{z})
\end{aligned}$$

(B.44)

where,

$$\begin{aligned}
I_{3,s}^1(m; \hat{z}) &= \int_0^{\hat{z}'} \exp\left(-\frac{\gamma_{ij}^{\omega,s}}{\mu_i \text{Kn}_{\omega,s}^d} [\hat{z}' - \hat{z}]\right) \cos(m\pi \hat{z}) d\hat{z} \\
&= \frac{1}{m^2 \pi^2 + \left(\frac{\gamma_{ij}^{\omega,s}}{\mu_i \text{Kn}_{\omega,s}^d}\right)^2} \left[\left(\frac{\gamma_{ij}^{\omega,s}}{\mu_i \text{Kn}_{\omega,s}^d} \cos(m\pi \hat{z}') + m\pi \sin(m\pi \hat{z}') \right) \right. \\
&\quad \left. - \frac{\gamma_{ij}^{\omega,s}}{\mu_i \text{Kn}_{\omega,s}^d} \exp\left(-\frac{\gamma_{ij}^{\omega,s}}{\mu_i \text{Kn}_{\omega,s}^d} \hat{z}'\right) \right] \\
I_{3,s}^2(m; \hat{z}) &= \int_{\hat{z}'}^1 \exp\left(\frac{\gamma_{ij}^{\omega,s}}{\mu_i \text{Kn}_{\omega,s}^d} [\hat{z}' - \hat{z}]\right) \cos(m\pi \hat{z}) d\hat{z} \\
&= \frac{1}{m^2 \pi^2 + \left(\frac{\gamma_{ij}^{\omega,s}}{\mu_i \text{Kn}_{\omega,s}^d}\right)^2} \left[\left(-\frac{\gamma_{ij}^{\omega,s}}{\mu_i \text{Kn}_{\omega,s}^d} (-1)^m \right) \exp\left(-\frac{\gamma_{ij}^{\omega,s}}{\mu_i \text{Kn}_{\omega,s}^d} (1 - \hat{z}')\right) \right. \\
&\quad \left. - \left(-\frac{\gamma_{ij}^{\omega,s}}{\mu_i \text{Kn}_{\omega,s}^d} \cos(m\pi \hat{z}') + m\pi \sin(m\pi \hat{z}') \right) \right]
\end{aligned}$$

Once again, as in the steady state condition, these general solutions for G_ω are substituted into the expression for heat flux and the suppression in thermal conductivity due to phonon boundary scattering is derived for the transient transport condition in the main article.